

Titre: Field-Induced Modulation of Single-Exciton Emission in ZnSe:Te₂
Title: Under Resonant and Non Resonant Excitation

Auteur: Anne-Laurence Phaneuf-L'Heureux
Author:

Date: 2022

Type: Mémoire ou thèse / Dissertation or Thesis

Référence: Phaneuf-L'Heureux, A.-L. (2022). Field-Induced Modulation of Single-Exciton Emission in ZnSe:Te₂ Under Resonant and Non Resonant Excitation [Thèse de doctorat, Polytechnique Montréal]. PolyPublie.
Citation: <https://publications.polymtl.ca/10558/>

 **Document en libre accès dans PolyPublie**
Open Access document in PolyPublie

URL de PolyPublie: <https://publications.polymtl.ca/10558/>
PolyPublie URL:

Directeurs de recherche: Sébastien Francoeur
Advisors:

Programme: Génie physique
Program:

POLYTECHNIQUE MONTRÉAL

affiliée à l'Université de Montréal

**Field-induced modulation of single-exciton emission in ZnSe:Te₂ under resonant
and non resonant excitation**

ANNE-LAURENCE PHANEUF-L'HEUREUX

Département de génie physique

Thèse présentée en vue de l'obtention du diplôme de *Philosophiæ Doctor*
Génie physique

Août 2022

POLYTECHNIQUE MONTRÉAL

affiliée à l'Université de Montréal

Cette thèse intitulée :

**Field-induced modulation of single-exciton emission in ZnSe:Te₂ under resonant
and non resonant excitation**

présentée par **Anne-Laurence PHANEUF-L'HEUREUX**

en vue de l'obtention du diplôme de *Philosophiæ Doctor*

a été dûment acceptée par le jury d'examen constitué de :

Alain ROCHEFORT, président

Sébastien FRANCOEUR, membre et directeur de recherche

Stéphane KÉNA-COHEN, membre

William A. COISH, membre externe

DEDICATION

“Behind them the moon was rising out of the sea that grew all radiant and transfigured in her light. Every little cove along the curving roads was a marvel of dancing ripples. The waves broke with a soft swish on the rocks below them, and the tang of the sea was in the strong, fresh air.

‘Oh, but it’s good to be alive and to be going home,’ breathed Anne.”

LUCY MAUD MONTGOMERY, *Anne of Green Gables*

ACKNOWLEDGEMENTS

I first would like to thank the jury members, Professors Alain Rochefort, Stéphane Kéna-Cohen and Bill Coish, for agreeing to evaluate this thesis, as well as the National Sciences and Engineering Research Council (NSERC) for funding this work through its Vanier Canada Graduate Scholarships program.

I also wish to thank my supervisor Sébastien Francoeur for having trained me since the third year of my undergraduate studies to become the researcher that I am today. Thank you for this opportunity of working on stimulating research projects and of developing a range of expertise essential to my work.

I thank from the bottom of my heart Alaric Bergeron, Gabriel Éthier-Majcher and Philippe St-Jean, my laboratory big brothers and mentors, who taught me everything. Thank you for your patience and enthusiasm in sharing your knowledge!

Thanks to my other lab colleagues, with whom I always had the best time working and chatting: Vincent Aymong, Alexandre Favron, Maxime Gendron-Paul, Jean-Francis Germain, Clément Gradziel, John Ibrahim, Patrick Lavoie, Simon Michel, Léonard Schué. Your presence was the path that I followed even in my darkest hours. Thanks also to the interns who contributed to the research projects in which I was involved.

A special thanks to Marcin Wajs for sharing the highs and lows of my last experiment and of the whimsical setup. Without your help, I would have been disheartened many times! Thanks also to Mathias Pont for improving the setup and the knowledge of our material. This made my life so much easier afterwards.

Thanks to my office colleagues and from other labs, who made my life as a graduate student extraordinary (and sometimes kindly lent me equipment!): Jean-Sébastien Boisvert, Étienne Boulais, Marie-Hélène Bussièrès-Hersir, Samuel Castonguay, François Daoust, Frédéric Monet, Amélie St-Georges-Robillard. A special thanks to Audrey Laurence, in which I found a dear friend. Our discussions always did me good, whether we would share experiences in our studies, passions or anecdotes from our lives. Thank you for understanding me so well.

Thanks to the technicians Eugène Babian, Émile Jetzer, Mikaël Leduc and Jean-Paul Lévesque, whose expertise and advice were precious. Without you, science would not be possible.

I now realize that I have crossed path with a lot of people during my **nine** years as a graduate student!

I also wish to express gratitude to my parents, first to my mother, Jacinthe, for her unconditional support. She would certainly be very proud if she were still with us today. Also, to my father, Laurent, for his presence, his generosity and for making me smile with his sense of humor. You always have put my education first, and it is largely because of your commitment to offer me the best that I am here defending my thesis today.

Thanks to Laurence Olivier Marion-Ouellet and his family for supporting me during the majority of my graduate studies. I am grateful to you, although our paths have now parted.

Thanks to my psychologist Amparo Garcia, who helped me develop invaluable tools to face difficulties and doubts. My Ph.D. has been psychologically exhausting and without the work that we did together, I would probably not have completed my thesis. In retrospect, I have grown from this experience, but at the price of superhuman efforts and great suffering. Mental health is a key success factor and must not be overlooked. I consequently wish to bring a message of compassion and understanding to future and current students. I encourage you strongly to discuss these issues and to reach out for any help you would need to feel comfortable. Suffering, in my humble opinion, is not essential to becoming a competent researcher, engineer or scientist. By opening up to others, you will see that everyone faces rough moments, it is simply human. To universities and faculties, I wish to emphasize the importance of addressing graduate student mental health issues and providing resources and training for those who supervise them.

Thanks to my friends who supported me through all these years: Patrick Chung, Pascal Dandavino-Forget, Anna Gagné-Landmann, Sylvain Gagnon, Isabelle Hallé, Minh-Han Le, Faiza Maskhouni, Gabriel Taillon. Moments spent relaxing with you were my oasis in the desert.

A special thanks to Sébastien Laberge for lending me his programming skills to solve the polariton equation. Thanks to you, my analysis has more weight! Thank you for your enthusiasm in keeping motivated to write. Your friendship is dear to me.

And, finally, an immeasurable thanks to my dear Alexandre, with whom I could find the courage and strength to complete this thesis. Your presence, listening and support made all the difference. With all my love, I thank you. Let's go riding our bicycles, now!

REMERCIEMENTS

Je désire d'abord remercier les membres du jury, les professeurs Alain Rochefort, Stéphane Kéna-Cohen et Bill Coish, d'avoir accepté d'évaluer cette thèse, ainsi que l'organisme subventionnaire qui a financé ces travaux: le Conseil de recherches en sciences naturelles et génie du Canada (CRSNG), avec son programme de bourses d'études supérieures du Canada Vanier.

Ensuite, je tiens à remercier mon directeur, Sébastien Francoeur, de m'avoir prise sous son aile dès ma troisième année de baccalauréat et de m'avoir formée à devenir la chercheuse que je suis maintenant. Merci pour cette opportunité de travailler sur des projets de recherche stimulants et de développer un éventail de compétences nécessaires à mon travail.

Je remercie du fond du coeur Alaric Bergeron, Gabriel Éthier-Majcher et Philippe St-Jean, mes grands frères de laboratoire, mes mentors, qui m'ont tout appris. Merci de votre patience et de votre enthousiasme à partager votre savoir!

Merci à mes autres collègues de laboratoire, avec qui j'ai toujours eu beaucoup de plaisir à travailler et à discuter: Vincent Aymong, Alexandre Favron, Maxime Gendron-Paul, Jean-Francis Germain, Clément Gradziel, John Ibrahim, Patrick Lavoie, Simon Michel, Léonard Schué. Votre présence a été le chemin sur lequel j'ai avancé, même dans mes heures les plus sombres. Merci également à tous les stagiaires qui ont contribué aux différents projets de recherche dans lesquels j'ai été impliquée.

Un merci tout spécial à Marcin Wajs d'avoir partagé avec moi les hauts et les bas de ma dernière expérience ainsi que les caprices des montages. Sans ton aide, je me serais effondrée de découragement des milliers de fois! Merci également à Mathias Pont pour les améliorations apportées au montage et à la compréhension de notre matériau, cela a grandement facilité ma vie par la suite.

Merci à mes collègues de bureau et d'autres laboratoires qui ont contribué à rendre ma vie étudiante extraordinaire (et m'ont parfois gentiment prêté du matériel!) : Jean-Sébastien Boisvert, Étienne Boulais, Marie-Hélène Bussièrès-Hersir, Samuel Castonguay, François Daoust, Frédéric Monet, Amélie St-Georges-Robillard. Un merci particulier à Audrey Laurence, en

qui j'ai trouvé une amie précieuse. Nos discussions m'ont toujours fait un grand bien, que nous partagions nos joies et peines aux études, nos passions ou des anecdotes de nos vies. Merci de m'avoir aussi bien comprise.

Merci aux techniciens Eugène Babian, Émile Jetzer, Mikaël Leduc et Jean-Paul Lévesque, dont l'expertise et les conseils ont été précieux. Sans vous, la science ne serait tout simplement pas possible!

Je réalise ainsi que j'en ai côtoyé, des gens, en **neuf** ans aux cycles supérieurs!

Je désire également exprimer une reconnaissance infinie à mes parents. À ma mère, Jacinthe, pour son support inconditionnel, qui serait sans aucun doute très fière de moi si elle était encore avec nous. À mon père, Laurent, pour sa présence, sa générosité et son humour qui me fait toujours sourire. Vous avez toujours misé coûte que coûte sur mon éducation, et c'est grâce à votre engagement à toujours m'offrir le meilleur que je suis ici aujourd'hui à soutenir ma thèse de doctorat.

Merci à Laurence Olivier Marion-Ouellet et à sa famille, qui m'ont soutenue pendant la grande majorité de mes études graduées. Malgré que nos chemins se soient maintenant séparés, je vous en suis reconnaissante.

Merci à ma psychologue Amparo Garcia, qui m'a aidée à développer des outils inestimables pour affronter les difficultés et les doutes. La période du doctorat a été pour moi extrêmement éprouvante émotionnellement, et sans le travail que nous avons réalisé ensemble, je n'aurais sans doute pas terminé cette thèse. Je peux avec le recul dire que je sors grandie de cette expérience, mais seulement au terme de souffrances indicibles et d'efforts surhumains. La santé mentale, ai-je appris, est un facteur déterminant dans la réussite et ne doit en aucun cas être négligée. Aux étudiants, futurs ou actuels, je souhaite apporter un message de compassion et de compréhension. Je vous encourage fortement à parler de ces enjeux et à aller chercher les outils dont vous avez besoin pour vous sentir bien. Il n'est pas nécessaire, à mon humble avis, de souffrir pour devenir un bon scientifique, un bon ingénieur ou un bon chercheur. En vous ouvrant aux autres, vous verrez également que tous se heurtent à des moments difficiles, c'est simplement humain. Aux universités et facultés, je souhaite souligner l'importance de s'intéresser à la santé mentale des étudiants gradués, de leur offrir des ressources et de fournir de la formation à ce sujet à ceux qui les encadrent.

Merci à mes amis, dont le support m'a toujours accompagnée : Patrick Chung, Pascal Dandavino-Forget, Anna Gagné-Landmann, Sylvain Gagnon, Isabelle Hallé, Minh-Han Le, Faiza Maskhouni, Gabriel Taillon. Les moments de détente passés à vos côtés ont été une véritable oasis dans le désert.

Un merci tout spécial à Sébastien Laberge de m'avoir prêté ses talents de programmeur pour résoudre l'équation du polariton. Grâce à toi, mon analyse a beaucoup plus d'aplomb! Merci également de tout l'enthousiasme que tu as mis à galvaniser ma motivation à rédiger. Ton amitié m'est précieuse.

Et, pour finir, un merci incommensurable à mon cher Alexandre, auprès de qui j'ai pu trouver le courage et la force nécessaires pour terminer cette thèse. Ta présence, ton écoute et tes encouragements ont fait toute la différence. Avec tout mon amour, je t'en remercie. Allons faire du vélo, maintenant!

RÉSUMÉ

L'avènement de l'information quantique incite au déploiement d'un réseau de télécommunication quantique permettant de connecter différents agents distants (tels des ordinateurs) entre eux, une technologie garantissant une sécurité absolue des communications. Les photons, en raison de la robustesse de leurs états quantiques et de leur grande vitesse de propagation, sont des candidats de choix à la transmission de l'information quantique sur de longues distances. Ainsi, la mise au point d'interfaces convertissant les degrés de liberté quantiques d'un photon en des équivalents matériels (et vice versa) est cruciale pour l'implantation d'un tel réseau. Ces dispositifs, nommés qubits contrôlés optiquement (QCO), doivent entre autres idéalement présenter une grande vitesse d'opération, être identiques, posséder un long temps de cohérence et interagir fortement avec la lumière.

Dans le cadre de ces travaux, nous avons étudié les propriétés d'émission sous excitation résonante et non résonante (NR) d'excitons liés à des molécules de tellure dans le sélénure de zinc (ZnSe:Te_2). Ces défauts atomiques de symétrie C_{2v} , dont la configuration dans le réseau cristallin est bien définie, sont d'intéressants potentiels QCO en raison de leur comportement de pseudo-accepteurs leur permettant de capturer un trou unique, un exciton, un trion positif ou un biexciton. Puisque le trou est fortement localisé sur le défaut, interagissant ainsi avec peu de spins nucléaires, que sa fonction d'onde possède un noeud à la position des noyaux et que le Te et le matériau hôte ont une faible concentration naturelle de spins nucléaires, les mécanismes de décohérence dus à l'interaction hyperfine sont présumés de moindre importance que dans les systèmes basés sur les semiconducteurs III-V tels les boîtes quantiques et les centres isoélectroniques dans l'arséniure de gallium (GaAs) et dans le phosphure de gallium (GaP). Deux séries de mesures ont été réalisées sur des excitons uniques liés à des molécules de Te_2 dans le but d'évaluer leur performance en tant que QCO: une mesure de photoluminescence-excitation (PLE) et une mesure d'excitation résonante.

En premier lieu, la PLE visait à caractériser les mécanismes de transfert entre un exciton lié et des états de plus haute énergie, ainsi qu'à identifier comment ces derniers, en particulier ceux impliquant les états excités de l'exciton, pourraient être exploités dans le cadre de protocoles de contrôle. Si les états excités n'ont pu être observés expérimentalement, les mesures ont démontré que les excitons libres du ZnSe , créés par excitation résonante à 2,805 eV, étaient efficacement capturés par les molécules de Te_2 et menaient à une aug-

mentation de l'intensité d'émission (I_{em}) de l'exciton lié. Un effet inattendu et intrigant a également été observé concernant l'énergie d'émission (E_{em}) de ce dernier : elle se trouvait à être périodiquement modulée par l'énergie d'excitation (E_{ex}). Comme la perspective de pouvoir ajuster finement l' E_{em} d'un émetteur est très intéressante pour le contrôle cohérent, les caractéristiques de ce phénomène ont été minutieusement examinées. D'abord, l'oscillation d' E_{em} affectait de façon synchronisée tous les émetteurs d'un même volume de détection sans égard à la polarisation de l'excitation et se déployait sur toute la plage d'énergie sondée (typiquement 2,795–2,815 eV). Ensuite, la période (T_{ex}) et l'amplitude (A_{em}) de l'oscillation variaient d'une région de l'échantillon à l'autre et prenaient les valeurs moyennes respectives de 1,103 meV et 44 μ eV. Un survol de la littérature a révélé qu'un tel comportement n'a jamais été, du moins au meilleur de mes connaissances, documenté par le passé.

Nous avons, dans le cadre de cette étude, attribué l'oscillation d' E_{em} à l'interaction de l'exciton lié avec des exciton-polaritons libres. Les polaritons créeraient en effet des ondes stationnaires dans la couche de ZnSe dont la position des ventres et des noeuds dépendrait périodiquement d' E_{ex} , d'une manière similaire à la courbe de transmission d'un étalon Fabry-Perot. Ils causeraient alors un décalage de l' E_{em} de l'émetteur au moyen d'interactions exciton-exciton ou de l'effet Stark DC, dont l'amplitude varierait au gré de l'intensité du champ polaritonique. Ce modèle a reproduit de façon satisfaisante T_{ex} et l'aspect général de l'oscillation. Cependant, il n'a pas su générer le comportement sur toute la plage expérimentale d' E_{ex} et ne menait pas à une T_{ex} constante. Afin de pallier ces problèmes, des explications alternatives au moyen de champs magnétiques internes, de couplage avec les polaritons assisté par phonons ou d'une séparation des transitions de l'exciton lié en doublets non résolus ont été explorées. Toutes ces options se sont avérées peu probables, désignant ainsi l'interaction avec les polaritons comme l'explication la plus convenable de l'oscillation d' E_{em} .

En second lieu, l'excitation résonante de l'exciton lié en régime pulsé avait pour but d'en démontrer le contrôle cohérent et d'extraire le moment dipolaire (d), le temps de relaxation (T_1) et le temps de cohérence (T_2) caractérisant son efficacité en tant que QCO. L'observation d'un comportement cohérent s'est néanmoins révélée être un défi, ainsi l'étude a dû être limitée à la démonstration d'oscillations de Rabi et à la détermination des mécanismes de population découlant de l'excitation résonante. Seuls 10,5 % des émetteurs sondés ont en effet démontré une cohérence claire à travers leur signal de photoluminescence (PL), sous la forme d'oscillations de Rabi fortement amorties. L'unique cycle d'oscillation présent était suivi d'une augmentation monotone d' I_{em} à plus forte puissance d'excitation (P_{ex}), signature

d'une contribution incohérente. Également, l'application conjointe à l'excitation résonante d'un laser NR de faible puissance a eu pour effet d'augmenter l' I_{em} globale, d'élargir le cycle d'oscillation et de déplacer le maximum local d' I_{em} à plus forte P_{ex} .

La présence d'un seul cycle d'oscillation a empêché d'extraire une valeur fiable de d des courbes de PL obtenues. Néanmoins, la portion cohérente du comportement observé a pu être modélisée au moyen des équations de Bloch optiques en considérant une fluctuation de la fréquence de Rabi (Ω) dont l'amplitude augmentait avec P_{ex} . Cet effet a été associé à la fluctuation de charges générées par le laser résonant, qui se trouvent piégées dans l'environnement de l'émetteur. Ces dernières créent un champ électrique dynamique qui induit un décalage spectral (Δ) entre la transition et l'excitation et mélange les états excitoniques, réorientant par le même fait d ou réduisant sa norme. Le laser NR pour sa part décharge l'environnement en injectant des porteurs libres qui peuvent neutraliser les charges piégées, stabilisant ainsi le système dans une configuration possédant de plus faibles Ω moyenne et Δ . La contribution incohérente à l'émission a quant à elle été attribuée à un effet tunnel rapide et efficace d'excitons situés sur des molécules de Te_2 adjacentes à l'émetteur d'intérêt vers ce dernier. Ces résultats représentent la première observation d'un comportement cohérent dans le ZnSe:Te_2 et la première étape vers le contrôle complet d'un qubit excitonique, puis d'un qubit de spin dans ce matériau.

Le fort impact qu'a l'environnement électrique d'un émetteur sur ses propriétés d'émission s'est également révélé dans les mesures de PLE par le phénomène de diffusion spectrale qui prenait la forme de sauts brusques ou d'une variation continue de l' E_{em} selon la proximité des charges en cause. Cet environnement bruité se trouve actuellement à être le principal facteur limitant le contrôle cohérent d'un exciton lié dans le ZnSe:Te_2 , malgré les efforts de stabilisation déployés, telle l'application du laser NR lors de l'excitation résonante, qui se sont montrés insuffisants à restaurer les propriétés cohérentes du système. En sachant que les semiconducteurs II-VI possèdent notoirement davantage de défauts que les III-V, un travail soutenu d'amélioration de la qualité et de la structure des échantillons est à prévoir pour s'assurer d'un environnement plus contrôlé. De tels progrès garantiraient une meilleure performance des QCO formés dans le ZnSe:Te_2 et accroîtraient leur intérêt comme alternative à des systèmes fortement étudiés comme les boîtes quantiques de semiconducteurs et les défauts atomiques dans le diamant.

ABSTRACT

The advent of quantum information processing calls for the establishment of a quantum telecommunication network to connect distant agents (such as computers), a technology guaranteeing an absolute security of communications. Photons, due to the robustness of their quantum states and high propagation speed, are the candidates of choice to convey quantum information over long distances. Hence, interfaces converting photon quantum degrees of freedom to material ones (and vice-versa) are of premium importance for the deployment of a quantum network. Such devices, often named optically addressable qubits (OAQs), must ideally, among other things, be ultrafast and identical to one another, as well as present a long coherence time and strong interaction with light.

In this work, we investigated the non resonant (NR) and resonant emission properties of excitons bound to isoelectronic tellurium molecules in zinc selenide (ZnSe:Te_2). These atomic defects of C_{2v} symmetry and well-defined atomic configuration are interesting OAQ candidates as they behave like pseudo-acceptors and therefore can bind single holes, excitons, positive trions and biexcitons. Since the hole is very localized on the defect, therefore interacting with only a few nuclear spins, that its wavefunction has a node at the position of the nuclei, and that both Te and host atoms have low nuclear-spin natural abundance, hyperfine interaction-related decoherence mechanisms are strongly suppressed compared to III-V semiconductors-based systems such as quantum dots or isoelectronic centers in gallium arsenide (GaAs) and gallium phosphide (GaP). Two measurement campaigns were conducted on single Te_2 -bound excitons in order to evaluate their potential as OAQs: PLE and resonant excitation.

First, PLE was aimed at characterizing transfer mechanisms between higher-energy states and a Te_2 -bound exciton, and identifying how any of them, especially those involving its excited states, could be exploited in a control protocol. Although excited states could not be experimentally observed, it was found that resonantly-created free excitons in the ZnSe host (FX, at 2.805 eV) were easily captured by the defects, leading to an increase of the bound-exciton emission. A peculiar and intriguing effect was also observed: a periodic modulation of the bound-exciton emission energy (E_{em}) as a function of the excitation energy (E_{ex}). As this remote means of tuning the E_{em} of an emitter could have great implications for coherent control, its characteristics were thoroughly studied. It was found that the E_{em} oscillation

synchronously occurred for all excitons in a single detection volume, over the whole E_{ex} range (typically 2.795–2.815 eV) and without regard to excitation polarization. The oscillation period (T_{ex}) and amplitude (A_{em}) varied in different sample regions and had average values respectively of 1.103 meV and 44 μeV . A survey of the literature revealed, to the best of my knowledge, that no such behavior was ever documented.

In this work, we have attributed the phenomenon to the interaction of the bound exciton with free exciton-polaritons. The polaritons would indeed create a standing wave pattern in the ZnSe layer that would depend on E_{ex} in a periodic, Fabry-Perot-like manner. They would then shift the emitter E_{em} according to the intensity of their field, through exciton-exciton interactions or a DC Stark effect. The model reproduced quite well T_{ex} and the general aspect of the oscillation. However, it failed to explain the experimental E_{ex} modulation range and the constancy of T_{ex} . Hence, alternative models involving internal magnetic fields, phonon-assisted coupling with polaritons or the splitting of the bound-exciton transitions into nearly-degenerate doublets were explored. All of these options proved to be unlikely, leaving at this stage of the investigation the interaction with free exciton-polaritons as the most satisfactory explanation for the E_{em} oscillation.

Second, resonant excitation in the pulsed regime aimed for its part at demonstrating coherent control of a Te_2 -bound exciton and extracting its performance parameters as an OAQ, namely its dipole moment (d), relaxation time (T_1) and coherence time (T_2). The overall challenge of observing coherent behavior limited the study to the achievement of Rabi oscillations and to the investigation of the population mechanisms at play during resonant excitation. Indeed, solely 10.5 % of the probed single emitters showed a clear evidence of coherence in their photoluminescence (PL) signal, in the form of a rapidly-damped Rabi oscillation curve presenting a single cycle. The oscillation was followed by a monotonic increase of the emission intensity (I_{em}) at higher excitation power (P_{ex}), signature of an incoherent contribution. Furthermore, the application of a weak, NR laser simultaneously to the resonant excitation increased the overall I_{em} , widened the single oscillation cycle and displaced the local I_{em} maximum towards higher P_{ex} .

The presence of a single oscillation cycle prevented a reliable determination of d . The coherent part of the behavior could nonetheless be modelled using the optical Bloch equations while considering a Rabi frequency (Ω) fluctuation, the amplitude of which increased with resonant P_{ex} . This effect was attributed to the resonant laser generating fluctuating charges,

trapped in ever greater number in the vicinity of the emitter. The latter establish a dynamical electric field that detunes the transition with respect to the excitation and mixes excitonic states, reorienting d or reducing its magnitude. The NR laser in turn discharges the environment by injecting free carriers to neutralize the trapped charges, leading to the stabilization of the system in a configuration of smaller average Ω and detuning (Δ). The incoherent contribution to the emission signal at higher P_{ex} was for its part attributed to the efficient and fast tunneling of excitons bound to neighboring, higher-energy Te_2 molecules onto the emitter of interest. These results consist in the first convincing observation of coherent behavior in ZnSe:Te_2 and in the first step towards a more complete control of the excitonic qubit, and, later, of the hole-spin qubit in this system.

The dramatic impact of the electrical environment of an emitter on its emission properties was also observed during PLE in the form of spectral diffusion, which happened as sudden E_{em} jumps or a continuous variation, depending on the proximity of the charging (or discharging) events. This noisy environment is unquestionably the dominant limiting factor to the coherent control of a Te_2 -bound exciton, in spite of attempted stabilization efforts such as the application of the NR laser during resonant excitation, which were insufficient to the restoration of the system coherence. Knowing that II-VI semiconductors have notoriously more defects than III-Vs, more work is required to obtain better-quality host matrices and ensure a more stable environment for the excitons. Such progress would undeniably improve the performance and interest of ZnSe:Te_2 -based OAQs as an alternative to extensively-studied systems such as semiconductor quantum dots and atomic defects in diamond.

TABLE OF CONTENTS

DEDICATION	iii
ACKNOWLEDGEMENTS	iv
REMERCIEMENTS	vii
RÉSUMÉ	x
ABSTRACT	xiii
TABLE OF CONTENTS	xvi
LIST OF TABLES	xx
LIST OF FIGURES	xxi
LIST OF SYMBOLS AND ACRONYMS	xxvi
LIST OF APPENDICES	xxxiii
CHAPTER 1 INTRODUCTION	1
1.1 Definitions and basic concepts	2
1.1.1 The quantum bit, basic quantum information unit	2
1.1.2 Optically addressable qubits and their implementation in matter	3
1.2 Problematics : OAQ candidates and their issues	4
1.2.1 III-V semiconductor quantum dots	6
1.2.2 Nitrogen-vacancy centers in diamond	7
1.2.3 Isoelectronic centers in semiconductors	9
1.3 Research objectives	12
1.4 Thesis outline	13
CHAPTER 2 LITERATURE REVIEW	14
2.1 Emission properties of bulk ZnSe	14
2.2 Isoelectronic centers in semiconductors	16
2.2.1 The Hopfield-Thomas-Lynch binding model for excitons	16
2.2.2 Configurations and emission energies	16

2.2.3	Excitonic wavefunctions and Hamiltonians in C_{2v} -symmetry systems .	21
2.3	The exciton-polariton, a quasi-particle describing the propagation of light in matter	26
2.3.1	Dielectric function of a material with a resonance	26
2.3.2	Spatial dispersion in the dielectric function	28
2.3.3	The polariton equation and dispersion relation	29
2.3.4	Polaritons in ZnSe	30
2.4	Optical coherent control of an excitonic qubit	32
2.4.1	Rabi oscillations	32
2.4.2	Optical Bloch equations	35
2.4.3	Dressed states and Mollow triplet	37
2.5	Impact of the environment on the resonant excitation of solid-state qubit systems	38
2.5.1	Optical gating with a weak non resonant laser	40
2.5.2	Voltage-controlled devices	41
2.6	Summary of the literature review	41
CHAPTER 3 EXPERIMENTAL METHODS		43
3.1	ZnSe:Te ₂ samples investigated	43
3.2	Measurement principles	45
3.2.1	Photoluminescence-excitation of a Te ₂ -bound exciton across the free exciton band	45
3.2.2	Resonant excitation in the pulsed regime	45
3.3	Experimental setup	48
3.3.1	PLE configuration	48
3.3.2	Resonant excitation configuration	49
3.3.3	Calibration of the detection system	50
3.3.4	Rejection of the excitation laser	51
3.3.5	Challenges with the setup	53
3.4	Fit of the emission lines	55
3.4.1	Zero-phonon line of a bound exciton	55
3.4.2	First LO phonon replica of the ZPL	57
CHAPTER 4 NON-RESONANT EXCITATION OF EXCITONS BOUND TO Te ₂ MOLECULES IN ZnSe		59
4.1	Emission of the ZnSe host	59
4.2	Non resonant optical properties of Te ₂ -bound excitons	60
4.2.1	NR emission spectrum and polarization response	60

4.2.2	Statistical distribution of Te_2 emission characteristics	62
4.2.3	Absorption spectrum at the free exciton energy	63
4.2.4	Nature of the emission structure at 2.805 eV	65
4.3	Increase of Te_2 population efficiency	65
4.4	Exciting a continuum of states through the FX band	67
4.5	Spectral diffusion of the excitonic emission lines under non resonant excitation	69
4.6	Conclusion on the NR excitation of $\text{ZnSe}:\text{Te}_2$	74
CHAPTER 5 REMOTE OPTICAL MODULATION OF $\text{ZnSe}:\text{Te}_2$ EMISSION PROP- ERTIES		75
5.1	Modulation of the emission energy of a Te_2 -bound exciton	76
5.1.1	Simultaneous oscillation of the X and Y transitions of a single exciton	77
5.1.2	Statistical distribution of the oscillation parameters	79
5.1.3	Influence of the environment on the oscillation parameters	80
5.1.4	Absence of interplay between absorption and the oscillation	83
5.1.5	Impact of excitation parameters	84
5.1.6	Effect of E_{ex} on the emission-line FWHM	85
5.1.7	Conclusion on the experimental observation of an E_{em} modulation dur- ing PLE	86
5.2	Interaction mechanisms possibly responsible for the E_{em} oscillation	86
5.2.1	Interaction with free exciton-polaritons	87
5.2.2	Magnetic field-induced effects	110
5.2.3	Phonon-assisted coupling with free exciton-polaritons	111
5.2.4	Splitting of the bound-exciton transitions into nearly-degenerate doublets	121
5.2.5	Conclusion on the origin of the E_{em} oscillation	128
5.3	General conclusion on the modulation of $\text{ZnSe}:\text{Te}_2$ emission properties	129
CHAPTER 6 RESONANT EXCITATION OF AN EXCITONIC QUBIT IN ZnSe .		131
6.1	Statistical distribution of the emission properties of excitons measured in Sam- ple B	132
6.2	Modelling of the resonant PL data	132
6.2.1	Coherent contribution: optical Bloch equations	134
6.2.2	Incoherent contribution: tunneling from adjacent Te_2 molecules . . .	138
6.3	Resonant excitation behaviors of $\text{ZnSe}:\text{Te}_2$	147
6.3.1	Monotonic increase of the resonant PL intensity without saturation .	147
6.3.2	Saturation of the resonant PL intensity	149
6.3.3	Single Rabi oscillation cycle: evidence of coherent behavior	152

6.3.4	Conclusion on the resonant excitation model of a Te_2 -bound exciton .	160
6.4	Attempts at stabilizing the environment of an emitter	162
6.4.1	Pulsed resonant excitation in the presence of a NR CW laser field . .	162
6.4.2	Impacts of a DC electric field on the emission signature of an emitter	163
6.5	Conclusion on the resonant excitation of a Te_2 -bound exciton in the pulsed regime	165
CHAPTER 7 CONCLUSION		168
7.1	Summary of works	168
7.1.1	Fulfilment of the research objectives	170
7.1.2	Originality	170
7.2	Limitations	171
7.3	Future research	171
7.3.1	Sample structure	172
7.3.2	E_{em} oscillation and the polariton model	172
7.3.3	Coherent control	173
REFERENCES		174
APPENDICES		197

LIST OF TABLES

Table 1.1	Emission and quantum properties of different OAQ systems	5
Table 1.2	Spin and relative abundance of isotope for Zn, Se and Te atoms . . .	11
Table 2.1	Emission energy and symmetry of different NN_i ICs in GaP	19
Table 5.1	Parameters for the calculation of the polaritonic dispersion relation in bulk ZnSe	90
Table 5.2	Eigenvalues and eigenfunctions of H_{Tot} for the hyperfine interaction of a Te_2 -bound exciton and a ^{125}Te 1/2 nuclear spin	124
Table 6.1	Default parameters used in the resolution of the optical Bloch equations	135
Table 6.2	Default transfer rates used in the numerical resolution of the balance of populations equations describing incoherent PL	142
Table 6.3	Parameters used in the simulation of the resonant emission from Exci- ton A	159

LIST OF FIGURES

Figure 1.1	Representation of the state of a qubit	2
Figure 1.2	ZnSe lattice with in-plane and out-of-plane Te_2 molecules	10
Figure 1.3	Ultrafast NR initialization scheme of a hole spin in ZnSe	12
Figure 2.1	PL spectrum of bulk and thin strained ZnSe	15
Figure 2.2	HTL model for a Te_2 molecule	17
Figure 2.3	Ensemble emission spectrum of GaP: N_2	18
Figure 2.4	Ensemble emission spectrum of GaAs: N_2	20
Figure 2.5	Ensemble emission spectrum of ZnSe: Te_2	21
Figure 2.6	Exciton fine structure in a C_{2v} -symmetry system and polarization of its associated transitions	25
Figure 2.7	One-dimensional array of uncoupled Lorentz oscillators	27
Figure 2.8	Real and imaginary parts of the dielectric function for a material with a single resonance	28
Figure 2.9	Typical dispersion relation for exciton-polaritons	30
Figure 2.10	Reflectance spectrum of a 2 μm -thick ZnSe layer on GaAs	31
Figure 2.11	Two-level system formed from the $n = 1$ energy level of an exciton and its ground state	32
Figure 2.12	Rabi oscillations of the ground and excited state populations of a TLS	34
Figure 2.13	Dressed states and transitions involved in the formation of the Mollow triplet upon the resonant or quasi-resonant excitation of a TLS	38
Figure 2.14	Random telegraph noise model of the interaction of a bound exciton with its environment	39
Figure 3.1	ZnSe: Te_2 samples investigated	44
Figure 3.2	Principle of the PLE measurement	46
Figure 3.3	Simplified schematic of the PLE and resonant excitation setup . . .	47
Figure 3.5	Fit example of the ZPL of an exciton doublet using Gaussian and Lorentzian functions	56
Figure 3.6	Fit example of the first LO phonon replica of a bound exciton . . .	58
Figure 4.1	Emission spectrum of the ZnSe host embedding the Te_2 molecules .	60
Figure 4.2	Emission spectra and polarization response of Te_2 -bound excitons .	61
Figure 4.3	Statistical distribution of the energy of the X transition of excitons in Sample A studied during PLE, of its FWHM and of its separation with the Y transition	63

Figure 4.4	PLE and NR emission spectra of four different bound excitons in different regions of the sample	64
Figure 4.5	Emission spectra for excitations at 2.870 eV and 2.805 eV	66
Figure 4.6	One-step binding mechanism of a FX to a Te_2 molecule	67
Figure 4.7	Excitation of a broad continuum of states	68
Figure 4.8	NR PL spectra with π_y and σ^+ excitations for two excitons that underwent a drift of their E_{em} with the modification of their electrical environment	70
Figure 4.9	Spectral diffusion of the X and Y transitions of two Te_2 -bound excitons	71
Figure 4.10	Charging events causing spectral diffusion of the bound exciton emission line	72
Figure 4.11	Fine-structure splitting of two Te_2 -bound excitons	73
Figure 4.12	PLE maps showing different drifts for distinct emission lines	73
Figure 5.1	PLE maps presenting the E_{em} oscillation of Te_2 -bound excitons . .	76
Figure 5.2	E_{em} oscillation as a function of E_{ex} for two excitons in different detection volumes	77
Figure 5.3	Zoom of a portion of the sine fit performed on the Y transition of Exciton A in Fig. 5.2	78
Figure 5.4	FFTs of the curves in Fig. 5.2	79
Figure 5.5	Statistical distribution of the oscillation period and the oscillation amplitude of the emission energy of the studied excitons	80
Figure 5.6	E_{em} oscillation of two excitons in the same detection volume	81
Figure 5.7	FFTs of the X_1 and X_2 E_{em} oscillation presented in Fig. 5.6	82
Figure 5.8	E_{em} oscillation of three excitons located in three different regions of the sample	82
Figure 5.9	PLE intensity and E_{em} of two excitons in different detection volumes	83
Figure 5.10	FWHM of the exciton in Fig. 5.2 (a) as a function of E_{ex}	85
Figure 5.11	Stationary waves created along the z axis of the sample, formed of a ZnSe layer on a GaAs substrate with Te_2 molecules at its center . .	88
Figure 5.12	Dispersion relation of free exciton-polaritons in bulk ZnSe	91
Figure 5.13	Electric fields involved in the derivation of an expression for the reflection and transmission coefficients of a stack formed of a ZnSe layer on top of a semi-infinite GaAs substrate	92
Figure 5.14	Electric-field distribution as a function of incoming photon energy in a 80-nm ZnSe layer on top of GaAs	94

Figure 5.15	Impact of the excitonic mass M on the polariton electric-field distribution at the center of the ZnSe layer	96
Figure 5.16	Impact of the oscillator strength $4\pi\beta$ on the polariton electric-field distribution at the center of the ZnSe layer	97
Figure 5.17	Impact of the damping parameter Γ on the polariton electric-field distribution at the center of the ZnSe layer	99
Figure 5.18	Comparison between the E_{ex} oscillation data and the simulation of the polariton electric-field distribution	100
Figure 5.19	Energy levels at play in a highly-detuned AC Stark effect of a Te_2 -bound exciton	102
Figure 5.20	Charge planes created by the polaritonic-field interference pattern .	105
Figure 5.21	Effect of the FX density in the vicinity of a Te_2 -bound exciton . . .	107
Figure 5.22	Blueshift of the emission lines of an exciton bound to a N_2 molecule in GaAs dependent on the position of the NR excitation	108
Figure 5.23	Phonon-assisted excitation of an excitonic system	112
Figure 5.24	Normalized PLE spectra of four distinct excitons	113
Figure 5.25	E_{em} oscillation of the FX emission line in monolayer MoSe_2 as a function of excess energy $E_{\text{ex}} - E_{\text{FX}}$	114
Figure 5.26	Phonon-assisted interaction between a resonantly-excited FX polariton and a Te_2 -bound exciton	115
Figure 5.27	Calculated phonon density of states for ZnSe	117
Figure 5.28	Energy at Γ of the first ten confined dilatational, flexural and shear phonon modes with rigid boundary conditions in a 80-nm ZnSe layer	119
Figure 5.29	Simulation of nearly-degenerate doublets forming the X and Y emission structures	122
Figure 5.30	Dynamical nuclear polarization performed by the means of the positive trion transition	126
Figure 6.1	NR emission statistics for Sample-B excitons investigated in the resonant excitation experiment	133
Figure 6.2	Resonant PL data of a single Te_2 -bound exciton	134
Figure 6.3	Effect of T_1 on the shape of the Rabi curves	136
Figure 6.4	Effect of d on the shape of the Rabi curves	136
Figure 6.5	Effect of Δ on the shape of the Rabi curves	137
Figure 6.6	Effect of T_2 on the shape of the Rabi curves	138
Figure 6.7	PLE spectra of the NN_1 molecule in GaP	139

Figure 6.8	Four-level system involved in the balance of populations model of the incoherent excitation of a Te_2 -bound exciton by the means of an adjacent Te_2 molecule	141
Figure 6.9	Effect of the dark exciton decay rate Γ_D on the incoherent PL intensity I_{em}	142
Figure 6.10	Effect of the bright exciton radiative recombination rate Γ_{rad} on the incoherent PL intensity I_{em}	143
Figure 6.11	Effect of the $T = 0$ K spin-flip rate γ_0 on the incoherent PL intensity I_{em}	144
Figure 6.12	Effect of the temperature, which determines the balance between the spin-flip rates γ_{sf} and γ'_{sf} , on the incoherent PL intensity I_{em}	144
Figure 6.13	Effect of the pumping rate per unit power G_{ex} on the incoherent PL intensity I_{em}	145
Figure 6.14	Effect of the tunneling rate between two Te_2 molecules $\gamma_{\text{Te}_2 \rightarrow X}$ on the incoherent PL intensity I_{em}	146
Figure 6.15	Effect of the number of neighboring Te_2 molecules n on the incoherent PL intensity I_{em}	147
Figure 6.16	Excitons presenting a linear increase of their I_{em} as a function of $P_{\text{ex}}^{1/2}$	148
Figure 6.17	Modelization of the linear response with the incoherent mechanism	148
Figure 6.18	Changes of regime in the resonant PL response of two excitons . . .	149
Figure 6.19	Resonant PL I_{em} as a function of resonant $P_{\text{ex}}^{1/2}$ for different P_{NR} , showing a saturation of I_{em}	150
Figure 6.20	Modelization of the I_{em} saturation response with the coherent mechanism	151
Figure 6.21	Coherent behavior of the resonant PL as a function of resonant $P_{\text{ex}}^{1/2}$ for different P_{NR} values	153
Figure 6.22	$P_{\text{ex}}^{1/2}$ at which the local maximum of the oscillation cycle is observed	154
Figure 6.23	Excitation-induced dephasing on a Rabi curve	155
Figure 6.24	Impact of a Ω fluctuation on the Rabi curve, for different T_2 behaviors	156
Figure 6.25	Combination of coherent and incoherent population mechanisms during resonant excitation	157
Figure 6.26	Comparison between simulation and experimental data for Exciton A	160
Figure 6.27	Comparison between simulation and experimental data for Exciton B	161
Figure 6.28	Variation of NR E_{em} as a function of voltage	164
Figure 6.29	Second, less common behavior of an exciton NR E_{em} as a function of voltage, showing a hysteresis	164

Figure 6.30	Resonant PL measured for two different applied voltages	165
Figure A.1	PLE maps of all excitons presenting an E_{em} oscillation as a function of E_{ex} (1 of 3)	197
Figure A.2	PLE maps of all excitons presenting an E_{em} oscillation as a function of E_{ex} (2 of 3)	198
Figure A.3	PLE maps of all excitons presenting an E_{em} oscillation as a function of E_{ex} (3 of 3)	199

LIST OF SYMBOLS AND ACRONYMS

Physical constants

c	speed of light in vacuum
e	elementary charge
\hbar	reduced Planck constant
k_{B}	Boltzmann constant
m_0	electron rest mass
ϵ_0	vacuum permittivity
μ_0	vacuum permeability

Quantum information and coherent control

c_X, c_0	excited and ground-state probability amplitudes
d	dipole moment
EID	excitation-induced dephasing
OAQ	optically addressable qubit
qubit	quantum bit
T_1	longitudinal relaxation time
T_2	coherence or transverse relaxation time
T_2^*	inhomogeneously-broadened coherence time
TLS	two-level system
Γ	longitudinal relaxation rate
γ_{\perp}	transverse relaxation rate
Δ	detuning
Θ	rotation angle
ρ_{X0}, ρ_{0X}	density-matrix coherence terms
ρ_{XX}, ρ_{00}	excited and ground-state populations
ω	driving-field angular frequency
Ω	Rabi frequency
$\tilde{\Omega}$	generalized Rabi frequency
ω_0	TLS resonance angular frequency
$ 0\rangle, X\rangle$	TLS ground and excited states
$ +, n\rangle, -, n\rangle$	dressed states with n photons

Materials and qubit systems

Al	aluminum
As	arsenic
Au	gold
CdSe	cadmium selenide
CdTe	cadmium telluride
GaAs	gallium arsenide
GaAs:N ₂	N ₂ molecule in GaAs
GaP	gallium phosphide
GaP:N ₂	N ₂ molecule in GaP
IC	isoelectronic center
In	indium
InAs	indium arsenide
InGaAs	indium-gallium arsenide
MoSe ₂	molybdenum diselenide
N	nitrogen
NV	nitrogen-vacancy
P	phosphorus
QD	quantum dot
QW	quantum well
Se	selenium
Si	silicon
SiC	silicon carbide
SiV	silicon-vacancy
Te	tellurium
Zn	zinc
ZnS	zinc sulfide
ZnSe	zinc selenide
ZnSe:Te ₂	Te ₂ molecule in ZnSe

Semiconductor physics

DOS	density of states
E_g	energy gap
HH	heavy hole

HTL	Hopfield-Thomas-Lynch
irrep	irreducible representation
LH	light hole
m_e, m_h	electron and hole effective masses
Γ	Brillouin zone center

Emission features and properties

D-A	donor-acceptor
D_0X	excitons bound to neutral donors
E_{det}	detection energy
E_{em}	emission energy
E_{ex}	excitation energy
FSS	fine-structure splitting
FWHM	full width at half maximum
FX	free exciton
HWHM	half width at half maximum
I_{em}	emission intensity
X	lower-energy observable state of a C_{2v} bound exciton
X^+	positive trion
XX	biexciton
Y	higher-energy observable state of a C_{2v} bound exciton
ZPL	zero-phonon line

Exciton Hamiltonians

e_i	exchange parameters, $i = \{1, 2, \dots, 9\}$
H_e	electron Hamiltonian
H_{ex}	exchange Hamiltonian
H_h	hole Hamiltonian
J_x, J_y, J_z	total angular-momentum operators
v_x, v_y, v_z	crystal-field parameters
$\sigma_x, \sigma_y, \sigma_z$	Pauli matrices
$ D_{hh}\rangle, D_{lh}\rangle$	heavy and light-hole dark excitons
$ X_{hh}\rangle, X_{lh}\rangle$	heavy and light-hole x -polarized excitons
$ Y_{hh}\rangle, Y_{lh}\rangle$	heavy and light-hole y -polarized excitons

$|Z_{hh}\rangle, |Z_{lh}\rangle$ heavy and light-hole z -polarized excitons

Exciton-polaritons

E_0	driving-field amplitude
\mathbf{k}	polariton wavevector
k	norm of the polariton wavevector
K	spring constant
LPB	lower polariton branch
m	oscillator mass
M	exciton effective mass
q	oscillator charge
UPB	upper polariton branch
Γ	damping parameter
Δ_{LT}	longitudinal-transverse splitting
ϵ	dielectric function
ϵ_∞	high-frequency dielectric constant
ω	driving-field angular frequency
ω_0	resonance angular frequency
ω_L	longitudinal-exciton angular frequency
$4\pi\beta$	oscillator strength

Instrumentation and methods

CCD	charge coupled device
FFT	fast Fourier transform
HWP	half-wave plate
LN ₂	liquid nitrogen
NA	numerical aperture
PL	photoluminescence
PLE	photoluminescence-excitation
PM	polarization-maintaining
QWP	quarter-wave plate
SNR	signal-to-noise ratio
T	temperature
t_{acq}	acquisition time

TEM	transverse electromagnetic
Ti:S	titanium:sapphire

Excitation parameters

CW	continuous-wave
NR	non resonant
P_{ex}	excitation power
P_{NR}	non-resonant power
P_{RMS}	root mean square power
S	excitation-beam area
π_x	x linear polarization
π_y	y linear polarization
σ^+	right-handed circular polarization
σ^-	left-handed circular polarization
τ_p	pulse duration
τ_R	pulse repetition period

Modulation of emission properties

A_{em}	oscillation amplitude
T_{ex}	oscillation period

Interference and matrix treatment of electric fields

E_I, E_{II}	total electric fields at interfaces I and II
$E_{i,m}$	incident electric field at interface m
E^l, E^u	electric fields from LPB and UPB modes
$E_{r,m}$	reflected electric field at interface m
$E_{r',m}$	incident electric field at interface m previously reflected at another interface
$E_{t,m}$	transmitted field at interface m
E_{tot}	total electric field at a specific z position
$E^{\alpha,+}, E^{\alpha,-}$	electric fields from polaritonic mode α travelling towards z^+ and z^-
\mathcal{F}	finesse
H_I, H_{II}	total magnetic fields at interfaces I and II

I	field intensity
\tilde{n}	complex refractive index
P	electric polarization
r	reflection coefficient
t	transmission coefficient
α	attenuation coefficient

Magnetic and electric perturbations

A	hyperfine constant
a_0	exciton Bohr radius
B_x, B_y, B_z	magnetic fields
c_i	electron magnetic-Hamiltonian parameters, $i = \{1, 2, 3, 4\}$
DNP	dynamical nuclear polarization
\mathcal{E}	electric field
H_e	electron magnetic Hamiltonian
H_{hf}	hyperfine Hamiltonian
H_{hh}	heavy-hole magnetic Hamiltonian
H_{SE}	DC Stark effect Hamiltonian
I_z, S_z	z projections of the nuclear and electron spins
I_+, I_-, S_+, S_-	nuclear and electron-spin ladder operators
m_X	exciton reduced mass
v_i	heavy-hole magnetic-Hamiltonian parameters, $i = \{1, 2, 3, 4, 5, 14, 15, 16\}$
μ	dipole operator
$\rho(\mathbf{r})$	charge density
ϕ	electric potential

Phonons

$c_{s,l}, c_{t,l}$	longitudinal and transverse speeds of sound
E_{int}	interaction energy
E_{Pol}	polariton energy
E_{X,n_a,n_o}	energy of a phonon-dressed exciton
H_{int}	interaction Hamiltonian
LA	longitudinal acoustic

LO	longitudinal optical
m_x	mass of atom x
n_a, n_o	number of acoustic and optical phonons
\mathbf{q}	phonon wavevector
TO	transverse optical
\mathbf{u}	atomic displacement
\mathbf{w}	atomic displacement amplitude
$\bar{\omega}$	average optical-phonon angular frequency
ω_a, ω_o	angular frequencies of acoustic and optical phonons
ω_{loc}	local-mode angular frequency
ω_p	phonon angular frequency
$ \text{Pol}\rangle$	polariton state
$ X, n_a, n_o\rangle$	phonon-dressed exciton

Nearly-degenerate doublet

$A_{X'}, A_{X''}$	transition amplitudes of a nearly-degenerate doublet
X', X''	transitions of a nearly-degenerate doublet

Exciton tunneling mechanism

$c_{\text{co}}, c_{\text{inc}}$	coherent and incoherent-population weighting factors
G_{ex}	pumping rate per unit power
n	number of neighboring Te_2 molecules
n_0	ground-state population
n_D	dark-exciton population
n_{Te_2}	population of excitons in the reservoir
n_X	bright X -exciton population
γ_0	$T = 0$ K spin-flip rate
Γ_D	dark-exciton recombination rate
Γ_{ex}	pumping rate
Γ_{rad}	bright X -exciton recombination rate
γ_{sf}	$X \rightarrow D$ spin-flip rate
γ'_{sf}	$D \rightarrow X$ spin-flip rate
γ_T	tunneling rate
$\gamma_{\text{Te}_2 \rightarrow X}$	$\text{Te}_2 \rightarrow X$ transfer rate

LIST OF APPENDICES

Appendix A	PLE maps of all Te_2 -bound excitons presenting an oscillation of their emission energy as a function of the excitation energy	197
Appendix B	Perturbation Hamiltonian in matrix form for an exciton bound to a C_{2v} -symmetry defect	200
Appendix C	Second-order energy shift of an hydrogen-like exciton induced by the DC Stark effect	203
Appendix D	Hyperfine Hamiltonian in the coupled HH exciton-nuclear spin basis .	205

CHAPTER 1 INTRODUCTION

Quantum information technologies have boomed in the last few years, especially with the fabrication of more and more powerful quantum processors. The latter have been successfully used, among other things, to generate random numbers [1], to simulate complex fermionic systems [2], exotic phases of matter [3] and Hamiltonians [4,5] and to solve optimization problems [6–8]. Some of these machines are even claimed to have reached quantum supremacy [1], the threshold over which a quantum computer can perform specific tasks unattainable to classical supercomputers in a reasonable time.

With the rise of quantum computing comes the challenge of connecting all of these machines to one another to create a quantum telecommunication network. This would allow access to distributed quantum computing, where different parts of a computation is sent to different machines, or even an absolutely secure quantum internet. Therefore, there is a keen interest to study systems that convert quantum degrees of freedom of matter, which are used to perform computations, to photon properties, the premium vector for quantum information. Indeed, these particles have very robust quantum states that ensure the successful propagation of quantum information over large distances and high data transfer rates.

The conversion of a certain photon property into a material quantum state generally uses the selection rules of an optical transition within the host material. Upon absorption of a photon of the right energy and polarization, an electron is promoted from its ground state to a higher-energy level. By controlling the temporal or spectral profile of the interaction between the system and the light field, the quantum state imprinted on the former can be precisely tailored.

In this introduction, I start by presenting basic concepts regarding quantum bits (qubits), the basic quantum information units, and their coherent control. I then discuss the technological importance of quantum matter-photon interfaces and how they are implemented in real devices. I finally review some of the most studied candidates and compared them to the subject of this thesis, the Te_2 molecule in ZnSe ($\text{ZnSe}:\text{Te}_2$).

1.1 Definitions and basic concepts

I begin this section by defining the qubit, which is to quantum information what a bit is to classical information. I briefly explain how one can control its state and what are its important performance parameters. Then, I discuss common implementations of its optically-controlled version, the spin-photon interface or OAQ, in matter.

1.1.1 The quantum bit, basic quantum information unit

A qubit defines a unit of quantum information and is encoded on a quantum system formed of two energy levels often labelled $|0\rangle$ (the ground state) and $|1\rangle$ (the excited state), with an allowed transition between them (Fig. 1.1 (a)). The state of this so-called two-level system (TLS) is described by the wavefunction:

$$|\Psi\rangle = c_0 |0\rangle + c_1 |1\rangle, \quad (1.1)$$

with c_0 and c_1 the probability amplitudes associated with $|0\rangle$ and $|1\rangle$. $|\Psi\rangle$ is conveniently represented as a vector on the Bloch sphere (Fig. 1.1 (b)), which represents the Hilbert space of pure states allowed to the qubit [9]:

$$|\Psi\rangle = \sin\left(\frac{\theta}{2}\right) |0\rangle + e^{i\phi} \cos\left(\frac{\theta}{2}\right) |1\rangle. \quad (1.2)$$

The Bloch vector has a norm of 1 for a pure state and < 1 for a mixed state.

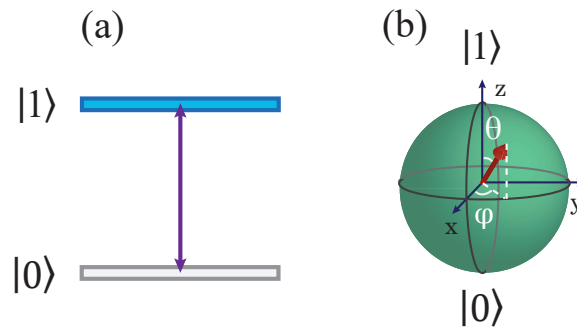


Figure 1.1 Representation of the state of a qubit. (a) Two-level system formed of a ground state $|0\rangle$ and an excited state $|1\rangle$ coupled through an allowed transition. (b) The Bloch sphere allows to represent any superposition or mixed state of $|0\rangle$ and $|1\rangle$ as a vector, with two defining angles θ and ϕ .

A very common implementation of quantum computing requires control on a single qubit, several so-called one-qubit gates, and also on combinations of two qubits, at least one two-qubit gate [10]. Control of a single qubit is realized by performing operations on it in a three-step sequence. First, it must be initialized in a defined state, usually $|0\rangle$. Then, one or more control steps (or gates) are applied to rotate its state on the Bloch sphere and obtain any required $|\Psi\rangle$. Finally, it is read out to extract the result of the control sequence. The probability of reaching the right result after any gate is designated as the fidelity of that gate.

The evolution of the Bloch vector is described by two characteristic times, the relaxation (T_1) and coherence (T_2) times, which are performance metrics of the qubit. T_1 acts on both population and coherence, relaxing the z component of the Bloch vector and bringing back the TLS to $|0\rangle$. T_2 , for its part, describes the time scale over which the evolution of the phase becomes unpredictable and the coherence is lost. Its upper bound is defined by the action of relaxation mechanisms on the phase: $T_2 = 2T_1$. However, as a qubit is not perfectly isolated from its environment, interactions with the latter can lead to additional decoherence mechanisms impacting the phase, but not the population, yielding $T_2 \leq 2T_1$. In order to successfully complete a computation, all required operations must in principle be carried out within T_2 [11], as computation errors might occur approaching this limit. Exceeding it leads to the loss of the information stored on the qubit. In practice, the limit is fixed at a much lower value than T_2 to allow for the implementation of fault tolerance. T_2 can also be shortened further due to low-frequency noise in its environment or inhomogeneity in the properties of a qubit ensemble, giving rise to an inhomogeneously broadened value, T_2^* . The application of specific gate sequences usually allows cancelling those effects and retrieving T_2 .

1.1.2 Optically addressable qubits and their implementation in matter

The realization of a quantum computer requires coupling qubits to one another, in order to achieve two-qubit gates. In the case where qubits are situated in different processors and therefore very distant, an efficient way to convey information between them is through the means of a photon. Therefore, a device that can map the quantum state of a photon onto matter and vice-versa is crucial for the advent of this and many other technologies.

This can be done by taking advantage of light-matter interactions in atoms and solids, giving rise to electronic transitions between a ground and an excited states ($|0\rangle$ and $|1\rangle$). The strength of this coupling with light is characterized by the dipole moment (d), a very impor-

tant parameter in the evaluation of the performance of an OAQ, along with T_1 and T_2 .

The most straightforward solution is to use the transition between two energy levels in an atom as $|0\rangle$ and $|1\rangle$. The interaction with the field causes the system to transition between its two states, a subject later detailed in Sect. 2.4.1, while the presence or absence of emission of a photon by the atom informs of its state prior to recombination. Here, the upper bound for T_1 is the spontaneous lifetime of the transition [12], a quantity that can be tailored through the use of a cavity. A similar qubit can be defined in semiconductors with a confined exciton, i.e. an electron-hole pair bound through a Coulomb potential that behaves like an atom.

In a solid, one can define another type of qubit based on the projections of the spin of a single charge carrier or of a collection of a few. The state can be controlled optically through spin-selective optical transitions. Their resonant excitation with adequately-polarized photons drives coherent rotations of the spin with the participation of a common excited state.

These strategies are some of the most commonly used real-life implementations of OAQs. Ideal candidates would in principle be easily integrable to present electronic technology and compatible with existing classical telecommunication systems, as well as demonstrate ultrafast operation, efficient interaction with light and long T_2 [10, 13, 14]. They would also be identical in order to ensure scalability [14] and ease of mutual coupling. Finally, their state would be fully controllable, allowing the implementation of quantum computing protocols [13]. The next section reviews the most mature of these technologies and comment on their advantages and weaknesses.

1.2 Problematics : OAQ candidates and their issues

Several OAQ systems have been proposed: among others, trapped atoms [15] and ions [16–18], vacancies in silicon carbide (SiC) [19–22], atomic defects in semiconductors [23–29], III-V semiconductor quantum dots (QDs) [13, 14, 30–48], and color centers in diamond (nitrogen-vacancy (NV) centers [10, 49–60] and silicon-vacancy (SiV) centers [61–69]). Unsurprisingly, none of them possess all of the desired characteristics stated above, and the search for new or improved platforms is more relevant than ever.

Table 1.1 Emission and quantum properties of different OAQ systems: emission broadening (em. broad., given for ensembles), T_1 , T_2^* and dipole moment (d). Values marked with \dagger are theoretical.

OAQ	Em. broad.	T_1	T_2^*	d (D)
Atom or ion	50–504 neV [70–73]	6.90 ns–1.11 s [70, 72, 74–76]	2.8–14.7 s [15, 16]	5.19–10.74 [70, 76]
III-V QD	10–15 meV [36, 37]	300–640 ps [36, 39, 41, 47, 77, 78]	30 ps–15.4 ns [30–32, 36, 37, 39, 40, 42, 44]	9–75 [31–33, 35, 38, 41, 45, 46]
NV center	300 meV [51]	2.9 ms–265 s [50, 56]	10 ns–40 μ s [57, 60, 79]	0.8 [80]
SiV center	115 μ eV [61]	1.72 ns–2.4 ms [62–64, 68, 69]	398 ps–13 μ s [63, 64, 67–69]	14.3 [66]
Vacancy in SiC	150 meV [19]	183–500 μ s [19, 21]	0.214–4.4 μ s [19, 20]	9–12 † [81]
GaAs:N ₂ IC	990 μ eV [82]	200–670 ps [25, 83]	115 ps [25]	27 [25]
ZnSe:Te ₂ IC	75 meV [84]	80 ps [28]	?	?

Table 1.1 presents performance metrics for these systems. Emission broadening refers to ensemble measurements, not single-emitter spectroscopy, and therefore includes inhomogeneous broadening due to the configuration distribution of the qubits. I rapidly overview the characteristics, strengths and weaknesses of the two most studied solid-state systems, namely semiconductor QDs and NV centers in diamond below, and compare them with the subject of this thesis, the Te_2 molecule in ZnSe ($\text{ZnSe}:\text{Te}_2$), a so-called isoelectronic center (IC). I do not review atomic systems, as, although they show by far the narrowest linewidths as well as the longest T_1 and T_2 [10], they are unlikely to play an important technological role in their current implementations due to the very elaborate traps they require, some of the components of which can hardly be miniaturized.

1.2.1 III-V semiconductor quantum dots

Quantum dots (QDs) are generally obtained in III-V semiconductors by a Stranski-Krastanov growth, during which three-dimensional islands are formed due to the lattice misfit between the substrate and its epilayer [85], or by thickness fluctuations at an interface. Therefore, their fabrication method is compatible with current electronic technologies, facilitating their future integration, and allows designing very elaborate structures to optimize qubit operation and stability, such as field-effect devices and cavities [14, 48].

Their major interest as OAQs comes from their atom-like optical properties, as a single QD present narrow Lorentzian emission lines with linewidths of 20–100 μeV [30, 38, 41] and definite selection rules, in addition to a large dipole moment of 9–75 D [31–33, 35, 38, 41] (and therefore a relatively short lifetime T_1 of 300–640 ps [36, 39, 41, 47, 77, 78]) ensuring efficient coupling with light. The controllable charge state of the QD allows to access both exciton and trion (i.e. charged exciton) transitions, defining respectively an excitonic and an optically-addressable spin qubit. However, the fabrication method leads to a large distribution of emission and electronic properties in an ensemble (e.g. an emission energy distribution as large as 10–15 meV [36, 37]), making it challenging to find two identical emitters.

Their all-optical, ultrafast operation has been demonstrated [30–37, 40, 42–47] which leads to operation times of less than 38 ps for electron spins [42] and 14–20 ps for hole spins [45, 46]. However, the presence of numerous nuclear spins in the QD leads to important decoherence mechanisms and limits T_2^* (especially in ensembles) to 30–170 ps for excitons [30–32, 36], 185 ps–5.5 ns for electron spins [36, 37, 39, 40, 42, 44] and 2.3–15.4 ns for hole spins [45, 46].

Elaborate pulse sequences, combined or not with the excitation of a single QD and the careful design of the sample microstructure, allows to access an extended T_2 , which reaches $\sim 3 \mu\text{s}$ for electron spins [37, 44] and $1.1 \mu\text{s}$ for hole spins [45].

These avenues can be refined to prolong T_2 even more. For example, a T_2 of 0.87 ms was reported in a related, non-OAQ system formed of a two-electron spin state trapped in an electrically-defined double QD in GaAs [86] with the application of up to 1536 control pulses. This demonstrates the efficiency of the so-called dynamical decoupling at mitigating the impact of nuclear-spin noise on the spin qubit. On another note, isotopic purification of the host material can be used to remove isotopes of non-zero nuclear spin and therefore greatly reduce nuclear noise, as it has been done in electrically-defined QDs [87, 88] and donor-bound electron spins [89] in silicon (Si), and could easily be employed in suitable QD OAQs to enhance their T_2 .

The spin-qubit performances, which are by far the most promising for applications in quantum information, are shadowed by the rather slow initialization and readout method, optical pumping, which requests one of the two trion transitions to be driven for several ns to achieve a fidelity above 90 % [42]. Also, the operation of a spin qubit requires a large magnetic field to increase the precession frequency [37, 42, 44, 48].

1.2.2 Nitrogen-vacancy centers in diamond

Nitrogen-vacancy (NV) centers in diamond are atomic defects of C_{3v} symmetry formed of a substitutional nitrogen and an adjacent carbon vacancy. Their negatively charged state possesses a two-electron spin ground state triplet 3A separated from an excited state triplet 3E by 1.945 eV, a transition that is optically active [51]. Their configuration is determined by the lattice, ensuring great qubit homogeneity. Their NR emission at low temperature suffers from a large phonon-assisted recombination sideband (width $\sim 0.3 \text{ eV}$) [51] that takes away photons from the zero-phonon line (ZPL) used in the control protocols. This feature can however be exploited for readout.

The electron spin is optically initialized by pumping 3E . The system subsequently relaxes from the $m_s = \pm 1$ spin projection of the excited state to the $m_s = 0$ projection of the ground state through a metastable intermediate singlet state 1A [52], with a fidelity of 72.1–99.7 % in 250–390 ns [10, 50, 54, 55]. This scheme can also be used for readout.

Control is most often carried out with microwave pulses of tens of ns matching the 2.88 GHz splitting between the $m_s = 0$ and $m_s = \pm 1$ 3A states [51], a rather slow operation rate compared to all-optical control. However, the latter has already been demonstrated [57], leading to operation times of the order of a few hundred ps [58].

All time constants describing the coherence and relaxation of electron spins are impressively long in this system. T_2 for instance can be as high as 0.23–1.8 ms [49, 51, 53, 57, 59], even at room temperature due to a low phonon density of states and the fact that diamond, especially if isotopically purified [53], is a relatively spin-free host [10]. T_2^* for its part ranges from 10 ns to 40 μ s [57, 60, 79], while a T_1 of 2.9–6.0 ms at 300 K [56] and even of 28–265 s at 1.9–2.3 K [50] has been reported for an ensemble.

The radiative recombination rate of the $^3A \leftrightarrow ^3E$ transition is however slow, making this system a not-so-bright emitter. Indeed, a T_1 of 7.3–13.7 ns has been reported for the excited state [51, 52, 55, 59, 79], with a T_2^* of 5.8–18.5 ns [52, 58]. The dipole moment is also quite small, ~ 0.8 D [80]. For that reason, NV centers are often embedded in micro-cavities to improve their emission rate [59].

Another interesting feature of the system is the possibility of coupling of the electron spins to a nearby nuclear spin (for example a ^{13}C or a ^{14}N spin). This gives access to a quantum register that could be used to implement a quantum memory [54], as nuclear spins in diamond have very long coherence and relaxation times (respectively of the order of the ms and 1.4–36 h) [51].

Diamond also hosts other color centers with a well-defined symmetry and interesting quantum properties, such as the negatively charged SiV center that has a very narrow ZPL at mK temperatures and long T_1 , T_2^* and T_2 (respectively 1.72 ns–2.4 ms [62–64, 68, 69], 398 ps–13 μ s [63, 64, 67–69] and 138 ns–13 ms [67, 69]). This material therefore presents premium quantum performances, but does not integrate as easily to semiconductor technology.

1.2.3 Isoelectronic centers in semiconductors

Isoelectronic centers (ICs) in a semiconductor are defects formed of one or more atoms that bear the same number of valence electrons as the atom (or atoms) they replace. Their electronegativity difference with the lattice creates states inside the bandgap through a very localized potential that can trap charge carriers by means of the so-called the Hopfield-Thomas-Lynch (HTL) binding mechanism [90] (see Sect. 2.2.1).

Similar to NV centers, their configuration and symmetry are determined by the lattice in which they are embedded, leading to lesser emission broadening than QDs in an ensemble measurement. The emission structures seen in such a measurement can be associated with particular atomic configurations of the defect, as it has been done for the N_2 molecule in GaP (GaP: N_2) [91,92] and the N_2 molecule in GaAs (GaAs: N_2) [27,93] (see Sect. 2.2.2). As detailed later in Sect. 2.2, these defects can bind excitons and trions, giving access to both excitonic and spin qubits. Their performances compare well to those of QDs, for example, the excitonic qubit in GaAs: N_2 has shown dipole moments ranging from 5 to 65 D, with an average of 27 D [25], a T_1 limited by its radiative lifetime (200–670 ps [25,83]) and a T_2^* of 115 ps.

IC systems share advantages of both QDs and atomic defects such as NV centers. First, since they are hosted in semiconductors, they profit from all the associated fabrication techniques and can easily be embedded in optical cavities or gated devices. Second, in a host of great crystalline quality, the low inhomogeneous broadening of a particular defect configuration allows efficient coupling between distinct qubits, a necessary ingredient for the implementation of two-qubit gates. Finally, ICs are a large family of defects that include numerous symmetries with different fine structure and selection rules to be exploited in control protocols (e.g. a degeneracy of states crucial for the generation of entangled photons or decoupled states useful for single-shot readout). These promising characteristics have set the basic motivations for studying the Te_2 molecule in ZnSe (ZnSe: Te_2).

Particularities of the ZnSe: Te_2 system, subject of this thesis

The defect designated as ZnSe: Te_2 in this work is an IC most probably formed of two tellurium (Te) first-neighbor atoms in the selenium (Se) sublattice, as it is known to bear C_{2v} symmetry from its emission selection rules [84,94,95]. There are two possible configurations, one in the $x'y'$ plane of the unit cell, in the [110] direction (designated as “in-plane”), the

other along the $[011]$ direction (“out-of-plane”), which form a 45° angle with one another both in plane and out of plane (Fig. 1.2). Here, coordinates with primes are lab coordinates, while those without are molecule coordinates. In the rest of the text, the polarization of transitions and the projection axes of angular momenta are always given with respect to the molecule coordinates, x , y and z , the latter being the direction of the C_2 -rotation axis.

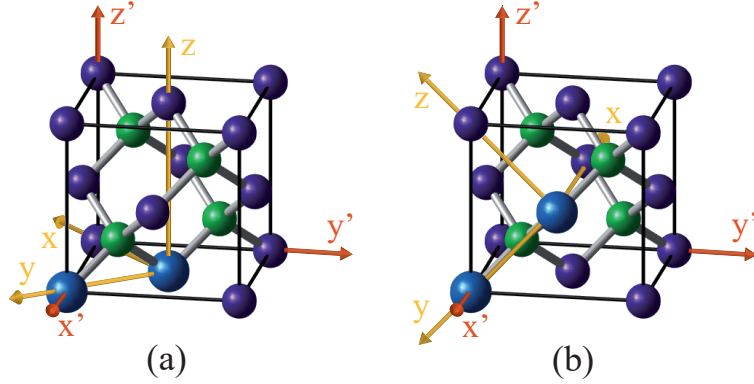


Figure 1.2 ZnSe lattice with (a) in-plane and (b) out-of-plane Te_2 molecules. Red axes are lab coordinates, while yellow ones are that of the defect. Green, purple and blue spheres are respectively Zn, Se and Te atoms.

The radiative lifetime of a Te_2 -bound exciton has been estimated to be shorter than 500 ps in Ref. [94], a value limited by their experimental resolution. T_1 for an excitonic qubit is therefore thought to be closer to the 80-ps value measured for a trion [28]. The large emission broadening mentioned in Table 1.1 is discussed in Sect. 2.2, where $\text{ZnSe}:\text{Te}_2$ emission properties are detailed. The system also offers a few additional characteristics that seem advantageous as an OAQ, which are listed below.

Hole spin qubits As the Te atom is larger than Se, it is more electropositive and can bind a hole or an exciton complex through the HTL mechanism. Consequently, in photoluminescence (PL) spectra, very narrow lines ranging from 2.6 to 2.8 eV are associated with the recombination of excitons and positive trions bound to $\text{ZnSe}:\text{Te}_2$ [84, 94, 96]. The latter is most interesting, as its recombination leaves behind a single hole, defining a hole spin qubit. This hole sits in a p -type valence band and therefore has a node at the position of each nucleus. Any hyperfine interaction leading to decoherence is consequently thought to be mitigated, as it has been demonstrated in III-V QDs [45].

Abundance of non-zero nuclear spin isotopes The most promising advantage of ZnSe:Te₂ might be that none of its constituting atoms have abundant isotopes with non-zero nuclear spins, as listed in Table 1.2, contrary to III-V materials. The probability that a particular nucleus in the lattice possess a non-zero spin is respectively 4.10 % for zinc (Zn), 7.64 % for Se and 8.04 % for Te. The spin environment in this material is relatively clean and one can therefore expect decoherence mechanisms involving random fluctuations of the nuclear spin background to be less important.

Table 1.2 Spin [97] and relative abundance of isotopes [98] for Zn, Se and Te atoms

Isotope	Spin	Mole percent (%)	Isotope	Spin	Mole percent (%)
⁶⁴ Zn	0	48.63	⁸² Se	0	8.73
⁶⁶ Zn	0	27.91	¹²⁰ Te	0	0.10
⁶⁷ Zn	5/2	4.10	¹²² Te	0	2.60
⁶⁸ Zn	0	18.75	¹²³ Te	1/2	0.91
⁷⁰ Zn	0	0.62	¹²⁴ Te	0	4.82
⁷⁴ Se	0	0.89	¹²⁵ Te	1/2	7.13
⁷⁶ Se	0	9.37	¹²⁶ Te	0	18.95
⁷⁷ Se	1/2	7.64	¹²⁸ Te	0	31.69
⁷⁸ Se	0	23.77	¹³⁰ Te	0	33.80
⁸⁰ Se	0	49.61			

Additionally, the possibility of having one Te spin in a Te₂ molecule binding a hole spin would lead to a quantum register similar to NV centers, taking advantage of the longer T_1 and T_2 of nuclear spins.

Possibility for new quantum control protocols Additionally, this system present an energy structure that allows for a new efficient control scheme: the ultrafast non resonant (NR) initialization of a hole spin in the absence of a magnetic field [28], depicted in Fig. 1.3. A circularly polarized laser pulse resonant with the donor-bound exciton transition (D_0X) in zinc selenide (ZnSe) creates an exciton with a definite spin, which in turn tunnels onto a Te₂ molecule in its vicinity before it has time to precess. In the case where the molecule was previously populated with a single hole, a trion is formed, and its recombination leaves the hole in a polarized spin configuration. The initialization time for a 98.5 % fidelity is less than 150 ps.

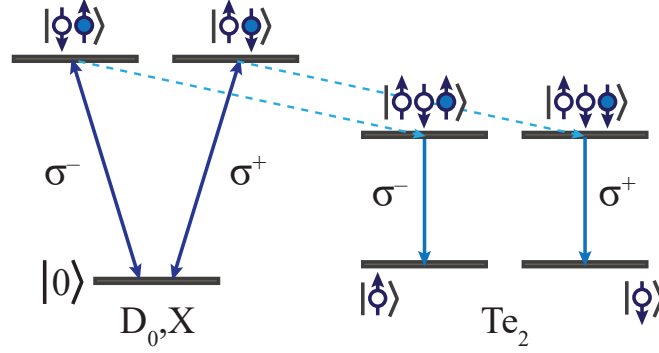


Figure 1.3 Ultrafast NR initialization scheme of a hole spin in ZnSe. First, an exciton of definite polarization is resonantly created on a nearby donor impurity (D_0X) by the absorption of a circularly-polarized photon (σ^+ , σ^-). It then tunnels onto a Te_2 molecule, which has already bound a hole. The resulting trion recombines, leaving behind a polarized hole spin. Blue circles are electrons, white ones are holes, arrows are spin projections and $|0\rangle$ is the donor ground state with no exciton.

1.3 Research objectives

Given the promising characteristics and initial results on ZnSe: Te_2 , this work was designed to further explore the potential of this IC as an OAQ through the following objectives:

1. Probe excited states of the Te_2 -bound exciton or any other states that could be exploited in the implementation of coherent control protocols.
2. Identify the mechanisms at play in the creation of a Te_2 -bound exciton through non resonant and resonant excitation.
3. Demonstrate coherent control of a single excitonic qubit bound to a Te_2 molecule and evaluate important performance metrics such as d , T_1 and T_2 .
4. Evaluate the impact of the environment on the emission properties of the center in the NR continuous-wave (CW) and resonant pulsed regimes used for coherent control.

In order to address these objectives, two sets of experiments were designed. The first one was a photoluminescence-excitation (PLE) measurement on single Te_2 molecules, where the excitation laser was scanned across higher-energy transitions while the PL emitted by a Te_2 -bound exciton was monitored. This allowed addressing Objectives 1, 2 and 4. As the measurements were performed, a new objective was formulated based upon its preliminary results, which next became dominant within this experiment:

5. Understand the mechanism behind the modulation of the emission energy of the Te_2 -bound exciton during PLE.

The second measurement campaign involved resonantly exciting an exciton in the pulsed regime and detecting its emission intensity for different excitation powers. It allowed addressing Objectives 2, 3 and 4. However, as coherent behavior remained rather elusive for most studied emitters, emphasis was put on Objective 4.

1.4 Thesis outline

This thesis is organized as follows. Chap. 2 reviews the optical properties of the host material (ZnSe) and of the studied OAQ system, as well as important quantum optics and solid-state physics concepts relating to the experiments and developed models. Chap. 3 describes the methods and experimental setups for the two experiments attempted in this work, along with the performance of crucial setup elements and the fit models used for data analysis. NR emission and PLE spectra of ZnSe:Te_2 are presented in Chap. 4, before digging into the core of the work. Chap. 5 details the modulation of the emission energy of a single Te_2 -bound exciton as the excitation energy is scanned across the ZnSe free exciton transition, demonstrating a way to remotely tune the emission properties of the emitter. This effect is assigned to the interaction between the bound exciton and free exciton-polaritons. Chap. 6 is dedicated to the resonant excitation in the pulsed regime of a single Te_2 -bound exciton. An atypical Rabi oscillation signature is observed, which is attributed to a competition between coherent and incoherent population mechanisms. The latter involves efficient tunneling of resonantly-created excitons on neighboring Te_2 molecules. Finally, Chap. 7 wraps up the work and presents limitations, improvements and future works to pursue the study of ZnSe:Te_2 as an OAQ.

CHAPTER 2 LITERATURE REVIEW

This chapter reviews the theory and literature relevant to this work. First, the emission properties of the ZnSe host material are presented so that experimental emission spectra presented in Chap. 4–6 can be better understood (Sect. 2.1). Then, the binding mechanism of excitons to isoelectronic centers (ICs), the emission energy of different configurations of such defects observed in several semiconductors, as well as their Hamiltonian and exciton-wavefunction basis in C_{2v} symmetry are detailed (Sect. 2.2). The exciton-polariton picture of light propagation in a material is afterwards discussed in Sect. 2.3, a concept extensively used in the discussion of Chap. 5. The dispersion relation linking the energy ω and the wavevector \mathbf{k} is demonstrated. In Sect. 2.4, the semi-classical treatment of the interaction between a quantum two-level system (TLS) and a classical light field is explored through Rabi oscillations, the optical Bloch equations and the dressed-state picture. Finally, the influence of charge fluctuations in the environment of a quantum emitter on its emission properties is presented in Sect. 2.5, along with strategies to mitigate its deleterious effects.

2.1 Emission properties of bulk ZnSe

Zincblende ZnSe is a semiconductor of T_d symmetry that has a direct bandgap of (2.800 ± 0.005) eV at 7 K and a $5.6692\text{-}\text{\AA}$ lattice constant at 300 K [99]. Single crystals can be obtained by liquid-phase epitaxy [100, 101], precipitation from a solution [102], zone melting [103] or vapor-phase growth after the sublimation of a powder or a polycrystal [104–106]. In more recent works, it is often epitaxially grown on [100] or [110] GaAs using metal-organic chemical vapor deposition [107–109] or molecular beam epitaxy [23, 24, 29, 84, 103, 110–112], as it is the case for our samples (see Sect. 3.1), which leaves the layer under biaxial compressive strain for thicknesses below 150 nm [103, 112] due to a 0.28 % lattice mismatch [99, 113] at 300 K. This strain pushes light holes (LH) to higher energy than heavy holes (HH) [110, 112]. Layers thicker than the threshold form dislocations, but are still under a residual tensile strain resulting from the difference in thermal expansion coefficients between ZnSe and GaAs [103].

Reflectance and PL measurements have led to the identification of free exciton (FX) and bound exciton transitions in the material, the energy of which depends on the thickness and strain level [103, 109–112], as well as on the stoichiometry of the ZnSe compound [114] and on the concentration of impurities in the crystal [105], leading to a significant variability in

literature results.

ZnSe single crystals generally present three bound exciton bands in addition to the HH and LH FX, which are, in the absence of strain, degenerate. On Fig. 2.1 (a), a spectrum from a single unstrained ZnSe crystal is shown, taken from [114]. One can see the FX structure (labeled Ex) at 2.8021 eV, the I_1 transition coming from the recombination of excitons bound to neutral acceptors at 2.7828 eV, the I_2 transition coming from excitons bound to neutral donors (D_0X) at 2.7970 eV and the I_3 lines associated with excitons bound to ionized donors between 2.793 and 2.797 eV. The first three transitions have also been respectively reported by other authors in the ranges 2.7990–2.8039 eV, 2.7825–2.7936 eV and 2.7967–2.7978 eV at temperatures between 1.6 and 9 K [101–106, 115].

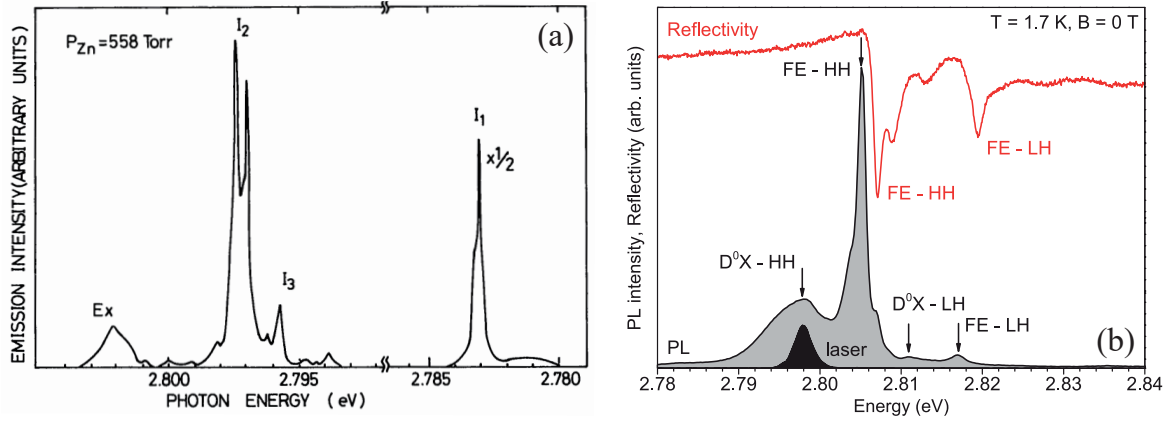


Figure 2.1 PL spectrum of bulk (a) and thin strained ZnSe (b). In (a), FX (Ex), excitons bound to neutral acceptors (I_1), to excitons bound to neutral donors (I_2) and to ionized donors (I_3) are observed. In (b), only lines related to HH and LH FX (FE-HH and FE-LH) and excitons bound to neutral donors (D^0X) are seen. The reflectivity curve confirms the position of the FX transitions as well as highlights the presence of exciton-polaritons through secondary absorption features. (a) Reprinted with permission from Ref. [114]. Copyright (1980) by the Physical Society of Japan and the Japan Society of Applied Physics. (b) Adapted with permission from Ref. [24].

In the case of thin ZnSe layers grown on GaAs (70–200 nm), the degeneracy of HH and LH FX is lifted and their respective emission structures are reported at 2.8041–2.8064 eV and 2.8123–2.8180 eV at temperatures between 1.7 and 12 K [24, 29, 103, 109]. The D_0X appear for their part between 2.7978 and 2.8015 eV. Fig. 2.1 (b) present an example spectrum for 70–100-nm thick layers adapted from Ref. [24], where FE stands for FX. The assignment of both FX transitions was supported by a reflectivity measurement, also displayed in the

figure. The shape of the D_0X greatly depends on the sample, mostly due to the magnitude of the strain, but also to the impurity and the layer thickness involved. Here, they bear two peaks, one involving the HH, the other the LH.

2.2 Isoelectronic centers in semiconductors

Here are reviewed several properties of ICs in semiconductors to complement those already mentioned in Sect. 1.2.3. First, the binding mechanism of excitonic complexes to such a defect is detailed, which dictates among other things what type of qubit is formed (exciton, or electron or hole spin). Then, the binding energy dependence on the atomic configuration of the defect molecules in several IC systems is discussed, followed by the presentation of Hamiltonians and wavefunctions describing excitonic complexes bound to defect configurations of C_{2v} symmetry, which is the specific case of ZnSe:Te₂.

2.2.1 The Hopfield-Thomas-Lynch binding model for excitons

The binding of an exciton to an IC happens through the two-step Hopfield-Thomas-Lynch (HTL) mechanism [90]. First, the primary charge is attracted by the local potential resulting from the electronegativity difference of the defect with the lattice. Once this electron or hole is bound, depending on whether the atoms are respectively sufficiently more electronegative or electropositive, the defect can further attract a charge of opposite sign through a Coulomb potential and form an exciton. The primary charge is then localized in a potential estimated to be the size of a unit cell. The secondary charge is much more delocalized and can be described with an effective-mass envelope function. Fig. 2.2 illustrates the binding of an exciton to a Te₂ molecule, where the primary charge is a hole. A trion (charged exciton) is formed if the defect already hosts a charge prior to exciton capture, and a biexciton (XX) can also be formed if the bound exciton captures another exciton.

2.2.2 Configurations and emission energies

The binding energy of a particular IC configuration depends on the number of atoms involved and on their atomic separation. As the position of the constituting atoms is determined by the anion sublattice sites they occupy, the symmetry of the configuration is well-defined and inhomogeneous broadening is low, typical of an atomic defect. Distinct emission lines with

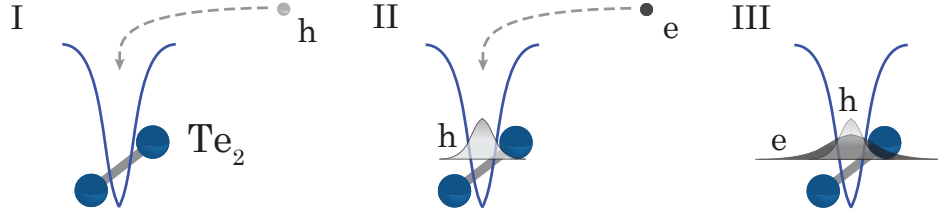


Figure 2.2 HTL model for a Te_2 molecule. An itinerant hole is attracted by the localized potential of the Te_2 molecule (I) and binds to it. Its Coulomb potential then attracts a free electron (II) to form an exciton (III) in which the electron is more delocalized.

clear polarization selection rules are observed. Due to these advantageous properties, PL measurements on ensembles and single defects have allowed to identify different IC configurations, especially in GaP and GaAs. ZnSe has proven to be slightly more complicated, as discussed below.

GaP: N_2

The most characterized IC system is the N_2 molecule in GaP (GaP: N_2). First thoroughly studied in Ref. [91], its emission spectrum consists of several relatively narrow lines at energies within the bandgap and is presented in Fig. 2.3 for an ensemble encompassing multiple defect configurations and orientations. The lines correspond to the recombination of excitons bound to ICs formed of at least two substitutional nitrogen (N) atoms in the phosphorus (P) sublattice [91, 116], with an electron as the primary bound charge as N is more electronegative than P. The transitions are traditionally labelled NN_i , where $i = 1, 2, \dots$ is an index indicating the separation between the two constituting atoms (i.e. first neighbors, second neighbors and so on). NN_∞ , a molecule of infinite separation, designates an isolated N atom and is often referred to as the *A* line [91].

The HTL binding model is valid for few-atom molecules and predicts that their binding energy increases with the number of atoms involved or with decreasing atomic separation. Consequently, the N_2 molecule presenting the lowest emission energy (E_{em}) on an emission spectrum should be NN_1 , the first-neighbor pair. The higher-energy transitions have been assigned accordingly, with increasing atomic separation. Table 2.1 summarizes the molecule labels and their E_{em} , as well as their predicted and experimentally-deduced symmetry, when available. Two potential three-N clusters have also been reported to emit at 2.071 eV [117], below NN_1 , and 2.285 eV [118].

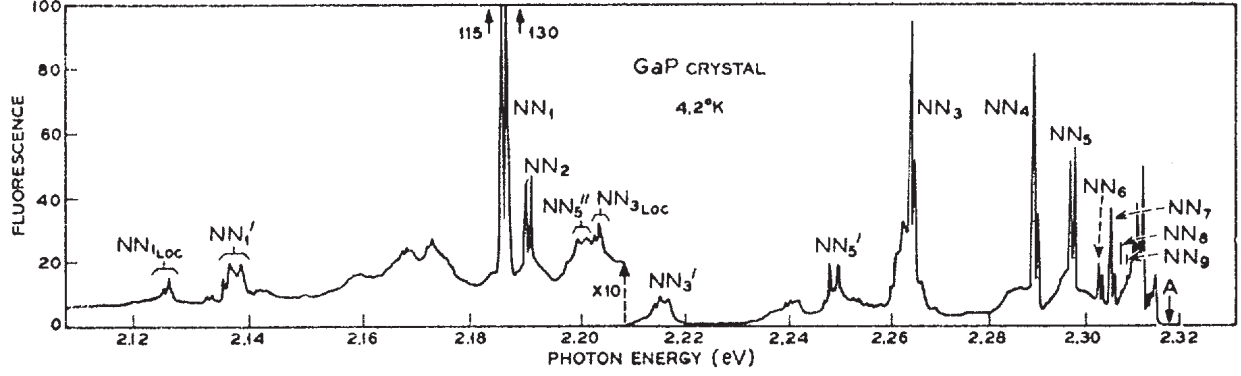


Figure 2.3 Ensemble emission spectrum of GaP:N₂, showing the series of very narrow emission lines associated with NN_{*i*} defects. NN₁ is the deepest level and is assigned to first-neighbor N₂ molecules, NN₂ to second-neighbor molecules and so on. The A line, not shown but only marked, corresponds to isolated N atoms, or molecules of infinite separation NN_∞. NN'_{*i*} are phonon replicas and NN_{*i*}Loc are local-mode replicas. Reprinted with permission from Ref. [91]. Copyright (1966) by the American Physical Society.

The matches of NN_{*i*} labels to the observed transitions are an hypothesis deduced solely from their relative energy positions in the spectrum. They are not based on a precise knowledge of the atomic arrangement and therefore can be erroneous. Indeed, further investigations of NN_{*i*} centers properties have suggested that a large portion of the N-related emission lines are not labelled properly or are not originating from two-atom molecules at all. Due to its hole binding energy, the magnitude of its surrounding strain field, its behavior under hydrostatic pressure and strain, as well as the dependence of its E_{em} on N isotopes, the emission line first attributed to NN₂ is now thought be a triple in the (111) plane [116]. PL measurements under uniaxial strain highlighted that NN₅-, NN₆- and NN₇-labelled lines have different symmetries as those predicted by their NN_{*i*} configurations (see Table 2.1) [92]. Only NN₁, NN₃ and NN₄ lines have shown a symmetry that is consistent with their assignment. Also, the abundance of extracted from the emission intensity of NN_{5,6} lines as a function of N concentration deviates from what is expected for fifth and sixth-neighbor N₂ molecules [118], another hint that their assignment should be reviewed.

Although their exact atomic configuration might not be known, NN_{*i*} ICs have well-defined E_{em} and symmetry and show very little inhomogeneous broadening in large ensemble measurements ($\sim 730 \mu\text{eV}$ for both NN₁ and NN₄ in Fig. 2.3) compared to QDs, properties that are very advantageous for qubit applications.

Table 2.1 Emission energy (E_{em}) and symmetry (sym.) of different NN_i ICs in GaP.

NN_i [91]	E_{em} (eV)	Predicted sym. [119]	Measured sym.
NN_1	2.1846–2.1874 [91, 117, 119–123]	C_{2v}	C_{2v} [92, 122, 123]
NN_2	2.1893–2.1922 [91, 92, 116, 117, 119, 121, 122]	D_{2d}	C_1 [116] (three-atom cluster)
NN_3	2.2603–2.2658 [91, 92, 117–123]	C_s	C_s [92]
NN_4	2.2888–2.910 [91, 92, 117–123]	C_{2v}	C_{2v} [92, 118, 122, 123]
NN_5	2.2963–2.2986 [91, 92, 117–122]	C_2	probably C_s [92]
NN_6	2.3027–2.3044 [91, 92, 117–121, 123]	C_{3v}	C_{3v} [91], D_{2d} , C_{2v} or C_s [92]
NN_7	2.3057–2.3068 [91, 92, 117, 119, 121]	C_1	C_{2v} [92]
NN_8	2.3076–2.3111 [91, 117, 121]	D_{2d}	
NN_9	2.3101–2.3102 [91, 121]	C_{2v} or C_s	
NN_{10}	2.3110–2.3115 [91, 121]	C_2	
A	2.3153–2.3173 [91, 118–125]	T_d	

GaAs: N_2

A N_2 molecule in GaAs (GaAs:N_2) is formed when two N atoms replace arsenic (As) atoms in the host matrix. The emission signature from N_2 molecules in ensemble measurements depends greatly on N concentration [126–129], as this parameter influences the average atomic separation and favors certain configurations. While several lines have been reported, their exact configuration (number of atoms, orientation, separation) is not known beyond any doubt.

Measurements under hydrostatic pressure have determined that energy levels associated with isolated N atoms and most N_2 molecules configurations (named NN_i according to GaP: N_2 nomenclature) are resonant with the conduction band [130–132]. Nevertheless, lines at 1.4954 and 1.5086 eV under atmospheric pressure were assigned the respective atomic configurations of NN_1 and NN_4 (also designated as X_2 and X_1) [82, 126, 127, 133], based on their C_{2v} symmetry emission signature [93, 129, 134]. Other N-related lines have been observed at, to name only a few, 1.4580, 1.4490 and 1.4435 eV and are most likely due to N clusters involving more than two atoms [133, 135], although some authors have erroneously assigned them to NN_i pairs [126–128, 136–139].

Fig. 2.4 presents a spectrum from Ref. [82] showing some of the most common emission fea-

tures, here marked as X_1 – X_5 . Despite the configurational uncertainty, it is clear that, similar to GaP:N₂, a particular defect type has relatively low inhomogeneous broadening despite the large measured ensemble (e.g. 0.99 meV for X_1 in Fig. 2.4, similar to GaP:N₂).

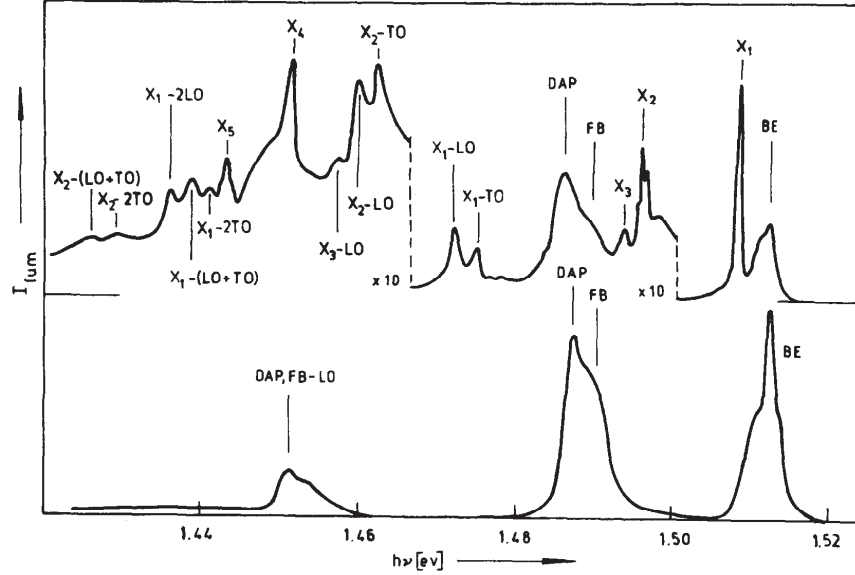


Figure 2.4 Ensemble emission spectrum of GaAs:N₂, showing (top) the N-related X_i , $i = 1, 2, \dots, 5$ transitions along with their LO and TO replica, as well as the spectrum of undoped GaAs (bottom). BE: excitons bound to neutral impurities, FB: free-to-bound transitions, DAP: donor-acceptor pair. Reprinted from Ref. [82], p. 169, Copyright (1985), with permission from Elsevier.

ZnSe:Te₂

In ZnSe:Te₂, the presence of a dislocation band at 2.60–2.61 eV [84,140] and multiple phonon replicas of donor-acceptor recombinations prevented the assignment of the emission energies of Te-related transitions to specific configurations in ensemble studies (as shown in Fig. 2.5). Only regions of broad emission (few hundred meV) centered at 2.63–2.70, 2.45–2.52 and 2.35 eV could be identified [96,141–153]. The first broad structure has been assigned to isolated Te atoms [143,145,146,148,149], Te₂ molecules [96,144,147,152,153] or several-atom clusters [142,144,150,151], the second to Te₂ molecules [143,146], Te_{n≥2} [145,150], Te₃ [144,147] or Te_{n≥3} [96,152,153] clusters and the latter to Te_{n≥3} clusters [147]. Some works suggested that isolated Te cannot bind excitons [96,141,147], others claimed that excitons bound to this center emit at 2.75–2.78 eV [145,150,151]. Still, it is expected that these ICs behave similarly to GaP:N₂ and GaAs:N₂ and that a specific atomic configura-

tion shows very small inhomogeneous broadening. Environmental fluctuations and efficient phonon-coupling would be responsible for the broad emission lineshapes reported [144].

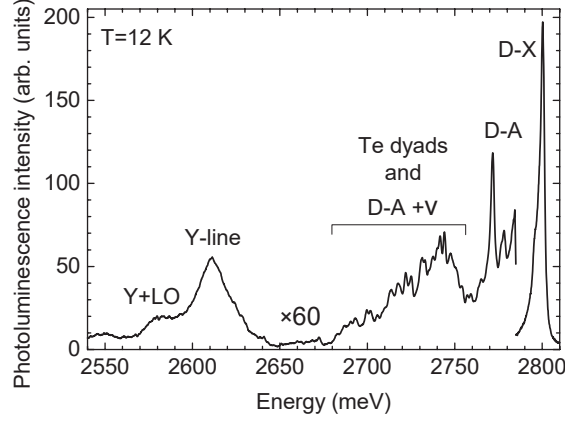


Figure 2.5 Ensemble emission spectrum of ZnSe:Te₂, on which Te₂-bound excitons lines are superimposed to the phonon replicas of donor-acceptor (D-A) recombinations. Excitons bound to neutral donors (D-X) and a dislocation-related structure (Y), along with its LO phonon replica, are also visible. Reprinted with permission from Ref. [84]. Copyright (2010) by the American Physical Society.

Micro-PL measurements on single emitters in the 2.6–2.8 eV range confirmed that these structures were of C_{2v} symmetry [84,94,95], supporting the first-neighbor Te₂ molecule hypothesis. In this work, I adopt this assignment while keeping in mind that the configuration has not been irrefutably confirmed. Other atomic arrangements such as a fourth-neighbor two-atom molecule or three atoms placed along the same $\langle 110 \rangle$ direction would indeed also be possible, but knowledge of the exact configuration has in the end little impact on the relevance of the results obtained as part of this work.

2.2.3 Excitonic wavefunctions and Hamiltonians in C_{2v} -symmetry systems

Excitonic wavefunctions and their Hamiltonian allow to predict the fine structure and polarization response of the radiative recombination of a particular bound exciton complex. Here, I concentrate on C_{2v} excitons, trions and biexcitons, as they are the case of interest in ZnSe:Te₂.

Excitons

The total excitonic Hamiltonian can be decomposed in three parts, one acting on the electron (H_e), another on the hole (H_h) and an exchange term acting on coupled electron-hole states (H_{ex}). It must necessarily be formed of terms that are invariant under all symmetry operations allowed by the point group describing the defect embedded in the crystal (here C_{2v}), as well as under time-reversal symmetry. In other words, it must globally transform as the Γ_1 irreducible representation (irrep). The system axes for the derivation are the same as those illustrated in Fig. 1.2. The z axis, by definition the highest-symmetry operation (a two-fold rotation C_2), is perpendicular to the Te_2 molecule. The y axis is oriented along the molecule, leaving x as the axis perpendicular to both y and z .

The spin and orbital angular-momentum parts of the excitonic wavefunction, which are sufficient to work out the selection rules and polarization of the transitions, are built by combining electron and hole single-particle states [154–156]. In the s -type conduction band, the electron spin $S_e = 1/2$ can take projection values of $m_{s,e} = \{-1/2, 1/2\}$ and the orbital angular momentum $L_e = 0$, the unique value of $m_{l,e} = 0$. The total angular momentum for an electron is thus equivalent to its spin and the two spin projections $|\uparrow\rangle = |1/2, 1/2\rangle$ and $|\downarrow\rangle = |1/2, -1/2\rangle$ can be used as a complete basis. The associated Hamiltonian is a 2×2 matrix constructed with Pauli matrices ($\sigma_x, \sigma_y, \sigma_z$) and the identity matrix. Without any perturbation, the two basis states are degenerate and the Hamiltonian is:

$$H_e = \begin{bmatrix} E_e & 0 \\ 0 & E_e \end{bmatrix}, \quad (2.1)$$

where E_e is the energy of the electron trapped by the IC.

The hole, for its part, is in a p -type valence band and has an orbital angular momentum of $L_h = 1$, in addition to its spin of $S_h = 1/2$. The total angular momentum J_h has two possible values, $J_h = 3/2$ with projections $m_{j,h} = \{3/2, 1/2, -1/2, -3/2\}$ and $J_h = 1/2$ with projections $m_{j,h} = \{1/2, -1/2\}$. The former form the LH and HH bands, respectively of $m_{j,h} = \pm 1/2$ and $m_{j,h} = \pm 3/2$, while the latter form the split-off band, which is pushed to higher (hole) energy by the spin-orbit interaction. It is therefore from now on neglected, especially since it is never observed in PL. The complete basis for the relevant hole states is consequently composed of $|\uparrow\rangle = |3/2, 3/2\rangle$, $|\uparrow_h\rangle = |3/2, 1/2\rangle$, $|\downarrow_h\rangle = |3/2, -1/2\rangle$ and $|\downarrow\rangle = |3/2, -3/2\rangle$. The hole Hamiltonian is formed using 16 4×4 linearly independent matrices, which are taken as powers and combinations of the total angular momentum operators J_x ,

J_y and J_z , plus the identity matrix. In the absence of an external perturbation, it bears four terms respecting the Γ_1 representation:

$$H_h = E_h \cdot \mathbb{1}^{(4 \times 4)} + v_x J_x^2 + v_y J_y^2 + v_z J_z^2, \quad (2.2)$$

where E_h is the energy of the captured hole and $\mathbb{1}^{(4 \times 4)}$ is a 4×4 identity matrix. The last three terms refer to crystal field interaction, which is characterized by the empirical v_i ($i = x, y, z$) parameters. They emerge from the fact that the hole is sitting in a p orbital, making it sensitive to the crystal atomic charge configuration. In a C_{2v} -symmetry anisotropic electric field, all three axes along which these orbitals (p_x, p_y, p_z) are aligned become non-equivalent, leading to a lifting of degeneracy of HH and LH states.

Both H_e and H_h must be expanded in terms of the 8×8 exciton basis formed with a Kronecker product, respectively with a 4×4 and 2×2 identity matrix. The electron-hole exchange Hamiltonian in the electron spin-hole total angular momentum basis for its part is:

$$\begin{aligned} H_{\text{ex}} = & \sigma_z \left(4e_1 J_z + 16e_2 J_z^3 + \frac{8}{\sqrt{3}} e_3 \{J_z, J_x^2 - J_y^2\} \right) \\ & + \sigma_x \left(4e_4 J_x + 16e_5 J_x^3 + 8e_6 \{J_x, J_y^2 - J_z^2\} \right) \\ & + \sigma_y \left(4e_7 J_y + 16e_8 J_y^3 + 8e_9 \{J_y, J_z^2 - J_x^2\} \right), \end{aligned} \quad (2.3)$$

where e_i ($i = 1, 2, \dots, 9$) are parameters and curly brackets define an anti-commutator for the two involved operators. Hamiltonians representing any type of additional interaction that could be applied to the system (e.g. an electric field, a magnetic field, strain) are detailed in Appendix B, as developed in Ref. [154].

Exciton wavefunctions are built from the tensor product of an electron and a hole wavefunction. Eq. 2.4 presents the 8 basis wavefunctions that have been expressed as linear combinations transforming as irreps of the C_{2v} symmetry point group:

$$\begin{aligned} |X_{hh}\rangle &= \frac{1}{\sqrt{2}} (|\downarrow\uparrow\rangle + |\uparrow\downarrow\rangle) & |X_{lh}\rangle &= \frac{1}{\sqrt{2}} (|\downarrow\downarrow_h\rangle + |\uparrow\uparrow_h\rangle) \\ |Y_{hh}\rangle &= \frac{i}{\sqrt{2}} (-|\downarrow\uparrow\rangle + |\uparrow\downarrow\rangle) & |Y_{lh}\rangle &= \frac{i}{\sqrt{2}} (-|\downarrow\downarrow_h\rangle + |\uparrow\uparrow_h\rangle) \\ |Z_{hh}\rangle &= \frac{1}{\sqrt{2}} (-|\downarrow\downarrow\rangle + |\uparrow\uparrow\rangle) & |Z_{lh}\rangle &= \frac{1}{\sqrt{2}} (-|\downarrow\uparrow_h\rangle + |\uparrow\downarrow_h\rangle) \\ |D_{hh}\rangle &= -\frac{i}{\sqrt{2}} (|\downarrow\downarrow\rangle + |\uparrow\uparrow\rangle) & |D_{lh}\rangle &= -\frac{i}{\sqrt{2}} (|\downarrow\uparrow_h\rangle + |\uparrow\downarrow_h\rangle). \end{aligned} \quad (2.4)$$

Crystal field and exchange interactions lift the degeneracy of all 8 exciton states. The four states on the left in Eq. 2.4 have HH character and are found at lower (hole) energy, 12.0–13.0 meV below the LH in thin compressed ZnSe [24, 84, 103, 112]. The four states on the right have LH character and are usually not observed in PL, as carrier relaxation to HH exciton states is fast. For both HH and LH excitons, one of the four transitions is dark ($|D_{ih}\rangle$, $i = l, h$), the other three are linearly polarized along x , y and z with respect to the defect axes ($|X_{ih}\rangle$, $|Y_{ih}\rangle$, $|Z_{ih}\rangle$) [154], as represented in Fig. 2.6 (a). $|Z_{hh}\rangle$ has a vanishing dipole moment and is therefore forbidden, unless HH-LH mixing is present, which is not expected in ZnSe:Te₂ due to the large HH-LH splitting.

With the optical axis along z' ([001], as defined in Fig. 1.2), only x - and y -polarized transitions are detected for an in-plane defect, while a small component of the z -polarized ones could in principle be seen for an out-of-plane one, as $z' \neq z$ in this case. Experimentally, we observe two linearly polarized and orthogonal transitions, $|X_{hh}\rangle$ and $|Y_{hh}\rangle$, upon non resonant, above-gap excitation. In the rest of the text, I refer to them as X and Y for simplicity. My convention is also to place the Y transition at higher energy, similarly to what was calculated for GaAs:N₂ [83]. However, as such a calculation was never made for ZnSe:Te₂, the ordering of the energy levels could be inverted.

Trions

In ZnSe:Te₂, trions are positive (X^+) and formed from a hole singlet and an unpaired electron, which lead to two circularly polarized transitions (respectively left-handed, σ^- , and right-handed, σ^+ , in the point of view of the source, see Fig. 2.6 (b)):

$$\begin{aligned} |m_s = -1/2\rangle &= \frac{1}{\sqrt{2}} (|\uparrow\downarrow\rangle - |\downarrow\uparrow\rangle) |\downarrow\rangle \\ |m_s = 1/2\rangle &= \frac{1}{\sqrt{2}} (|\uparrow\downarrow\rangle - |\downarrow\uparrow\rangle) |\uparrow\rangle. \end{aligned} \tag{2.5}$$

In the absence of a magnetic field, both spin configurations are degenerate and a single unpolarized emission line is observed. These complexes are very interesting for quantum information processing, since their recombination leaves a single hole on the Te₂ molecule, which can be used as a spin qubit and optically controlled through the trion transitions. However, they seem rarer in our samples and were not studied in this work.

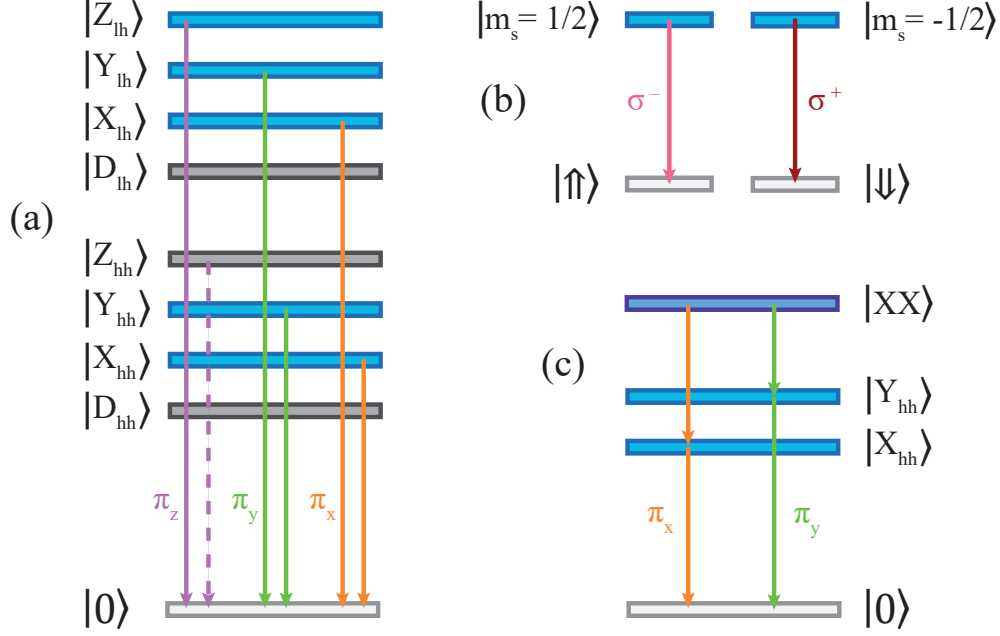


Figure 2.6 Exciton fine structure in a C_{2v} -symmetry system and polarization of its associated transitions (not to scale). (a) Exciton with its eight non-degenerate energy levels, four with LH character and four with HH character. Five are optically active (blue) and linearly polarized along x (orange), y (green) and z (purple). The remaining three are forbidden (gray). The $|Z_{hh}\rangle$ transition, although forbidden, is indicated with a dashed arrow to illustrate its polarization. (b) The two degenerate trion levels in absence of a magnetic field, giving rise to circularly polarized transitions. The recombination of a trion leaves a single hole on the Te_2 molecule. (c) Biexcitonic cascade involving the X and Y HH excitonic transitions. Two emission doublets of equal energy separation are formed, one with the y -polarized transition at higher energy, the other with the x -polarized transition.

Biexcitons

The XX state is formed of a hole and an electron singlet:

$$|XX\rangle = \frac{1}{2} (|\uparrow\downarrow\rangle - |\downarrow\uparrow\rangle) (|\uparrow\downarrow\rangle - |\downarrow\uparrow\rangle). \quad (2.6)$$

Such a wavefunction considers that spin interaction between particles of same nature (which share the same orbital wavefunction and envelope) is stronger than between particles of different nature. This should in principle lead to the absence of a biexcitonic fine structure, a fact that is validated experimentally. Indeed, the measurement of the biexcitonic cascade confirms that a single biexciton level is involved, as it gives rise to an extra pair of emission lines which, in the case of ZnSe:Te_2 , has only been observed at slightly lower energy than the exciton lines. These are separated by the same fine-structure splitting (FSS or ΔE_{XY}),

but with opposite linear polarization (Fig. 2.6 (c)). The interest of this system resides in the fact that biexcitons (bound to atomic defects or trapped in QDs) can be used to implement sources of entangled photon pairs, but this subject is beyond the scope of this work.

2.3 The exciton-polariton, a quasi-particle describing the propagation of light in matter

Strong coupling of light and matter leads to the definition of a new quasi-particle, the polariton [157]. It describes the interplay between a mechanical oscillator representing a polarization in the material and the travelling electromagnetic wave. Intuitively, this is sensible, as an oscillating polarization leads to the emission of radiation, while radiation itself creates a polarization in a material. When the oscillator in question is an exciton, the quasi-particle is called an exciton-polariton. This concept is extensively used in the discussion of Chap. 5, thus I introduce it in detail in this section.

The propagation of light in a material involves a joint propagation of polarization and electromagnetic waves, the combination of which is described by its own dispersion relation $\omega(k)$. This relation links the angular frequency of the polariton ω to the norm of its wavevector $|\mathbf{k}| = k$ and differs from that of non-interacting photons or excitons. In the following, I obtain $\omega(k)$ through a classical derivation, the quantum treatment of polaritons being out of the scope of this work. I start by expressing the dielectric function in the vicinity of an excitonic resonance using a mechanical oscillator model. Then, I add so-called “spatial dispersion” to the oscillator to take into account the parabolic behavior in k of the excitonic eigenfrequency. Finally, I introduce the polariton equation and describe the shape and behavior of its solutions, giving the different branches of the dispersion relation.

2.3.1 Dielectric function of a material with a resonance

A simple, yet quite accurate treatment to obtain the dielectric function and other optical properties of a semiconductor is the Lorentz oscillators model [158, 159]. It involves a series of identical, uncoupled mechanical harmonic oscillators of mass m , arranged in a one-dimensional chain and carrying a charge $\pm q$ at both their extremities, as illustrated in Fig. 2.7. They are driven by an electromagnetic field of angular frequency ω and wavevector $k\hat{\mathbf{z}}$ and polarized parallel to the motion of the oscillators, say the x axis. Since there is no cou-

pling between the oscillators, their resonance angular frequency is independent of wavevector, $\omega_0(k) = \omega_0$. The individual motion for the oscillator at $z = 0$ is described by the differential equation:

$$m\ddot{x} + i\Gamma\dot{x} + Kx = qE_0e^{i\omega t}, \quad (2.7)$$

with K the spring constant of the oscillator, E_0 the amplitude of the driving electric field and Γ a damping rate. Choosing a steady-state solution of the form $x(t) = x_0e^{i\omega t}$, one obtains an expression for the oscillation amplitude x_0 :

$$x_0 = \frac{qE_0}{m(\omega_0^2 - \omega^2 - i\Gamma\omega)}, \quad (2.8)$$

where K/m has been replaced by ω_0^2 . The dipole associated with this displacement is $\mathbf{p} = qx\hat{\mathbf{x}}$ and is linked to a macroscopic polarization $\mathbf{P} = N\mathbf{p}$, with N the density of oscillators. From the definition of electric displacement $\mathbf{D} = \epsilon_0\mathbf{E} + \mathbf{P} = \epsilon\epsilon_0\mathbf{E}$, one can write an expression for the dielectric function $\epsilon(\omega)$:

$$\epsilon(\omega) = \epsilon_\infty + \frac{Nq^2}{\epsilon_0m(\omega_0^2 - \omega^2 - i\Gamma\omega)}, \quad (2.9)$$

where a non-resonant contribution to the susceptibility of the material χ_{nr} has been included in $\epsilon_\infty = 1 + \chi_{\text{nr}}$, the high-frequency dielectric constant.

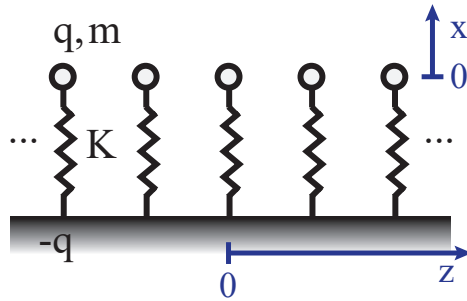


Figure 2.7 One-dimensional array of uncoupled Lorentz oscillators of mass m , charge q and spring constant K . Their movement along x is driven by an electric field propagating along the direction of the chain, z .

Finally, to take into account the quantum nature of the interaction of excitons with light, Eq. 2.9 must be rewritten to include the probability of transition through the dimensionless

oscillator strength $4\pi\beta$, which includes the relevant dipole matrix element:

$$\epsilon(\omega) = \epsilon_\infty + \frac{4\pi\beta\omega_0^2}{\omega_0^2 - \omega^2 - i\Gamma\omega}. \quad (2.10)$$

The latter equation assumes a single type of oscillators (i.e. a single resonance), the $1S$ HH exciton in our case of interest. The shape of its real and imaginary parts are shown in Fig. 2.8, which are typical of a resonance. This simple model is widely used and quite successful at explaining the properties of phononic resonances, leading to the phonon-polariton formalism. However, in the case of an excitonic resonance, the picture is not yet complete. A last ingredient to correctly describe the optical properties of exciton-polaritons is indeed still missing, spatial dispersion.

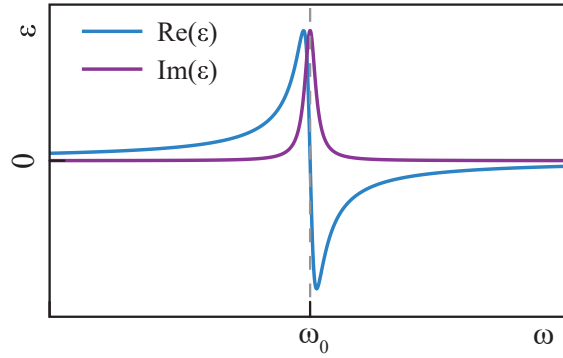


Figure 2.8 Real and imaginary parts of the dielectric function for a material with a single resonance. Both curves are normalized in order to facilitate their representation.

2.3.2 Spatial dispersion in the dielectric function

Excitons are solutions to the hydrogen-like Coulomb interaction of an electron and a hole in their respective parabolic band, a state describing a quantum of excitation of a N -particle system [160]. They are therefore not isolated oscillators but part of a complex electronic system, a condition leading their resonance angular frequency ω_0 to be a function of k [157], the so-called spatial dispersion:

$$\omega_0(k) = \omega_0 + \frac{\hbar k^2}{2M}, \quad (2.11)$$

with ω_0 their resonance angular frequency at $\mathbf{k} = \mathbf{0}$ and $M = m_e + m_h$ the exciton effective mass (m_e and m_h are the effective masses of the electron and the hole) [161]. The parabolic behavior in k is a consequence of the parabolic band approximation. Neglecting

any dependence of the numerator and Γ on \mathbf{k} , one can replace ω_0^2 in Eq. 2.10 with $\omega_0^2(k)$:

$$\epsilon(\omega, k) = \epsilon_\infty + \frac{4\pi\beta\omega_0^2}{\omega_0^2 + \frac{\hbar k^2}{M}\omega_0 - \omega^2 - i\Gamma\omega}. \quad (2.12)$$

Eq. 2.12 also neglects a term in k^4 in the expansion of $\omega_0^2(k)$ as $k \ll \pi/a$, with a the lattice constant. This expression consists in a more accurate picture of the excitonic dielectric function and is used to derive the exciton-polariton dispersion relation $\omega(k)$.

2.3.3 The polariton equation and dispersion relation

The polariton equation leading to $\omega(k)$ is simply the well-known relation between the dielectric function, ω and k involving c , the speed of light in vacuum:

$$\epsilon(\omega, k) = \frac{k^2 c^2}{\omega^2}. \quad (2.13)$$

Taking the expression for $\epsilon(\omega, k)$ given in Eq. 2.12, one obtains two solutions for $\omega(k)$, or two branches. Fig. 2.9 shows a schematic representation of solutions for $\Gamma = 0$, named lower (LPB) and upper (UPB) polariton branches. They describe the two transverse propagation modes for an electromagnetic wave in matter. In other words, for a given photon energy, there can be up to two modes in a material for a single oscillator type, each with its own wavevector. The case illustrated in Fig. 2.9 is real, but solutions are complex for $\Gamma \neq 0$, giving rise to absorption.

The branches anti-cross at the junction of the transverse exciton (Eq. 2.11) and photon ($\omega_p(k) = ck/\sqrt{\epsilon_\infty}$) dispersion relations. Consequently, portions of both branches have a parabolic behavior or excitonic character (they are then qualified as “exciton-like”), while others are “photon-like” with a linear behavior.

The longitudinal branch for its part describes the propagation of a polarization parallel to its wavevector. It is the solution to the equation $\epsilon(\omega = \omega_L, k) = 0$ and is illustrated by the gray curve in Fig. 2.9. If $\Gamma = 0$, its analytic expression is:

$$\omega_L(k) = \left[\omega_0^2 \left(\frac{4\pi\beta}{\epsilon_\infty} + 1 \right) + \frac{\hbar k^2 \omega_0}{2M} \right]^{1/2}. \quad (2.14)$$

At $\mathbf{k} = \mathbf{0}$, it takes the same value $\omega_L = \omega_0 (4\pi\beta/\epsilon_\infty + 1)^{1/2}$ as UPB and is involved in defining

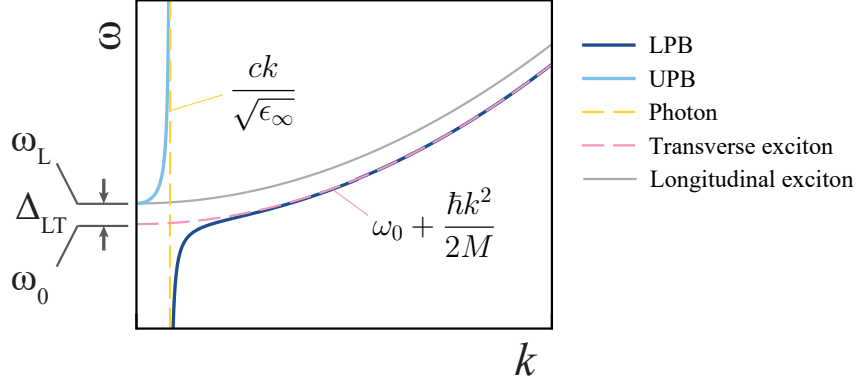


Figure 2.9 Typical dispersion relation for exciton-polaritons. The two transverse branches, LPB and UPB, anti-cross at the junction of the non-interacting photon and transverse exciton dispersion relations, and possess both photonic and excitonic characters. The longitudinal branch and UPB share the same initial energy ω_L , and their energy separation with the exciton energy at $\mathbf{k} = \mathbf{0}$, ω_0 , defines the longitudinal-transverse splitting, Δ_{LT} .

the longitudinal-transverse splitting $\Delta_{LT} = \omega_L - \omega_0$. However, since this branch does not couple to transverse radiation, it is not considered in the rest of the thesis.

2.3.4 Polaritons in ZnSe

Due to their relatively large exciton binding energy and oscillator strength, II-VI materials are particularly suitable for the observation of polaritons [112, 162, 163]. Indeed, one of the first direct observations of Bose-Einstein condensation of cavity exciton-polaritons was performed in cadmium telluride (CdTe) [163], an experiment requiring strong polariton-polariton interactions.

In ZnSe, the exciton binding energy and oscillator strength $4\pi\beta$ of the $1S$ HH FX transition are indeed quite large and respectively of value (18.86 ± 0.02) meV [99] and 5.78×10^{-3} – 5.03×10^{-2} [112, 162, 164–166], leading to the easy observation of polaritonic effects in the bulk in Brillouin scattering experiments [165]. Also, modulations in the reflectance curve of ZnSe layers grown on GaAs (without sophisticated structures such as Bragg mirrors) were associated with the presence of exciton-polaritons [112, 162]. Fig. 2.10 shows one of the results, where local maxima in the reflectance spectrum above the resonance are due to interference of polaritons in the layer. Quantized wavevectors $k = m\pi/d$ associated with these energies, with m the interference order and d the layer thickness, can be extracted

using the Fabry-Perot condition for constructive interference at normal incidence [162]:

$$\begin{aligned} E_{\text{phot}}(m, d) &= \frac{\hbar c}{\sqrt{\epsilon_{\infty}}} \left(\frac{m\pi}{d} \right), \\ E_{\text{ex}}(m, d) &= \frac{\hbar^2 m^2 \pi^2}{2M d^2}, \end{aligned} \quad (2.15)$$

where the equations concern the photonic and excitonic parts of the dispersion relation. These have been reported on the calculated dispersion relation with good correspondence (Fig. 2.10 (b)). Four resonances in the dielectric function were considered in this case: the 1S-LH and HH FX, as well as the 2S and 3S-HH FX, leading to a 5-branch polariton dispersion relation. One can see that the observed Fabry-Perot modes involve the third one, which spans from the 1S-LH to the 2S-HH FX resonances. Similar and very convincing results were also obtained in GaAs layers [167].

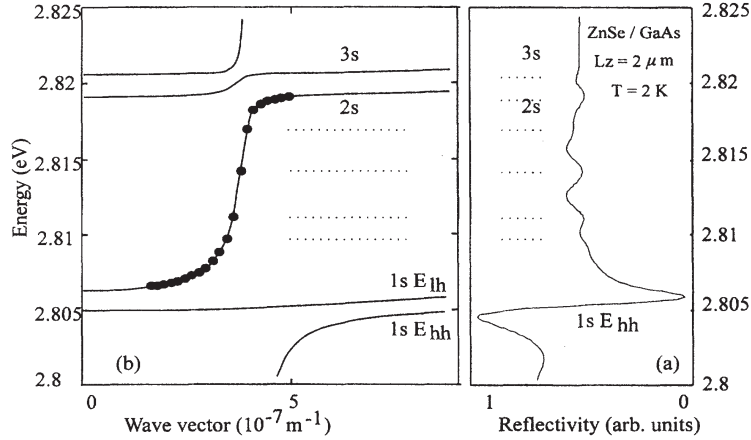


Figure 2.10 (a) Reflectance spectrum of a 2 μm -thick ZnSe layer on GaAs. Resonance of the polaritonic Fabry-Perot modes are clearly seen, as well as that of 1S, 2S and 3S HH free-exciton transitions. (b) The Fabry-Perot resonance energies and associated wavevectors are reported on the dispersion relation with good agreement. Reprinted with permission from Ref. [162]. Copyright (1995) by the American Physical Society.

It is clear from the results presented above that exciton-polaritons have non-negligible effects on the optical properties of ZnSe. In Chap. 5, their interactions with Te₂-bound excitons are considered to explain some of our NR emission results (Sect. 1.3, Obj. 5).

2.4 Optical coherent control of an excitonic qubit

This work focused on investigating ZnSe:Te₂ as a potential OAQ candidate, therefore it attempted to coherently control the state of an excitonic qubit in this system through optical means and determine its performance parameters (Sect. 1.3, Obj. 3). The following section develops the basis of this control method by detailing the coherent interaction of a classical electric field and a quantum two-level system (TLS). This formalism applies directly to a C_{2v} -symmetry excitonic qubit, as its exciton states are all non-degenerate and thus can be addressed individually.

2.4.1 Rabi oscillations

The TLS under study consists in the $1S$ (X) and ground (0) states of a bound HH exciton. It has a resonance frequency ω_0 and a dipole moment \mathbf{d} (Fig. 2.11). It interacts with a classical light field \mathbf{E} of frequency ω , amplitude E_0 and polarization $\hat{\epsilon}$, which can be expressed as [168]:

$$\mathbf{E} = \hat{\epsilon} \frac{E_0}{2} (e^{-i\omega t} + e^{i\omega t}) = \mathbf{E}_0^+ e^{-i\omega t} + \mathbf{E}_0^- e^{i\omega t}. \quad (2.16)$$

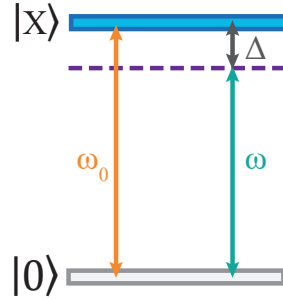


Figure 2.11 Two-level system formed from the $n = 1$ energy level of an exciton and its ground state (absence of an exciton). ω_0 is the resonance frequency of the system, ω , that of the driving electric field, and $\Delta = \omega - \omega_0$ is the detuning between the transition and the field.

The Hamiltonian includes terms for the energy of the exciton system and for the exciton-field interaction. In the dipole approximation,

$$H = \hbar\omega_0 |X\rangle \langle X| - \mathbf{d} \cdot \mathbf{E} = \hbar\omega_0 \sigma^\dagger \sigma - \langle 0 | \mathbf{d} | X \rangle \cdot \mathbf{E} (\sigma + \sigma^\dagger), \quad (2.17)$$

with $\sigma = |0\rangle \langle X|$, $\sigma^\dagger = |X\rangle \langle 0|$ and the dipole matrix elements being real. As the expectation value of σ varies as $e^{-i\omega_0 t}$, the rotating-wave approximation allows us to keep only the two

slow varying terms of Eq. 2.17, which evolve as $e^{\pm i(\omega - \omega_0)t} = e^{\pm i\Delta t}$, $\Delta = \omega - \omega_0$ being the detuning:

$$\begin{aligned} H &= \hbar\omega_0\sigma^\dagger\sigma - \langle 0 | \hat{\epsilon} \cdot \mathbf{d} | X \rangle \left(E_0^- \sigma e^{i\omega t} + E_0^+ \sigma^\dagger e^{-i\omega t} \right) \\ &= \hbar\omega_0\sigma^\dagger\sigma + \frac{\hbar\Omega}{2} \left(\sigma e^{i\omega t} + \sigma^\dagger e^{-i\omega t} \right), \end{aligned} \quad (2.18)$$

where $E_0^+ = E_0^- = \frac{E_0}{2}$ and $\Omega = -\frac{E_0}{\hbar} \langle 0 | \hat{\epsilon} \cdot \mathbf{d} | X \rangle$ is the Rabi frequency. The time evolution of the qubit state due to Eq. 2.18 can now be investigated using Schrödinger's equation. Let $|\Psi\rangle = c_X |X\rangle + c_0 |0\rangle$ be the general form of the state, with c_X and c_0 the probability amplitudes associated with the excited and ground states. Schrödinger's equation thus gives a system of two coupled differential equations for those coefficients:

$$\begin{aligned} \frac{\partial}{\partial t} c_0 &= -i\frac{\Omega}{2} c_X e^{i\omega t} \\ \frac{\partial}{\partial t} c_X &= -i\omega_0 c_X - i\frac{\Omega}{2} c_0 e^{-i\omega t}. \end{aligned} \quad (2.19)$$

To solve, we apply the rotating frame transformation, where we are interested in the slower time evolution of the state with respect to the angular frequency of the field, by defining $\tilde{c}_X = c_X e^{i\omega t}$. The differential equations now become:

$$\begin{aligned} \frac{\partial}{\partial t} c_0 &= -i\frac{\Omega}{2} \tilde{c}_X \\ \frac{\partial}{\partial t} \tilde{c}_X &= i\Delta \tilde{c}_X - i\frac{\Omega}{2} c_0 \end{aligned} \quad (2.20)$$

and the Hamiltonian is rewritten as:

$$H = -\hbar\Delta\sigma^\dagger\sigma + \frac{\hbar\Omega}{2} (\sigma + \sigma^\dagger), \quad (2.21)$$

where the driving field has also been transformed into the rotating frame. Eqs. 2.20 can be decoupled by differentiating with respect to t and replacing the appropriate expressions, giving [169]:

$$\begin{aligned} \left(\frac{\partial^2}{\partial t^2} - i\Delta \frac{\partial}{\partial t} + \frac{\Omega^2}{4} \right) c_0 &= 0 \\ \left(\frac{\partial^2}{\partial t^2} - i\Delta \frac{\partial}{\partial t} + \frac{\Omega^2}{4} \right) \tilde{c}_X &= 0. \end{aligned} \quad (2.22)$$

The solutions to these equations have the form, with initial conditions $c_0(0)$ and $\tilde{c}_X(0)$:

$$\begin{aligned} c_0(t) &= e^{i\frac{\Delta}{2}t} \left[c_0(0) \cos\left(\frac{\tilde{\Omega}}{2}t\right) - \frac{i}{\tilde{\Omega}} [\Delta c_0(0) + \Omega \tilde{c}_X(0)] \sin\left(\frac{\tilde{\Omega}}{2}t\right) \right] \\ \tilde{c}_X(t) &= e^{i\frac{\Delta}{2}t} \left[\tilde{c}_X(0) \cos\left(\frac{\tilde{\Omega}}{2}t\right) + \frac{i}{\tilde{\Omega}} [\Delta \tilde{c}_X(0) - \Omega c_0(0)] \sin\left(\frac{\tilde{\Omega}}{2}t\right) \right] \end{aligned} \quad (2.23)$$

where $\tilde{\Omega} = \sqrt{\Omega^2 + \Delta^2}$ is the generalized Rabi frequency. For a TLS originally in its ground state, $c_0(0) = 1$ and $\tilde{c}_X(0) = 0$, giving the following populations of the states:

$$\begin{aligned} |c_0(t)|^2 &= \cos^2\left(\frac{\tilde{\Omega}}{2}t\right) + \frac{\Delta^2}{\tilde{\Omega}^2} \sin^2\left(\frac{\tilde{\Omega}}{2}t\right) \\ |\tilde{c}_X(t)|^2 &= \frac{\Omega^2}{\tilde{\Omega}^2} \sin^2\left(\frac{\tilde{\Omega}}{2}t\right) \end{aligned} \quad (2.24)$$

Thus, when interacting with an AC electric field, the populations undergo an oscillation as a function of the angle $\Theta = \tilde{\Omega}t$. On perfect resonance, i.e. when $\Delta = 0$, both populations oscillate out-of-phase with respect to one another between 0 and 1, giving rise to the so-called Rabi oscillations (Fig. 2.12). $\Delta \neq 0$ reduces the contrast of the oscillations and increases the frequency $\tilde{\Omega}$. The Rabi-oscillation phenomenon consists in an optical control tool of a qubit, which allows to rotate the state along a single axis.

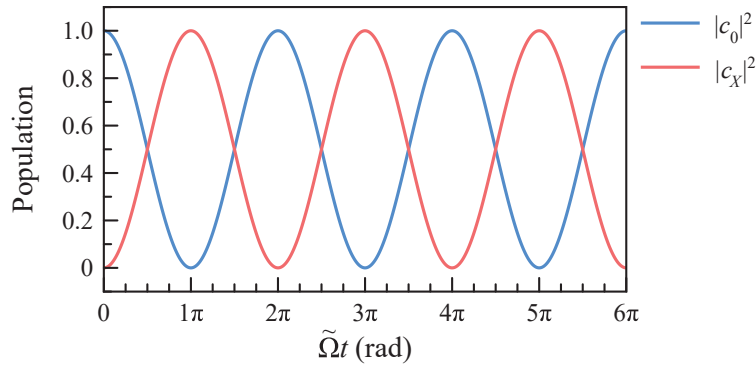


Figure 2.12 Rabi oscillations of the ground and excited state populations of a TLS in perfect resonance ($\Delta = 0$). The populations oscillate out of phase with full contrast from 0 to 1.

Rabi oscillations with a time-dependent excitation

Although Eqs. 2.24 were derived for a constant field amplitude E_0 , the result is considered valid for a resonant time-dependent field ($\Delta = 0$) if its envelope varies on scale much slower than optical frequencies (of the order of a few hundreds of THz) [169]. One can in this case calculate the rotation angle Θ by integrating the Rabi frequency over time:

$$\Theta = \int_{-\infty}^{\infty} \Omega(t) dt \quad (2.25)$$

and use it directly in Eqs. 2.24. For a Gaussian pulse of temporal full width at half maximum (FWHM) τ_p and amplitude E_0 , one obtains:

$$\Theta = \frac{E_0 d \tau_p}{2\hbar} \sqrt{\frac{\pi}{\ln 2}}, \quad (2.26)$$

with d the magnitude of the dipole matrix element. Since $E_0 = \sqrt{2ZP/S}$, with P the electric field power, S the beam area and $Z = \sqrt{\mu/\epsilon}$ the impedance of the host material (ϵ and μ are respectively its permittivity and permeability), Eq. 2.26 rewrites [170]:

$$\Theta = \frac{d \tau_p}{2\hbar} \sqrt{\frac{2\pi Z P}{S \ln 2}} \quad (2.27)$$

For a train of Gaussian pulses with a repetition rate of $1/\tau_R$, P can be expressed as a function of the measurable quantity P_{RMS} , the root-mean-square power, yielding:

$$\Theta = \frac{d}{\hbar} \sqrt{\frac{Z \tau_R \tau_p P_{\text{RMS}}}{S} \left(\frac{2\pi}{\ln 2} \right)^{1/2}}. \quad (2.28)$$

Experimentally, changing the P_{RMS} of a pulsed laser, measuring the PL emitted by the TLS, which is proportional to $|c_X|^2$, and plotting the obtained intensity as a function of $P_{\text{RMS}}^{1/2}$ lead to a Rabi oscillation curve in the form of Fig. 2.12.

2.4.2 Optical Bloch equations

Another representation of the evolution in the rotating frame of the TLS state $|\tilde{\Psi}\rangle$ in the presence of a driving electric field is through its density operator $\tilde{\rho} = |\tilde{\Psi}\rangle\langle\tilde{\Psi}|$:

$$\tilde{\rho} = \begin{bmatrix} \tilde{\rho}_{XX} & \tilde{\rho}_{X0} \\ \tilde{\rho}_{0X} & \tilde{\rho}_{00} \end{bmatrix}. \quad (2.29)$$

Here, for a pure state, $\tilde{\rho}_{XX} = \tilde{c}_X \tilde{c}_X^* = c_X c_X^* = \rho_{XX}$ and $\tilde{\rho}_{00} = c_0 c_0^* = \rho_{00}$ are respectively the populations of the excited and ground states, while $\tilde{\rho}_{X0} = \tilde{c}_X c_0^* = c_X c_0^* e^{i\omega t} = \rho_{X0} e^{i\omega t}$ and $\tilde{\rho}_{0X} = \tilde{c}_X^* c_0 = c_X^* c_0 e^{-i\omega t} = \rho_{0X} e^{-i\omega t}$ are the coherence terms. ρ_{ij} with $i, j = \{0, X\}$ are the density matrix elements in the laboratory (fixed) frame.

Using the results of Eq. 2.20, one can define motion equations for the density operator elements. The advantage of doing so resides in the fact that they allow to easily keep track of the evolution of $\tilde{\rho}_{X0}$ and $\tilde{\rho}_{0X}$, which is less explicit in the treatment with probability amplitudes of Sect. 2.4.1. One obtains:

$$\begin{aligned}
\frac{\partial}{\partial t} \rho_{XX} &= i \frac{\Omega}{2} (\tilde{\rho}_{X0} - \tilde{\rho}_{0X}) \\
\frac{\partial}{\partial t} \rho_{00} &= -i \frac{\Omega}{2} (\tilde{\rho}_{X0} - \tilde{\rho}_{0X}) \\
\frac{\partial}{\partial t} \tilde{\rho}_{X0} &= i \Delta \tilde{\rho}_{X0} + i \frac{\Omega}{2} (\rho_{XX} - \rho_{00}) \\
\frac{\partial}{\partial t} \tilde{\rho}_{0X} &= -i \Delta \tilde{\rho}_{0X} - i \frac{\Omega}{2} (\rho_{XX} - \rho_{00}).
\end{aligned} \tag{2.30}$$

To account for the relaxation of populations and decay of coherence, one must add extra damping terms to the previous equations. First, due to spontaneous emission, ρ_{XX} decreases proportionally to its own magnitude at a rate $\Gamma = 1/T_1$, with T_1 the lifetime of the transition or longitudinal relaxation time, while ρ_{00} increases simultaneously by the same amount. Second, the coherence terms relax at a rate $\gamma_{\perp} = 1/T_2$, with T_2 the coherence or transverse relaxation time. One therefore can write the optical Bloch equations describing the time evolution of the density matrix elements [170]:

$$\begin{aligned}
\frac{\partial}{\partial t} \rho_{XX} &= i \frac{\Omega}{2} (\tilde{\rho}_{X0} - \tilde{\rho}_{0X}) - \Gamma \rho_{XX} \\
\frac{\partial}{\partial t} \rho_{00} &= -i \frac{\Omega}{2} (\tilde{\rho}_{X0} - \tilde{\rho}_{0X}) + \Gamma \rho_{XX} \\
\frac{\partial}{\partial t} \tilde{\rho}_{X0} &= -(\gamma_{\perp} - i \Delta) \tilde{\rho}_{X0} + i \frac{\Omega}{2} (\rho_{XX} - \rho_{00}) \\
\frac{\partial}{\partial t} \tilde{\rho}_{0X} &= -(\gamma_{\perp} + i \Delta) \tilde{\rho}_{0X} - i \frac{\Omega}{2} (\rho_{XX} - \rho_{00}).
\end{aligned} \tag{2.31}$$

Solving these equations numerically allows evaluating the populations and coherences as a function of time in more complex cases than Sect. 2.4.1, such as detuned pulsed excitations of various lengths in the presence of damping.

2.4.3 Dressed states and Mollow triplet

The Hamiltonian of Eq. 2.21 is not expressed in a basis leading to stationary solutions in the rotating frame for a CW interaction of the TLS with the optical field, as it is not diagonal. States expressed in this basis indeed evolve according to the optical Bloch equations described above and undergo Rabi oscillations. The diagonalization of Hamiltonian 2.21 leads to new dressed eigenvectors [171]:

$$\begin{aligned} |+\rangle &= \sin \theta |0\rangle + \cos \theta |X\rangle \\ |-\rangle &= \cos \theta |0\rangle - \sin \theta |X\rangle, \end{aligned} \quad (2.32)$$

where $\tan 2\theta = -\Omega/\Delta$ with $0 \leq \theta < \pi/2$, describing the new states of the system in the presence of the optical field. The latter mixes the TLS ground and excited states according to its intensity and its detuning with the transition. The associated energies E_+ and E_- depend on the same parameters and are expressed as:

$$E_{\pm} = -\frac{\hbar\Delta}{2} \pm \frac{\hbar\tilde{\Omega}}{2}, \quad (2.33)$$

which are separated by $\hbar\tilde{\Omega}$. This field-induced energy shift is often referred to as the AC Stark shift.

To describe the TLS-field system entirely, one must then couple the dressed TLS basis of Eq. 2.32 to the photonic Fock states $|n\rangle$, with n the photon number. The total energy of the levels becomes $E_{\pm} + n\hbar\omega$.

The detected emission from the TLS is then formed of three lines involving four transitions between the $|\pm, n+1\rangle$ and $|\pm, n\rangle$ states for large n , illustrated in Fig. 2.13. The central recombination has the same energy as the exciting field, while the two “sidebands” are $\hbar\tilde{\Omega}$ above and below the main line. This feature is the so-called Mollow triplet, a signature of CW resonant and quasi-resonant excitation of a TLS.

The application of an optical field on a TLS therefore leads to the formation of dressed states and to new eigenenergies. This formalism is exploited in the discussion of Chap. 5, where the AC Stark shift is explored as the cause of the oscillation of the bound exciton emission energy during PLE.

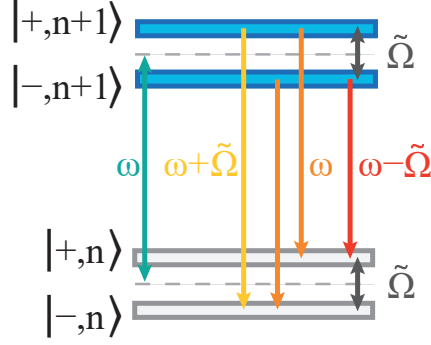


Figure 2.13 Dressed states and transitions involved in the formation of the Mollow triplet upon the resonant or quasi-resonant excitation of a TLS. Two of them have the same energy as the excitation photons, while the remaining two are separated from the resonant emission by $\pm\hbar\tilde{\Omega}$.

2.5 Impact of the environment on the resonant excitation of solid-state qubit systems

Solid-state qubit systems are coupled to their environment, which can disrupt their quantum properties. In a resonant excitation experiment on a TLS, the intense excitation laser may interact with the host material if the latter is not free from any form of imperfections. For example, the laser can photocreate carriers that can in turn be randomly trapped at neighboring defects, at interfaces or in the substrate of the semiconductor heterostructure containing the qubits. This dynamic electrostatic background leads to spectral diffusion and broadening of the bound-exciton lines through Coulomb interactions [77, 172–175] and can even completely suppress resonant emission [78, 176].

The number of these charges, which can be of either sign, and their position with respect to the emitter fluctuate in time and influence the resulting electric field experienced by the TLS. The energy of its transition is dynamically shifted through a DC Stark effect, hence the integration of the PL signal over long periods of time (at least of the order of 1 s) or its averaging over numerous laser pulses ($\sim 10^8$ pulses per second) samples multiple charge configurations, leading to a broadening of the detected emission structure. The exact knowledge of the complex microscopic charge configuration is nevertheless unnecessary to adequately describe its effects, as one can instead rely on a simple, yet powerful random telegraph noise model.

In this description, a TLS (here, a bound exciton) interacts with a reservoir of $n + 1$ inde-

pendent two-level traps [172,173,175]. The complete TLS-environment system is represented in Fig. 2.14 as a ladder of equally-spaced levels, where $i = 0$ corresponds to a fully discharged environment (i.e. the unperturbed TLS) and $i = n$ to a fully charged one. This bounded energy distribution is chosen as it satisfactorily models experimental observations while maximizing entropy. It therefore allows extracting a maximum of information from the system without making specific assumptions. The energy of the micro-states decreases with n due to the sign of the DC Stark effect responsible for the shift. Each of the defects charges and discharges at rates γ_c and γ_d , transitioning to an adjacent state on the scale and inducing a spectral jump $\mp\delta E$ on the bound exciton. Intrinsic charging rates have been reported to be in the 10^3 – 10^5 Hz range [77] and even as high as 10^{11} Hz [172] for III-V QDs and the shifts, from a few to tens of μeV [173,174]. In ZnSe:Te_2 , δE was estimated at $15 \mu\text{eV}$ [175].

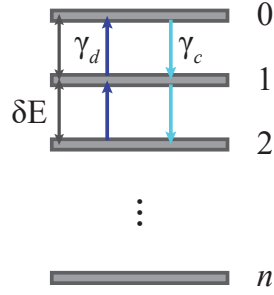


Figure 2.14 Random telegraph noise model of the interaction of a bound exciton with its environment, described as a ladder of equally-spaced energy levels which correspond to the charge states of $n + 1$ defects in the vicinity of the emitter. Each trap charges and discharges at rates γ_c and γ_d . Only transitions between adjacent levels are allowed.

Here, the emission broadening depends on the values of γ_c and γ_d with respect to the radiative lifetime (T_1) or the measurement time (depending on which is most relevant) [77,177]. Indeed, if the charge fluctuations are very fast and happen on a time scale much shorter than T_1 , they average out and no broadening occurs. Conversely, if they are slower than the acquisition time (t_{acq}), the environment looks frozen to the emitter [174] and, here again, no broadening is observed. Between these two extremes are situated the fluctuations with the most impact on the emission spectrum, namely those occurring on time scales greater than T_1 , but shorter than t_{acq} .

By acting on γ_c and γ_d to force the system in a maximally discharged or charged configuration, or by strongly increasing the rates at which fluctuations occur, one obtains an improvement of the FWHM, approaching that dictated by T_1 , a process called motional narrowing [172,175].

This stabilizes and restores the quantum properties of single emitters and is therefore crucial for the correct operation of a solid-state qubit. Two main avenues for achieving this effect are pursued in the literature and are detailed in the sections below.

2.5.1 Optical gating with a weak non resonant laser

The first strategy used to stabilize the environmental charge fluctuations around the qubit is the use of a weak NR optical drive that photocreates carriers leading to the neutralization of trapped charges or to the screening of their electric field, a process sometimes referred to as “optical gating” [177]. The name refers to the fact that, for QD systems, the NR laser forces the recombination of single charges populating the dot, removing the Coulomb blockade sometimes preventing the resonant excitation of an exciton [176].

This technique achieves motional narrowing by balancing the actions of the resonant and NR lasers, which act respectively upon γ_c and γ_d . Indeed, the first generates charges in the lower-gap substrate, at the interfaces and on defects inside the host matrix, while the second favors the recombination of these trapped charges with the creation of free carriers. A judicious balance of these two contributions has led to the reduction of the resonant emission FWHM from 65 to 18 μeV in ZnSe:Te_2 , by forcing the environment into a ultrafast fluctuating, fully discharged configuration [175]. Another report of the effect using an exclusively NR excitation stated that the emission FWHM of indium arsenide (InAs)/GaAs QDs increased from 21 to 155 μeV with excitation power [172].

Drawbacks of optical gating are that it is not very practical due to the need of a second laser and that its effects are quite sample-dependent. Additionally, its parameters must be chosen carefully as it can otherwise have deleterious effects such as the quenching of resonant emission [177] or the accentuation of the charge fluctuations around the emitter [172, 175]. Nevertheless, optical gating has proven efficient to control spectral diffusion in single emitters and is employed in Chap. 6 to tailor the resonant emission response of a Te_2 -bound exciton in the pulsed excitation regime.

2.5.2 Voltage-controlled devices

The second avenue for achieving motional narrowing consists in embedding the qubit in a gated voltage-controlled device tuning the charge state of the qubit as well as of nearby defects [78,177]. This solution has two major advantages over optical gating: it allows for a closer, more systematic control of the environment and qubit charge states, therefore preventing PL quenches due to Coulomb blockade and spectral diffusion [78], and it is compatible with the design of quantum devices, which are often fabricated in Schottky diode structures [177].

The reduction of spectral diffusion takes place from a fast phonon-assisted tunneling of the charges out of their trapping defects. In other words, the applied electric field increases γ_d with respect to γ_c , bringing the system in a discharged configuration [173]. For example, in indium-gallium arsenide (InGaAs) QDs, a linewidth reduction of $\sim 9 \mu\text{eV}$ was achieved for gate voltages ranging from -0.18 to -0.28 V at 30 K [173].

These promising results in a system of very similar physics to ours encouraged us to attempt a similar stabilization method on single bound excitons in Chap. 6.

2.6 Summary of the literature review

We have seen in this chapter general properties of the ZnSe host and of ICs in zincblende semiconductors. Then, the Te_2 molecule in ZnSe was described in detail as a C_{2v} -symmetry defect that binds excitons, trions and biexcitons, with a hole as the primary charge, and its major emission properties were reviewed. Next, an overview of the exciton-polariton formalism was given, as its description of the excitation of a material near a resonance in its dielectric function is extensively used in Chap. 5. The basic physics of coherent control of an excitonic qubit was also established, as well as the motional narrowing model of the impact of the electrical environment on the energy and linewidth of an emission line.

Using these concepts, this thesis first aims at clarifying the mechanisms at play as $\text{ZnSe}:\text{Te}_2$ is subjected to a below-gap, non resonant excitation. Specifically, the possible involvement of exciton-polaritons, phonons, magnetic fields and splitting mechanisms in the emission-energy modulation of a Te_2 -bound exciton as the excitation energy is tuned in the vicinity of the ZnSe free exciton (FX) is evaluated. Second, the first clear demonstration of coherent control

of an excitonic qubit in this system is achieved and the impact of the electrical environment on the coherent response obtained upon resonant excitation is assessed.

CHAPTER 3 EXPERIMENTAL METHODS

The observation of the ultrafast initialization of a hole spin in ZnSe:Te₂ by St-Jean *et al.* [28] involving a circularly-polarized pulse resonant with the so-called donor-bound excitons posed this system as an interesting OAQ candidate. Consequently, the present work has been designed to study its emission properties under continuous-wave (CW) non resonant (NR) and pulsed resonant excitation. For this purpose, two experiments were designed: photoluminescence-excitation (PLE) and resonant excitation, where all results were obtained on single Te₂ emitters.

On the one hand, PLE involved probing the absorption of higher energy levels and their transfer efficiency to a single Te₂ molecule. It aimed at investigating the exciton transfer mechanisms responsible for the initialization process and deepening our understanding of the interplay between the different host energy levels leading to the binding of an exciton on a Te₂ molecule. We wished at the same time to identify energy levels potentially available for quantum control schemes, such as excited states of the bound exciton.

On the other hand, resonant excitation was performed with the objective of demonstrating coherent control of an excitonic qubit and of evaluating some of its relevant performance parameters. As demonstrated in Chap. 6, it proved difficult to observe coherence due to the influence of the environment. Nonetheless, Rabi oscillations were observed, which rotated the qubit state over a single axis on the Bloch sphere.

The present chapter details all the relevant methods to the conduct of these two experiments: the structure of the studied samples, the measurement principles behind both experiments, the peculiarities of their respective setup, the performance of the laser rejection methods employed to discriminate the signal from the excitation, as well as the fit models used to analyse the data.

3.1 ZnSe:Te₂ samples investigated

Sample A was a 80-nm thick ZnSe layer grown on (001) GaAs with a single δ -doped Te layer at its center. The Te concentration of 2500 μm^{-2} was such that the maximal surface

concentration of molecules was estimated at $1 \mu\text{m}^{-2}$, which is sufficiently low to allow for the observation of single defects in our diffraction-limited microscope. It was investigated during the PLE experiment.

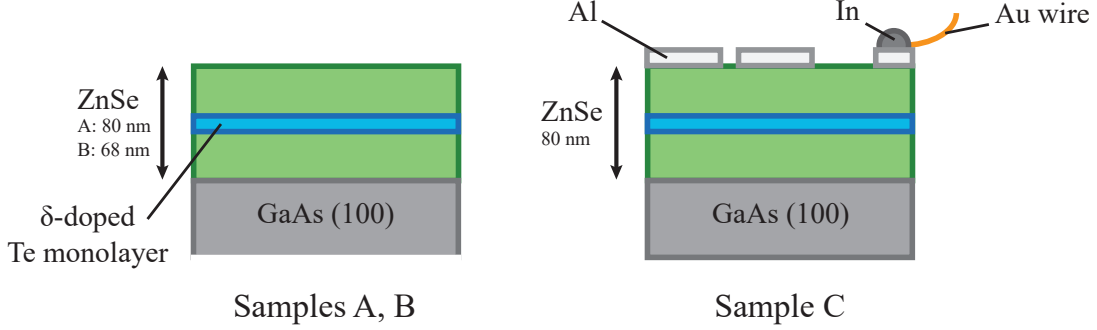


Figure 3.1 ZnSe:Te₂ samples investigated, formed of a 80 (A, C) or 68-nm ZnSe layer on top of a (100) GaAs substrate. A fractional Te monolayer is grown in the middle, a process called δ -doping. Sample C has an Al layer deposited on top, which allowed to make an electrical contact through an In-bonded Au wire. Sample A was investigated in PLE, while B and C were part of the resonant excitation experiment.

Samples B and C were part of the resonant excitation experiment. B was a 68-nm thick ZnSe layer grown on a 150-nm (100) GaAs buffer layer, with a single, fractional Te-doped ZnSe monolayer at the center (Se/Te ratio of 10^3).

Sample C was a 80-nm thick ZnSe with a single δ -doped Te monolayer on (100) GaAs similar to Sample A, on top of which an aluminum (Al) layer was deposited. An electrical contact was made with the latter layer by soldering a 50 μm -diameter gold wire with an indium (In) droplet. The gate could be used to generate an electric field acting on the emitter and its environment, to induce a DC Stark shift of its emission lines or to deplete residual charges in its vicinity. Delamination spots in the Al layer allowed for the observation of Te₂ molecules.

For thicknesses as those of our samples, the ZnSe layer is under biaxial compressive strain that pushes the LH energy levels 12.0–13.0 meV [24, 84, 103, 112] above (in hole energy) the HH. Due to the fast hole relaxation, all dominant transitions observed had HH character.

3.2 Measurement principles

I now review briefly the physics behind the two experiments and the information one expects to gain from them.

3.2.1 Photoluminescence-excitation of a Te_2 -bound exciton across the free exciton band

Photoluminescence-excitation (PLE) consists in varying the energy of a light source exciting a material (such as a tunable laser) while detecting the emission intensity (I_{em}) of a particular transition within that material. The collected intensity at each excitation energy (E_{ex}) is then a product of the absorption efficiency, the probability for the excited carriers to relax in the emitting state and the probability for that state to recombine radiatively, as illustrated in Fig. 3.2 for our case of interest. No emission is observed if E_{ex} does not correspond to any optically active state in the material. Conversely, if a state exists and if it transfers efficiently to the emitting state, an increase in I_{em} is observed. PLE is therefore a powerful tool to probe the presence of states that cannot be observed in PL due to their short lifetime, but nonetheless generate some absorption.

In high-quality semiconductor quantum well (QW) samples with very long non-radiative lifetimes and at low temperature, the probability for carrier relaxation into the emitting state is mostly independent of the carrier initial energy, and the PLE spectrum is very similar to that of absorption [178]. If these conditions are not met, the absorption is modulated by the relaxation and capture efficiencies, which produces a distinct spectrum.

In this work, the detected signal consisted in PL originating from the recombination of a Te_2 -bound exciton, and the targeted higher-energy states were the FX, impurity states in ZnSe and excited states of the bound exciton, in the 2.795–2.815 eV range.

3.2.2 Resonant excitation in the pulsed regime

Resonant excitation in the pulsed regime was performed on a Te_2 -bound exciton with the hopes of observing a coherent Rabi oscillation of its population, as detailed in Sect. 2.4.1. It involved varying the excitation power (P_{ex}) of a pulsed laser tuned in resonance with the transition, which rotated the exciton state of an angle $\Theta \propto P_{\text{ex}}^{1/2}$ on the Bloch sphere. The

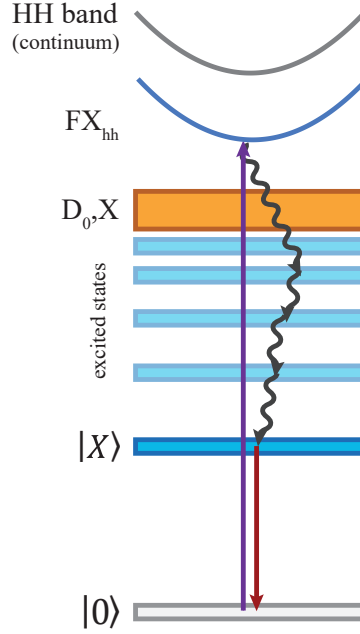


Figure 3.2 Principle of the PLE measurement. Excitation of the system to one of its energy levels, whether it be the HH conduction band, the HH FX, the D_0^+X or an excited state of the bound exciton, leads to the creation of charge carriers. After relaxation to the ZnSe:Te₂ level $|X\rangle$, if such a mechanism exists, radiative recombination occurs towards the vacuum state $|0\rangle$ and a photon is emitted. If E_{ex} does not correspond to a state, no absorption nor emission occurs.

detected emitted signal was proportional to the excited state population ρ_{XX} attained after the pulse. By plotting the emission intensity as a function of $P_{\text{ex}}^{1/2}$, a Rabi curve similar to Fig. 2.12 is expected.

Such an experiment is the first step in demonstrating optical coherent control of an excitonic qubit in ZnSe:Te₂ and a gateway to the control of a hole spin qubit. It allows extracting the dipole moment of the transition, an important metric to evaluate the performance of an OAQ and gives insight on some of the mechanisms at play during coherent control.

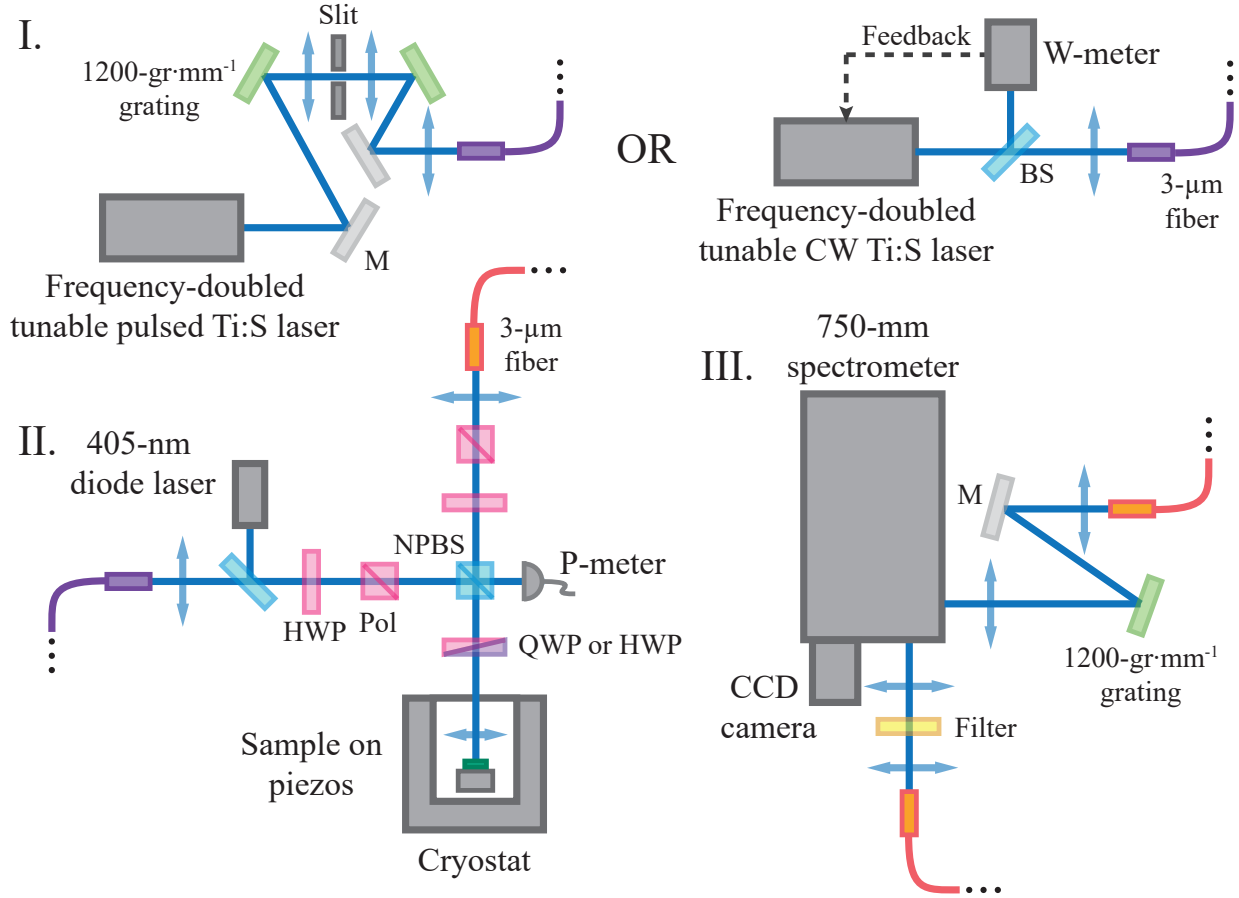


Figure 3.3 Simplified schematic of the PLE and resonant excitation setup. I. Excitation arm with a CW tunable, frequency-doubled Ti:S laser with or without active wavelength stabilization depending on the wavelength meter (W-meter) employed. The laser light is injected in a 3- μm single-mode fiber and directed towards the experiment arm. A pulsed frequency-doubled Ti:S laser can also be selected as the main excitation source. Its ~ 100 fs pulses are widened to ~ 1 ps by passing through a pulse shaper made of two gratings, two lenses and a slit. II. Experiment arm. The polarization and power of the excitation beam are controlled using a series of waveplates (WP) and polarizers (Pol). The excitation beam is focused on the sample kept at low temperature (7–11 K) and the resulting retro-emitted signal is collected in another single-mode fiber. A 405-nm laser diode is available for NR excitation. III. Detection arm with a 750-mm spectrometer and a CCD camera. A 1200 grooves·mm⁻¹ grating (PLE) or a sharp-edged long-pass filter (resonant excitation) is used for laser rejection. BS: beamsplitter, HWP: half-wave plate, M: mirror, NPBS: non-polarizing beamsplitter, P-meter: power-meter, QWP: quarter-wave plate, \updownarrow : lens.

3.3 Experimental setup

Both experiments were carried out in similar setups involving a homemade cryogenic confocal microscope (Fig. 3.3). Laser excitation was routed to the experiment arm through a single-mode optical fiber with a 3- μm core to a series of polarizers and waveplates that allowed for controlling the excitation and detection polarization, as well as rejecting the laser. Then, it was focused on the sample, which was kept at cryogenic temperatures in a closed-cycle helium-free cryostat equipped with piezoelectric positioners. The signal from the sample was collected through a second single-mode fiber to ensure confocal mode and sent to a 750-mm spectrometer (*Andor Shamrock 750*) equipped with a charge coupled device (CCD) camera.

The setups however differed in the type of laser excitation (CW or pulsed), the polarization-controlling optics (linear or circular), the focalizing lens at the sample, the detector and the laser rejection strategy (polarizers, grating or filter). These specifications are detailed for both cases below.

3.3.1 PLE configuration

In this experiment, E_{ex} was varied across the ZnSe FX transition, on a 2.795–2.815 eV range. Since the resolution of the PLE technique depends on the excitation linewidth and energy step that can be achieved, a CW, frequency-doubled and tunable titanium:sapphire (Ti:S) laser (*MSquared SolsTiS*) displaying an emission FWHM of less than 50 kHz served as the excitation (Fig. 3.3 I, right). Although the laser is fully automated, the frequency doubler is not and its alignment needed constant readjustment in order to keep the phase matching condition. E_{ex} was monitored at the source through a wavelength meter based on a scanning Michelson interferometer (*Burleigh WA-20*) or a Fizeau interferometer (*HighFinesse WS6-600*). The latter was used as feedback to stabilize the Ti:S cavity and ensured an accuracy of the laser wavelength below 600 MHz. The uncertainty on E_{ex} in our working range was 6 μeV with the *WA-20* and 0.6 μeV with the *WS6-600*.

NR spectra were obtained with an above-gap excitation from a 405-nm laser diode (*OZ-Optics OZ-2000-405*) or the *SolsTiS* tuned at 432 nm. Fig. 3.3 depicts the three different arms of the setup, excitation, experiment and detection.

The sample was kept at 7–11 K in a custom-made cryostat (*Cryomech PT410RM* cryogenic

refrigerator coupled to a *Janis Research PTCM-950* cryostat) in which an aspheric lens with a 4-mm focal length and a 0.60 numerical aperture (NA) focalized the excitation and collected the PL. The quarter-wave plate (QWP) placed in front of the cryostat allowed switching from linear to circular polarization. It was mounted on a motorized rotation actuator that automated polarization-resolved measurements. A thermoelectrically cooled CCD camera (*Andor Newton*) detected the signal dispersed in the spectrometer. A 405-nm blazed 1200-grooves·mm⁻¹ grating was placed in front of the slits in quasi-Littrow configuration for additional laser rejection (more on that in Sect. 3.3.4).

The global setup offered a spectral resolution of $\sim 70 \mu\text{eV}$ and a spatial resolution of $\sim 0.45 \mu\text{m}^2$. This performance easily allowed for resolving single Te₂ molecules. The experiment was carried out in the high excitation regime, with fluences of 284–567 $\mu\text{W} \mu\text{m}^{-2}$.

Performance of the PLE setup

At the beginning of the PLE experiment, the setup was not optimized for operation in the blue visible range. I had to make numerous modifications to ensure good performance and relative stability of the alignment on a single emitter. The best that could be achieved at that time was to keep the same Te₂ molecule over a two-day period, which limited the extent of the measurements that could be performed on a particular emitter. The spatial stability and signal-to-noise ratio (SNR) were significantly improved between this experiment and the resonant excitation study (Sect. 3.3.2), specifically with the arrival of a new back-illuminated CCD camera with larger efficiency in our working wavelength range, more stable fiber mounts and sharp interference filters to remove laser light.

3.3.2 Resonant excitation configuration

Rabi rotation attempts used resonant laser pulses of $\sim 1\text{-ps}$ width and various powers obtained from a frequency-doubled Ti:S laser (*Spectra Physics Tsunami*) running through a 4-*f* pulse shaper (Fig. 3.3 I, left). A weak NR laser diode (405 nm) was used to restore the quantum properties of the emitter by flushing the charges in its environment, according to motional narrowing principles presented in Sect. 2.5. The sample was kept at 7 K in the *Cryomech* cryostat, and later in a *Montana Instruments X-Plane* cryostat equipped with a 100x microscope objective (*Zeiss EC Epiplan* 100x, NA = 0.85, 0.87-mm working distance). The signal was acquired on a back-illuminated liquid nitrogen (LN₂) cooled CCD camera

(*Princeton Instruments PyLon ExceLon*), which ensured a spectral resolution of $\sim 90 \mu\text{eV}$. Reflected laser light was rejected by a sharp-edged, tunable long-pass filter (*Semrock TP01-448*) placed in front of the spectrometer slits.

Voltage was applied to Sample C with a *Keithley 2400* source-measure unit. Current could be monitored through the same apparatus, leading to the $I - V$ curve of the sample (not shown in the thesis).

Uncertainty on P_{ex}

The resonant excitation power (P_{ex}) had an instrumental uncertainty of $0.001 \mu\text{W}$ for displayed values of $0.050\text{--}1.600 \mu\text{W}$, $0.01 \mu\text{W}$ for $1.60\text{--}16.00 \mu\text{W}$, $0.1 \mu\text{W}$ for $16.0\text{--}160.0 \mu\text{W}$, 0.001mW for $0.160\text{--}1.600 \text{mW}$, 0.01mW for $1.60\text{--}16.00 \text{mW}$ and 0.1mW for $16.0\text{--}50.0 \text{mW}$. However, as P_{ex} increased, its value measured on the power-meter (which has a considerably slower response than the Rabi oscillations we were interested in, with a bandwidth up to 100kHz) increasingly fluctuated on a s timescale, probably due to a more efficient frequency generation in the excitation optical fiber. Although the amplitude of this instability could reach $10\text{--}20 \%$ in the worst case at the largest available powers ($1.000\text{--}1.600 \text{mW}$), its impact on the experiment was considered minimal due to the great timescale difference. In any case, a 20% P_{ex} fluctuation was nowhere near enough to account for the Rabi-frequency damping reported in Chap. 6.

3.3.3 Calibration of the detection system

Calibration of the detection system (spectrometer and CCD camera) was performed using a krypton spectral lamp, displaying very narrow emission lines. A spectrum was taken at the desired spectrometer grating position, and the tabulated values for the emission wavelengths of the observed lines served as input to convert the pixels of the camera to wavelengths with a linear regression. The statistical variation of the calibration was 0.12% on the slope and 0.05% on the intercept, including events where the spectrometer grating had been moved prior to calibration. These values lead respectively to a maximum uncertainty of the order of 0.14 and 1.2meV on each pixel. The energy axis of the spectra, referred to as the detection energy (E_{det}) in subsequent figures, was thus reliable enough for our needs, as we were interested in relative energies of peaks with one another and not their absolute position. Uncertainty on the position of an emission line was further reduced through fitting to less

than $10\text{ }\mu\text{eV}$ (see Sect. 3.4).

3.3.4 Rejection of the excitation laser

Experiments close to or in resonance require extra care in rejecting the excitation laser, as it would otherwise completely overwhelm the signal. In order to prevent this, we resorted to a combination of four strategies to filter the unwanted laser light, which based themselves on spectral, spatial and polarization filtering.

Spectral rejection

The first strategy was to spectrally separate the excitation from the emitter signal, so that the laser photons would not hit the CCD matrix in the spectral window of interest and cause it to saturate. This was rather easy to achieve in the PLE experiment, as FX and Te_2 molecules are naturally 35.7 meV apart on average. However, in resonant excitation, a witness state had to be employed: the longitudinal optical (LO) phonon replica of orthogonal polarization, 31.7 meV below the main excitonic transition [179]. Still, the rejection was not strong enough to prevent stray light from the laser to pollute the data, and other strategies had to be implemented. Fig. 3.4 summarizes the relevant levels and transitions for NR excitation and the PLE experiment in (a), as well as for resonant excitation in (b).

The second strategy, which was only available to us for the resonant excitation experiment, involved the use of a very sharp long-pass filter in front of the spectrometer slits, which blocked wavelengths shorter than the cutoff wavelength and let through longer ones. We used a tunable filter (*Semrock* TLP01-448) so that its cutoff could be precisely adjusted slightly above the studied excitonic transition. It ensured a theoretical rejection of $\sim 10^7$, with a 6.4 meV -wide transition at 2.7454 eV (0° incidence) and a 20.2 meV -wide transition at 3.1208 eV (60° incidence).

Polarization rejection

Polarization rejection consisted in exciting in a determined polarization and detecting the orthogonal one. To ensure this, we used a combination of optics in the experiment arm of the setup, as illustrated in Fig. 3.3 II. First, the beam went through a horizontal polarizer

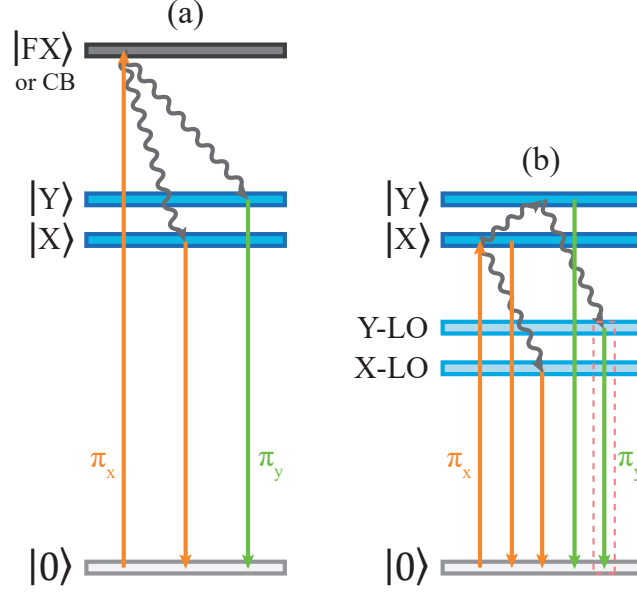


Figure 3.4 Energy levels, transitions and polarizations relevant the two experiments, allowing for spectral and polarization filtering. Excitation of the bandgap or the FX (a) leads to the population of both X and Y regardless of the polarization. Resonant excitation of the X level (b) transfers population to Y , X -LO and Y -LO through non-radiative transfer mechanisms. The detected transition, Y -LO for the case illustrated, is indicated with a pink dashed box.

defining the excitation polarization as $\pi_{x'}$, where x' refers to the axis that is both parallel to the surface of the optical table and perpendicular to the optical axis in lab coordinates. Next, the polarization was modified by a waveplate (half or quarter, depending on the experiment) placed in front of the cryostat window. After travelling to the sample, the laser was back-reflected, which left linear polarization unchanged, but reversed the helicity of circular polarization. The emitted PL followed the same path and was polarized as dictated by its selection rule. Both of the beams went through the waveplate, which brought the laser back to its original $\pi_{x'}$ polarization in the linear case, or to a vertical polarization $\pi_{y'}$ in the circular case. A sequence of a half-wave plate (HWP) and a vertical polarizer then allowed to reject the laser by selecting the $\pi_{y'}$ (linear case) or $\pi_{x'}$ (circular case) component.

The achieved extinction ratio of the technique was up to four orders of magnitude ($\sim 10^{-4}$). Optimum performance could be attained by walking the polarizers (i.e. turning one slightly and compensating with the other) so that their axes were aligned with those of the setup exhibiting minimal birefringence. An extra QWP was in some cases added between the cryostat and the motorized HWP or QWP to correct for any residual birefringence.

PL could be detected regardless of the choice of detection polarization, as long as the studied single Te_2 molecule was populated (Fig. 3.4). For a NR excitation in the FX band or above the gap, the polarization of the excitation was not conserved by the relaxation mechanisms populating the defect, which lead to PL emitted from both X and Y . In resonance, the polarization of the excitation had to respect the selection rule, but emission could occur from an orthogonal state through a non-radiative transfer mechanism. The witness state chosen thus was the LO phonon replica of the Y transition for an excitation of X and vice versa.

“Spatial” rejection

This last rejection technique was used in the PLE experiment and involved placing a grating in front of the spectrometer slits so that it dispersed the signal coming out of the fiber. By adjusting precisely its angle with respect to the beam path, one could select a wavelength window entering the slits that excluded the laser, but included the emission energy of the monitored exciton.

3.3.5 Challenges with the setup

We were met with several challenges while building and operating the setups for the two experiments. I review briefly the most important ones below.

Highly coherent CW laser

The *SolsTiS* laser, with its ultranarrow linewidth and very long coherence length (> 1 km), proved to be quite challenging and time-consuming. First, as mentioned above, its frequency doubler frequently had to be manually realigned as E_{ex} was tuned during PLE. The phase-matching condition needed precise alignment, which was often very hard to achieve and therefore caused issues with available power, especially because the cavity tended to walk out of alignment as the experiment was repeated.

Second, the non-linear crystal had to be kept in a state of extreme cleanliness to achieve optimal working conditions. Although the cavity is designed to be sealed and flushed with a clean inert gas to prevent adsorption of water on the crystal surface, it could not be operated

as so because of the frequent frequency changes and their required realignments. The output power consequently periodically degraded quite fast after each cleaning process.

Third, the high coherence forced the review of the type of optical fibers employed on the setup. Prior to the use of the *SolsTiS*, we used to work with polarization-maintaining (PM) fibers without much issues. However, injecting such a monochromatic and coherent laser in a fiber with even the slightest angle with respect to the PM axis lead to a beating of the two guided orthogonal polarization modes. This translated into an important power fluctuation after the first polarizer on the experiment arm, rendering the PLE experiment impossible to carry out. The use of single-mode, non-PM fibers removed the beating.

Ultrafast pulsed laser

We did not know the exact temporal width τ_p of our laser pulse. Its spectrum could in fact not be used as an indicator since it was greatly broadened by non-linear processes in the excitation optical fiber (purple fiber between I and II in Fig. 3.3). We however estimated τ_p to be ~ 1 ps from similarities with previous experiments [28]. The important spectral broadening complicated the laser rejection and caused an important background to appear in higher- P_{ex} spectra. This could be worked around in future works by using a free-space excitation passing through a pinhole to ensure confocal operation instead of fibers.

Also, such a broad-band pulse had a very different focus than the weak NR laser used to stabilize the environment, making the overlap of both excitation spots and the optimization of the PL signal quite challenging. More precise controls could be installed on the NR laser arm to allow for a finer alignment.

Choosing the right emitter

The choice of emitters to study in resonant excitation was much more critical than for PLE and several criteria had to be met in order to maximize the chances of Rabi rotation to succeed. As this required the most coherent emitter possible, a narrow linewidth and a long-term stability of the E_{em} were sought after, ensuring that the surroundings were as quiet as possible in terms of electrical noise. A proper Te_2 -molecule candidate was thus selected from its NR PL spectrum. It had to emit a respectable quantity of light, for the sake of the length

of the measurement, and be isolated from other emitters to avoid their contribution to the signal. Also, it had to present a visible, if not strong, phonon replica of its excitonic transition, which was to be used as a witness state probing the population of the emitter of interest.

However, even with all those precautions, we could not come up with a clear protocol to predict which emitter would behave properly in coherent control and quantum optics experiments. None of the aforementioned criteria, or even its emission energy, its fine-structure splitting and the presence of other emitting structures in its vicinity, seemed to guarantee coherence and we could therefore not bring out a clear pattern.

3.4 Fit of the emission lines

This section details the emission profiles used to extract parameters such as the center energy or emission energy (E_{em}), the full width at half maximum (FWHM) and the intensity (area) from the ZPL or the first LO phonon replica of a bound exciton, by curve fitting after the removal of a baseline from the signal. Since these fits are at the center of my further analysis and conclusions, it is crucial to discuss their goodness and the emission profiles chosen.

3.4.1 Zero-phonon line of a bound exciton

The ZPL of a single bound exciton is usually considered as an homogeneously broadened profile modelled by a Lorentzian curve, with its width determined by its finite lifetime. However, since spectral diffusion originating from fluctuations of the electrical environment around the emitter and the impulse response of the instrumentation can add inhomogeneous broadening components to the profile, a Gaussian or a Voigt (the convolution of a Gaussian and a Lorentzian) function could be more appropriate in modelling the emission lines in some cases. I therefore comment on the adjustment of Lorentzian and Gaussian curves on spectra taken during the PLE experiment, subject of Chaps. 4 and 5.

Fig. 3.5 presents fit examples from a spectrum taken with the *Newton* CCD camera during PLE, along with the value of their parameters and associated standard deviation. While the Lorentzian appears to be better adjusted to the low-intensity “wings” of the curve, it overshoots dramatically the height of the peak in some cases (as for the *X* transition in (b)), causing major issues with the area under the curve. The Gaussian, for its part, cuts the base

of the peak a little short, but reproduces well the amplitude. In general, Lorentzian and Gaussian functions lead to similar results and uncertainties on area and E_{em} fit parameters. The FWHM varied more between the two, especially if the Lorentzian overshoot the data like in Fig. 3.5 (b).

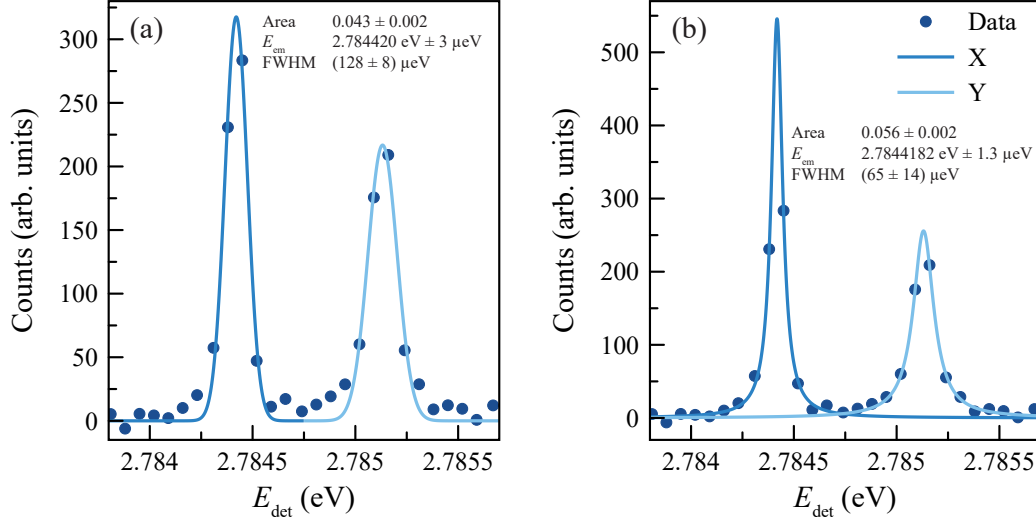


Figure 3.5 Fit example of the ZPL of an exciton doublet (X and Y) using (a) Gaussian and (b) Lorentzian functions. In this case, the Lorentzian curve modelling the X transition overestimates the area under the curve, but better models its wings. The values of fit parameters are given for the X transition, showing a very low uncertainty on the determination of E_{em} and very similar results for Gaussian and Lorentzian functions for this parameter.

As E_{em} is a very important parameter for the analysis of Chap. 5, we were seeking to obtain its value as precisely as possible. In the example of Fig. 3.5, the Lorentzian gives a slightly smaller uncertainty than the Gaussian on the parameter. However, it was not always the case of each emitter: the opposite would have been true if the fit interval contained important background noise or other peaks. The uncertainty is nevertheless very small with both models, of the order of a few μeV and well below the size of one pixel on the *Newton* camera ($70 \mu\text{eV}$), since each emission line is formed of at least four data points. It thus allowed us to write E_{em} to the sixth decimal in Chaps. 4 and 5. With this criterion, both models provide an accurate estimate of E_{em} and its evolution during the experiments.

The FWHM obtained by fitting is for its part approximately one order of magnitude greater than the intrinsic linewidth of the Lorentzian excitonic transition, $\sim 16.5 \mu\text{eV}$ from its lifetime of 80 ps [28]. One can thus assume that spectral diffusion generated by environmental

fluctuations around the emitter and the instrumentation response play non negligible roles in establishing the extracted FWHM. Instrumentation broadening was particularly important in the case of the the *PyLoN* camera, which possesses less numerous, slightly larger pixels (90 μeV) than the *Newton*, leading emission lines to be defined with only three points. Here, Gaussian functions undoubtedly performed better.

In the light of this analysis, I chose Gaussian functions to model emission peaks for both cameras. A Voigt function would probably have been more accurate in the case of the *Newton*, but I still chose a Gaussian for simplicity, while not too much sacrificing the quality of the fit. With this profile, the resolution on the parameters, especially on E_{em} , is good and adequate to discuss every phenomenon regarding the ZPL highlighted in the coming analysis of Chaps. 4–6.

3.4.2 First LO phonon replica of the ZPL

In the resonant excitation experiment of Chap. 6, as discussed above, we detected the first LO phonon replica of the bound exciton ZPL for laser rejection purposes. The intensity I_{em} of this line can be satisfactorily modeled by an equation usually describing the quasi-equilibrium distribution of kinetic energy of the FX that participate in a radiative recombination involving a phonon [180]:

$$I_{\text{em}}(E) = A\sqrt{E - E_0} e^{-\frac{E-E_0}{k_{\text{B}}T}}, \quad E \geq E_0, \quad (3.1)$$

where A is an amplitude parameter, E is the energy, E_0 is the “central” energy of the phonon replica, k_{B} is the Boltzmann constant and T is the temperature. In the case of a bound exciton, the kinetic energy distribution comes from the uncertainty principle between position and wavevector.

Because of the square root term, this model cannot take into account the low-energy side of the asymmetrical peak, as illustrated in Fig. 3.6. It also sometimes underestimates the amplitude. The discrepancy is however reasonably small and acceptable considering the rather simple form of Eq. 3.1.

This is therefore the line profile used in Chap. 6 to extract Rabi curves (peak area as a function of the square root of the excitation power) from the spectra. As one can see from the fit results in Fig. 3.6, A has the largest relative uncertainty, here 10.67 %, followed closely by T

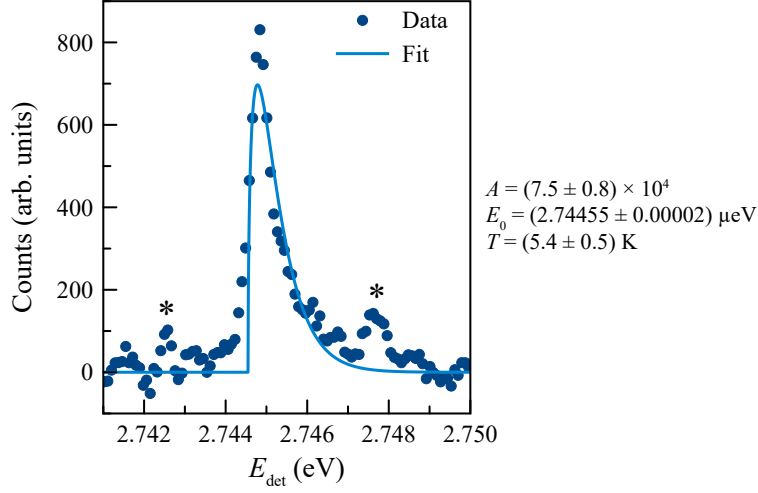


Figure 3.6 Fit example of the first LO phonon replica of a bound exciton. The adjustment is satisfactory, even though the fit function does not reproduce the low-energy side of the peak. The two peaks marked with “*” are other phonon replicas, probably involving a LO and some acoustic phonons. The experimental sample temperature was 6.5 K.

with 9.26 %. E_0 is determined quite precisely, up to tens of μeV , giving a relative uncertainty of 7.29×10^{-4} % in the current example.

Another non-negligible strength of the model is the simple analytical expression for its integral, which takes the form of a Gamma function and gives the integrated intensity of the emission line:

$$\begin{aligned}
 \text{Area} &= A \int_0^\infty \sqrt{E - E_0} e^{-\frac{E-E_0}{k_B T}} dE = A \int_{-E_0}^\infty \sqrt{u} e^{-\frac{u}{k_B T}} du \\
 &= A \int_0^\infty \sqrt{u} e^{-\frac{u}{k_B T}} du = A \sqrt{k_B T} \Gamma\left(\frac{3}{2}\right) = \frac{A \sqrt{\pi k_B T}}{2},
 \end{aligned} \tag{3.2}$$

the function being zero for $E < E_0$. Both A and T have approximately equal contributions to the area uncertainty.

Disappointingly, the presence of noise and other peaks in the spectrum (as in Fig. 3.6) did not allow improvement of fit SNR at higher P_{ex} , as it is seen on the error bars displayed on the experimental curves in Chap. 6. The model nevertheless stays the best fitting option we had for the phonon replica.

CHAPTER 4 NON-RESONANT EXCITATION OF EXCITONS BOUND TO Te_2 MOLECULES IN ZnSe

This chapter is dedicated to presenting general emission properties of Te_2 -bound excitons in our ZnSe samples under non resonant (NR) excitation. These always consist in the first steps in characterizing an emitter prior to the more complex measurements treated in Chaps. 5 and 6, as they allow getting a broad picture of the emitter, its behavior and that of its surroundings. First, PL spectra from the host and typical polarization-resolved spectra from a bound exciton are discussed, followed by a statistical distribution of the emission characteristics of all excitons measured in Sample A. Then, PLE spectra of a single bound exciton are analyzed to bring out the efficient contribution of free excitons (FX) to the bound-exciton population and that of various defect species present in the detection volume. Finally, PLE measurements also investigate the important spectral diffusion to which bound exciton emission lines are subjected due to the photo-induced charging of their environment.

4.1 Emission of the ZnSe host

The NR emission spectrum of the ZnSe layer in Sample A is presented in Fig. 4.1 for an above-gap, 2.870-eV excitation. The two narrow features seen at 2.797 and 2.803 eV are Raman transitions involving respectively two LO and a combination of one LO and one transverse optical (TO) phonons, at 63.4 meV and 57.6 meV [179] below the exciting laser energy. Their presence in the ZnSe emission band is a consequence of our very narrow linewidth laser and the choice of excitation energy (E_{ex}), and is handy for keeping precisely track of the latter. Next, two broad features are observed at 2.8005 eV and 2.8055 eV. From similarities with the FX emission profile in Fig. 2.1 (a) and with the energies reported in strained ZnSe layers as in Fig. 2.1 (b), the second of the two mentioned transitions can be assigned to the radiative recombination of HH FX. The remaining lower energy transition can be associated with the recombination of excitons bound to neutral donor impurities (D_0X) although it is at slightly higher energy (~ 3 meV) than what is most frequently reported in the literature. This discrepancy is presumably due to a difference in strain in the ZnSe layer, and the donor species involved.

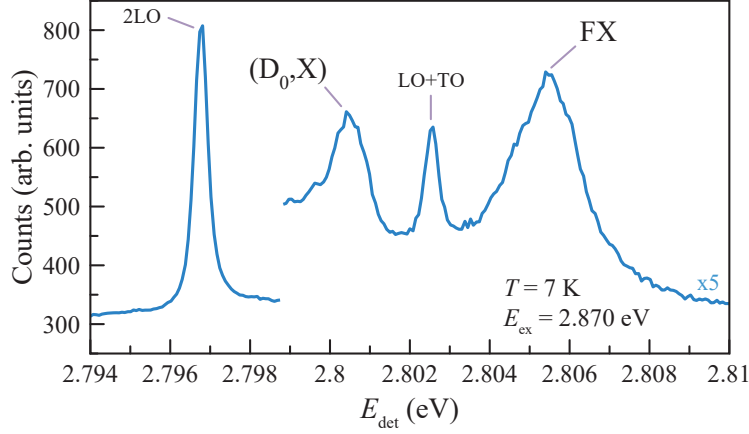


Figure 4.1 Emission spectrum of the ZnSe host embedding the Te_2 molecules, taken at 7 K and with $E_{\text{ex}} = 2.870$ eV. Two broad emission features assigned to excitons bound to neutral donors (D_0X) and free excitons (FX) are seen, as well as two narrow ZnSe Raman peaks, 2LO and LO+TO. E_{det} , the detection energy, corresponds to the calibrated energy axis of the CCD camera.

4.2 Non resonant optical properties of Te_2 -bound excitons

In this section are the discussed the NR PL spectrum of single Te_2 -bound excitons, their polarization response, the statistical distribution of their emission energy (E_{em} , extracted by a Gaussian fit of the bound-exciton emission lines), fine-structure splitting (FSS) and full width at half maximum (FWHM), as well as their PLE spectrum.

4.2.1 NR emission spectrum and polarization response

The emission of Te_2 molecules in our samples took the form of very narrow doublets in the 2.74–2.79 eV range. Depending on the polarization of the detection and the orientation of the defect, both X and Y transitions or only one of the two were visible. Fig. 4.2 presents typical emission spectra along with a polarization color map formed of spectra at different detection polarizations. Two types of polarization scans were performed, whether we worked with linear or circular polarization. The former was more convenient for studying excitons, while the latter was more interesting for the control or initialization of a single hole spin through the trion transition.

The emitter in (a) showed an emission energy of its X transition (E_X) and of its Y transition (E_Y) respectively of 2.743276 and 2.744263 eV, with an energy separation ΔE_{XY} , or

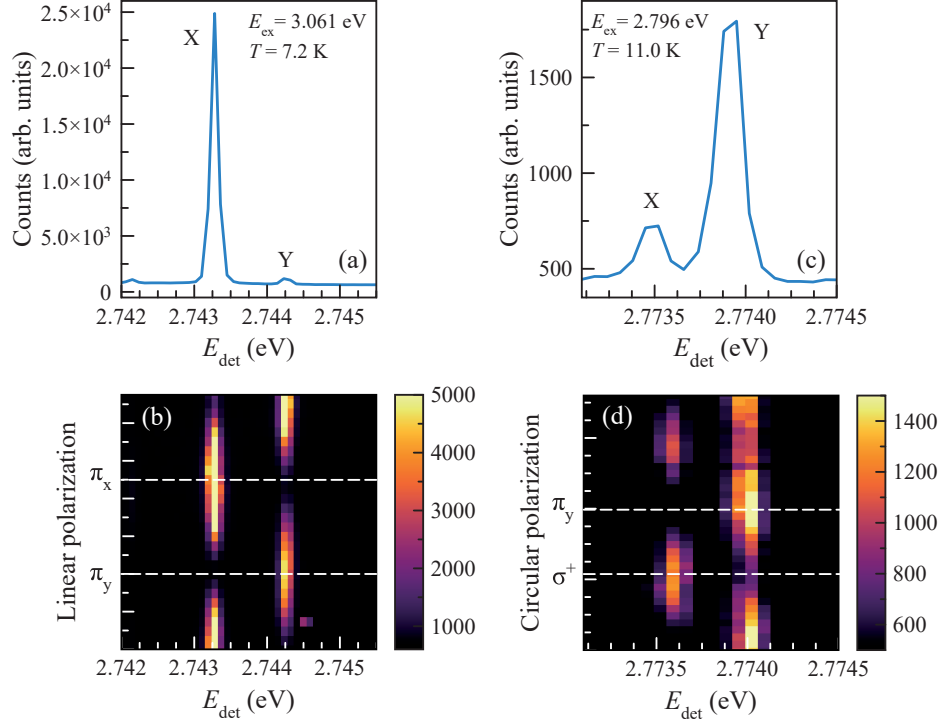


Figure 4.2 Emission spectra (a,c) and polarization response (b,d) of Te_2 -bound excitons. Both X and Y transitions appear as narrow lines. In (b), the polarization color map involves linear polarizations (y axis) from π_x to π_y . In (d), the polarization presents different ellipticities from π_y to σ^+ . This map has been taken with $E_{\text{ex}} = 2.870$ eV. The exciton underwent a slight shift of its E_{em} between (c) and (d). The difference in emission intensity in (a) and (c) could be linked to a difference in alignment or in the surroundings of both emitters, or to their distinct orientation.

FSS, of $987 \mu\text{eV}$. Their FWHM were 63 and $65 \mu\text{eV}$. These values varied from emitter to emitter according to the magnitude of the crystal field of their surroundings and of their exchange interaction, which can be influenced by the presence of charges [181]. One can see on panel (b) that X and Y are orthogonally polarized, as expected from a C_{2v} -symmetry emitter. Indeed, one emission line appears maximal when the other is minimal. Additionally, the x -polarized transition is roughly aligned with the x' laboratory axis (corresponding to the origin of the y axis on the map). As the orientation of the substrate in the cryostat placed the x' and y' axes along $[110]$ and $[\bar{1}10]$, this molecule was in-plane (see Fig. 1.2). However, as it was discussed in Sect. 2.2.3, we do not know whether Y, the high-energy transition of the doublet, is aligned along the x or y molecule axis. The polarization axes of the emission could be rotated 90° with respect to the defect main axis and lead to the same result.

The polarization map in (d) was taken with a quarter-wave plate, modifying the excitation polarization from linear along y (π_y) to elliptical, then to right-handed circular polarization (σ^+) and all the way back to π_y . The detection polarization was at all times parallel to that of the excitation. With σ^+ excitation, both X and Y transitions are seen, with maximal intensity for X and minimal intensity for Y . Here, the orientation of the substrate was such that x' and y' axes were along $[010]$ and $[100]$. The polarization response suggests an out-of-plane molecule with its Y transition corresponding to x' . E_X and E_Y were respectively 2.773487 and 2.773912 eV, leading to a ΔE_{XY} of 425 μeV , and their FWHM was respectively 97 and 80 μeV .

4.2.2 Statistical distribution of Te_2 emission characteristics

Previous studies have shown that the environment of bound excitons is a determining factor of their absorption and emission properties [84, 94, 144, 175]. Fig. 4.3 shows the statistical distribution of the energy and FWHM of the X transition of the 20 excitons studied in the PLE experiment, along with their FSS (ΔE_{XY}). As illustrated in Fig. 4.3 (a), the emission energy is spread over a large 38.47 meV range, with a median of 2.768 440 eV.

ΔE_{XY} , in (b), is concentrated around 216 μeV in a 223 μeV interquartile interval ($Q_3 - Q_1$, where Q_1 and Q_3 are respectively the first and third quartiles), with few outliers. The outliers situated below the median might be trions, as their energy separation is lower than the resolution of the setup (here, 70 μeV with the *Newton* CCD camera). However, without applying a magnetic field and lifting the degeneracy of the two spin states, which wasn't done in this experiment for practical reasons, we cannot know for sure. ΔE_{XY} depends on the crystal field and exchange interaction, both of which vary with strain and the charge configuration of the environment. Such changes could be the result, for example, of the presence of charged and uncharged crystalline defects in the vicinity of the emitter. These effects are also probably responsible for shifting the emission lines at different E_{em} , giving rise to the large E_X distribution.

The FWHM distribution for its part has an average of 158 μeV and median of 138 μeV . These values are larger than what is expected from the 80-ps lifetime measured for the trion ($\sim 16.5 \mu\text{eV}$) [28], hence it is broadened by instrumentation or by an inhomogeneous mechanism. The distribution has a lower bound of about 90 μeV on the low energy side, which is close to the resolution limit of the setup.

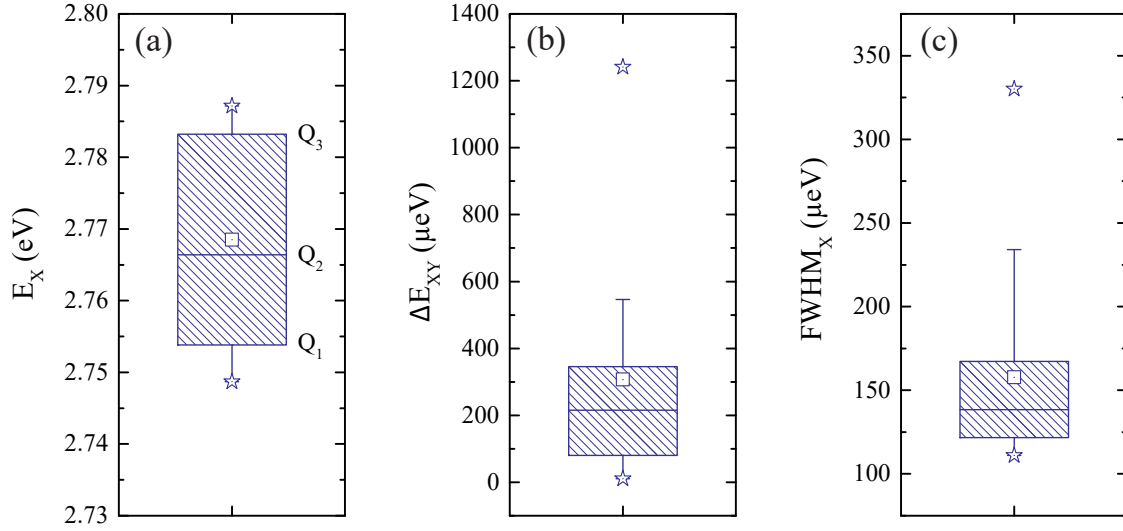


Figure 4.3 Statistical distribution of (a) the energy of the X transition of excitons in Sample A studied during PLE (E_X), (b) of its separation with the Y transition (ΔE_{XY}) and (c) of its FWHM (FWHM_X). The vertical limits of the hatched box represent the quartiles (Q_1 and Q_3), the middle line corresponds to the median (Q_2). Its extensions mark the position of the farthest data point included in 1.5 times the interquartile interval ($Q_3 - Q_1$) below Q_1 or above Q_3 . The square marker indicates the mean and the stars, the minimum and maximum values of the data set.

4.2.3 Absorption spectrum at the free exciton energy

In order to investigate NR population mechanisms of Te_2 -bound excitons, a PLE experiment was conducted, as described in Sect. 3.3.1. Fig. 4.4 displays four differently shaped absorption curves obtained from integrating the emission line of the X transition (except for (d), where the energy of Y is presented) of four distinct Te_2 molecules, found at different positions in the sample, as E_{ex} was varied across the FX band. The PLE spectra have been superimposed to the emission (NR PL) spectra obtained with above gap excitation (~ 2.870 eV) to allow correspondence between absorption bands populating a Te_2 molecule, and emitting energy levels in the material.

All presented excitons (a–d) in Fig. 4.4 show a clear increase of their absorption at 2.805 eV, the FX energy. Some have a very pronounced and sharp maximum at this energy, with (a) or without (b) a substructure, which is thought to be representative of the intrinsic behavior of the $\text{ZnSe}:\text{Te}_2$ system. Others display broader features (d) or even a plateau (c), which reveal

the presence of a continuum of absorbing states such as defects and impurities. Some also present a secondary maximum at lower energy (seen in panels (a), (b) and (d) respectively at 2.80266, 2.80232 and 2.79892 eV), which could be attributed to a D_0X band. The emission from the Te_2 molecule is still visible for energies several meV from the FX center energy, although the absorption is in most cases significantly less efficient, even at the D_0X energy (~ 2.800 eV). Interestingly, the absorption structure of the exciton in panel (a) is formed of two peaks that are separated by 1.09 meV, a value close to the longitudinal-transverse splitting (Δ_{LT}) between the lower polariton (LPB) and upper polariton (UPB) branches in ZnSe (1.2 meV [182] and 1.5 meV [112] from reflectance measurements and (1.45 ± 0.05) meV from Brillouin scattering [166]). The splitting could therefore show polaritonic effects in the host material.

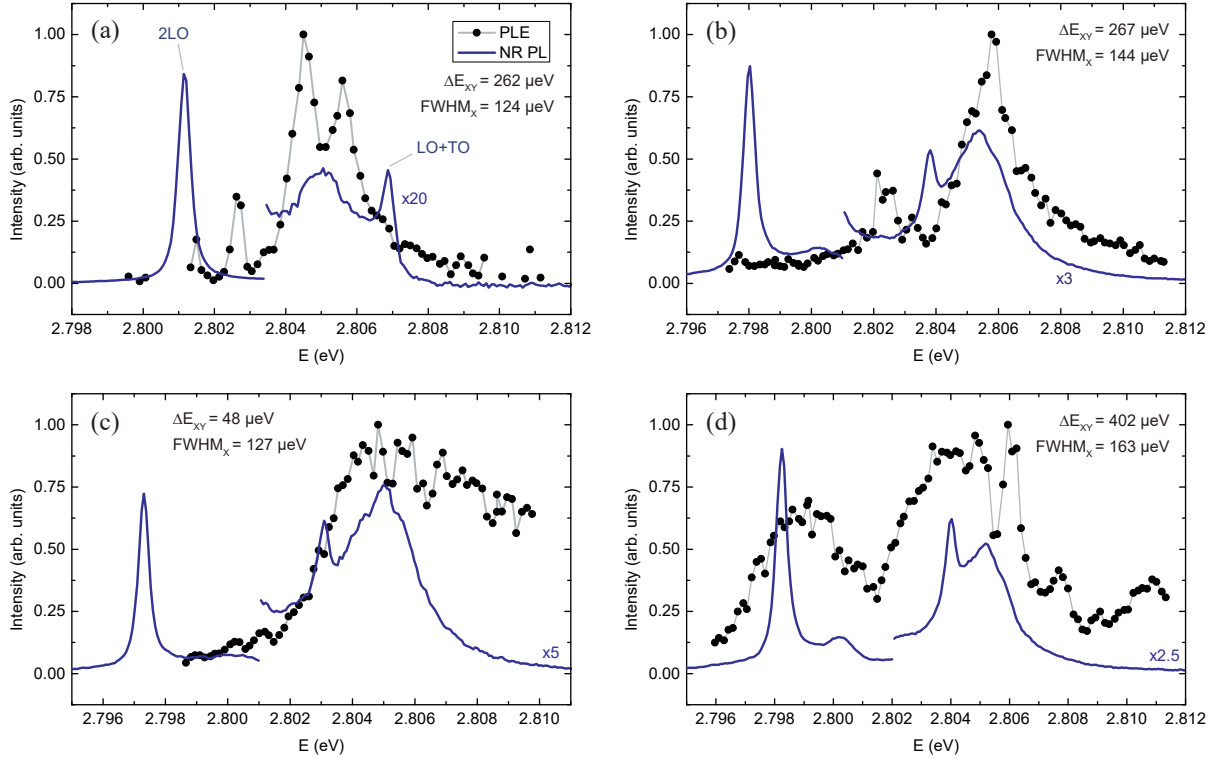


Figure 4.4 PLE (gray lines with black dots) and NR PL (dark blue lines) spectra of four different bound excitons in different regions of the sample. The x axis corresponds to E_{ex} for PLE curves and to E_{det} for NR PL. On the latter curves are seen Raman transitions in the ZnSe host (2LO and LO+TO), the FX emission structure at 2.805 eV and the D_0X at 2.800 eV.

In short, there is notable inhomogeneity in the absorption behavior of Te_2 molecules situated

in different areas of the sample, a consequence of the variation in strain and in the composition of their environment.

4.2.4 Nature of the emission structure at 2.805 eV

In Sect. 4.1, I have assigned the emission band at 2.805 eV to the FX based upon the similarity of its shape and energy with reports from the literature. However, this identification differs from the interpretation of Ref. [28], previously published by our group. I want to discuss this aspect in more details, as my findings could lead to a reinterpretation of the presented initialization mechanism of a single hole on a Te_2 molecule.

In Ref. [28], the ZnSe host emission band formed of two features respectively at 2.8008 eV and 2.8050 eV is attributed to excitons bound to neutral donors (D_0X). The sample studied in this work is very similar to Sample A, described in Sect. 3.3.1. The main result of the work, as presented in Sect. 1.2.3, consists in the ultrafast initialization of a single hole bound to a Te_2 molecule through the trion transitions by the means of a pulsed excitation resonant with the 2.8050-eV band. The mechanism proposed was that the laser pulse resonantly creates a D_0X , which then tunnels onto the Te_2 molecule containing a single hole to form a trion. The recombination of the trion would lead to the initialization of the hole, as proven by the high degree of circular polarization of the emission.

The fact that the maximal degree of polarization in Ref. [28] is reached at the exact same energy as the absorption maximum in my PLE results strongly points towards the involvement of the same energy levels in both phenomena. From the correspondence of the absorption maximum with the FX emission energy and its efficiency in populating Te_2 molecules, I believe that the mechanism responsible for initialization developed in Ref. [28] could be reinterpreted as involving the FX instead of or in addition to the D_0X .

4.3 Increase of Te_2 population efficiency

In this section, it is demonstrated that emission spectra from Te_2 molecules are influenced by the choice of E_{ex} . It is also argued that the presence of a maximum at the FX energy in Te_2 -molecule PLE spectra suggests that the latter are populated through a very efficient mechanism involving the direct capture of resonantly-created FX, different from the HTL

model detailed in Sect. 2.2.1. Indeed, exciting the FX band (2.805 eV) often led to finding more numerous and brighter bound excitons compared to above-gap excitation (3.061 and 2.870 eV, or 405 and 432 nm).

The spectra in Fig. 4.5 have been taken respectively at 2.870 eV and 2.805 eV and display very different emission lines. For instance, there are about twice as much transitions seen in the 2.805-eV spectrum as in the 2.870-eV one. Although the emission intensity (I_{em}) of the two spectra cannot be directly compared due to differences in experimental conditions, these transitions have a relative I_{em} with the main 2.762 540 eV exciton (i.e. for which the alignment was optimized) ranging from 0.07 to 0.29 for a 2.805-eV excitation, and from 0.05 to 0.17 for a 2.870-eV excitation. This translates to a relative- I_{em} average value respectively of 0.17 and 0.12, a 42 % increase. These values exclude the 2.722130-eV outlier for which the alignment at 2.805 eV seemed somewhat poorer.

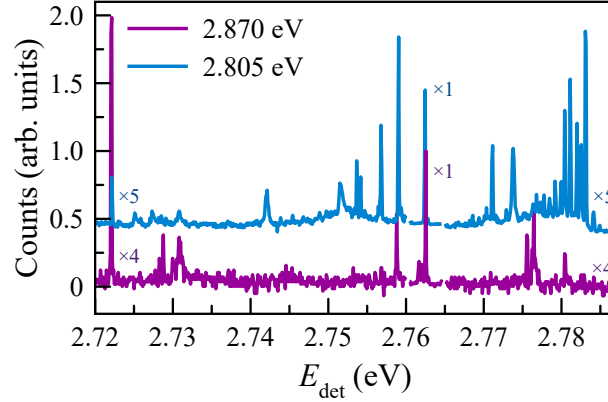


Figure 4.5 Emission spectra for excitation at 2.870 eV (above-gap) and 2.805 eV (resonant with the FX). Both curves have been normalized to their maximum value and multiplication factors were applied to lower-intensity regions. Numerous new transitions are seen when E_{ex} is resonant with the FX, and the relative intensity of certain transitions is also modified. The SNR difference in the two spectra originates mostly in their distinct t_{acq} .

These results can be explained by considering the effect of E_{ex} on the population mechanisms taking place, favoring certain recombination paths over others. Indeed, during above-gap excitation, electrons and holes are photo-generated in the conduction and valence bands without interacting with one another. They are highly energetic, and binding to a Te_2 molecule through the HTL model described in Sect. 2.2.1 is only one of the many options these carriers have to dissipate their energy. There is consequently more competition with other

non-radiative transitions, or with radiative ones happening at distinct energies than the selected detection window.

The HTL mechanism being a two-step process, two probabilities must be taken into account: that of the hole to first fall into the potential, and then that of the hole to attract and bind an electron to form the exciton. It is therefore fairly reasonable to consider that only a small proportion of carriers recombine radiatively according to this path. However, when exciting the FX band, one efficiently creates numerous correlated electron-hole pairs free to move around in the lattice. These excitons can bind to a Te_2 molecule in a single step [152], as illustrated in Fig. 4.6, making it a much more probable binding mechanism and leading to a greater I_{em} .

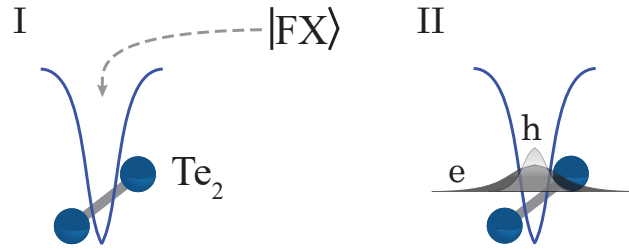


Figure 4.6 One-step binding mechanism of a FX to a Te_2 molecule. After its photo-generation, the FX diffuses in the lattice and falls into the narrow potential well created by the molecule (I), creating a bound exciton (II).

As exciting the FX states in the bandgap cuts off a lot of other possible recombination paths and relaxation mechanisms, it leaves more of them available to bind to Te_2 molecules and other in-gap defects. Along with the one-step capture mechanism, it explains the more intense and numerous excitons lines in the 2.805-eV spectrum of Fig. 4.5. In light of these results, one can conclude that exciting the FX band is a more efficient way of creating Te_2 -bound excitons than above-gap excitation.

4.4 Exciting a continuum of states through the FX band

The prevalent population mechanism for a FX-band excitation reported in Sect. 4.3 also applies to any state within the gap such as defects, dislocations, impurities and other Te_2 molecules [84]. Hence, a FX can fall into any trap energetically available in its diffusion length and recombine radiatively afterwards. These traps can be quite numerous in ZnSe

and thus are likely to be present in the detection volume. As FX are created in greater numbers in resonance than with an above-gap excitation, they are statistically more likely to be involved in one of those transitions, similarly to what was discussed for Te_2 molecules in Sect. 4.3. The combination of the emission from all these excitons bound to different defects, so numerous that they cannot be individually resolved, along with the effect of their immediate environment shifting and broadening their emission lines according to the local fluctuating electric field, leads to the appearance of a broad feature in PL spectra in the form of a background signal, clearly visible in Fig. 4.7.

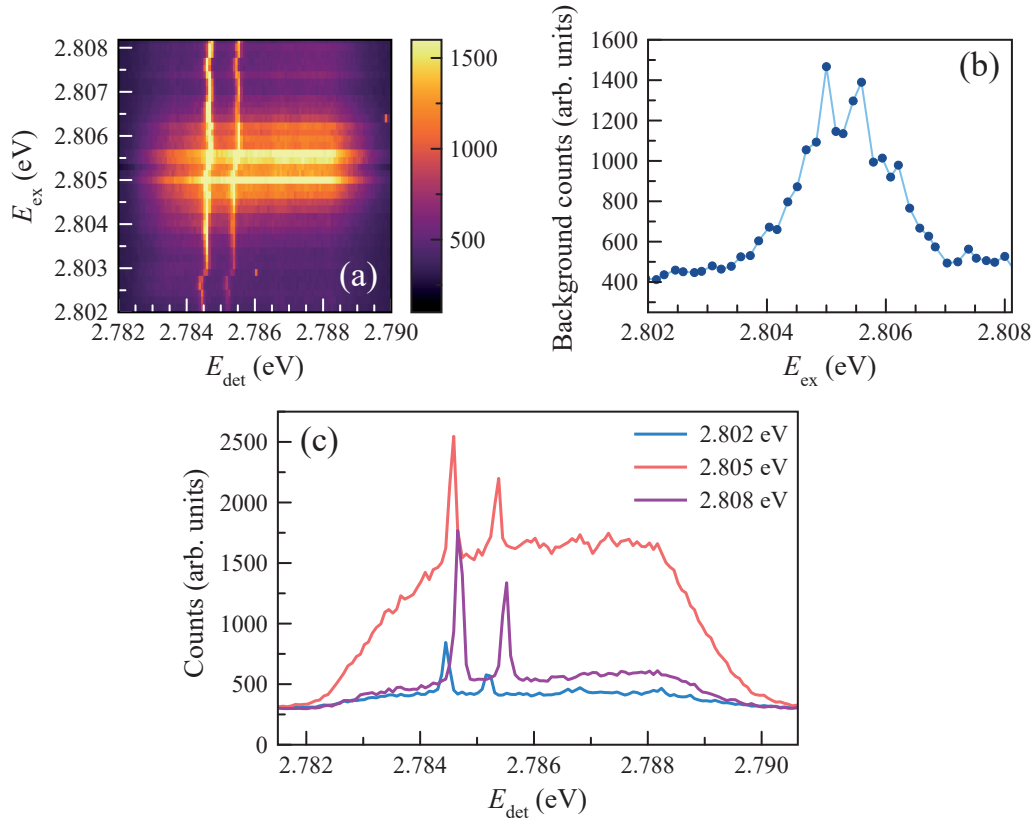


Figure 4.7 Excitation of a broad continuum of states. (a) PLE color map presenting the emission intensity (color scale) as a function of detection (E_{det}) and excitation (E_{ex}) energies of a Te_2 -bound exciton. A broad emission appears as E_{ex} is swept between 2.804 and 2.806 eV over the FX band. The E_{det} range is limited by the presence of the rejection grating in front of the spectrometer slits. The background therefore spans on a larger range than the displayed 8 meV. (b) Median value of the background intensity over the E_{det} range in (a) as a function of E_{ex} , showing that the maximum of this emission is exactly at the FX energy. (c) PL spectra for E_{ex} before, right on top of and after the FX resonance.

In panel (a), a color map is formed of emission spectra (x axis) at different E_{ex} (y axis), three

of which are depicted in panel (c), and its color scale quantifies I_{em} . Panel (b) presents for its part the background intensity as a function of E_{ex} , taken as the I_{em} median value in each spectrum displayed in panel (a). One can see from the graph the low background value on both sides of the FX band and its reaching of a maximum at 2.805 eV. This demonstrate the efficiency of the FX in populating sub-bandgap energy states compared to above-gap excitation, to such extent that all of the available radiative recombination paths form a “continuum of states”.

The origin of the participating states is unknown, but we have made the assumption that this emission is not Te_2 -related. Candidates reside in phonon replicas of donor-acceptor (D-A) recombinations that were observed in the same energy range [84]. From now on, the background is removed from all presented data in order to focus on the phenomena involving the bound exciton emission lines.

4.5 Spectral diffusion of the excitonic emission lines under non resonant excitation

NR excitation can act upon the electrical environment of a Te_2 -bound and in this way influence its E_{em} , as was discussed in Sect. 2.5. This drift (i.e. spectral diffusion), or its temporal version (i.e. jitter), is associated with the random fluctuation of defect charge states in the vicinity of the potential trapping the exciton. These create an electric field that perturbs the system and leads to E_{em} shifts through the DC Stark effect. Emission lines subjected to the same drift or jitter are assumed to be originating from excitonic complexes bound to the same Te_2 molecule. They are indeed expected to experience the same electric perturbations [84, 95, 183], since the sampling rate is generally greater than that of the diffusion. In our system, photons in the 2.798–2.812 eV range efficiently create FX that can bind as whole excitons or separate electrons and holes to defects in the vicinity of the emitter of interest. Also, as they are well above the GaAs energy gap (1.519 eV at 10 K [113]), they generate free carriers that accumulate at the interface between the substrate and the epitaxial layer. Both mechanisms add charged entities to the surrounding of the bound exciton that interact with it, resulting in the observed shift.

During the PLE experiment, a great number of the observed excitons experienced spectral diffusion caused by laser-induced changes in their electrical environment. Fig. 4.8 presents two series of NR PL spectra for two different excitation polarizations, which identified the

displayed lines as the X and Y transitions of an excitonic doublet. These excitons are used in the following discussion to demonstrate that, as expected from the results reported in the literature, emission lines associated with the same Te_2 molecule experience a simultaneous drift of similar amplitude. Their polarization behavior indicates that they are bound to out-of-plane molecules with their Y transition aligned along the x' laboratory axis.

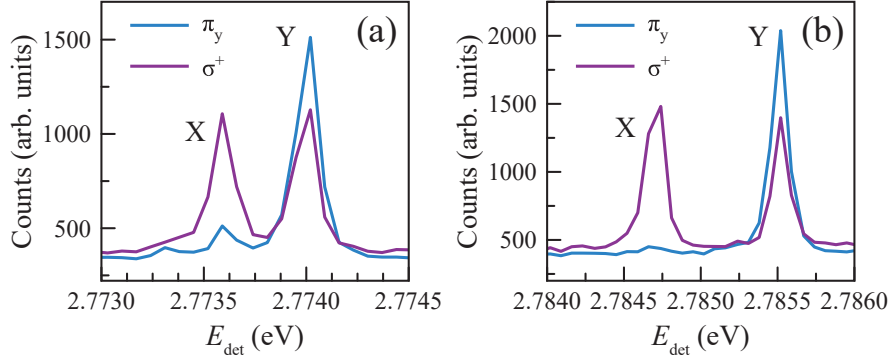


Figure 4.8 NR PL spectra with π_y and σ^+ excitations for two excitons that underwent a drift of their E_{em} with the modification of their electrical environment. Both are bound to an out-of-plane molecule and have their Y transition oriented along x' in the laboratory frame.

Their E_{em} is presented as a function of E_{ex} in Fig. 4.9. One can see in panel (a) the most common behavior, a smooth and continuous variation probably originating from the modification of a distant portion of the electrical environment, which acts as a slowly-evolving mean field (in a min-h timescale). In panel (b), an occasional behavior where the perturbation caused sudden E_{em} jumps of amplitude $\sim 100\text{--}150\text{ }\mu\text{eV}$ is shown, most likely the consequence of discrete charging events close to the emitter (see Sect. 2.5) [77, 174, 177]. Both cases are illustrated in the schematic of Fig. 4.10. The small-amplitude oscillation superimposed to the drift behavior in Fig. 4.9 is discussed in detail in Chap. 5. Nevertheless, in both cases, both doublet peaks presented a simultaneous drift of similar amplitude, as is expected from emission lines coming from the same Te_2 potential. This gives us a criterion to discriminate which lines are coming from a particular emitter and which must be associated with another.

Moreover, Fig. 4.11 illustrates a variation in FSS caused by the electrical perturbation. The perturbation Hamiltonian developed for excitons bound to C_{2v} -symmetry defects [154], detailed in Appendix B, infers an electric field along x or y causes mixing of the hole part of the $|X_{hh}\rangle$ and $|Y_{hh}\rangle$ exciton wavefunctions with LH states, shifting their energy by different amounts (considering solely the dominant effect of linear terms). Also, as reported in QDs,

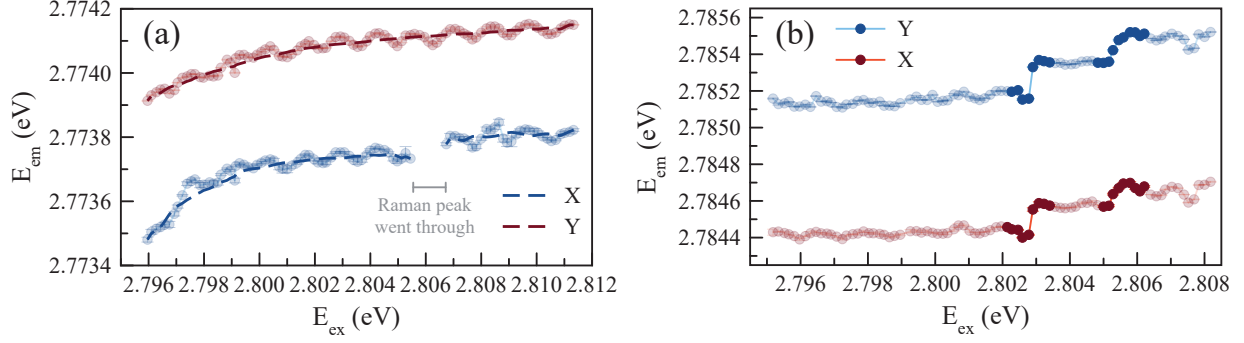


Figure 4.9 Spectral diffusion of the X and Y transitions of two Te_2 -bound excitons, smooth and continuous in (a) and sudden in the form of jumps in (b). In both cases, the drift behavior is identical for both doublet transitions. The excitation polarization is close to π_y in (a) and σ^+ in (b). Missing data points in (a) are due to the passage of the LO Raman peak on top of the X transition. The dashed lines are moving-average curves of the data to show the trend. In (b), the sudden events have been highlighted. The small oscillation of E_{em} superimposed to the drift is the subject of Chap. 5.

the presence of an electric field modifies the overlap of the electron and hole spatial wavefunctions, which has a major effect on electron-hole exchange interaction [181] and therefore adds another contribution to the change in energy splitting. By comparing Fig. 4.9 with Fig. 4.11, it appears that the largest ΔE_{XY} changes happen as the emission lines undergo their most dramatic shifts to higher energy. This observation tends to prove that the two phenomena are simultaneous and share a common cause, i.e. a fluctuating electric field in the emitter surroundings.

With this in mind, one can assign the different emission lines in the PLE maps of Fig. 4.12 to multiple Te_2 -bound excitons in the same detection volume experiencing different drifts. For example, in panel (a), two peaks (at 2.780500 and 2.782210 eV for $E_{\text{ex}} = 2.805$ eV, the second being marked by a dashed line) undergo a synchronized and similarly shaped diffusion, suggesting that they originate from the same Te_2 molecule. The magnitude of the shift differs for both peaks (respectively ~ 660 and 110 μeV), demonstrating again how the FSS can be altered by a change in the environmental charge configuration. Four other peaks also appear on the map, which are not linked to the same emitter, as they remain mostly unchanged during the whole PLE scan. These differences in behavior show that the surrounding charge configuration varies on an even smaller scale than the spatial resolution of the microscope, which is of the order of $0.76 \mu\text{m}$.

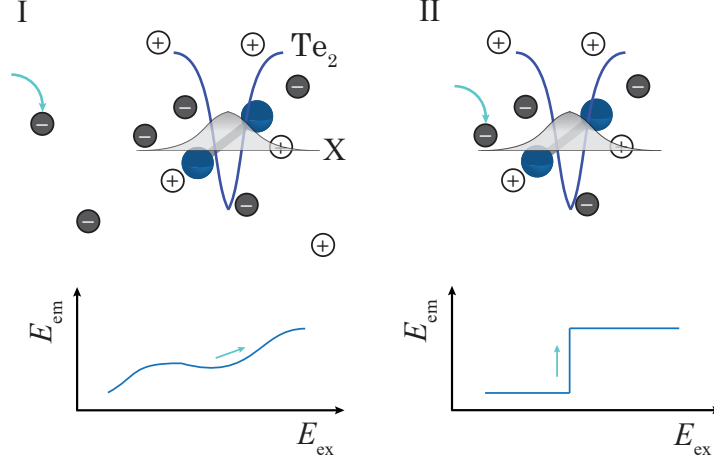


Figure 4.10 Charging events causing spectral diffusion of the bound exciton emission line. I. Charge fluctuations in the far environment of the bound exciton are seen as a minute change of the mean electric field and lead to a smooth and gradual variation of E_{em} . II. An added (or removed) charge in close proximity to the bound exciton leads to a sudden jump in E_{em} .

In panel (d), as E_{ex} was swept from high to low energies, two emission lines suddenly appeared at $E_{ex} \sim 2.80234$ eV, which could be the consequence of several effects. The lines could result from a change in exciton charge state from trion to exciton or vice versa, since the binding energy for those two excitonic complexes differs. The lines could also be coming from a sudden and large E_{em} shift of a transition initially outside the detection window, caused by the fluctuation of the electrical environment. Finally, the variation in E_{ex} could also favor the population of a defect that would, through its electrical field, open a capture channel on a nearby emitter. An example of such a channel is the tunneling of an exciton from a nearby defect onto an emitting center. Reversely, the quenching of an emitter, which is not shown on Fig. 4.12, can also occur through similar mechanisms, by the escape of the bound exciton through tunneling or the loss or gain of a charge.

In summary, charge fluctuations lead to spectral diffusion of excitonic lines, a phenomenon that can be used to identify transitions associated with a single emitter, and also to a modification of their FSS. These E_{em} changes can be gradual or abrupt depending on the proximity of the charges responsible. Obviously, such effects are deleterious to the coherent control of a qubit state and must be mitigated with, for example, motional narrowing (as discussed in Sect. 2.5).

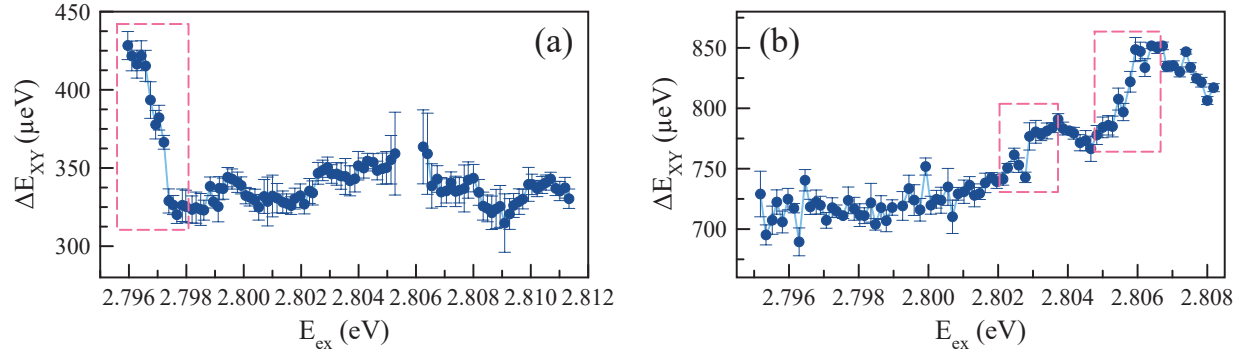


Figure 4.11 Fine-structure splitting of two Te_2 -bound excitons, which is influenced by the laser-induced electrical perturbation. The most dramatic changes in ΔE_{XY} , highlighted by pink dashed boxes, happen as E_{em} undergoes its greatest variations in Fig. 4.9.

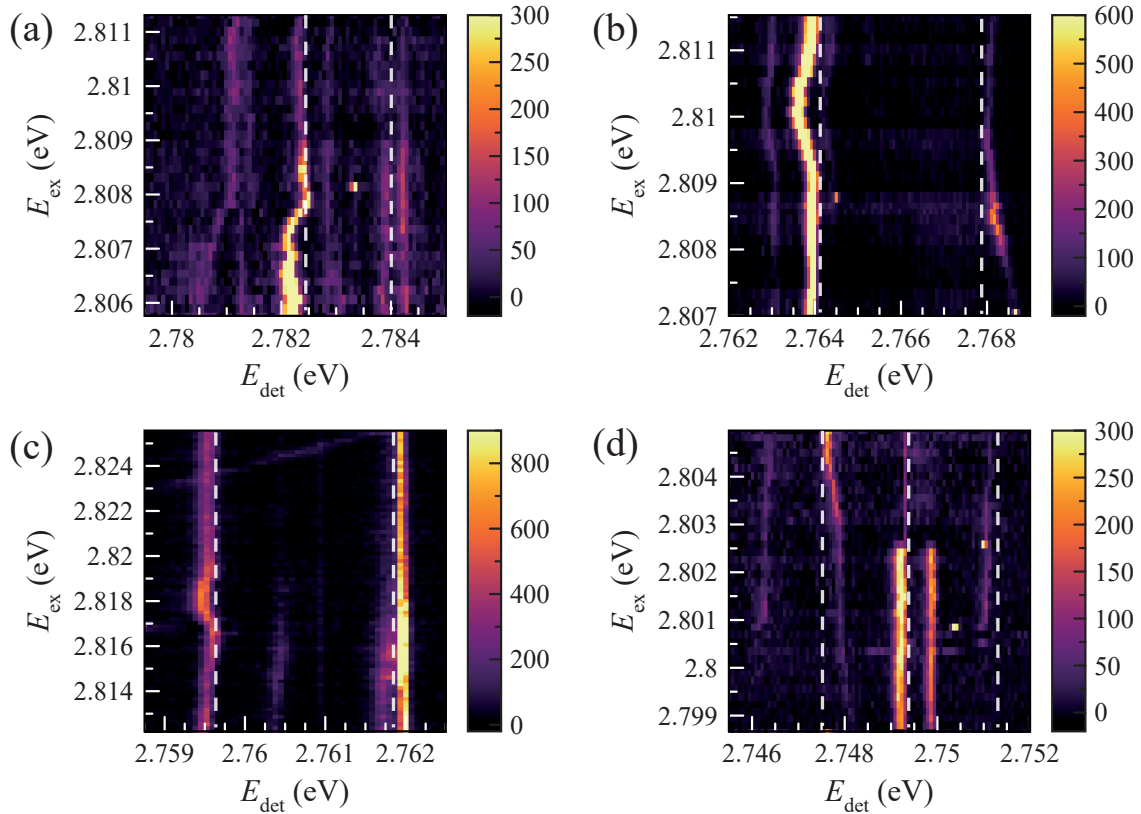


Figure 4.12 PLE maps showing different drifts for emission lines coming from distinct centers. The dashed lines are guides to the eye placed slightly beside the transitions for clarity. In (d), two lines suddenly appear, a consequence of tunneling from another defect, the change in charge state or the capture of a FX. A baseline has been subtracted in order to emphasize on exciton behavior.

4.6 Conclusion on the NR excitation of ZnSe:Te₂

In this chapter, general NR emission properties of our samples were presented. First, PL spectra from single emitters displayed the two main emission features of the ZnSe host, associated respectively to the recombination of free excitons (FX) at 2.805 eV and excitons bound to neutral donors (D_0X) at 2.800 eV. Te₂-bound excitons themselves presented two linearly-polarized, orthogonal transitions (X and Y) at energies spanning from 2.74 to 2.79 eV, with an average full width at half maximum (FWHM) of 158 μ eV and an average fine-structure splitting (FSS) of 307 μ eV.

Bound-exciton photoluminescence-excitation (PLE) spectra show a maximum at the FX energy, giving proof of an efficient population mechanism most likely involving the direct capture of a whole FX, differing from the Hopfield-Thomas-Lynch (HTL) model which involves the sequential capture of a hole and an electron. The shape of the PLE curve is however greatly dependent on the emitter, sometimes presenting a clear maximum, sometimes taking the shape of a plateau. A non-negligible fraction of emitters also presented a second, lower-energy maximum that could be due to the D_0X .

The direct capture of a FX is further supported by the approximate two-fold increase in the number of observed single emitters under 2.805-eV excitation compared with above-gap excitation, along with their average 42-% greater brightness. A similar effect is responsible for a background increase in the PL spectra as the excitation comes into resonance with the FX, since the latter can be captured by other numerous and unresolved defects.

Finally, an important spectral diffusion was observed during PLE scans, leading to an energy shift of the X and Y exciton transitions and to a change in their separation (i.e. FSS or ΔE_{XY}). This was attributed to changes in the electrical environment of the Te₂ molecules that induce a DC Stark effect. On top of this drift was seen a small-amplitude oscillation of the emission energy (E_{em}) as a function of excitation energy (E_{ex}). This effect is investigated in great detail in the next chapter, and several possible explanations for its origin are developed.

CHAPTER 5 REMOTE OPTICAL MODULATION OF ZnSe:Te₂ EMISSION PROPERTIES

We have seen above in the previous chapters that PLE is a powerful technique that allows probing states in a material that both absorb light and possess a relaxation channel toward an emitting witness state. Its resolution is determined by the linewidth of the excitation laser employed and the energy steps available, and therefore can be very high. Consequently, using this technique, I was interested in better understanding the exciton transfer mechanism between higher-energy states such as what is referred to in Ref. [28] as a neutral donor (D_0X) and a Te₂ molecule in ZnSe. I was also hoping to identify the energy of the 1S LH bound exciton and excited states of the HH bound exciton, as well as to see if I could exploit them for control schemes of an excitonic or a spin qubit. The PLE data instead unveiled an unexpected phenomenon, but nonetheless very intriguing and rich.

The present chapter describes this surprising effect, along with a detailed exposition of its principal characteristics. I show that an energetically remote excitation of the FX band in the ZnSe host has an important effect on the emission energy (E_{em}) of Te₂-bound excitons. In particular, I report an oscillatory behavior of E_{em} as a function of excitation energy (E_{ex}), which, to the best of my knowledge, has never been described in any of the single emitter systems that I have surveyed. Such a coupling is interesting as it may provide the means for an ultrafast manipulation of the E_{em} of a localized exciton, a tool that could prove useful as quantum information processing requires to turn on and off coupling between distinct qubits or between an emitter and a cavity.

The chapter is structured as follows. First, I present PLE experimental data highlighting the E_{em} oscillation and demonstrate its statistical significance. I then describe its most revealing characteristics. Finally, I provide a few physical explanations for the influence of a FX-resonant excitation on the E_{em} of Te₂-bound excitons. Albeit considerable efforts have been made to understand the origin of the periodic modulation of the Te₂ E_{em} , we have not yet found the model that provides a comprehensive picture of the phenomenon.

5.1 Modulation of the emission energy of a Te_2 -bound exciton

More than solely giving out information on the absorption and transfer behavior of FX towards a Te_2 molecule, our PLE experiment unveiled effects of E_{ex} on the E_{em} of our emitters. A small-amplitude, periodic E_{em} oscillation was observed for a majority of them, showing that it is possible to reliably act upon the emission properties of the system with NR optical means. This phenomenon is easily identified in Fig. 5.1, displaying color maps of the emission intensity as a function of both E_{ex} and detection energy (E_{det}) for the same two excitons appearing in Figs. 4.8, 4.9 and 4.11. Both X and Y transitions are visible in (a) and (b), respectively at $E_X = 2.773\,954\text{ eV}$, $E_Y = 2.773\,996\text{ eV}$ and $E_X = 2.784\,705\text{ eV}$, $E_Y = 2.785\,520\text{ eV}$. In addition to the E_{em} oscillation, they also experience a gradual energy drift in (a) and abrupt jumps in (b), discussed in Sect. 4.5. This spectral diffusion is subtracted from the data in the discussion below in order to concentrate on the oscillation behavior, which is the subject of the current chapter.

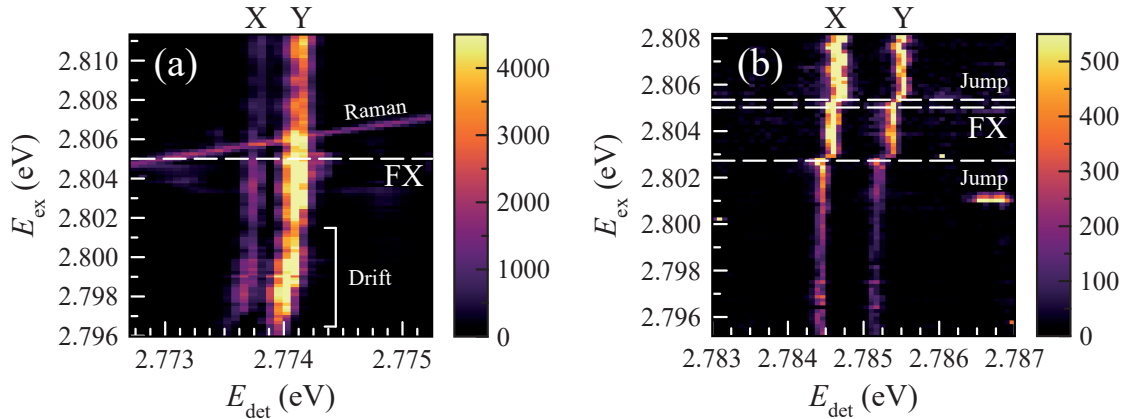


Figure 5.1 PLE maps presenting the E_{em} oscillation of Te_2 -bound excitons. (a) Excitonic doublet near 2.774 eV, with its X and Y transitions following the same drift and oscillation. The oblique line is the LO Raman transition from the ZnSe host. (b) Excitonic doublet from another detection volume undergoing a drift in the form of sudden jumps. X and Y also follow the same oscillation.

The next sections demonstrate that excitonic transitions oscillate synchronously as long as they are situated in the same detection volume, whether they belong to the same emitter or not. They also list the impacts of absorption efficiency and excitation parameters on the observed oscillation.

5.1.1 Simultaneous oscillation of the X and Y transitions of a single exciton

Fig. 5.2 presents E_{em} as a function of E_{ex} for the X and Y transitions of both excitons presented on the maps of Fig. 5.1, after the subtraction of the drift. The synchronous oscillation of x and y -polarized transitions clearly stands out and its characteristics can be analyzed. Uncertainty on E_{em} is of the order of a few μeV , as reported in Sect. 3.4, and is indicated on the graph by error bars. For most of the data points, these are smaller than the size of a symbol.

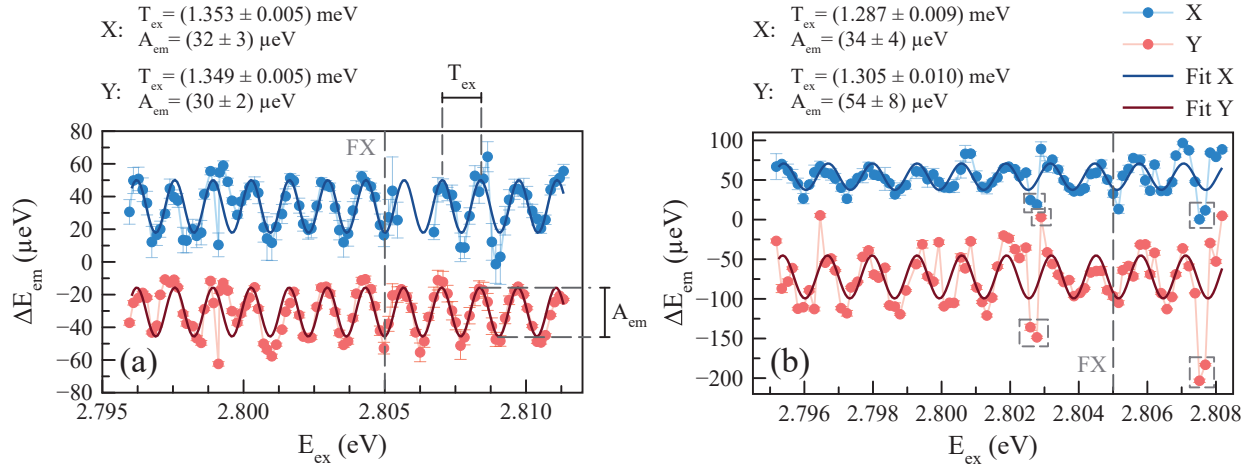


Figure 5.2 E_{em} oscillation as a function of E_{ex} for two excitons in different detection volumes. The E_X and E_Y oscillations are synchronous in both (a) and (b). The data has been arbitrarily translated and a drift was subtracted to emphasize on the oscillation behavior. The data points framed by dashed gray boxes in (b) have been excluded from the fit. They are a consequence of the imperfect subtraction of spectral diffusion at the position of the jumps.

A fit of a single sine function with a constant frequency leads to the extraction of the oscillation period (T_{ex}) and the peak-to-peak amplitude (A_{em}) for both transitions. The results for both excitons are given on top of panels (a) and (b). One can see that Exciton A has overlapping T_{ex} and A_{em} for both transitions, meaning that both dipoles experience the same perturbation. However, although X and Y share similar T_{ex} for Exciton B, the values for A_{em} do not overlap, meaning that the dipoles are affected by different perturbations. From comparison with other doublets (not shown here, see Appendix A), such a behavior is exceptional.

The fit however systematically underestimates A_{em} , as can be seen on Fig. 5.3. The sine function indeed fails to reproduce the sharper extrema of the data, especially the minima, which are generally more tapered than the maxima. The function is nonetheless useful to

extract the main period of the oscillation, and its contribution to the overall A_{em} . Attempts to fit other functions such as a rectified sine curve gave for most of the emitters very similar results in terms of T_{ex} and A_{em} with slightly larger uncertainties. The sine fit was therefore kept for the sake of simplicity. The rectified sine fit however better followed the shape of the minima. In all graphs below, the A_{em} value given is the one extracted from the sine fit, if not specified otherwise.

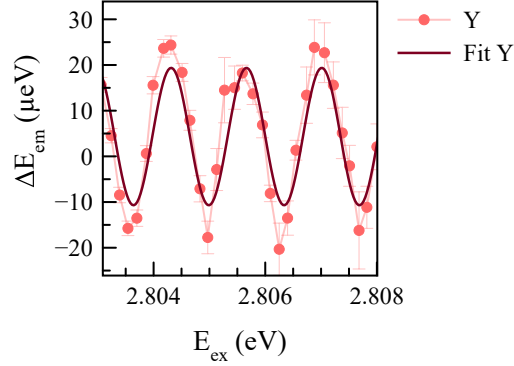


Figure 5.3 Zoom of a portion of the sine fit performed on the Y transition of Exciton A in Fig. 5.2. The function underestimates A_{em} as it fails to reproduce the sharper extrema of the data set.

Fig. 5.4 shows fast Fourier transforms (FFTs) of the oscillation curves. In both cases, X and Y have the same dominant frequency $1/T_{\text{ex}}$, 0.7407 meV^{-1} for Exciton A and 0.7788 meV^{-1} for Exciton B. These correspond respectively to $T_{\text{ex}} = 1.350 \text{ meV}$ and $T_{\text{ex}} = 1.284 \text{ meV}$ and are consistent with the values obtained from the fits. Unsurprisingly, other lower-amplitude frequencies are involved, as the oscillation trace is not perfectly sinusoidal.

In (a), FFTs for X and Y are almost identical, since their data in Fig. 5.2 show very similar T_{ex} and A_{em} . In (b), Y displays several other non-negligible frequencies, the two most important being 0.9498 and 1.235 meV^{-1} . These come from the additional fluctuations presented by Y in Fig. 5.2 (b). However, part of these are due to spectral jumps that were not perfectly removed by the subtraction of the drift (data in dashed gray boxes).

In short, both emission lines of an excitonic doublet have their E_{em} oscillating in phase with one another as a function of E_{ex} . A_{em} can for its part differ, but that is generally not the case for most emitters. The oscillation behavior is not quite sinusoidal, but its main period T_{ex} can be extracted with confidence by a sine fit, while A_{em} is slightly underestimated.

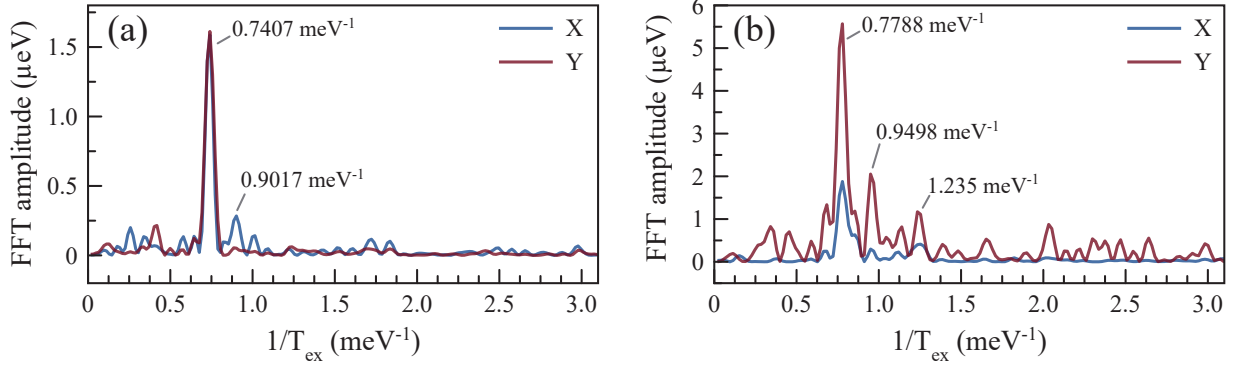


Figure 5.4 FFTs of the curves in Fig. 5.2. The dominant frequency in each graph is consistent with the T_{ex} values extracted from the fits. In (b), Y has more than one non-negligible frequency.

5.1.2 Statistical distribution of the oscillation parameters

The E_{em} oscillation was unambiguously observed and studied for an important number of 12 emitters out of a total of 20. The leftover eight presented unreliable results: three of them had important spectral diffusion masking the oscillation behavior and those remaining presented atypical or noisy behaviors or were perturbed to the point of escaping their binding potential. We attribute these failed measurements to a particularly perturbed environment, be it by charges in the vicinity of the emitter or defects in the semiconductor host.

The excitons were energetically separated from the FX by 17.8–53.5 meV, a wide spread which does not systematically correspond to any optical phonons or one of their combinations in ZnSe. Indeed, the energy of LO phonons at the Brillouin zone center (Γ) is 31.7 meV and that of TO phonons is 25.9 meV [179]. Therefore, the oscillating excitons were not a special kind preferentially coupled to the FX through optical phonons. This possibility is discussed in more details later in Sect. 5.2.3.

Fig. 5.5 summarizes the distribution of the oscillation characteristics of the oscillating excitons. T_{ex} ranges from 0.672 to 1.607 meV, with a mean of 1.103 meV. A_{em} , for its part, is contained within a minimum of 30 μeV and a maximum of 68 μeV , and averaged at 44 μeV .

In light of these observations, one can confidently state that a majority of excitons under-

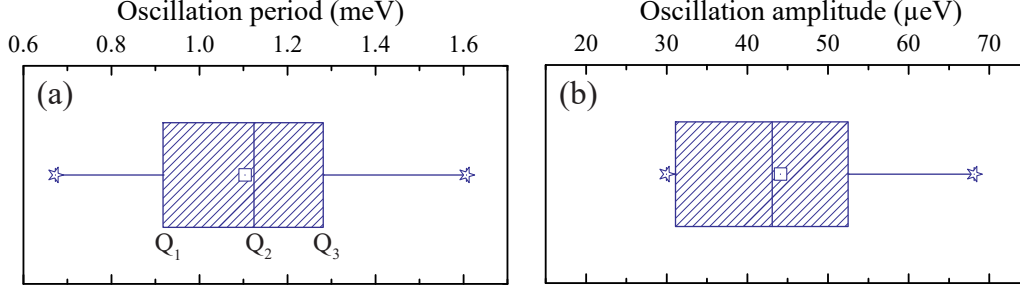


Figure 5.5 Statistical distribution of (a) the oscillation period and (b) the oscillation amplitude of the emission energy of the studied excitons. The total number of excitons in the distribution is 12. The box delimits the quartiles (Q_1, Q_2, Q_3), the dotted square marks the mean and the stars, the maximum and minimum values of the data set. The extensions mark the position of the farthest data point that is included in 1.5 times the interquartile interval ($Q_3 - Q_1$) below Q_1 or above Q_3 .

went an oscillation of their E_{em} during PLE, with a period of the order of the meV and an amplitude of a few tens of μeV . These excitons are not at first glance preferentially coupled with FX through optical phonons.

5.1.3 Influence of the environment on the oscillation parameters

We have found in Sect. 5.1.1 that both lines of an excitonic doublet oscillate in phase. Here, we demonstrate that this synchronicity extends to excitons bound to distinct Te_2 molecules in the same detection volume ($\sim 0.92 \mu\text{m}^3$). Fig. 4.12 (a) presents the NR emission spectra of two distinct excitons, X_1 and X_2 , for circularly (σ^+) and linearly (π_y) polarized above-gap excitations. Both doublets can be seen, with distinct FSS of respectively 402 and 362 μeV . Also, their polarization behavior indicates that X_1 is bound to an out-of-plane molecule (with its Y_1 transition polarized along the x' lab axis, I here recall my convention of naming Y the highest-energy transition) and X_2 to an in-plane one.

Fig. 5.6 (b) illustrates that both X_1 and X_2 E_{em} oscillate synchronously with similar amplitudes, having indeed respectively a T_{ex} of (1.353 ± 0.005) and (1.344 ± 0.008) meV and an A_{em} of (32 ± 3) and (31 ± 4) μeV . Both parameters overlap within their uncertainty. In panel (c), their separation energy does not show a clear oscillatory behavior, another sign of their synchronicity. Also, the orientation of the molecules with respect to the excitation polarization, here linear along the x' laboratory axis ($\pi_{x'}$) and corresponding to the [010] sample axis, does not impact the oscillation.

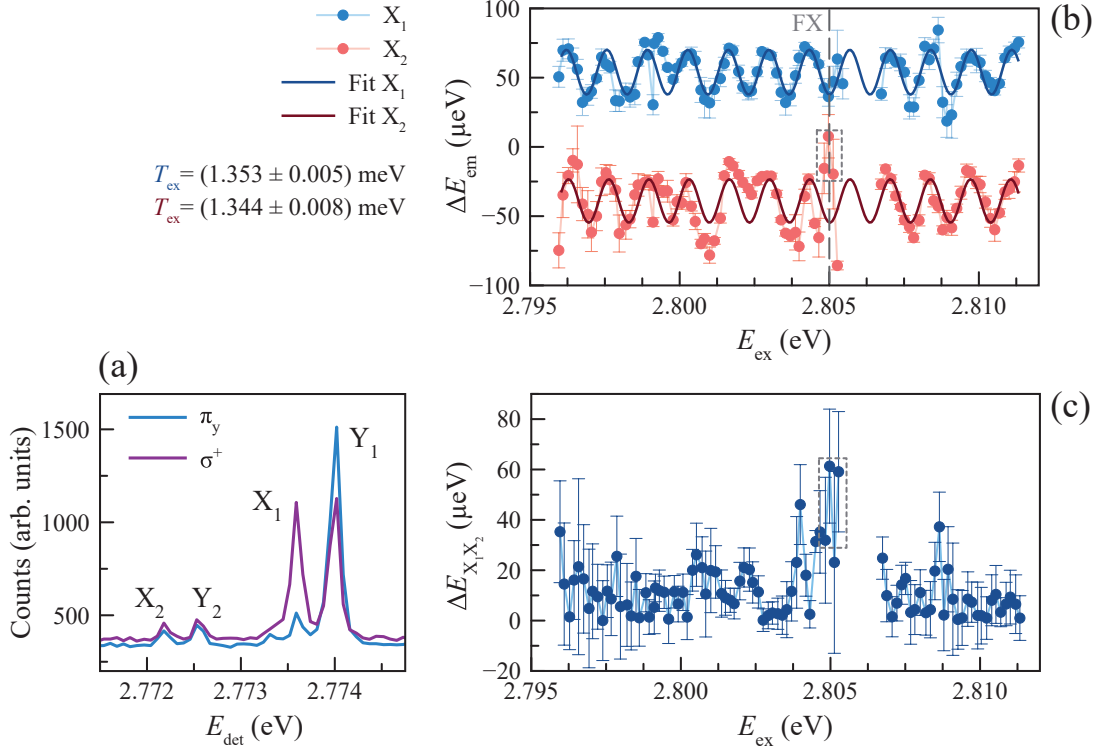


Figure 5.6 E_{em} oscillation of two excitons in the same detection volume. (a) NR PL spectra for the two excitons, for two excitation polarizations (σ^+ and π_y). (b) E_{em} of the X transitions of both excitons, presenting a synchronous oscillation. (c) Energy separation between the two X transitions ($\Delta E_{X_1X_2}$), showing no clear oscillatory signature and thus illustrating that the two peaks move parallel to one another with similar amplitudes. The dotted boxes in (b) and (c) indicate points where an intense and large structure complicated the fit of X_2 .

Additionally, the FFT of the oscillation leads to very similar dominant frequencies for both X_1 and X_2 , as shown on Fig. 5.7. However, the confidence of the fits for X_2 is weaker for certain data points where the peak had smaller intensity or was in the vicinity of other intense and wide transitions that suddenly appeared near the FX resonant energy, especially in the dotted boxes indicated on panels (a) and (b). The passage of the LO Raman peak also prevented the fits for excitation energies between 2.8050 and 2.8064 eV. This explains why its FFT contains more frequencies than that of X_1 .

The fact that distinct emitters share the same oscillation characteristics points out that the cause of the phenomenon does not involve the immediate environment of the emitter, as it is the case for spectral diffusion. It instead results from a much more spatially extended effect,

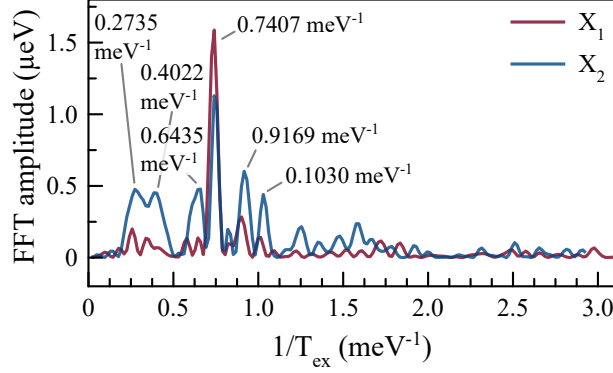


Figure 5.7 FFTs of the X_1 and X_2 E_{em} oscillation presented in Fig. 5.6. Both have their maximum intensity at the same frequency. X_2 contains additional non-negligible frequencies, as its oscillation data is noisier.

a mesoscopic field on a scale similar to the measurement probe (diameter of $\sim 0.76 \mu\text{m}$). However, this field varies from one region to the other. The data in Fig. 5.8 demonstrates that excitons from different areas of the sample (i.e. in different detection volumes) exhibit different average oscillation periods, respectively (1.353 ± 0.005) , (1.188 ± 0.007) and (1.43 ± 0.03) meV. This suggests that sample characteristics have an impact on T_{ex} , but that they vary over distances larger than a detection volume.

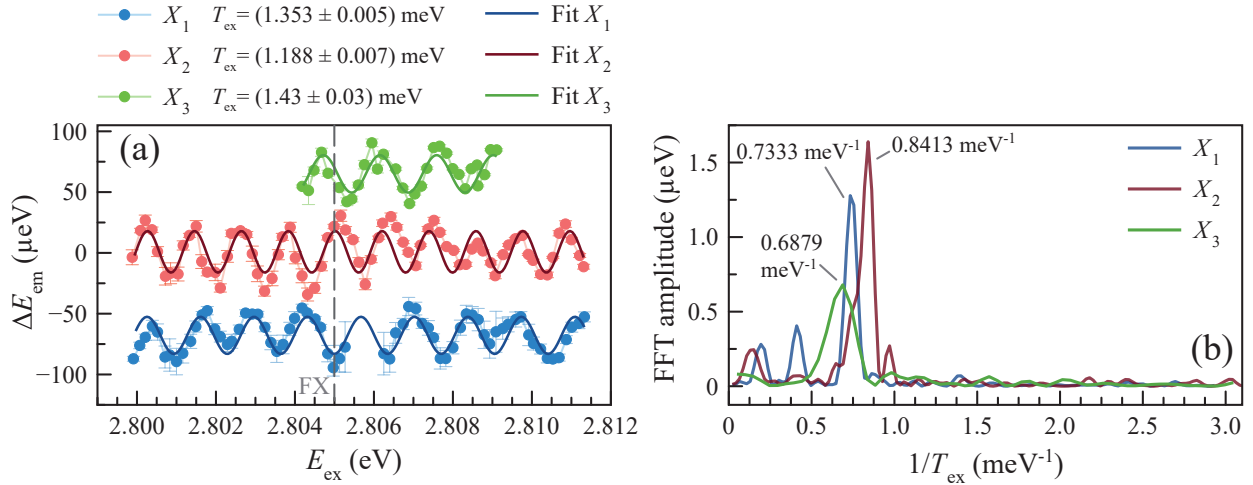


Figure 5.8 (a) E_{em} oscillation of three excitons located in three different regions of the sample. (b) FFTs of the curves in (a), showing different dominant frequencies for each exciton. X_3 shows a broader peak, most likely due to the small number of periods in the data. X_1 is the same as Exciton A in Fig. 5.2.

5.1.4 Absence of interplay between absorption and the oscillation

T_{ex} and A_{em} are relatively constant over the scanned range, regardless of the absorption and exciton transfer efficiency displayed in the PLE spectra, as can be seen on Fig. 5.9. The top panels present the PLE intensity as a function of E_{ex} , which is maximum around the FX energy. In (a), the curve takes the form of a plateau centered at 2.805 289 eV with a width of 2.9 meV, a more occasional but not extraordinary behavior. In (b), one sees the typical curve with a maximum at 2.805 784 eV and a secondary maximum at 2.802 391 eV most likely attributed to D_0X . Emission is seen over the whole investigated E_{ex} range.

A comparison of top and bottom panels shows that while there is a factor of (a) ~ 8 and (b) ~ 12 between the PLE baseline and the highest intensity data point in the PLE curves, T_{ex} and A_{em} show little variation. This suggests that the cause of the oscillation is not a direct interaction between FX and the bound excitons, as one would then expect A_{em} to be proportional to the FX density and to follow the same trend as the PLE curve, reaching its minima and maxima jointly with absorption.

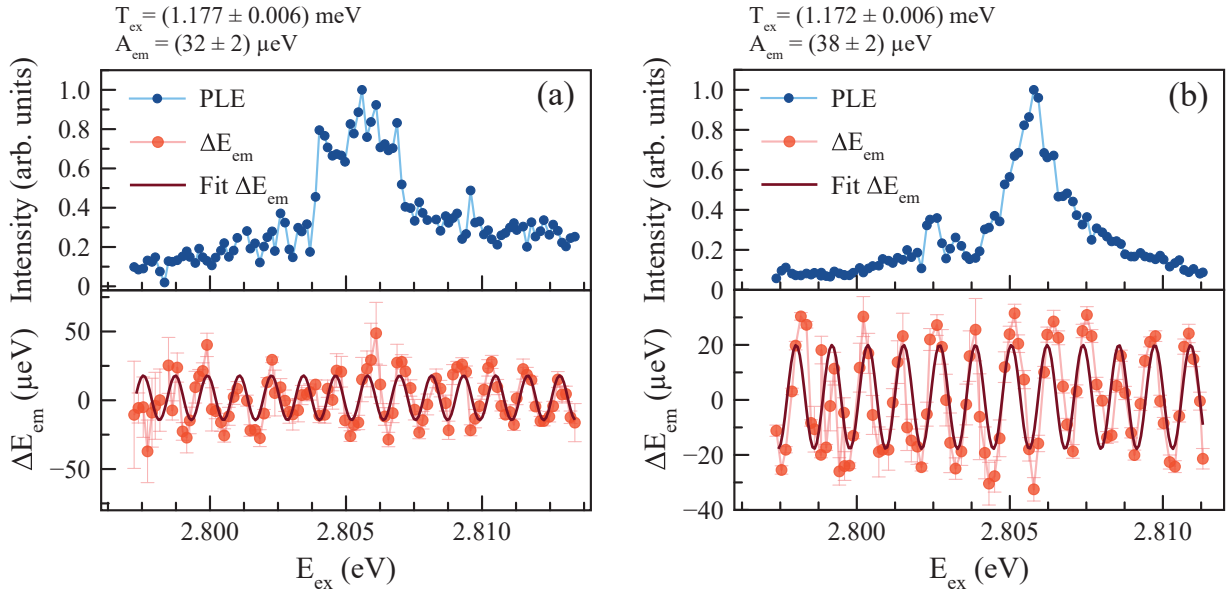


Figure 5.9 PLE intensity (top panels) and E_{em} (bottom panels) of two excitons (a,b) in different detection volumes. The data does not suggest any correlation between the absorption efficiency and the amplitude or period of the oscillations.

Moreover, one could expect variations in E_{em} following the PLE curve, since the creation of a larger number of FX leads in principle to an increase of charge concentration around the

studied emitter, which in turn perturbs its E_{em} . However, no clear trend could be established in that sense. For example, in Fig. 5.9 (a), A_{em} seems to locally increase around 2.806 107 eV, but does not do so at the two maxima on both sides, which are also situated in the maximum PLE plateau. Furthermore, a similar slight increase is seen around 2.799 891 eV, with no correspondence on the PLE curve which is in its minimal portion. In panel (b), there might be a slight decrease in A_{em} after the PLE maximum, but the effect is very faint and absent on the other side of the extremum. Therefore, no link between A_{em} and the PLE intensity could be established. Absorption and transfer efficiencies from FX to bound excitons do not seem to play a significant role in the occurrence of the E_{em} oscillation.

5.1.5 Impact of excitation parameters

Excitation parameters had no impact on the observation of the E_{em} oscillation. Indeed, the polarization of the excitation laser, the starting energy and the direction of the scan did not influence A_{em} nor T_{ex} .

Excitation polarization

Among the 12 oscillating excitons, some were excited with linear (π_x or π_y) and circular (σ^+) polarization without any difference in the oscillation behavior being noted. For example, in Fig. 5.2, Excitons A and B were respectively measured with π_y and σ^+ polarization and presented comparable T_{ex} and A_{em} for their X transition, respectively (1.353 ± 0.005) meV and (32 ± 3) μeV , and (1.287 ± 0.009) meV and (34 ± 4) μeV . One thus gets similar oscillation signatures regardless of the helicity of the excitation polarization and of the intensity of its component oriented along the detected transition.

Additionally, these measurements were performed in crossed polarization in the linear case (i.e. the detection polarization was perpendicular to that of the excitation), for laser rejection purposes. The oscillation therefore does not need the excitation polarization to be parallel to that of the detected transition to occur. In light of these observations, one can say that polarization has no impact on the oscillation phenomenon.

Starting energy and direction of the scan

The direction of the scan (from high to low E_{ex} or vice versa) and the starting energy also did not influence the observation of the oscillation behavior. Indeed, the PLE curves of some excitons were obtained with a starting E_{ex} above the FX resonance and going towards lower energies as Exciton B in Fig. 5.2 and X_3 in Fig. 5.8. Others had a starting E_{ex} below the FX going towards higher energies, as Exciton A in Fig. 5.2 and X_2 in Fig. 5.8. The oscillation behavior was very similar regardless of the direction of the scan. This points towards an absence of hysteresis or of a memory effect in the system and that the occurrence of the oscillation is not linked for example to the charging of specific defects in a certain sequence.

5.1.6 Effect of E_{ex} on the emission-line FWHM

Although the excitonic emission FWHM could be expected to be affected by a change of E_{ex} , it does not present a clear behavior and is therefore not a key ingredient in developing a model for the E_{em} oscillation. Fig. 5.10 shows the FWHM data for the exciton in Fig. 5.2 (a), along with its FFT. No oscillatory behavior or non-zero frequency stand out of the graphs. Specifically, in panel (b), the dominant frequency is very close to 0 Hz for both X and Y , meaning that they present a mostly constant behavior. Y shows off a lot of additional frequencies as it is very “noisy”, but no trend can be extracted. The change of FWHM, if any, is clearly smaller than what the resolution of our system allows to detect, and the data conveys no information on the oscillation mechanism at play.

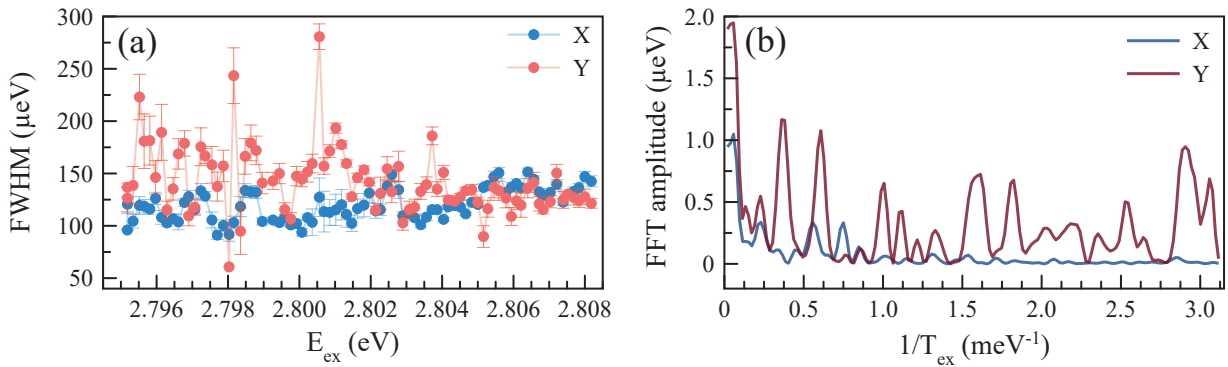


Figure 5.10 (a) FWHM of the exciton in Fig. 5.2 (a) as a function of E_{ex} . No clear oscillation behavior is observed. (b) FFT of the data in (a). The dominant frequency is very close to 0 Hz, showing that the FWHM is mainly constant.

5.1.7 Conclusion on the experimental observation of an E_{em} modulation during PLE

PLE measurements have shown that a remote E_{ex} scan over the FX band has a direct impact on the E_{em} of Te_2 -bound excitons in ZnSe. The characteristics of the effect are summarized as follows:

1. E_{em} oscillates as a function of E_{ex} for a majority of studied emitters (60 %), with an average T_{ex} of 1.103 meV and A_{em} of 44 μeV .
2. For a single exciton, both X and Y transitions typically have the same oscillation parameters and are synchronized with one another.
3. Distinct emitters in the same detection volume also oscillate synchronously with similar parameters, regardless of their orientation with respect to the excitation polarization.
4. Both T_{ex} and A_{em} are uncorrelated to the absorption and transfer efficiency in the FX band.
5. Orientation and helicity of the excitation polarization play no role in the oscillation.
6. The starting point and direction of the PLE scan also have no impact on the oscillation behavior.
7. The emission FWHM could in principle be affected, but the available resolution of our detection system was not sufficient to observe any significant variation.

These key observations point towards a polarization-independent mechanism acting on a mesoscopic scale and influenced by sample characteristics varying over dimensions greater than a detection volume. No hysteresis or charging sequence of nearby defects seem to be involved. The development of a model combining a majority of the enumerated characteristics is attempted in the following section.

5.2 Interaction mechanisms possibly responsible for the E_{em} oscillation

In this section, I attempt at explaining the oscillatory behavior of the emission energy (E_{em}) of a Te_2 -bound exciton as a function of the excitation energy (E_{ex}) in the FX energy range. The main goal is to find a mechanism that could lead among other characteristics to a period T_{ex} of 1.103 meV and an amplitude A_{em} of 44 μeV . For that purpose, I divide the argument

in four topics, all of which may generate the oscillation. First, I look at optical interference, with and without a resonance in the dielectric function of ZnSe, and interactions of bound excitons with free exciton-polaritons. Second, I survey the possibility of a varying magnetic field causing Zeeman and diamagnetic shifts of the bound-exciton emission lines. Third, I explore phonon-assisted coupling of the bound excitons with exciton-polaritons. Finally, I consider the splitting of the bound-exciton energy levels into nearly degenerate doublets.

Each of these mechanisms are detailed, evaluated on their likelihood in our system of interest and compared with experimental data if relevant. At the end of the discussion, I make a recommendation on the most satisfying explanation.

5.2.1 Interaction with free exciton-polaritons

The first phenomenon considered to explain the E_{em} oscillation is an interaction between the Te_2 -bound exciton and free exciton-polaritons in the ZnSe host. Indeed, at energies near an excitonic resonance in a material, light propagates in the form of hybrid electromagnetic field-exciton quasi-particles named exciton-polaritons, as described in Sect. 2.3. Such a formalism consequently appears appropriate to describe an excitation of the ZnSe FX band.

The distribution of the polaritonic electric field is determined by the sample structure, a ZnSe layer on a GaAs substrate with a partial Te monolayer at its center (Fig. 3.1). When a particular energy verifies the interference condition, the associated electric field creates a standing wave across the ZnSe-layer thickness (z direction), as in Fig. 5.11. The amplitude of the field varies between two extremes: waves presenting an anti-node at the center, where the Te_2 molecules sit, and those presenting a node.

The distribution of the field also dictates the shape of the polariton wavefunction and, in the case of an ensemble, the local polariton density. The quasi-particle can interact with the bound exciton through either the photonic or excitonic part of its wavefunction, causing a shift of the bound exciton emission line through an AC or DC Stark effect, or exciton-exciton interactions.

In this section, I demonstrate that optical interference induces a periodic variation of the field intensity at the emitter position with a monotonic E_{ex} sweep. Then, I show that the

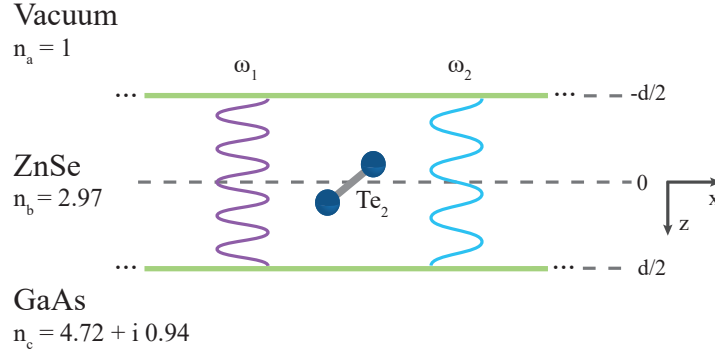


Figure 5.11 Stationary waves created along the z axis of the sample, formed of a ZnSe layer on a GaAs substrate with Te_2 molecules at its center. Two different waves respecting the interference condition are represented. ω_1 presents an anti-node at the position of the Te_2 molecules, maximizing the electric field and the local density of free exciton-polaritons. ω_2 presents a node and thus an electric-field and polariton-density minimum.

addition of an excitonic resonance in the ZnSe dielectric function and the inclusion of exciton-polaritons in the formalism describing the field distribution in a layered structure allows for reducing the oscillation period (T_{ex}) to match closely our observations. Finally, I discuss the mechanisms by which polaritons could interact with the bound exciton to influence its E_{em} .

Dependence of the stationary laser field distribution in the ZnSe layer on E_{ex}

Sample A, a 80-nm thick ZnSe layer on GaAs (Fig. 3.1(c)), can be modelled by a low-quality factor Fabry-Perot resonator, in which the electric field from the excitation laser interferes and forms a stationary wave in the z confinement direction, perpendicular to the surface. In this picture, the two interfaces forming the cavity, vacuum-ZnSe and ZnSe-GaAs, are described by Fresnel reflective coefficients at normal incidence given by [184]:

$$r = \frac{\tilde{n}_t - \tilde{n}_i}{\tilde{n}_t + \tilde{n}_i} \quad (5.1)$$

where \tilde{n}_t and \tilde{n}_i are the complex refractive indices of the media containing the incident and transmitted beams. With $\tilde{n}_i = 1$ (vacuum) and $\tilde{n}_t = 2.97$ (ZnSe [185]) for the first interface, absorption being negligible in both materials, and $\tilde{n}_i = 2.97$ and $\tilde{n}_t = 4.72 + i 0.94$ (GaAs [186]) for the second interface, one obtains reflection coefficients r_1 and r_2 respectively of 0.50 and $0.24 + i 0.09$ at 450 nm.

The finesse of a cavity is defined as [187]:

$$\mathcal{F} = \frac{\pi\sqrt{|r_1 r_2|}}{1 - |r_1 r_2|}. \quad (5.2)$$

It represents the ratio of the separation of two adjacent maxima in the transmission function (i.e. the free spectral range) to the half width at half maximum (HWHM) of one of those maxima. This leads to a quite low finesse of 1.29 for the cavity formed by our sample. Consequently, our sample is unsurprisingly far from being a selective etalon.

As one scans the incident laser energy, the period of the standing wave inside the cavity changes and its nodes and anti-nodes are displaced along the z axis. Using the expression for the phase ϕ in a Fabry-Perot interferometer, the condition for having a node at a defined depth z in the cavity for two successive laser wavelengths λ_1 and λ_2 at normal incidence is:

$$|\phi_2 - \phi_1| = 2\pi n d \left| \frac{1}{\lambda_2} - \frac{1}{\lambda_1} \right| = 2\pi, \quad (5.3)$$

where $n = \text{Re}(\tilde{n})$ and d is the distance between the two reflecting surfaces of the interferometer. With the refractive index of ZnSe and the E_{ex} of two consecutive experimental maxima in the E_{em} of an exciton (for example, in Fig. 4.9 (a), 2.801780 and 2.802920 eV), one obtains $d = 366 \mu\text{m}$. This result is several orders of magnitude greater than the ZnSe-layer thickness in our sample (80 nm).

Additionally, the GaAs substrate does not support interference at excitation wavelengths around 450 nm. Indeed, the attenuation coefficient α [188]:

$$\alpha = \frac{4\pi}{\lambda_0} \kappa, \quad (5.4)$$

where λ_0 is the wavelength in vacuum and $\kappa = \text{Im}(\tilde{n})$, allows to calculate the penetration depth d_p of the electric field, where its intensity is reduced by a factor e . With $\alpha = 0.0262 \text{ nm}^{-1}$ for GaAs at 450 nm, one obtains $d_p = 38.1 \text{ nm}$, which is several orders of magnitude smaller than the wafer thickness ($\sim 350 \mu\text{m}$). Hence, the wave is strictly evanescent and does not reach the GaAs-vacuum interface. The substrate can therefore be considered as semi-infinite.

To summarize, since the ZnSe thickness of Sample A is too small and the wave is strictly

evanescent in the GaAs substrate, optical interference with a small refractive index cannot account for our oscillation observations. However, in the vicinity of an excitonic resonance, the refractive index is enhanced and the thickness required to obtain a T_{ex} similar to the experiment is significantly reduced, as demonstrated below.

Stationary field generated by free exciton-polaritons

The resonance in the ZnSe dielectric function at the FX energy calls for the use of Eq. 2.12 as the expression for the dielectric function and of the polariton equation 2.13 to describe the propagation of light modes in the sample. Indeed, the literature demonstrates that polaritonic effects are relatively easily observed in the reflectance spectrum of ZnSe due to its large exciton binding energy and oscillator strength, as discussed in Sect. 2.3.4. Polaritons are hence likely to play a part in the optical properties of our sample.

Fig. 5.12 shows the lower (LPB) and upper (UPB) polariton-branch solutions of Eq. 2.13, using the ZnSe parameters listed in Table 5.1, which are inspired from our experimental results and Ref. [162]. The curves lead to a longitudinal-transverse splitting (Δ_{LT}) of 1.26 meV and an energy of the longitudinal exciton (ω_L) of 2.806 262 eV. This result was employed to the calculation of the electric-field distribution associated with exciton-polaritons in a ZnSe layer, using the dispersion relation and a transfer-matrix formalism [189] detailed below. The use of the bulk dispersion relation is a reasonable simplification, since the confinement in the cavity is not very strong.

Table 5.1 Parameters for the calculation of the polaritonic dispersion relation in bulk ZnSe. The exciton effective mass M is given as a function of the electron rest mass m_0 . “Exp” in the reference column means the parameter value has been taken from our experimental data.

Parameter	Symbol	Value	Reference
FX energy	ω_0	2.805 eV	Exp
Oscillator strength	$4\pi\beta$	8×10^{-3}	[162]
Exciton effective mass	M	$0.89m_0$	[162]
Damping rate	Γ	1×10^{-4} eV	[162]
High-frequency dielectric constant	ϵ_∞	8.1 ¹	[190]

¹This is in fact ϵ_b , the static dielectric constant, as I could not find a value for ϵ_∞ at the time of the simulation. The latter has instead a value of 5.8 [99]. This should not change the overall behavior of the dispersion relation.

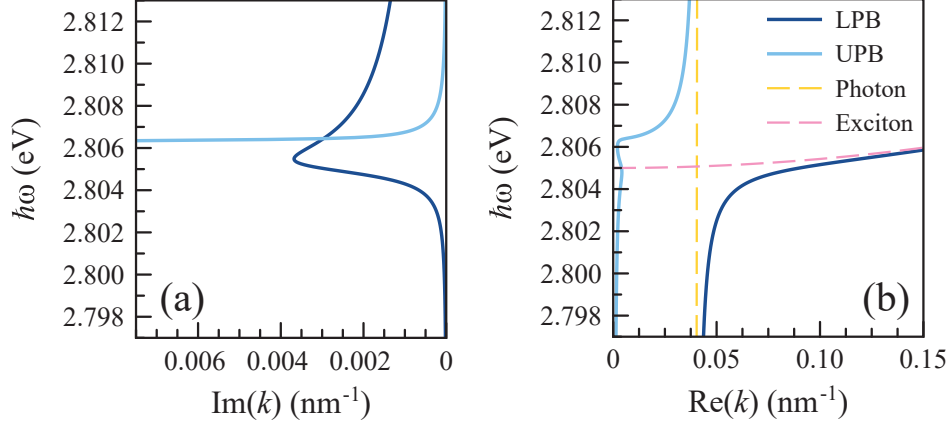


Figure 5.12 Dispersion relation of free exciton-polaritons in bulk ZnSe, formed of the lower (LPB) and upper (UPB) polaritonic branches, displayed as a function of the imaginary (a) and real (b) parts of the wavevector k . Photon and exciton dispersion relations are superimposed in (b) to show their anti-crossing. The FX energy is fixed at the experimental value of 2.805 eV. The values of all parameters are listed in Table 5.1.

Fig. 5.13 illustrates the interfaces between vacuum (medium a), ZnSe (medium b) and GaAs (medium c), the different electric fields at play and the axes definition. At normal incidence, assuming without loss of generality that all electric fields are polarized along x , one can describe the total electric and magnetic fields (E , H) at both interfaces (I , II) by a sum of incident (i), reflected (r) or transmitted (t) fields. In the ZnSe layer, there are four fields at each interface, two per polariton branch or propagation mode. The GaAs layer is considered as semi-infinite. Due to the continuity of the tangential electric-field components at an interface, we have:

$$\begin{aligned} E_I &= E_{i,I} + E_{r,I} = E_{t,I}^l + E_{r',II}^l + E_{t,I}^u + E_{r',II}^u \\ E_{II} &= E_{i,II}^l + E_{r,II}^l + E_{i,II}^u + E_{r,II}^u = E_{t,II}, \end{aligned} \quad (5.5)$$

and

$$\begin{aligned} H_I &= \sqrt{\frac{\epsilon_0}{\mu_0}} n_a (E_{i,I} - E_{r,I}) = \sqrt{\frac{\epsilon_0}{\mu_0}} n_b^l (E_{t,I}^l - E_{r',II}^l) + \sqrt{\frac{\epsilon_0}{\mu_0}} n_b^u (E_{t,I}^u - E_{r',II}^u) \\ H_{II} &= \sqrt{\frac{\epsilon_0}{\mu_0}} n_b^l (E_{i,II}^l - E_{r,II}^l) + \sqrt{\frac{\epsilon_0}{\mu_0}} n_b^u (E_{i,II}^u - E_{r,II}^u) = \sqrt{\frac{\epsilon_0}{\mu_0}} n_c E_{t,II}, \end{aligned} \quad (5.6)$$

as $\mathbf{H} = \sqrt{\frac{\epsilon_0}{\mu_0}} n_j \hat{\mathbf{k}} \times \mathbf{E}$ in a non-magnetic medium at normal incidence for a transverse electromagnetic (TEM) wave. ϵ_0 and μ_0 are respectively the permittivity and the permeability of vacuum, n_j is the refractive index ($i, j = a, b, c$) and $\hat{\mathbf{k}}$ is the unit propagation vector. Note

that H is exclusively polarized along y . In Eqs. 5.5 and 5.6, the r' subscript designates a wave that was reflected at another interface and propagated to the interface of interest. The superscript l or u describing the fields in the ZnSe layer correspond respectively to the LPB and UPB, which experience different complex refractive indices. The latter are defined as:

$$n_b^\alpha = \sqrt{\frac{c^2 k_\alpha^2}{\omega^2} - \epsilon_0} \quad (5.7)$$

from the polariton dispersion relation 2.13, with $\alpha = \{l, u\}$ to simplify the notation.

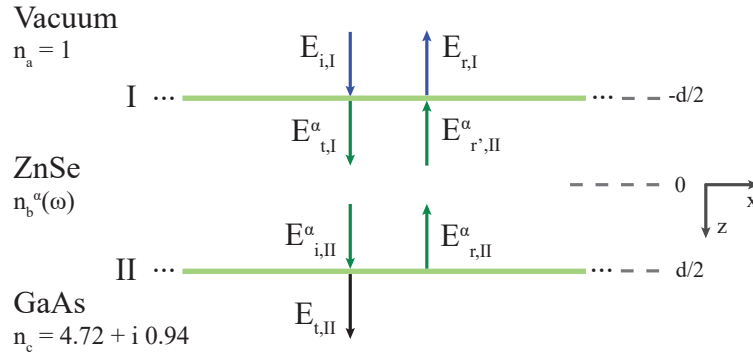


Figure 5.13 Electric fields involved in the derivation of an expression for the reflection and transmission coefficients of a stack formed of a ZnSe layer (medium b) on top of a semi-infinite GaAs substrate (medium c). The subscripts I and II refer to the interface, while i , r , r' and t stand for “incident”, “reflected”, “reflected, then propagated” and “transmitted”. The number of fields represented in the ZnSe layer has been reduced by half to simplify the schematic, through the use of the $\alpha = \{l, u\}$ superscript respectively for LPB and UPB polaritonic modes.

One can further derive a relation between the two total polaritonic fields in ZnSe, E^l and E^u . Let $E^{l,+}$ and $E^{l,-}$ be the amplitude of the LPB electric fields respectively travelling towards z positive and negative, and $E^{u,+}$ and $E^{u,-}$ the same for UPB. With Pekar boundary conditions stating that field polarization P vanishes at both interfaces ($P(\pm d/2) = 0$), with d the thickness of the ZnSe layer:

$$\begin{aligned} P_I &= (n_b^l)^2 \left(E^{l,+} e^{-ik_l \frac{d}{2}} + E^{l,-} e^{ik_l \frac{d}{2}} \right) + (n_b^u)^2 \left(E^{u,+} e^{-ik_u \frac{d}{2}} + E^{u,-} e^{ik_u \frac{d}{2}} \right) = 0 \\ P_{II} &= (n_b^l)^2 \left(E^{l,+} e^{ik_l \frac{d}{2}} + E^{l,-} e^{-ik_l \frac{d}{2}} \right) + (n_b^u)^2 \left(E^{u,+} e^{ik_u \frac{d}{2}} + E^{u,-} e^{-ik_u \frac{d}{2}} \right) = 0. \end{aligned} \quad (5.8)$$

Written in matrix form, this system of equations becomes:

$$\begin{bmatrix} E^{u,+} \\ E^{u,-} \end{bmatrix} = - \underbrace{\left(\frac{n_b^l}{n_b^u} \right)^2 \begin{bmatrix} e^{ik_u \frac{d}{2}} & e^{-ik_u \frac{d}{2}} \\ e^{-ik_u \frac{d}{2}} & e^{ik_u \frac{d}{2}} \end{bmatrix}}_Q^{-1} \begin{bmatrix} e^{ik_l \frac{d}{2}} & e^{-ik_l \frac{d}{2}} \\ e^{-ik_l \frac{d}{2}} & e^{ik_l \frac{d}{2}} \end{bmatrix} \begin{bmatrix} E^{l,+} \\ E^{l,-} \end{bmatrix}. \quad (5.9)$$

The fields in Eq. 5.9 can be linked to those of Eq. 5.5 by observing that $E^{\alpha,+} = E_{t,I}^\alpha e^{ik_\alpha \frac{d}{2}}$ and $E^{\alpha,-} = E_{r,II}^\alpha e^{ik_\alpha \frac{d}{2}}$. Taking into account that some fields in Eqs. 5.5 and 5.6 are related by a phase ($E_{i,II}^\alpha = E_{t,I}^\alpha e^{ik_\alpha d}$, $E_{r,II}^\alpha = E_{r',II}^\alpha e^{-ik_\alpha d}$), we obtain expressions of E_I , H_I , E_{II} and H_{II} as a function of $E^{\alpha,+}$ and $E^{\alpha,-}$:

$$\begin{aligned} \begin{bmatrix} E_I \\ H_I \end{bmatrix} &= \begin{bmatrix} e^{-ik_l \frac{d}{2}} & e^{ik_l \frac{d}{2}} \\ n_b^l \sqrt{\frac{\epsilon_0}{\mu_0}} e^{-ik_l \frac{d}{2}} & -n_b^l \sqrt{\frac{\epsilon_0}{\mu_0}} e^{ik_l \frac{d}{2}} \end{bmatrix} \begin{bmatrix} E^{l,+} \\ E^{l,-} \end{bmatrix} + \begin{bmatrix} e^{-ik_u \frac{d}{2}} & e^{ik_u \frac{d}{2}} \\ n_b^u \sqrt{\frac{\epsilon_0}{\mu_0}} e^{-ik_l \frac{d}{2}} & -n_b^u \sqrt{\frac{\epsilon_0}{\mu_0}} e^{ik_l \frac{d}{2}} \end{bmatrix} \begin{bmatrix} E^{u,+} \\ E^{u,-} \end{bmatrix} \\ \begin{bmatrix} E_{II} \\ H_{II} \end{bmatrix} &= \begin{bmatrix} e^{ik_l \frac{d}{2}} & e^{-ik_l \frac{d}{2}} \\ n_b^l \sqrt{\frac{\epsilon_0}{\mu_0}} e^{ik_l \frac{d}{2}} & -n_b^l \sqrt{\frac{\epsilon_0}{\mu_0}} e^{-ik_l \frac{d}{2}} \end{bmatrix} \begin{bmatrix} E^{l,+} \\ E^{l,-} \end{bmatrix} + \begin{bmatrix} e^{ik_u \frac{d}{2}} & e^{-ik_u \frac{d}{2}} \\ n_b^u \sqrt{\frac{\epsilon_0}{\mu_0}} e^{ik_u \frac{d}{2}} & -n_b^u \sqrt{\frac{\epsilon_0}{\mu_0}} e^{-ik_u \frac{d}{2}} \end{bmatrix} \begin{bmatrix} E^{u,+} \\ E^{u,-} \end{bmatrix}. \end{aligned} \quad (5.10)$$

Using 5.9 and 5.10, the relation between the total fields at both interfaces becomes:

$$\begin{aligned} \begin{bmatrix} E_I \\ H_I \end{bmatrix} &= \left(\begin{bmatrix} e^{-ik_l \frac{d}{2}} & e^{ik_l \frac{d}{2}} \\ n_b^l \sqrt{\frac{\epsilon_0}{\mu_0}} e^{-ik_l \frac{d}{2}} & -n_b^l \sqrt{\frac{\epsilon_0}{\mu_0}} e^{ik_l \frac{d}{2}} \end{bmatrix} + \begin{bmatrix} e^{-ik_u \frac{d}{2}} & e^{ik_u \frac{d}{2}} \\ n_b^u \sqrt{\frac{\epsilon_0}{\mu_0}} e^{-ik_l \frac{d}{2}} & -n_b^u \sqrt{\frac{\epsilon_0}{\mu_0}} e^{ik_l \frac{d}{2}} \end{bmatrix} Q \right) \\ &\quad \left(\begin{bmatrix} e^{ik_l \frac{d}{2}} & e^{-ik_l \frac{d}{2}} \\ n_b^l \sqrt{\frac{\epsilon_0}{\mu_0}} e^{ik_l \frac{d}{2}} & -n_b^l \sqrt{\frac{\epsilon_0}{\mu_0}} e^{-ik_l \frac{d}{2}} \end{bmatrix} + \begin{bmatrix} e^{ik_u \frac{d}{2}} & e^{-ik_u \frac{d}{2}} \\ n_b^u \sqrt{\frac{\epsilon_0}{\mu_0}} e^{ik_l \frac{d}{2}} & -n_b^u \sqrt{\frac{\epsilon_0}{\mu_0}} e^{-ik_l \frac{d}{2}} \end{bmatrix} Q \right)^{-1} \begin{bmatrix} E_{II} \\ H_{II} \end{bmatrix}. \end{aligned} \quad (5.11)$$

The matrix linking E_I, H_I to E_{II}, H_{II} in Eq. 5.11 is designated from now on as M . With the definitions $E_I = E_{i,I} + E_{r,I} = (1 + r)E_{i,I}$, $H_I = n_a \sqrt{\frac{\epsilon_0}{\mu_0}} (1 - r)E_{i,I}$ and $E_{II} = E_{t,II} = tE_{i,I}$, an expression for the layer reflection and transmission coefficients, r and t , is found using its elements M_{ij} ($i, j = 1, 2$):

$$r = \frac{n_a \sqrt{\frac{\epsilon_0}{\mu_0}} \left(M_{11} + n_c \sqrt{\frac{\epsilon_0}{\mu_0}} M_{12} \right) - M_{21} - n_c \sqrt{\frac{\epsilon_0}{\mu_0}} M_{22}}{n_a \sqrt{\frac{\epsilon_0}{\mu_0}} \left(M_{11} + n_c \sqrt{\frac{\epsilon_0}{\mu_0}} M_{12} \right) + M_{21} + n_c \sqrt{\frac{\epsilon_0}{\mu_0}} M_{22}}, \quad (5.12)$$

$$t = \frac{2n_a \sqrt{\frac{\epsilon_0}{\mu_0}}}{n_a \sqrt{\frac{\epsilon_0}{\mu_0}} \left(M_{11} + n_c \sqrt{\frac{\epsilon_0}{\mu_0}} M_{12} \right) + M_{21} + n_c \sqrt{\frac{\epsilon_0}{\mu_0}} M_{22}}. \quad (5.13)$$

It is now possible to evaluate the fields at any depth in the ZnSe layer by fixing a value for $E_{i,I}$ and calculating the matrix elements in Eq. 5.11 for a specific excitation energy. One must use the polariton dispersion relation 2.13 to obtain the wavevectors k and the refractive index n_b^α (with Eq. 5.7) for the relevant polaritonic modes at this energy. Then, r can be computed with Eq. 5.12, which leads in turn to E_I and H_I , and consequently to $E^{\alpha,+}$ and $E^{\alpha,-}$ through Eqs. 5.10 and 5.9. These can be propagated at the desired depth and summed to obtain the value of the total electric field, E_{tot} .

Taking the parameters of Table 5.1, $n_a = 1$ (air) and $n_c = 4.72 + i0.94$ (GaAs), the E_{tot} distribution (in the form of $I = \bar{E}_{\text{tot}} E_{\text{tot}}$) as a function of depth z and photon energy $\hbar\omega$ in our sample was evaluated and is presented in Fig. 5.14 (a). In (b) is shown a cross-section at the center of the ZnSe layer where most of the δ -doped Te_2 molecules are situated. One can clearly see an oscillation that begins around the FX energy (ω_0), in a curve similar to that of a Fabry-Perot etalon. The oscillation happens where LPB displays a parabolic dispersion, and persists over the whole studied energy range above ω_0 . It is however absent in the photon-like linear portion of the dispersion at lower energy. At any depth, the field intensity (color map scale) oscillates as a function of $\hbar\omega$ with an increasing period between two consecutive maxima (from $T_{\text{ex}} = 0.691$ meV between 2.805896 and 2.806587 eV to $T_{\text{ex}} = 1.982$ meV between 2.817695 and 2.819677 eV).

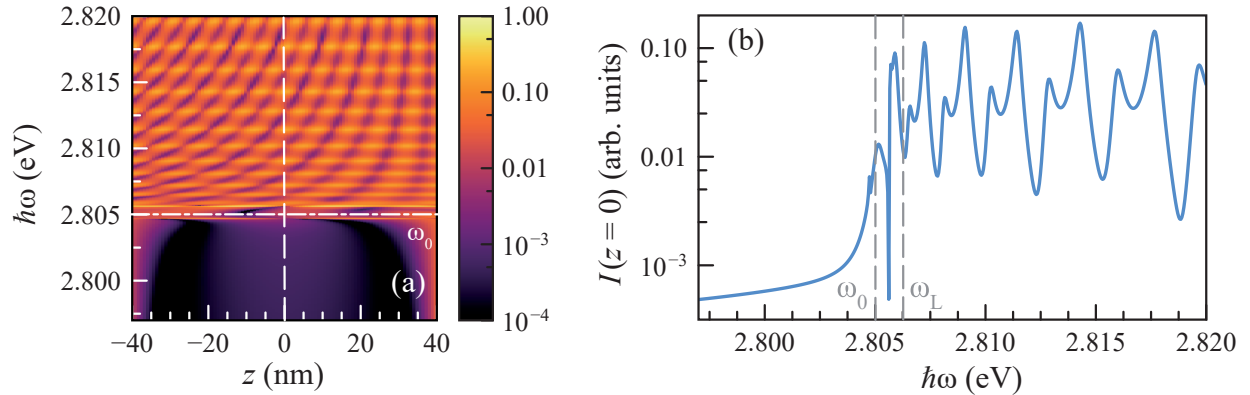


Figure 5.14 Electric-field distribution as a function of incoming photon energy $\hbar\omega$ in a 80-nm ZnSe layer on top of GaAs. (a) Color map presenting the intensity of the field at different depths in the ZnSe layer. (b) Cross-section of the map at $z = 0$ (vertical white dashed line in (a)). The polaritonic resonance at the FX energy ($\omega_0 = 2.805$ eV) marks the beginning of the oscillatory behavior of the field intensity.

In short, the oscillation period of the field intensity due to an interference effect in a thin

layer can be reduced by considering a resonance in the ZnSe dielectric function at the FX energy and using an exciton-polariton treatment of light propagation in the material.

Effect of simulation parameters on the polaritonic dispersion relation and field distribution

Due to the complex nature of the simulation, which involved numerically solving Eq. 2.13 and then computing the electric-field distribution in the ZnSe layer with the matrix formalism detailed above, no fitting of the parameters to the experimental oscillation data was attempted. However, one can discuss the impact of their values on the simulation behavior and estimate the set that best matches the experiment.

My objective for this section is to determine the conditions in which an E_{em} oscillation is observed, more precisely what influences its T_{ex} and over which energy range it occurs. In the following simulations, Γ had a default value of 10^{-5} , as the polariton-equation solver worked better for that case. The rest of the parameters are the same as in Table 5.1, unless specified. The obtained results give a good idea on how the parameters influence the electric-field distribution in the ZnSe layer.

Excitonic mass Fig. 5.15 (a) and (b) present the real and imaginary parts of the polariton dispersion relation for three excitonic masses $M = 0.89 m_0$, $2M$ and $4M$. In panel (a), this parameter influences the curvature of the parabolic portion of LPB, while leaving UPB mostly unchanged. The LPB curvature indeed decreases with an increase of M , tending to a straight horizontal line as $M \rightarrow \infty$. The latter case completely removes the oscillatory behavior of the electric field distribution (not shown), establishing the exciton dispersion as a necessary condition for its occurrence. The k values in the imaginary part of LPB also increase with M around ω_0 , as shown in panel (b).

Keeping this in mind, panel (c) presents the electric-field intensity at the center of the ZnSe layer as a function of the laser excitation energy ω for the three masses. The starting energy of the oscillation starts is the same for all three simulations and the amplitude of the electric field variation is similar on all three curves. T_{ex} , while increasing with ω for a particular M , reduces as M increases, showing that the LPB curvature plays a role in defining its value. For example, the energy difference between two adjacent intensity maxima around 2.810 eV is

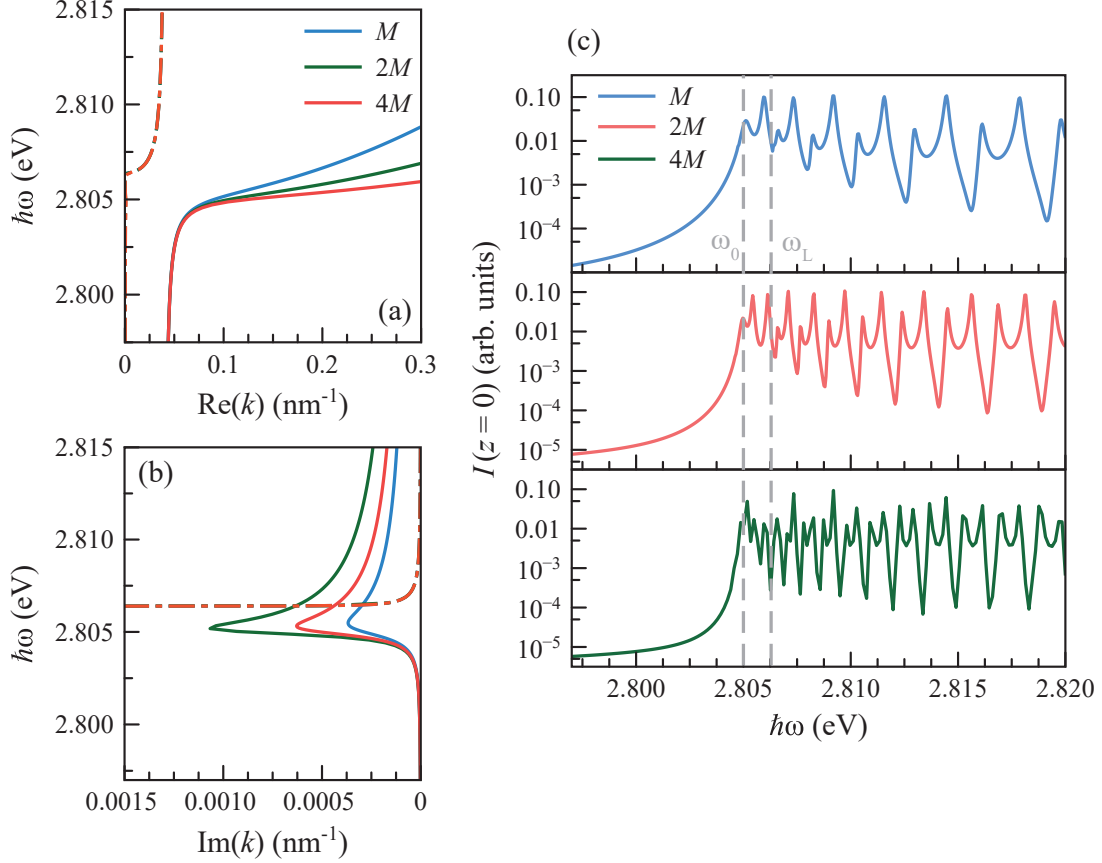


Figure 5.15 Impact of the excitonic mass M on the polariton electric field distribution at the center of the ZnSe layer. Real (a) and imaginary (b) parts of the polaritonic dispersion relation of bulk ZnSe for masses of M , $2M$ and $4M$, with $M = 0.89 m_0$. The curvature of the exciton-like real part of LPB (continuous line) is reduced as M increases. The imaginary part of LPB increases with M , while UPB (dash-dotted line) is unchanged. (c) Electric-field intensity as a function of ω . The oscillation period diminishes as M increases. The $4M$ curve has lower resolution due to the performance of the polariton-equation solver.

respectively 1.153, 0.830 and 0.617 meV for M , $2M$ and $4M$. Around 2.818 eV, these values become 1.982, 1.383 and 0.926 meV. Looking at these results, $M = 0.89 m_0$ seems to be reasonable as it gives, on its whole occurrence range, a T_{ex} that is similar to the experimental values (0.672–1.607 meV) and to the average value of 1.103 meV. $2M$ would have also been a sensible choice, but M was kept since the polariton-equation solver performed better for this case.

Oscillator strength The oscillator strength $4\pi\beta$ acts upon the longitudinal-transverse splitting (Δ_{LT}) by pushing ω_L towards higher energy as it increases. From $4\pi\beta = 8 \times 10^{-3}$

to $16\pi\beta = 32 \times 10^{-3}$, ω_L , originally at 2.806 262 eV, increases by 4.243 meV to reach the value of 2.810 505 eV (Fig. 5.16 (a)). An increasing $4\pi\beta$ also diminishes the steepness of the LPB bottleneck (i.e. its transition section between photonic and excitonic dispersion) and the LPB maximum imaginary k component at the resonant energy ω_0 .

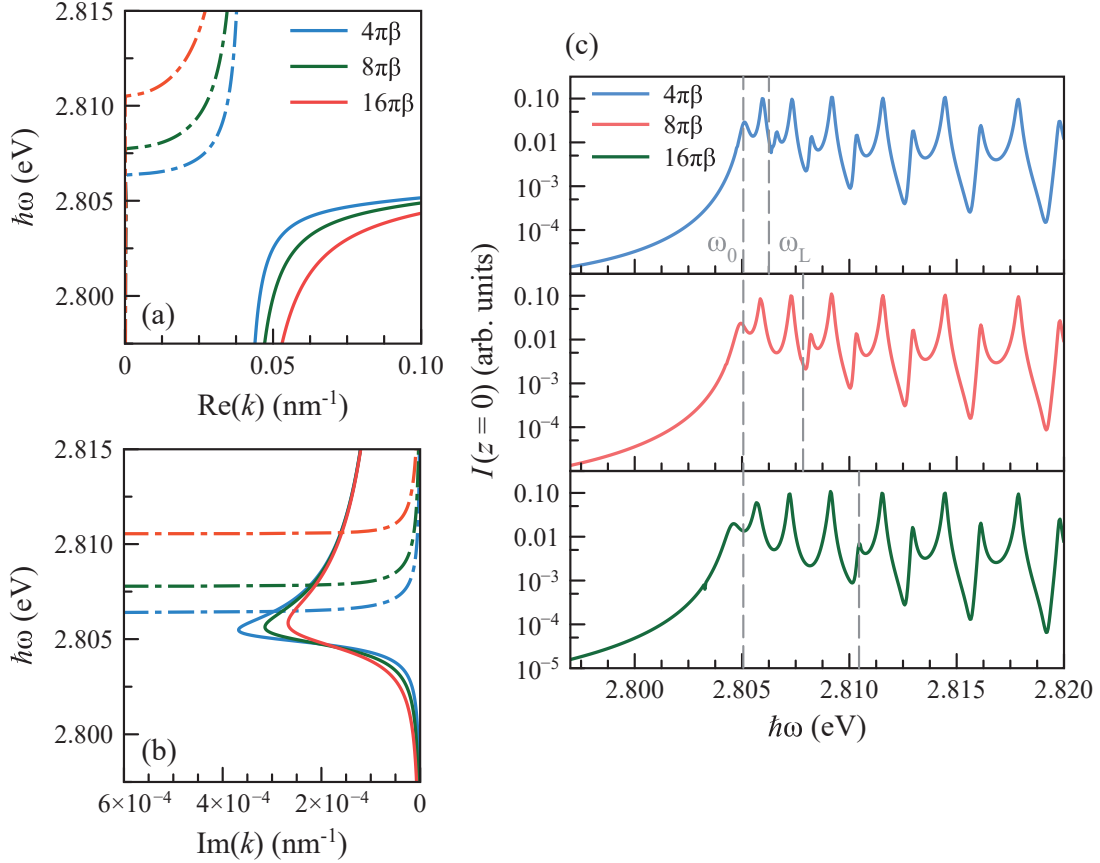


Figure 5.16 Impact of the oscillator strength $4\pi\beta$ on the electric-field distribution at the center of the ZnSe layer. Real (a) and (b) parts of the polaritonic dispersion relation of bulk ZnSe for $4\pi\beta$, $8\pi\beta$ and $16\pi\beta$, with $4\pi\beta = 8 \times 10^{-3}$. ω_L is pushed at higher ω , and the steepness of the LPB (continuous line) bottleneck and the imaginary part of LPB are reduced as $4\pi\beta$ increases. (c) Electric-field intensity as a function of ω . The contribution of UPB (dash-dotted line on panels (a) and (b)) to the interference pattern occurs at higher ω as $4\pi\beta$ increases.

The displacement of ω_L with increasing $4\pi\beta$ causes real UPB k values to have an impact on the shape of the electric-field intensity curve at higher energy, as seen on Fig. 5.16 (c). On a single curve, the periodic pattern indeed changes from a single resonance below ω_L (the result of LPB), to a double peak above ω_L once UPB starts to contribute noticeably. Once the contribution of UPB is established, no significant difference in T_{ex} is observed between

the different $4\pi\beta$ values.

The change of pattern at larger $4\pi\beta$ leads to a more constant-looking maximum-to-maximum T_{ex} . At $16\pi\beta$, it starts at 1.567 meV for an ω value of 2.805 665 eV, decreases to 1.095 meV around $\omega = 2.810\,470$ eV and finishes at 1.982 meV for $\omega = 2.817\,880$ eV. It remains at all times greater than 1 meV and is therefore much more stable than in the lower- $4\pi\beta$ curves and closer to the experimental behavior. For this reason, this value is kept for further comparison with the data.

Damping rate The damping rate Γ gives rise to the imaginary part of the dielectric function ϵ_i and determines the width of the resonance in the absorption curve. As it increases, it adds in the real dispersion relation UPB solutions of larger k below ω_L and increases the absorption width and amplitude of LPB near the resonance (Fig. 5.17 (a) and (b)).

In panel (c), Γ takes the values of 10^{-5} , 10^{-4} and 10^{-3} eV. As it increases, it moves the maxima at lower energy and reduces their sharpness. T_{ex} only undergoes a minor change: for example, at ~ 2.810 eV it diminishes slightly from 1.153 to 1.080 meV. Since the parameter does not impact too much T_{ex} , physical arguments were used to select its value. 10^{-3} eV was rejected as it leads to an electric-field distribution showing I values greater than 1 at specific energies, a probable simulation artifact since we do not expect the medium to present gain. 10^{-4} eV was chosen as it is closer to the expected FX FWHM, while also corresponding to one of its reported values in the literature [162].

In light of this analysis, the parameter with the most impact on T_{ex} is M and is chosen as $0.89 m_0$ to reproduce the shape of the experimental data. A larger oscillator strength (32×10^{-3}) leads to a more constant apparent T_{ex} , closer to the sought experimental behavior, due to the later appearance of the UPB contribution to the interference pattern which create a second resonance. Γ has little impact on T_{ex} and its literature value of 10^{-4} eV is therefore considered suitable. None of the parameters could however generate oscillations below ω_0 .

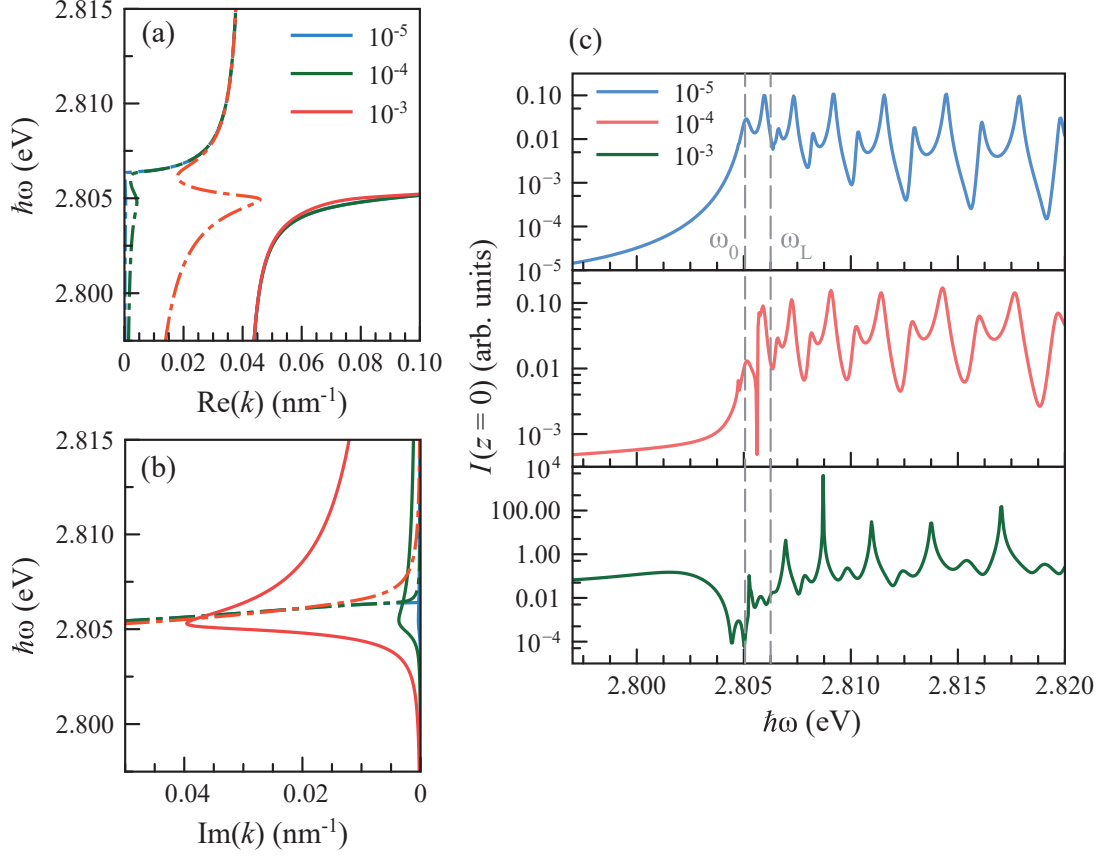


Figure 5.17 Impact of the damping parameter Γ on the electric-field distribution at the center of the ZnSe layer. Real (a) and imaginary (b) parts of the polaritonic dispersion relation of bulk ZnSe for a Γ of 10^{-5} , 10^{-4} and 10^{-3} eV. UPB (dash-dotted line) gains real solutions at higher k for greater Γ and LPB (continuous line) has a larger absorption near ω_0 . (c) Electric-field intensity as a function of ω . The period is minimally affected, while maxima are displaced towards low energy and become less sharp. The 10^{-3} -eV curve gives an intensity above 1 for certain ω values, which is most probably a simulation artifact.

Comparison with experimental data

Taking values from the literature for M ($0.89 m_0$) and Γ (10^{-4} eV), an experimental value for ω_0 (2.805 eV) and a larger $4\pi\beta$ (32×10^{-3}) to account for a more constant-looking T_{ex} , we obtained an electric-field distribution bearing most of the characteristics of the E_{em} oscillation of a Te_2 -bound exciton. Fig. 5.18 presents experimental data side by side with the simulation. The fitted T_{ex} of the data is (1.172 ± 0.006) meV and stays nearly constant over the whole PLE scan range (2.797370–2.811 310 eV). T_{ex} in the simulation, for its part, ranges from 0.784 to 1.934 meV, with an average value of 1.362 meV. The rather low minimum value comes from a sudden phase shift at $\sim 2.808\,293$ eV, which seems to be a consequence of Γ .

Although the general trend of T_{ex} is to increase with ω and that it becomes slightly too high at large ω , it is still comparable to the experimental value and could be fine-tuned by adjusting M and $4\pi\beta$.

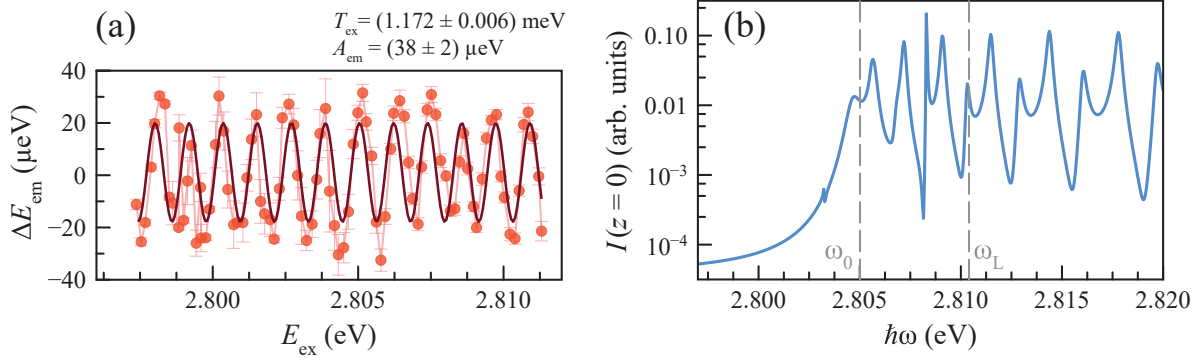


Figure 5.18 Comparison between the E_{ex} oscillation data (a) and the simulation of the polariton electric-field distribution (b). T_{ex} in the simulation takes values between 0.784 and 1.934 meV, with an average value of 1.362 meV. A sudden phase shift happens at $\sim 2.808\,293$ eV.

The data also suggests that the oscillation starts at an even lower E_{ex} than the lowest value probed in the measurement, 2.797 370 eV. The simulation does not reproduce this behavior, as previously mentioned, but rather generates interference fringes at the resonance frequency ω_0 and above. This could in theory be corrected by considering a lower-energy resonance in the dispersion relation than the FX. However, we could not find a known ZnSe transition suitable for this role. Indeed, the second most important state after the FX in the considered energy range is the donor-bound excitons (D_0X) at 2.8005 eV, which is still too high in energy. Other defects are expected to play an even smaller role in the optical properties of the host matrix and were consequently discarded.

On the other end of the energy range, the behavior of both the data and the simulation coincide: both show no sign of stopping. The shape of the simulated curve, which is Fabry-Perot-like, could be matched to that of the experiment if it were broadened further, for example, with lower reflection coefficients due to surface roughness or interface defects. This could account for the sharper extrema in the data compared with a sine function (as in Fig. 5.3).

Now, in order to translate the polariton-field intensity oscillation into a bound-exciton E_{em}

oscillation, one must consider interactions between the bound exciton and the excitonic and photonic part of the polariton wavefunction. In the next section, AC and DC Stark effects, as well as exciton-exciton interactions are explored for that purpose.

Bound-exciton emission energy shift caused by exciton-polaritons

The simulation above has revealed that as E_{ex} is varied above the FX energy, the intensity of the polaritonic electric field at a specific position in the ZnSe layer follows an oscillatory pattern, with a period of the order of the meV. A Te_2 -bound exciton is consequently in the presence of an oscillating exciton-polariton probability density (or concentration), which is proportional to its field distribution, and their interaction leads to an E_{em} modulation. In this section, I consider several interaction mechanisms of the photonic and excitonic components of the polariton wavefunction with a Te_2 -bound exciton and conclude on the role they could play in explaining our observations.

Highly-detuned AC Stark effect The interaction between the photonic part of the polaritonic wavefunction and the bound exciton could take the form of a highly-detuned AC Stark effect of the bound-exciton TLS. As discussed in Sect. 2.4.3, exciting a TLS in resonance induces mixing of its ground and excited states, creating new eigenstates separated by the generalized Rabi frequency $\tilde{\Omega} = \sqrt{\Omega^2 + \Delta^2}$ (Eqs. 2.32 and 2.33), with Δ the detuning and Ω the Rabi frequency. In the limit of very large Δ , this picture is reduced to a single observable transition, a situation depicted in Fig. 5.19 (a) for $\Delta > 0$. This dominant transition involves initial and final states majorly respectively formed of $|X\rangle$ and $|0\rangle$, as a radiative recombination in the TLS always involves annihilating $|X\rangle$ and ending up in $|0\rangle$ by emitting a photon. For positive Δ , the initial and final states in the dressed-state picture are $|-, n+1\rangle$ and $|+, n\rangle$, as emphasized by Eq. 2.32, where $\tan(2\theta) = -\Omega/\Delta \rightarrow 0^-$, leading to $\theta \rightarrow \pi/2$. Similarly, for negative Δ , $\tan(2\theta) \rightarrow 0^+$ and $\theta \rightarrow 0$. The most intense transition is thus $|+, n+1\rangle \rightarrow |-, n\rangle$. With $|\Delta| \gg \tilde{\Omega}$, a first-order Taylor expansion of Eq. 2.33 gives the recombination energy for both cases:

$$E_{\text{em},\pm} = \hbar\omega_0 \mp \frac{\hbar\Omega^2}{2|\Delta|} \quad (5.14)$$

where \pm here refers to the sign of Δ and ω_0 is the energy of the transition. The shift is proportional to Ω^2 and consequently to E_0^2 , the intensity of the electric field driving the TLS. It however diminishes with $|\Delta|$, meaning that the drive becomes less and less efficient at

dressing the TLS states as it moves out of resonance.

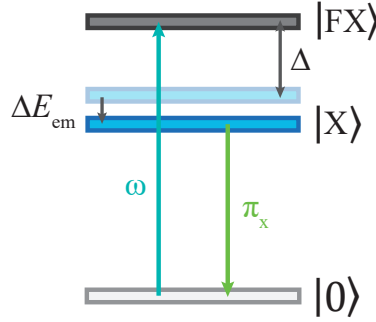


Figure 5.19 Energy levels at play in a highly-detuned AC Stark effect of a Te₂-bound exciton, for $\Delta > 0$. The dominant transition involves $|X\rangle \rightarrow |0\rangle$, as mixing of the ground and excited states of the exciton TLS is very small for a large Δ .

Experimentally, shifts of the order of 150 μeV for Δ up to 15 meV between the excitation laser and the bound-exciton transition have been observed in InGaAs QDs embedded in micropillar cavities, for strong enough electric fields [191].

In our system, exciting the FX band leads to a positive detuning with respect to the bound-exciton transition and therefore would translate as a red shift of its energy according to Eq. 5.14. Since in our polaritonic picture the field intensity oscillates with E_{ex} (Fig. 5.14), it modulates Ω^2 and the Stark shift accordingly. However, our excitation is detuned 35.7 meV on average from the bound-exciton transition, a value more than twice as large as that in Ref. [191], not to mention that our sample does not have the structure of a well-designed cavity. We consequently do not expect an efficient coherent coupling with the light field.

Finally, in order for AC Stark effect to occur, the polarization of the exciting field must be coincident with that of the TLS transition. Our experiment did not fulfill that condition in most cases. Indeed, as mentioned in Sect. 3.3.4, most of the PLE experiment was performed with a horizontally-polarized excitation (x' in the laboratory axes), while the selected detection polarization was vertical (y'). Therefore, for a good majority of the measured emitters which were aligned with either x' or y' , the excitation was orthogonal to their probed transition and could not coherently interact with them. In light of this argument as well as those stated above, we can exclude AC Stark shift with confidence as the mechanism causing the E_{em} oscillation.

DC Stark effect The photonic part of the polariton wavefunction is most likely responsible for creating charges on impurities in the vicinity of the bound exciton. The resulting electric field could then shift the bound-exciton emission lines through the DC Stark effect. Such an effect was observed during resonant excitation of ZnSe:Te₂ [175].

By approximating the bound exciton as a hydrogen-like atom, with the tightly bound hole as the “nucleus” and the electron experiencing a spherical potential ($O(3)$ symmetry), one can use the $|nlm\rangle = R_{nl}Y_l^m$ hydrogen eigenfunctions, with R_{nl} the radial wavefunction and Y_l^m the angular wavefunction or spherical harmonic, and a perturbative treatment to come up with an order of magnitude for the exciton energy shift under an electric field [192]. I start by finding an expression for the Hamiltonian of the problem, before I give the correction to E_{em} for the ground state $|100\rangle$ in the presence of the DC field. Finally, I evaluate the latter with typical parameters of our system to settle if this mechanism could be the origin of the oscillation.

The multi-polar expansion of an electric potential ϕ to the first order leads to:

$$\phi(\mathbf{r}) = \phi(\mathbf{r}_0) + \nabla\phi(\mathbf{r}_0) \cdot (\mathbf{r} - \mathbf{r}_0), \quad (5.15)$$

where \mathbf{r}_0 is the potential origin and \mathbf{r} is the position at which the potential is evaluated. The interaction energy of a charge distribution $\rho(\mathbf{r})$ in a volume V with the potential is:

$$E = \phi(\mathbf{r}_0) \int_V \rho(\mathbf{r}) d^3r + \nabla\phi(\mathbf{r}_0) \cdot \int_V \rho(\mathbf{r}) (\mathbf{r} - \mathbf{r}_0) d^3r. \quad (5.16)$$

The first term vanishes since the atom is neutral, and is therefore discarded in what comes next. The second term contains the dipole operator $\boldsymbol{\mu} = \int_V \rho(\mathbf{r}) (\mathbf{r} - \mathbf{r}_0) d^3r$ and the electric field $\boldsymbol{\mathcal{E}} = -\nabla\phi$.

By considering a simpler model of an electron and proton (or, in our case, hole) gravitating around one another, $\boldsymbol{\mu}$ can be expressed as $-e(\mathbf{r} - \mathbf{r}_0)$, with $-e$ the charge of the electron, and the DC Stark effect Hamiltonian is written:

$$H_{\text{SE}} = -\boldsymbol{\mu} \cdot \boldsymbol{\mathcal{E}}. \quad (5.17)$$

With no loss of generality, one can decide to orient $\boldsymbol{\mathcal{E}}$ along z , $\boldsymbol{\mathcal{E}} = \mathcal{E}\hat{\mathbf{z}}$. The first-order

correction of the energy for $|100\rangle$ is:

$$E_{100}^{(1)} = \langle 100 | H_{\text{SE}} | 100 \rangle = e\mathcal{E} \langle 100 | z | 100 \rangle = 0, \quad (5.18)$$

due to the symmetry argument that z is odd and $|100\rangle$ is even. Indeed, a neutral atom with spherical symmetry does not have a permanent dipole moment.

However, the electric field can induce a dipole moment by distorting the electronic cloud, leading to a second-order correction to the energy:

$$E_{100}^{(2)} = e^2 \mathcal{E}^2 \sum_{nlm \neq 100} \frac{|\langle 100 | z | nlm \rangle|^2}{E_{100}^{(0)} - E_{nlm}^{(0)}}, \quad (5.19)$$

with $E_{nlm}^{(0)} = -m_X e^4 / [2(4\pi\epsilon)^2 \hbar^2 n^2]$, where $m_X = m_e m_h / (m_e + m_h)$ is the exciton reduced mass, function of the effective masses of the electron and hole m_e and m_h , and ϵ is the permittivity of ZnSe. With $m_e = 0.137 m_0$, $m_{hh} = 0.76 m_0$ [99] and $\epsilon = 8.1 \epsilon_0$ [190], one obtains $m_X = 0.116 m_0$.

Eq. 5.19 can be reduced by considering the selection rules for the dipole operator, $\Delta l = \pm 1$ and $\Delta m = 0$:

$$E_{100}^{(2)} = \frac{2(4\pi\epsilon)^2 \hbar^2 \mathcal{E}^2}{m_X e^2} \sum_{n=2}^{\infty} \frac{|\langle 100 | z | n10 \rangle|^2 n^2}{1 - n^2}. \quad (5.20)$$

The sum is rather complicated to evaluate, but with a clever operator trick (as in Ref. [192], see Appendix C), one gets:

$$E_{100}^{(2)} = -\frac{9}{4} (4\pi\epsilon a_0^3 \mathcal{E}^2), \quad (5.21)$$

where $a_0 = 4\pi\epsilon\hbar^2/(m_X e^2)$ is the exciton Bohr radius and is equal to 3.129 nm. The shift is therefore proportional to the field intensity \mathcal{E}^2 . The magnitude of the field is for its part proportional to the polaritonic field amplitude in the vicinity of the Te_2 molecule, responsible for the creation of charges. The minus sign and the square dependence of Eq. 5.21 on \mathcal{E} implies a red shift.

To get an order of magnitude of that shift, let's consider the electric field created by a single charge (say, an electron) at a distance d :

$$\mathcal{E} = -\frac{e}{4\pi\epsilon d^2}. \quad (5.22)$$

At $d = a_0$, the extent of the exciton $1S$ wavefunction, the amplitude of the electric field created by the single electron is $-1.82 \times 10^7 \text{ V m}^{-1}$, and the associated energy shift is -127.8 meV , several orders of magnitude greater than what is observed experimentally. At the edge of the excitation spot ($d = 0.38 \text{ }\mu\text{m}$), $\mathcal{E} = -1.23 \times 10^{-3} \text{ V m}^{-1}$ and $E_{100}^{(2)} = -0.588 \text{ neV}$, which is in turn too small. Hence, it is more likely that the field felt by the exciton is a consequence of the averaging of the contribution of a great number of charges, which would also be more consistent with the excitation regime and the behavior uniformity of the measured excitons.

The interference pattern of the polaritonic field in our sample preferentially creates charges at field anti-nodes (Fig. 5.20). The charges are therefore organized in planes within the excitation volume and on both sides of the emitter. The electric fields they generate can partially compensate each other and give rise to the required DC Stark shift of the order of several tens of μeV . As E_{ex} is monotonically scanned, the position of the anti-nodes is displaced (as in Fig. 5.14 (a)) and the distance between the charges and the emitter is modulated, which in turn impacts the electric field felt by the bound exciton and thus its E_{em} shift.

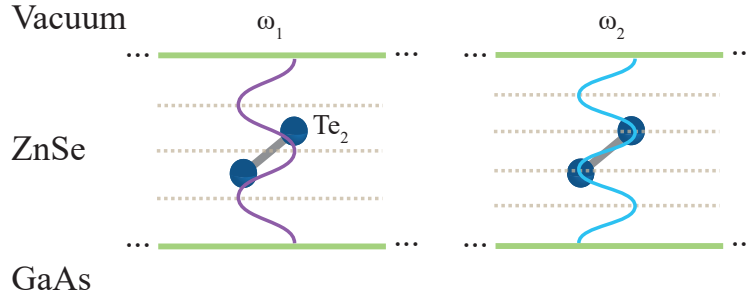


Figure 5.20 Charge planes (pale dotted lines) created by the polaritonic-field interference pattern. The change of E_{ex} from $\hbar\omega_1$ to $\hbar\omega_2$ modifies the distance between the charge planes and the emitter, and therefore the induced E_{em} shift.

Finally, as DC Stark effect does not depend on polarization, it stands as a likely candidate in explaining the E_{em} oscillation within the polariton formalism.

Exciton-exciton interactions The exciton part of the polariton wavefunction can also interact with the bound exciton to cause a shift of its E_{em} . Such shifts due to exciton-exciton interactions are associated with systems of reduced dimensionality and are absent from bulk semiconductors [193]. To the best of my knowledge, no calculation or experimental results

have been reported specifically on the effect of a three-dimensional FX gas on bound states such as an exciton on an atomic defect. Reports in the literature instead mostly concern two-dimensional exciton gases in III-V QWs [193–195], or simpler systems such as a biexciton confined in a QD [196]. I anyhow use these results to describe the physics of the exciton-exciton interaction and understand how they translate to ZnSe:Te₂.

The case of a biexciton confined in a small-sized III-V QD shows that direct Coulomb repulsive interaction between same-type particles (electron or hole) dominates the attraction between particles of distinct type [196]. The resulting repulsion exceeds the binding contribution of exchange interaction between excitons, leading to a net anti-binding effect. Confinement nonetheless dominates this repulsion, giving rise to a stable biexciton state that is blueshifted compared to two non-interacting excitons.

2D exciton gases in QWs are subjected to similar effects in the high-density limit. The reduced dimensionality lowers the attractive contribution of long-range many-body direct Coulomb interaction (i.e. van der Waals interactions between excitons) compared to exchange interaction between particles belonging to distinct excitons [193, 195]. The result is a small blue shift linear in n_X , the 2D density of photo-created excitons, expressed as (at $T = 0$ K) [195]:

$$\Delta E_{\text{em}} = 16\pi n_X a_{2\text{D}}^2 \left(1 - \frac{315\pi^2}{2^{12}} \right) E_{X,2\text{D}}, \quad (5.23)$$

where $a_{2\text{D}} = a_0/4$ is the two-dimensional exciton Bohr radius (a_0 is the usual three-dimensional Bohr radius) and $E_{X,2\text{D}}$ is the binding energy of an exciton in the QW, which is four times the three-dimensional binding energy obtained with an hydrogen-like model. Although derived for the two-dimensional case, this result has proven experimentally valid for quasi-2D excitons in QWs with thicknesses of the same order of magnitude as $2a_0$ (~ 10 nm). Blue shifts of the exciton absorption peak have indeed been observed for 4–15 nm-thick QWs after the creation of a large exciton density with a subpicosecond laser pulse [193, 194]. These experiments involved rather large emission lines (~ 4 – 7.5 meV) requiring high excitation powers for a shift to be observed. Due to its very narrow emission line (158 μeV on average), our bound exciton could be sensitive to much weaker perturbations.

Our sample thickness is 80 nm, one order of magnitude larger than the Bohr diameter of a 3D exciton in ZnSe (6.26 nm). Therefore, the resonantly created FX in our PLE experiment cannot be regarded as two-dimensional. However, due to the very small emission FWHM

of the bound exciton, any imbalance of its direct and exchange Coulomb interaction with the surrounding FX exciton gas could lead to a detectable shift of its E_{em} . In this scenario, the modulation of the free exciton-polariton density by an E_{ex} sweep would directly lead to a proportional displacement of the bound-exciton emission peak, from unperturbed at low densities to maximally shifted at high densities (Fig. 5.21). The sign of the displacement, however, would depend on whether direct or exchange interaction dominates.

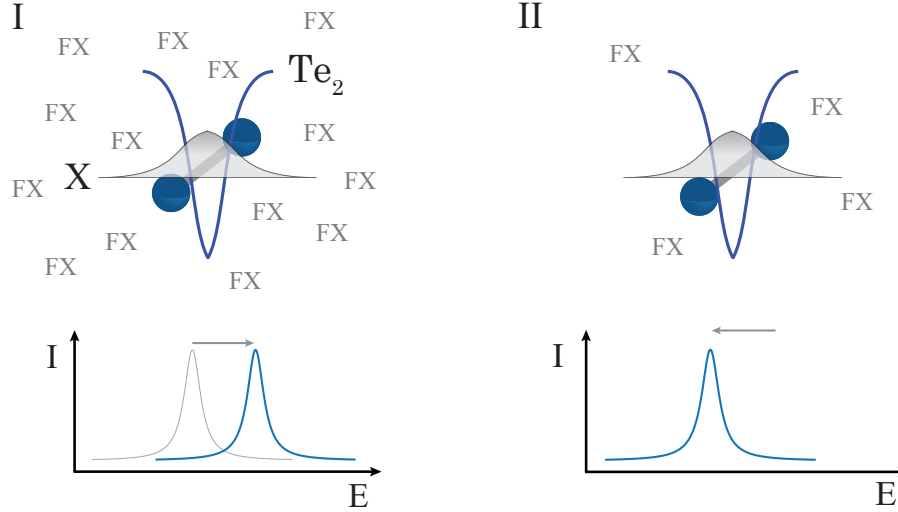


Figure 5.21 Effect of the FX density in the vicinity of a Te₂-bound exciton (white wavefunction in a blue potential well, not to scale). I. High FX density, leading to a blue shift (if exchange interaction dominates) of the bound-exciton recombination line due to exciton-exciton repulsive interactions. II. At low density, the interaction is weaker and the line shift back to its unperturbed position.

Unpublished work by Francoeur *et al.* [197] on GaAs:N₂ tends to support this idea. Fig. 5.22 shows their observations. The E_{em} shift of an exciton bound to a N₂ molecule was found to be dependent on the position of the NR excitation laser with respect to the detection area, from minimal for far excitation to maximal (60 μeV in panel (b)) for coincident excitation. The results were interpreted in terms of creation of free electron-hole pairs and excitons in the GaAs host by the above-gap excitation, with which the bound exciton interacts strongly if they are in its vicinity, weakly or not at all if they are far.

In short, from the similarity of GaAs:N₂ with our ZnSe:Te₂ system and the sensitivity of IC emitters to external perturbations, especially due to their narrow emission lines, exciton-exciton interactions are strong candidates to the explanation of our E_{em} oscillation result.

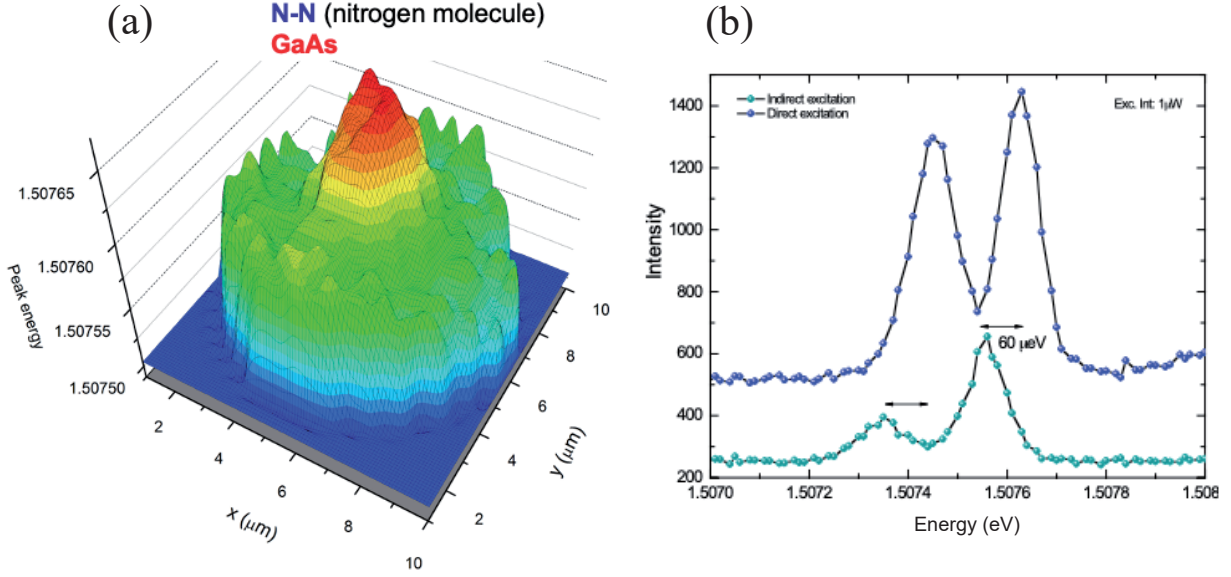


Figure 5.22 Blueshift of the emission lines of an exciton bound to a N_2 molecule in GaAs dependent on the position of the NR excitation. As the laser is scanned from far to close to the emitter, the excitonic emission lines blueshift (up to 60 μeV). (a) E_{em} as a function of excitation position (x, y) , (b) PL spectra for very far (cyan) and coincident (blue) excitations. Reprinted with permission from [197].

Proposed interaction mechanism We have seen above that DC and AC Stark effects caused by the photonic part of the polaritonic wavefunction would induce a red shift of the bound exciton emission line, while exciton-exciton interactions would lead to a blue or red shift depending on the dominant Coulomb interaction. AC Stark shift has been rejected as its effect should be polarization-dependent, which was not the case experimentally.

We are left with two possible mechanisms, and one must dominate. We nevertheless do not have enough information to conclude which one. On the one hand, DC Stark shift of the bound-exciton emission line due to charges trapped at defects in its vicinity has been reported in the literature for ZnSe:Te_2 [175]. Those charges also play a role in the bound exciton dynamics, as argued in Chap. 6, suggesting that their influence cannot be neglected. However, the number of those charges and the magnitude of the electric field they create are uncertain, as the anti-node in the polaritonic field are a few nm apart and generate charges in close proximity with the emitter. One could expect that these would lead to very large Stark shifts unless they almost perfectly cancel each other's effect out. A larger A_{em} distri-

bution should additionally be observed among emitters, as many configurations should exist, unless we measured only excitons that were subjected to small Stark shifts, the others being quenched or pushed out of our detection window.

On the other hand, exciton-exciton interactions are held partly responsible for the shift observed in GaAs:N₂ as the excitation is scanned across a single emitter [197]. They are consistent with the fact that, in the simulation, the oscillation occurs for energies corresponding to a parabolic dispersion in the LPB, where the polaritonic wavefunction is more exciton-like. However, the geometry of the system does not allow to predict without doubt that direct and exchange interactions between the bound excitons and the polaritons would not compensate each other.

In light of these arguments, both mechanisms have assets and drawbacks, but none is entirely refuted or confirmed by the data. More experiments or simulations would be required to settle the matter. For example, calculations of the magnitude of the direct and exchange Coulomb interactions between the bound exciton and the excitonic part of the polariton wavefunction could be made to determine if an imbalance exists in the two contributions. Also, an excitation-position scan as in Ref. [197] and pump-probe time-resolved absorption measurements as in Refs. [193,194] could unveil if exciton-exciton interactions are responsible for the observed shift.

Conclusion on the polaritonic interaction model between the excitation field and a bound exciton

In conclusion, in this section, the electric-field intensity distribution of free exciton-polaritons at the center of the ZnSe layer was computed with a matrix formalism and the bulk polariton dispersion relation for different parameters such the excitonic mass M , the oscillator strength $4\pi\beta$ and the damping parameter Γ . It led to an oscillation of the field intensity as a function of excitation energy (E_{ex}) for values above the resonance energy ω_0 , in a Fabry-Perot-like function showing an increasing oscillation period (T_{ex}). T_{ex} was most sensitive to M , while $4\pi\beta$ influenced the occurrence of the UPB contribution, reducing the apparent T_{ex} between two adjacent maxima.

The electric-field distribution is directly linked to an E_{em} shift of the bound exciton, as it represents the amplitude of the exciton-polariton wavefunction and therefore modulates

its interaction with the bound exciton through its photonic (DC Stark effect) or excitonic (exciton-exciton interactions) part. Both mechanisms have been qualified as probable, but our data did not allow us to decide between the two.

The oscillation period (T_{ex}) obtained with the model is satisfactorily close to the experimental value (1.362 vs 1.103 meV) while using parameters from the literature (M, Γ), from our experimental results (ω_0) and from the observation of the simulation behavior ($4\pi\beta$). The shape of the calculated curve could also resemble that of the data if additional broadening were admitted. The simulation however did not reproduce the right E_{ex} range for the oscillation, which experimentally started below the FX energy. Furthermore, its increasing T_{ex} was in opposition with the constancy showed by the parameter in the experimental data. However, we saw that this effect could be in part mitigated by a judicious choice of M and $4\pi\beta$.

These discrepancies appear to point out that the exciton-polariton model is incomplete, if not unsuitable for explaining the E_{em} oscillation. In the rest of this chapter, I survey alternative mechanisms such as an interaction with a magnetic field, hyperfine interaction and a coupling assisted by phonons. I discuss their strengths, weaknesses and likelihood, as well as if they describe the data better than the present polaritonic mechanism.

5.2.2 Magnetic field-induced effects

I now examine the possibility of a variable magnetic field being responsible for the oscillation. The perturbation Hamiltonian from Ref. [154], presented in Appendix B, shows that a magnetic field $\mathbf{B} = B_x\hat{\mathbf{x}} + B_y\hat{\mathbf{y}} + B_z\hat{\mathbf{z}}$ leads to two contributions to H_e , the electron Hamiltonian, one linear in B_i ($i = \{x, y, z\}$) responsible for the Zeeman effect, and a quadratic one, contributing to the diamagnetic shift, which affects both spins equally:

$$H_e = c_1 (B_x^2 + B_y^2 + B_z^2) \cdot \mathbb{1} + 2c_2\sigma_x B_x + 2c_3\sigma_y B_y + 2c_4\sigma_z B_z, \quad (5.24)$$

with $\sigma_x, \sigma_y, \sigma_z$ the Pauli matrices and where $c_i, i = \{1, 2, 3, 4\}$ are constants. In the case of the heavy hole, there are also diamagnetic and linear (Zeeman) terms:

$$H_{hh} = 4 \left(v_1 J_z^2 + v_2 J_x^2 + v_3 J_y^2 \right) (B_x^2 + B_y^2 + B_z^2) + \frac{2}{\sqrt{3}} v_4 \{J_y, J_z\} B_x \\ + \frac{2}{\sqrt{3}} v_5 \{J_z, J_x\} B_y + \left(2v_{14} J_z + 8v_{15} J_z^3 + \frac{2}{\sqrt{3}} v_{16} \{J_z, J_x^2 - J_y^2\} \right) B_z, \quad (5.25)$$

with $J_i, i = \{x, y, z\}$ the total angular momentum matrices and $v_j, j = \{1, 2, 3, 4, 5, 14, 15, 16\}$, some constants to be determined. The exchange Hamiltonian is considered here as magnetic-field independent for the sake of simplicity. Adding H_e and H_h to get the exciton magnetic Hamiltonian, one obtains a linear and a quadratic contribution of all field components.

The addition of a magnetic field caused by a linearly-polarized excitation in a material is expected to be very small, if not negligible compared to the C_{2v} crystal field. Also, as the X and Y wavefunctions of the C_{2v} exciton are linear combinations of spin up and spin down electron and HH (see Eq. 2.4), one can reasonably expect the states to remain unaffected at low \mathbf{B} fields as long as the crystal field terms of the total Hamiltonian dominate the magnetic ones. Consequently, the response of a bound exciton to a magnetic field is most likely quite small and the Hamiltonians of Eqs. 5.24 and 5.25 can be treated as perturbations.

Experimentally, a shift of $-18 \mu\text{eV}$ for X and of $37 \mu\text{eV}$ for Y has been observed with the application of a 5.5-T field in Faraday configuration (B_z) [95]. Therefore, a very large magnetic field would be required to induce a 44- μeV shift. With a linearly-polarized excitation, no net polarization of electron or nuclear spins should occur, and thus no net magnetic field should result. Furthermore, magnetic field-induced shifts are different for X and Y due to the Zeeman term, which has a different sign, and cannot account for the identical oscillation behavior most commonly observed for the excitonic doublet. Any form of magnetic interaction therefore appears unlikely to explain the E_{em} oscillation of the bound exciton.

5.2.3 Phonon-assisted coupling with free exciton-polaritons

I now investigate how the interaction of a bound exciton with a combination of acoustic and optical phonons and free exciton-polaritons could explain the oscillation. The dressing of an exciton with phonons leads to the formation of a ladder of levels $|X, n_a, n_o\rangle$ with energies $E_{X, n_a, n_o} = E_X + n_a \hbar \omega_a + n_o \hbar \omega_o$, where E_X is the exciton energy, $n_{a,o}$ are respectively the

number of involved acoustic and optical phonons and $\omega_{a,o}$ are their angular frequency. It has indeed been reported in the literature that phonons have an important impact on the absorption and emission properties of an exciton [198,199]. Fig. 5.23 (b) illustrate the most common signature of phonon involvement in the absorption process, in this case in monolayer molybdenum diselenide (MoSe₂). The emission intensity (I_{em}) periodically increases as E_{ex} comes into resonance with phonon-dressed FX energy levels (here, the phonons involved are longitudinal acoustic (LA), of energy $\hbar\omega_{\text{LA}} = 18.5 \text{ meV}$) and reaches a minimum when E_{ex} is in the middle of two levels, as depicted in panel (a). Absorption can efficiently take place if the combination of phonons respects the conservation of momentum necessary to the creation of a Γ -point exciton.

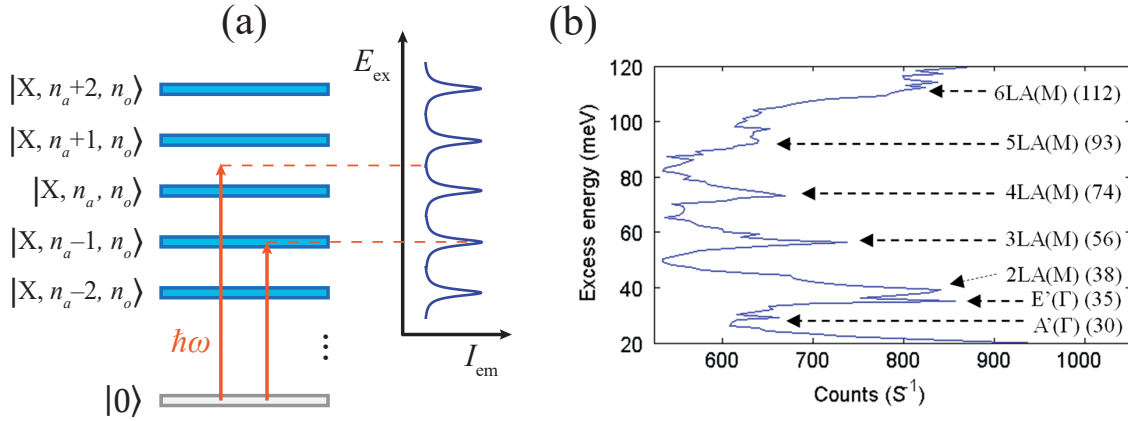


Figure 5.23 Phonon-assisted excitation of an excitonic system. (a) Typical behavior where I_{em} reaches a local maximum as E_{ex} comes in resonance with the exciton energy plus an integer number of acoustic (n_a) and optical (n_o) phonons. This effect is repeated periodically at multiples of the phonon energy, here chosen as that of an acoustic phonon. (b) Phonon-enhanced PLE spectrum of monolayer MoSe₂, where I_{em} periodically increases as the excitation corresponds to an excess energy of several M -point LA phonons above the FX level. A' and E' are zone-center phonons also enhancing absorption. Adapted with permission from Ref. [199], Chow *et al.*, © The Authors 2017, Creative Commons Attribution 4.0 International License, <https://creativecommons.org/licenses/by/4.0/>.

In ZnSe:Te₂, we have not observed such periodic and systematic structures in the PLE spectra and therefore no clear evidence of the involvement of specific phonons in the absorption process. The spectra from Sample A, a few of which are presented in Fig. 5.24, indeed show two absorption peaks near the FX and D_0X energies, as discussed in Sect. 4.2.3. The exact position of these transitions varies with strain in the sample and their shape and amplitude differ from emitter to emitter.

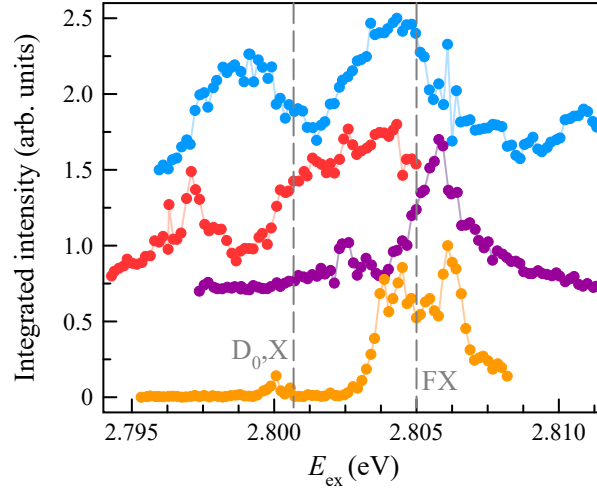


Figure 5.24 Normalized PLE spectra of four distinct excitons, showing a broad absorption maximum near the FX energy and occasionally a lower-energy one that is most probably due to donor-bound excitons (D_0X), but no clear periodic structure confirming the involvement of phonons. The response manifests an important variability depending on the emitter and the sample region. The curves were normalized and vertically translated for clarity.

Interestingly, the supplementary material of Ref. [199] reports, in addition to the I_{em} enhancement shown in Fig. 5.23 (b), an E_{em} oscillation of the FX emission line with the same period as that of I_{em} (the energy of a LA phonon) and a $\pi/2$ phase (the shaded regions in Fig. 5.25 indicate where I_{em} is maximum). The amplitude of this oscillation decreases with E_{ex} from 1.3 to 0.3 meV and is at least one order of magnitude greater than what we observed. Although the authors do not conclude on the mechanism responsible for their observation, this result has motivated the exploration of phonon-related models to explain our data.

Phonon-mediated interactions between two energy levels

Knowing that phonons can play such an crucial role in the excitation and relaxation dynamics of a system, I have tentatively elaborated a phonon-assisted coupling mechanism between the bound-exciton state of uncoupled energy E_X and exciton-polaritons created in the FX band by the resonant laser. As E_{ex} is scanned across the FX band, it resonantly creates exciton-polaritons and, by the capture mechanism described in Sect. 4.3, a bound exciton on the Te_2 molecule of interest. For specific E_{ex} values, the created FX polaritons are in resonance with one of the bound-exciton ladder states of formed by its dressing with a certain number

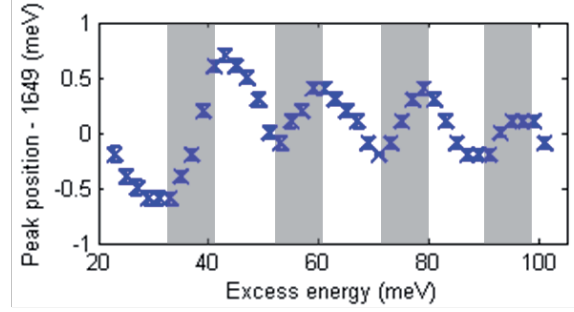


Figure 5.25 E_{em} oscillation of the FX emission line in monolayer MoSe_2 as a function of excess energy $E_{\text{ex}} - E_{\text{FX}}$. The minimum displacement happens when I_{em} is maximum (grey regions). Adapted with permission from the supplementary material of Ref. [199], Chow *et al.*, © The Authors 2017, Creative Commons Attribution 4.0 International License, <https://creativecommons.org/licenses/by/4.0/>.

of phonons, noted $|X, n_a, n_o\rangle$ and of energy E_{X, n_a, n_o} . This energy correspondence between the two levels favors an efficient interaction that leads to mixing and a shift, as illustrated in Fig. 5.26 (a).

To describe the mechanism, I only consider the dominant coupling of the FX polariton ($|\text{Pol}\rangle$) with the closest energy level of the bound-exciton ladder and neglect all others to reduce the system to a simple TLS model. The Hamiltonian H_{int} describing this situation is expressed in its most general form as:

$$H_{\text{int}} = \begin{bmatrix} E_{X, n_a, n_o} & E_{\text{int}} \\ E_{\text{int}} & E_{\text{Pol}} \end{bmatrix}, \quad (5.26)$$

with $E_{\text{int}} = \langle \text{Pol} | H_{\text{int}} | X, n_a, n_o \rangle$ the coupling term. The diagonalization of Eq. 5.26 gives new eigenenergies for the system, $E_{1,2}$:

$$E_{1,2} = \frac{E_{X, n_a, n_o} + E_{\text{Pol}}}{2} \pm \frac{1}{2} \sqrt{(E_{X, n_a, n_o} - E_{\text{Pol}})^2 + 4E_{\text{int}}^2}. \quad (5.27)$$

As the bound exciton wavefunction is responsible for this interaction and shared by all of the phonon-dressed states, their energy is simultaneously shifted by the same amount (Fig. 5.26 (a)).

The coupling strength E_{int} depends on the alignment of the FX with the bound-exciton ladder, ranging from minimum for a FX level in the middle of two ladder levels (Fig. 5.26 (b)) to maximum for a FX level resonant with one of the ladder levels (Fig. 5.26 (a)). The en-

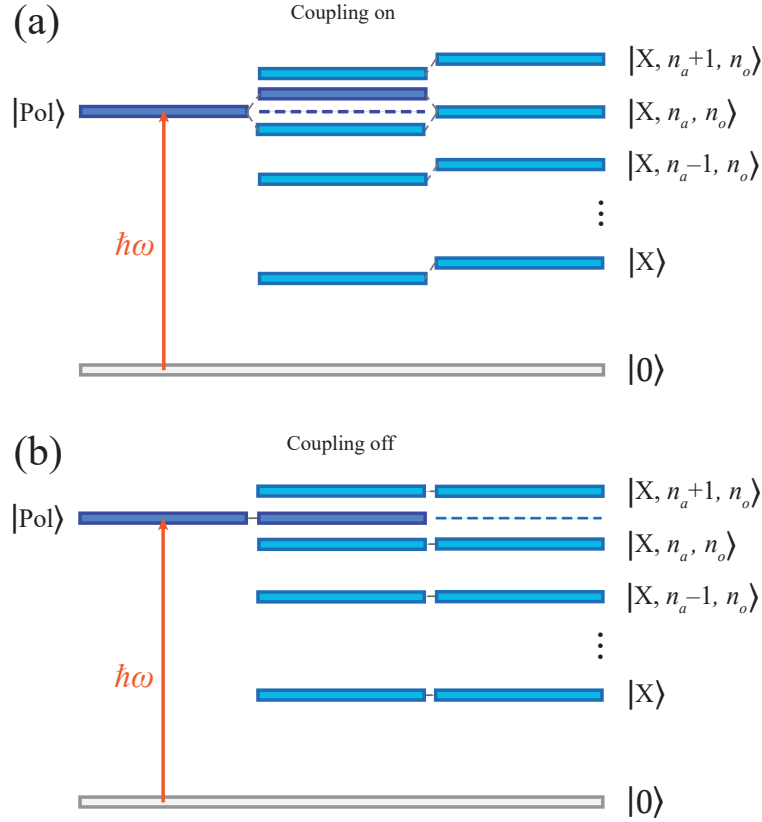


Figure 5.26 Phonon-assisted interaction between a resonantly-excited FX polariton and a Te_2 -bound exciton. (a) The coupling is maximum when the polariton is resonant with a phonon-dressed bound-exciton state, and so is the induced energy shift. The whole bound-exciton ladder is affected by the same amount. (b) The coupling and the shift are minimum when the polariton level is in the middle of two bound-exciton levels.

energy difference between these two extreme cases determines the sought-after E_{em} oscillation amplitude (A_{em}), while the oscillation period (T_{ex}) is set by the energy spacing of the ladder, i.e. the energy of the involved phonon ($\hbar\omega_a$ in this example). One must therefore find a $\sim 1\text{-meV}$ phonon to reproduce the experimental oscillation behavior.

Phonons candidates in creating the energy scale

With this interaction mechanism in mind, I next survey the phonons observed in ZnSe and determine the conditions under which they could play a part in the E_{em} oscillation through the dressing of the bound-exciton state.

LO phonons ZnSe is a polar semiconductor, therefore the dominant coupling happens with LO phonons through the Fröhlich mechanism, in which atomic movements create an oscillating macroscopic polarization that interacts with charge carriers and excitonic particles [200]. This is the reason why LO phonon replicas are easily visible in the emission spectrum of this material. However, as discussed in Sect. 5.1.2, no integer combination of these 31.7-meV phonons fits the energy separation between Te₂-bound excitons and FX, which ranges from 17.8 to 53.5 meV. Also, $\hbar\omega_{\text{LO}}$ is incompatible with the experimental T_{ex} (1.103 meV) and therefore its interaction with the bound exciton alone cannot be responsible for the E_{em} periodicity.

Small-wavevector optical and acoustic phonons Charge carriers and excitons can also interact with small-wavevector \mathbf{q} optical and acoustic phonons through the deformation potential, by which the atomic movement induced by the phonon leads respectively to a local or macroscopic distortion of the lattice. This deformation shifts the energy bands proportionally to the atomic displacement and is described by a strain tensor [200]. TO phonons, with their energy of 25.9 meV [179], are, similarly to LO phonons, too energetic to be the cause of T_{ex} .

Acoustic phonons on the other hand can have arbitrarily small energies depending on their wavevectors and are more likely candidates. Their density of states (DOS) in ZnSe (Fig. 5.27) presents its lowest-energy high-density region in the $\sim 4.3\text{--}12.7$ meV range, with a maximum around 8.5–9.1 meV [201, 202], which is higher than our target. However, mechanisms such as confinement, discussed below, could favor smaller-energy modes.

Confined acoustic phonons Acoustic phonons in semiconductor heterostructures are subjected to boundary conditions that impose restrictions on the energy and wavevector of allowed modes. This might in principle favor the sought-after 1.103-meV phonon. Although the linearity of the acoustic-phonon dispersion relation near Γ generally prevents their confinement [203], the latter effect has been observed and reported to impact non negligibly several physical properties in very thin semiconductor layers, such as the electron mobility [204]. Confined phonons are therefore worth investigating for our phonon interaction model. In this section, I come up with an expression for their dispersion relation and energy, to see if they could be the origin of T_{ex} .

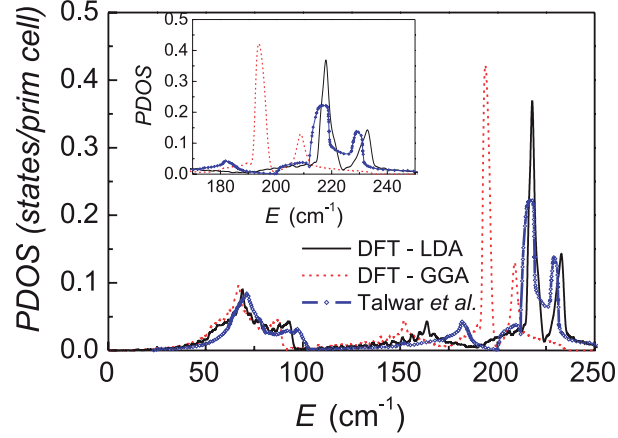


Figure 5.27 Calculated phonon density of states (PDOS) for ZnSe. The first local maximum happens at $\sim 8.5\text{--}9.1\text{ meV}$. Reprinted with permission from Ref. [201]. Copyright (2012) by the American Physical Society.

The most general boundary conditions for this problem dictate the continuity of atomic displacement \mathbf{u} at the interfaces and of the strain component perpendicular to the interfaces [203]. However, these lead to complicated differential equations for \mathbf{u} that must be solved numerically. For the sake of simplicity, I limit the discussion to the approach of Ref. [204], which calculates the limit cases of rigid ($\mathbf{u} = 0$ at the interface) and free-standing (vanishing components of the strain tensor perpendicular to the interface) boundary conditions. I present solely the rigid case, as both lead to similar dispersion relation expressions. More realistically, our system must be between rigid and free-standing, as one side of the layer is in vacuum and the other is resting on a substrate.

The allowed modes are solutions of the wave equation for \mathbf{u} in an isotropic medium:

$$\ddot{\mathbf{u}} = c_{s,t}^2 \nabla^2 \mathbf{u} + (c_{s,l}^2 - c_{s,t}^2) \nabla (\nabla \cdot \mathbf{u}), \quad (5.28)$$

where $\ddot{\mathbf{u}}$ is the second-order time derivative of \mathbf{u} and $c_{s,t}$ and $c_{s,l}$ are the transverse and longitudinal speeds of sound. Solutions are found in the form:

$$\mathbf{u}(\mathbf{r}_{\parallel}, z) = \mathbf{w}(\mathbf{q}_{\parallel}, z) e^{i(\mathbf{q}_{\parallel} \cdot \mathbf{r}_{\parallel} - \omega_p t)}, \quad (5.29)$$

for a sample structure consisting of a semiconductor layer of thickness d , with axes as in Fig. 5.13. This geometry ensures that phonons propagate in the xy plane parallel to the interfaces and create a standing wave along z , where the wavevector is quantized by confinement. In

Eq. 5.29, \mathbf{q}_{\parallel} is the propagation phonon wavevector, \mathbf{r}_{\parallel} is a position vector with x and y components, ω_p is the phonon angular frequency and $\mathbf{w}(\mathbf{q}_{\parallel}, z)$ is a vector expressing the displacement amplitude in all three directions. For simplicity and without loss of generality, \mathbf{q}_{\parallel} can be defined as $q_x \hat{x}$ and $\mathbf{w}(\mathbf{q}_{\parallel}, z)$ as $\mathbf{w}(z)$. By injecting Eq. 5.29 in Eq. 5.28, one obtains three differential equations for the components of $\mathbf{w}(z)$:

$$\begin{aligned} -\omega_p^2 w_x &= \left(c_{s,t}^2 \frac{\partial^2}{\partial z^2} - c_{s,t}^2 q_x^2 \right) w_x + i \left(c_{s,l}^2 - c_{s,t}^2 \right) q_x \frac{\partial}{\partial z} w_z \\ -\omega_p^2 w_y &= c_{s,t}^2 \left(\frac{\partial^2}{\partial z^2} - q_x^2 \right) w_y \\ -\omega_p^2 w_z &= \left(c_{s,l}^2 \frac{\partial^2}{\partial z^2} - c_{s,t}^2 q_x^2 \right) w_z + i \left(c_{s,l}^2 - c_{s,t}^2 \right) q_x \frac{\partial}{\partial z} w_x. \end{aligned} \quad (5.30)$$

The first and third equations are coupled and give rise to the so-called dilatational and flexural solutions, while the second describes the shear solutions. With rigid boundaries ($\mathbf{u}(\mathbf{r}_{\parallel}, \pm d/2) = \mathbf{0}$), solving Eqs. 5.30 lead to conditions on ω_p and q_x :

$$\begin{aligned} q_x^2 \tan\left(\frac{q_t d}{2}\right) + q_l q_t \tan\left(\frac{q_l d}{2}\right) &= 0 \\ q_x^2 \tan\left(\frac{q_l d}{2}\right) + q_l q_t \tan\left(\frac{q_t d}{2}\right) &= 0 \\ \left[q_x^2 + \left(\frac{n\pi}{d}\right)^2 \right] c_{s,t}^2 &= \omega_p^2, \end{aligned} \quad (5.31)$$

respectively for the dilatational, flexural and shear motions, with n the mode-order quantum number. q_t and q_l are defined as:

$$\omega_p^2 = c_{s,l}^2 (q_x^2 + q_l^2) = c_{s,t}^2 (q_x^2 + q_t^2). \quad (5.32)$$

The dispersion relations for the numerous allowed modes derived from Eqs. 5.31 have $\omega_p \neq 0$ at Γ ($q_x = 0$).

The energy of any confined mode at Γ for a 80 nm-thick ZnSe layer like Sample A can be calculated using $c_{s,t} = 2670 \text{ m s}^{-1}$ and $c_{s,l} = 4210 \text{ m s}^{-1}$ (values at 10 K along [100] [166]). The results are plotted in Fig. 5.28. The energy separation between two consecutive modes is 0.218 meV for dilatational modes, 0.137 meV for flexural modes and 0.069 meV for shear modes. There are indeed modes with an energy of $\sim 1 \text{ meV}$, such as the $n = 4, 5$ dilatational modes and the $n = 7, 8$ flexural modes, but it is unclear why they should be favored over the

others.

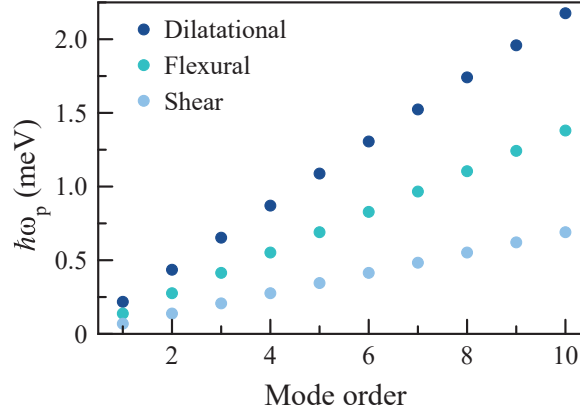


Figure 5.28 Energy at Γ of the first ten confined dilatational, flexural and shear phonon modes with rigid boundary conditions in a 80-nm ZnSe layer.

On another note, guided LA phonons of the order of a few tens of μeV were experimentally observed in μm -thick ZnSe thin films grown on GaAs [205]. The Brillouin scattering intensity of these phonons tends to decrease as the film thickness is reduced, as they leak more and more into decaying shear modes. This is to be expected in a sample as thin as ours. Consequently, in summary, since the energy of guided phonons is too small to contribute to T_{ex} , that, to my knowledge, the existence higher-energy modes has not been reported and that there is no evidence that any $\sim 1\text{-meV}$ mode should be favored, I conclude that the participation of confined phonons in the oscillation mechanism is unlikely.

Local phonon modes Local phonon modes come from the vibration of impurities that are lighter than the atoms they replace [206] and usually have energies in the tens of meV for zincblende solids [91, 124, 206, 207]. Hence, Te cannot form local modes, as it is heavier than Se.

However, if we admit that the presence of two Te atoms in the vicinity of a lighter Zn atom can perturb the vibration of the latter, one can estimate the energy of the new local mode with the approach of Ref. [91]. Assuming the Zn atom now vibrates against two Se and two Te atoms, and that the spring constant remains the same for all links, the new mode energy

is:

$$\hbar\omega_{\text{loc}} = \hbar\bar{\omega} \left(\frac{1}{m_{\text{Zn}}} + \frac{1}{m_{\text{Se}}} \right)^{-1/2} \left(\frac{1}{m_{\text{Zn}}} + \frac{1}{2m_{\text{Se}} + 2m_{\text{Te}}} \right)^{1/2}, \quad (5.33)$$

with m_i , $i = \{\text{Zn}, \text{Se}, \text{Te}\}$ the atomic masses and $\hbar\bar{\omega} = 1/3(\omega_{\text{LO}} + 2\omega_{\text{TO}})$ a mean value for the optical-phonon energies. One obtains $\hbar\omega_{\text{loc}} = 22.2 \text{ meV}$, of the order of magnitude of an optical phonon.

Therefore, from the values reported in the literature for other zincblende semiconductors, the fact that Te does not create local modes and the value estimated above for an hypothetical one involving Zn, local modes are not considered here, as they are too energetic.

Conclusion on the interaction with phonons

In conclusion, the dressing of a bound exciton with phonons, creating a energy-level ladder, could in principle lead to a periodic interaction with the resonantly-created FX polaritons. The coupling strength would be modulated by the alignment of the polariton level with the bound-exciton ladder following a periodic pattern. A_{em} would be determined by the interaction energy, while T_{ex} would rise from the ladder energy spacing, fixed by the phonon energy.

This pictures however suffers from a few drawbacks. First, no known ZnSe phonon could provide the required 1.103-meV energy for T_{ex} . Although small- \mathbf{q} or confined acoustic phonons could in principle bear such an energy, it remained unclear why a particular mode not corresponding to any zone high-symmetry point or local maximum in the DOS should be favored.

Also, the typical signature of phonon coupling in the PLE spectra, where I_{em} increases as the excitation comes into resonance with the transition plus a certain number of phonons, was never observed. Finally, as FX are energetically very far from the bound exciton, a great number of 1-meV phonons (15–50), or a combination of different phonons, would be required to bring the bound exciton in resonance. A process involving such a large number of excitations is not very likely. Consequently, the phonon-assisted coupling of a bound exciton with polaritons has been discarded as a potential explanation of the E_{em} -oscillation phenomenon.

5.2.4 Splitting of the bound-exciton transitions into nearly-degenerate doublets

This section explores whether the E_{em} oscillation could result from a mechanism involving the splitting of both bound-exciton emission lines X and Y into nearly-degenerate doublets, noted X', X'' and Y', Y'' . A variation of the relative amplitude of the doublets elements as a function of E_{ex} could be interpreted as a shift of their unresolved resulting emission structure. This could happen for example if the parity of the doublet wavefunctions with respect to a C_{2v} symmetry operation differed, while that of the resonantly-created FX changed periodically with E_{ex} . Preferential coupling to X' or X'' would consequently happen according to Fermi's golden rule.

Without the need of getting into the details of the coupling, as it is demonstrated below, I first check if this picture could indeed occur in the context of our experiment, taking into account the physical characteristics of the detector and the spectral resolution of the system. Then, I review different mechanisms that could form the doublets and discuss their likelihood in ZnSe:Te₂.

Amplitude-variation simulation of an unresolved doublet

Due to the finite resolution of the detection system, a variation of the relative amplitude of the two lines forming a doublet could be interpreted as the shift of a single unresolved broader structure. The latter is indeed reshaped into a more or less asymmetrical peak, influencing the subsequent fit performed to extract its central position.

A simulation with X' and X'' as two Lorentzian lines separated in energy by a few tens of μeV was performed to evaluate if this scenario is compatible with the parameters and results of our experiment. The width of each transition was considered limited by instrumentation and fixed at $70 \mu\text{eV}$. The Lorentzians were discretized and summed to emulate the integration area relating to the finite size of the CCD camera pixels. A Gaussian fit was then applied to the result, reproducing the processing of experimental data. Fig. 5.29 summarizes the quantities and energy levels at play (panel (a)) and shows the fit for three different relative amplitudes of the two lines (panels (b)–(d)). An energy separation of $30 \mu\text{eV}$ was chosen as it reproduces the best the A_{em} experimental results.

In panel (b) is shown the extreme case where X' has an amplitude $A_{X'} = 1$ and X'' , an ampli-

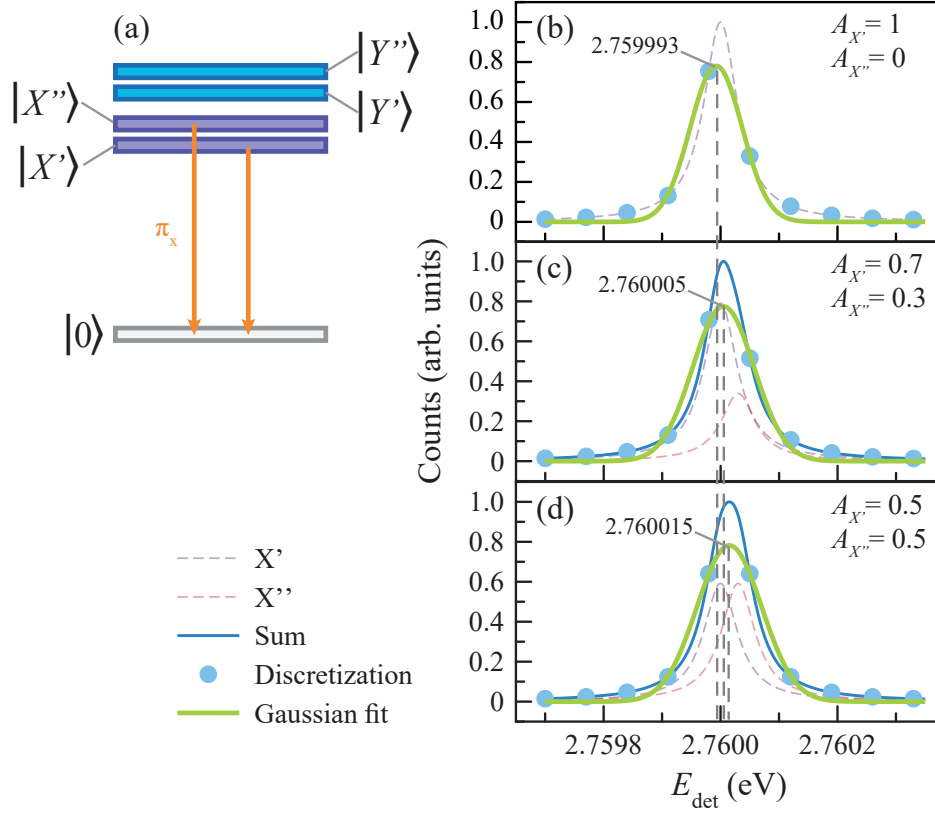


Figure 5.29 Simulation of nearly-degenerate doublets forming the X and Y emission structures. (a) Energy structure involved. The X' , X'' and Y' , Y'' doublets are respectively polarized along x and y . (b-d) Simulations of the X emission structure with the discretization and Gaussian fit of a sum of two Lorentzian functions separated by 30 μeV . The modification of the components relative amplitude causes the fit center position to change, leading to a total shift amplitude of 44 μeV from $A_{X'} = 1, A_{X''} = 0$ to $A_{X'} = 0, A_{X''} = 1$.

tude $A_{X''} = 0$, giving the lower bound for E_{em} . An equal E_{em} displacement with respect to the doublet central energy is expected for the opposite case of $A_{X'} = 0, A_{X''} = 1$ and is therefore not shown. An intermediate case with $A_{X'} = 0.7$ and $A_{X''} = 0.3$ and the central case where $A_{X'} = A_{X''} = 0.5$ are also illustrated respectively in panels (c) and (d). It is obvious from the Lorentzian sum and the discretization that the two transitions cannot be resolved by our detection system. Also, as $A_{X'}$ and $A_{X''}$ vary with respect to one another, the center position of the Gaussian fit is modified. For a doublet with a 30- μeV splitting, the simulation gives a peak-to-peak shift amplitude of 44 μeV , corresponding to the experimental average A_{em} value.

A nearly-degenerate doublet can therefore reproduce the experimental E_{em} variation observed during an oscillation. The next sections now overview possible physical causes of the forma-

tion of the X', X'' and Y', Y'' doublets and discuss their likelihood in light of the experimental parameters and results.

Symmetry of the defect

The presumed additional lift of degeneracy of the X (or Y) exciton lines into X' and X'' cannot be a consequence of symmetry breaking or strain, as C_{2v} is already maximally non-degenerate and includes all the effects of crystal field and exchange interaction. All states have been indeed accounted for in C_{2v} IC systems [84, 123]. As has been seen in Sect. 4.2.2, the energy difference between E_X and E_Y (ΔE_{XY}) in ZnSe:Te₂ ranges from 11 to 1241 μeV with a mean value of 307 μeV (Fig. 4.3), which is in most cases far too large compared to the required A_{em} . Furthermore, polarization is preserved in the X', X'' doublet, hence states of different polarization (X, Y and Z) cannot be involved. Therefore, symmetry alone cannot account for the oscillation and another component must be added to the system if one hopes to adequately describe the phenomenon.

Hyperfine coupling

Next, I explore hyperfine coupling with a nuclear spin as a possible mechanism behind the lift of degeneracy of X', X'' and Y', Y'' levels. The major contribution to a spin interaction involving an exciton and a nucleus comes from the electron wavefunction, which is s -type and maximum at the position of the nucleus. The p -type hole wavefunction, for its part, presents instead a node, which greatly suppresses the so-called Fermi contact interaction. The hyperfine Hamiltonian is therefore written [208]:

$$H_{\text{hf}} = A' \left[S_z I_z + \frac{1}{2} (S_+ I_- + S_- I_+) \right] \quad (5.34)$$

where $A' = AV_0|\psi(\mathbf{r}_{\mathbf{n}})|^2$ is a constant expressing the strength of the interaction, proportional to the hyperfine constant A , the unit cell volume V_0 and the square of the norm of the electron envelope wavefunction ψ at the position of the nucleus $\mathbf{r}_{\mathbf{n}}$. S_z and I_z respectively are the z projection of the electron and the nuclear spins and S_{\pm} and I_{\pm} are the ladder operators for both spins. H_{hf} contains an effective magnetic field term and two joint spin-flip (flip-flop) terms. Its matrix form in the coupled HH exciton-nucleus spin 8×8 basis is developed in Appendix D for $S = I = 1/2$.

Hyperfine constants for non-zero spins isotopes of Zn, Se and Te are respectively reported as $3.7 \mu\text{eV}$ for ^{67}Zn (spin $5/2$) [24], 6.87 [209] and $33.6 \mu\text{eV}$ [24] for ^{77}Se (spin $1/2$), $12.0 \mu\text{eV}$ for ^{123}Te (spin $1/2$) [209], $14.4 \mu\text{eV}$ for ^{125}Te (spin $1/2$) [209] and even $-45 \mu\text{eV}$ as an average value for both Te isotopes [210]. These values are not negligible compared to the energy scale of the crystal field and exchange interaction splitting the X , Y , Z and D energy levels, therefore the total Hamiltonian $H_{\text{Tot}} = H_0 + H_{\text{hf}}$ must be diagonalized to extract the new energies. Here, H_0 is the diagonal form of the C_{2v} HH-exciton Hamiltonian (see Eqs. 2.1–2.3) extended by a tensor product with a 2×2 identity matrix to express it in the coupled exciton-nucleus basis. The values of the diagonal elements can be obtained from the experimental energy values extracted from emission spectra.

Table 5.2 presents a numerical example of the H_{Tot} diagonalization using the experimental average value of $\Delta E_{XY} = 216 \mu\text{eV}$ from this work. Since the energy positions for Z and D are not known for our system of interest, I have used values computed for GaAs:N₂ [83] (respectively 171.7 and $164.6 \mu\text{eV}$ below X). The nuclear spin considered comes from the most abundant of non-zero spin Te isotope, ^{125}Te , such that $A' = 14.4 \mu\text{eV}$. The new eigenstates form four degenerate doublets with wavefunctions containing a high level of mixing of X , Y , Z and D excitons.

Table 5.2 Eigenvalues and eigenfunctions of H_{Tot} for the hyperfine interaction of a Te₂-bound exciton and a ^{125}Te $1/2$ nuclear spin. All eigenvalues are given with respect to the lowest energy level in the H_0 basis, Z . \uparrow_n, \downarrow_n refer to the nuclear spin projections, $\pm 1/2$.

Eigenvalue (μeV)	Eigenfunctions
-14.6613	$i0.1119 X, \uparrow_n\rangle + (-0.0031 + i0.0018) X, \downarrow_n\rangle - 0.0539 Y, \uparrow_n\rangle + (0.0009 + i0.0015) Y, \downarrow_n\rangle + (-0.0216 + i0.0124) Z, \uparrow_n\rangle - i0.7730 Z, \downarrow_n\rangle + (0.0100 + i0.0173) D, \uparrow_n\rangle + 0.6213 D, \downarrow_n\rangle$
	$-i0.0036 X, \uparrow_n\rangle + (-0.0970 + i0.0559) X, \downarrow_n\rangle + 0.0017 Y, \uparrow_n\rangle + (0.0269 + i0.0467) Y, \downarrow_n\rangle + (-0.6698 + i0.3860) Z, \uparrow_n\rangle + i0.0249 Z, \downarrow_n\rangle + (0.3102 + i0.5383) D, \uparrow_n\rangle - 0.0200 D, \downarrow_n\rangle$
18.3292	$i0.0080 X, \uparrow_n\rangle - (0.0116 + i0.0004) X, \downarrow_n\rangle - 0.0035 Y, \uparrow_n\rangle + (-0.0018 + i0.0051) Y, \downarrow_n\rangle + (0.4970 + i0.1771) Z, \uparrow_n\rangle + i0.3405 Z, \downarrow_n\rangle + (-0.2194 + i0.6159) D, \uparrow_n\rangle + 0.4219 D, \downarrow_n\rangle$
	$i0.0124 X, \uparrow_n\rangle + (0.0075 + i0.0027) X, \downarrow_n\rangle - 0.0054 Y, \uparrow_n\rangle + (0.0012 - i0.0033) Y, \downarrow_n\rangle - (0.3207 + i0.1143) Z, \uparrow_n\rangle + i0.5276 Z, \downarrow_n\rangle + (0.1416 - i0.3975) D, \uparrow_n\rangle + 0.6538 D, \downarrow_n\rangle$
173.2725	$i0.9809 X, \uparrow_n\rangle + (-0.0890 + i0.1156) X, \downarrow_n\rangle - 0.0550 Y, \uparrow_n\rangle + (0.0065 - i0.0050) Y, \downarrow_n\rangle + (0.0072 - i0.0093) Z, \uparrow_n\rangle + i0.0792 Z, \downarrow_n\rangle - (0.0098 + i0.0075) D, \uparrow_n\rangle + 0.0829 D, \downarrow_n\rangle$
	$-i0.1459 X, \uparrow_n\rangle + (-0.5984 + i0.7773) X, \downarrow_n\rangle + 0.0082 Y, \uparrow_n\rangle + (0.0436 + i0.0335) Y, \downarrow_n\rangle + (0.0483 - i0.0628) Z, \uparrow_n\rangle - i0.0118 Z, \downarrow_n\rangle - (0.0657 + i0.0506) D, \uparrow_n\rangle + 0.0123 D, \downarrow_n\rangle$
389.5595	$i0.0614 X, \uparrow_n\rangle + 0.9970 Y, \uparrow_n\rangle - i0.0333 Z, \downarrow_n\rangle + 0.6538 D, \downarrow_n\rangle$
	$(0.0436 + i0.0433) X, \downarrow_n\rangle + (-0.7023 + i0.7076) Y, \downarrow_n\rangle + (0.0237 + i0.0235) Z, \uparrow_n\rangle + (0.0239 + i0.0241) D, \uparrow_n\rangle$

As can be seen from Table 5.2, hyperfine coupling with a single nuclear spin leads to new eigenstates that are too well separated in energy to be responsible for the oscillation effect. Moreover, their emission polarization severely deviates from what is expected of a C_{2v} exciton, while no such change was observed experimentally. These arguments point towards discarding hyperfine interaction as the cause of the splitting of X and Y into doublets.

Probability of occurrence The natural abundance of Te non-zero spin isotopes listed in Table 1.2 brings out that the probability of at least one of the two Te atoms in the Te_2 molecule bearing a spin $1/2$ is $1 - (1 - 0.0804)^2 = 0.1544$. We consider here that the low Te-doping concentration ensures that the only two Te atoms seen by the exciton are the ones forming its trap. Hyperfine interaction with a Te spin thus cannot account for the very high proportion of studied emitters clearly presenting an oscillation, i.e. 60 %, while the expected value would be the 15 % calculated above.

Furthermore, the number N of Zn and Se spins enclosed in the $1S$ excitonic wavefunction volume ($V_{\text{ex}} = 4\pi a_0^3/3 = 128.19 \text{ nm}^3$, with $a_0 = 3.129 \text{ nm}$ the exciton Bohr radius in ZnSe) is:

$$\begin{aligned} N_{\text{Zn}} &= 4 \cdot P(^{67}\text{Zn}) \cdot \frac{V_{\text{ex}}}{V_{\text{cell}}} = 4 \cdot 0.0410 \cdot \frac{128.19}{0.182} \simeq 115 \\ N_{\text{Se}} &= 4 \cdot P(^{77}\text{Se}) \cdot \frac{V_{\text{ex}}}{V_{\text{cell}}} = 4 \cdot 0.0764 \cdot \frac{128.19}{0.182} \simeq 215 \end{aligned} \tag{5.35}$$

since there are four atoms of each type in a ZnSe zincblende unit cell and its lattice constant a_{ZnSe} is 0.56692 nm [99], giving $V_{\text{cell}} = a_{\text{ZnSe}}^3 = 0.182 \text{ nm}^3$. P stands for the probability of occurrence of the relevant isotope (Table 1.2). The electron is therefore interacting with an important number of nuclear spins, the effect of which most likely averages out to zero unless nuclear polarization is achieved.

Nuclear polarization requirement A polarization of nuclear spins can be obtained optically through the dynamical nuclear polarization (DNP) mechanism, involving a spin transfer from a population of optically polarized unpaired electrons to a population of nuclei through the H_{hf} flip-flop terms [210]. This effect takes advantage of the longer lifetime of the nuclear spin ensemble, which are less coupled to the lattice compared to charge carriers, and leads to a non-vanishing nuclear magnetic field. DNP has been achieved in several qubit systems

such as QDs [210–212] and atomic impurities in semiconductors [213].

To reach significant nuclear polarization, electrons must be constantly pumped in a non-equilibrium spin state, for example in semiconductors through circularly-polarized trion transitions. As electrons relax toward their equilibrium distribution, some undergo a spin-flip and can transfer angular momentum to the nuclei through the hyperfine flip-flop terms. They are afterwards pumped and polarized again to perpetuate the mechanism. Fig. 5.30 illustrates an example of DNP for a positive trion (X^+) in the absence of a magnetic field, which can solely occur within the lifetime of the trion as it is also the time during which the unpaired electron exists and can interact with a nucleus [212]. Here, the hole must flip its spin before another DNP cycle can begin.

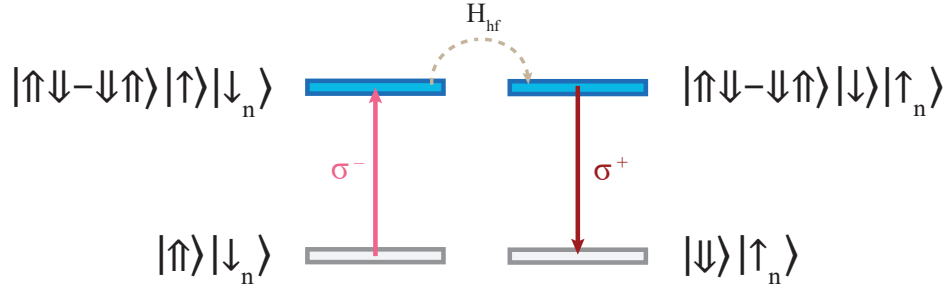


Figure 5.30 Dynamical nuclear polarization performed by the means of the positive trion transition. A σ^- -polarized excitation creates a positive trion on a Te_2 molecule that hosts a spin-up hole (\uparrow) in the vicinity of a spin-down nuclear spin (\downarrow_n). The resulting polarized electron (spin up, \uparrow) can interact with the nuclear spin through the hyperfine-Hamiltonian flip-flop terms H_{hf} and transfer its angular momentum within the trion lifetime. The recombination leaves a spin-down hole (\downarrow) and a spin-up nuclear spin (\uparrow_n) on the defect. The hole must first flip its spin before it can be re-pumped and perform the process again on another nuclear spin.

Achieving a large nuclear polarization with DNP is challenging. Values from 12 to 65 % have been reported for III-V QDs [210–212]. The resulting Overhauser nuclear magnetic field felt by electrons for a 100 % nuclear polarization could cause energy shifts up to 135 μeV in GaAs [212], 315 μeV in InAs and 230 μeV in InGaAs QDs [210]. Hence, one can expect that the nuclear polarization necessary for obtaining the sought-after $\sim 30 \mu\text{eV}$ splitting in ZnSe to be unattainable working with neutral C_{2v} excitons, which contains a superposition of spin $\pm 1/2$ electrons, and a linearly polarized excitation.

Finally, no difference in the oscillation behavior was experimentally noted working with linear and circular excitations, which suggests that DNP cannot be responsible for our observations.

Conclusion on the contribution of hyperfine interaction To wrap up, with the order of magnitude of the quantities relevant to our problem, hyperfine interaction with a single nuclear spin does not lead to the formation of energy levels separated by the desired energy and causes a dramatic change in the emission polarization, which is not verified by the experiment.

Interaction with a nuclear ensemble would require an important nuclear polarization unattainable by working with a neutral exciton and a linear excitation. Therefore, hyperfine interaction is most likely not the mechanism responsible for an hypothetical splitting of X and Y into doublets.

Bonding and anti-bonding levels of a Te cluster

The X', X'' doublet could also be formed of bonding and anti-bonding combinations of the X levels of two interacting excitons bound to a Te cluster, for example two Te_2 molecules. This cluster would have to bear C_{2v} symmetry and therefore all of its constituting atoms would have to be placed along the same $\langle 110 \rangle$ direction. The strength of the interaction would be determined by the atomic separation, giving rise to the $X'-X''$ splitting and to A_{em} .

A specific separation could in principle lead to the sought-after splitting of $40 \mu\text{eV}$. The distribution of Te atoms in the sample is however random and we would instead expect to see a rather large distribution of atomic separations, contradicting our experimental observation of a very narrow A_{em} range (mostly between $30\text{--}50 \mu\text{eV}$, see Fig. 5.5).

Finally, as reviewed in detail in Sect. 2.2.2, emission attributed to $\text{Te}_{n \geq 3}$ clusters happens in few hundred meV-wide structures centered between 2.45 and 2.52 eV [96, 144, 145, 147, 150, 152, 153], significantly lower than our observation range ($2.748\text{--}2.788 \text{ eV}$). The latter is much more in agreement with reported emission energies for Te_2 molecules ($2.6\text{--}2.8 \text{ eV}$ [84, 94–96, 144, 147, 152, 153]). With all of these arguments in mind, the hypothesis of a bonding–anti-bonding doublet can be rejected with confidence.

Conclusion on the nearly-degenerate doublet

To summarize, the splitting of excitonic transitions into nearly-degenerate doublets could in principle be seen as an unresolved broadened feature due to the resolution of our detection system. As E_{ex} is scanned, the relative amplitudes of the constituting transitions could periodically vary according to a cyclic coupling with the FX (involving for example alternating wavefunction parities) and lead to a perceived displacement of the emission structure.

However, after investigating all mechanisms that we could think capable of creating the doublets, i.e. symmetry splitting, hyperfine coupling and energy levels of a Te cluster, we must conclude that none of them can realistically be involved in the E_{em} oscillation, as they each do not match at least one of the following characteristics: a $\sim 30 \mu\text{eV}$ and statistically constant splitting and an emission polarization respecting C_{2v} symmetry. Consequently, we discard the hypothesis of a nearly-degenerate bound-exciton doublet without the need of exploring the mechanism at play in its coupling with the FX.

5.2.5 Conclusion on the origin of the E_{em} oscillation

After surveying multiples mechanisms that could be responsible for the E_{em} oscillation, it appears that the most complete and probable explanation for this phenomenon is the interaction, through exciton-exciton attraction or repulsion, or a DC Stark effect, of the bound exciton with free exciton-polaritons resonantly created by the excitation field. The strength of this interaction is modulated by the electric-field intensity distribution of the standing waves created in the ZnSe layer, which follows an oscillatory pattern as a function of E_{ex} . Although it does not grasp certain aspects of the experimental results, such as the E_{ex} range over which the oscillation occurs and the constancy of T_{ex} , the model leads to T_{ex} values in agreement with the data and to a curve shape that could easily correspond to that of the experiment if additional broadening were to be considered.

The other surveyed mechanisms have all been judged unlikely. Diamagnetic shifts and Zeeman effects would require large magnetic fields to produce an E_{em} shift of a few tens of μeV , not expected with linear excitation polarization. Phonon-assisted coupling with the FX requires a $\sim 1\text{-meV}$ phonon to account for T_{ex} , which is very unlikely, if not non-existent in ZnSe. Finally, the possibility for the bound exciton of forming a nearly-degenerate doublet through symmetry, hyperfine coupling or the formation of Te clusters has also been rebutted,

as none of these effects would give the approximate and constant 30- μeV splitting required to generate an A_{em} of 44 μeV .

5.3 General conclusion on the modulation of ZnSe:Te₂ emission properties

In this chapter, we have seen that the emission energy (E_{em}) of a Te₂-bound exciton undergoes an oscillation of constant amplitude as a function of excitation energy (E_{ex}) during PLE in the 2.785–2.815 meV excitation range, which includes the FX band. This effect affects synchronously both the X and Y transitions of all excitons in a same detection volume and is independant of excitation polarization and scan direction. The oscillation period (T_{ex}) varies from regions to regions in the sample, is included between 0.672–1.607 meV and has a mean value of 1.103 meV. The oscillation amplitude (A_{em}), for its part, ranges from 30 to 68 μeV , has a mean value of 44 μeV and is not correlated the PLE intensity.

Several mechanisms were explored to describe this surprising phenomenon. The first and most complete explanation was the interaction of the bound exciton with free exciton-polaritons resonantly created by the laser. Calculations involving the polariton dispersion relation at the FX resonance in ZnSe and a transfer-matrix treatment of the fields and interfaces have shown that at any specific position in the sample, the electric-field intensity distribution follows a periodic, Fabry-Perot-like behavior as a function of E_{ex} and contains resonances for both the lower (LPB) and upper (UPB) polariton branches. Exciton-exciton interactions arising from an imbalance between direct and exchange Coulomb interactions or a DC Stark effect due to charges generated by the polaritonic field would then lead to a E_{em} shift of the bound-exciton emission lines proportional to the field distribution. This model gave rise to a satisfactory value for T_{ex} (0.784–1.936 meV) and would reproduce well the general shape of the data if broadening were added by considering lower reflection coefficients. However, contrary to the experimental data, the oscillation did not happen below the resonance energy and had an increasing T_{ex} from cycle to cycle. These discrepancies justified the exploration of other mechanisms.

None of the alternative models would nonetheless prove to perform better than the polariton description. Indeed, any magnetic field-related effect caused by the excitation laser is expected to be negligible as it would require a large field magnitude (a few T at least) to cause a shift of a several tens of μeV . This would have presumably been very unlikely as the excitation was linearly polarized. Alternatively, coupling between a free exciton-polariton

level and a ladder of states composed of a bound exciton dressed by phonons of T_{ex} energy could in principle lead to an E_{em} shift of variable amplitude. Indeed, if the polariton were created in resonance with a state of the phonon-dressed exciton ladder, the interaction (and thus the shift) would be maximal, while it would be minimal for a polariton in the middle of two ladder states. However, no optical, acoustic, confined or local phonon mode was found suitable for the creation of the energy ladder, either by having the wrong energy or by being unlikely. Finally, the splitting of the excitonic transitions into nearly-degenerate doublets was considered, but no appropriate mechanism could be elaborated. Symmetry, hyperfine coupling and the formation of Te clusters were all rebutted due to their unlikeliness or the discrepancies between their properties and those of the experimental data, such as emission polarization and the statistical distribution of A_{em} .

Although its origin is still unclear, the remote modulation of ZnSe:Te₂ emission properties opens interesting avenues for control protocols, and in that sense, is worth further studies. The phenomenon could indeed allow the tuning of an emitter with a cavity or with another emitter, especially if the modulation amplitude A_{em} could be controlled and enhanced. Experiments could be designed to further explore the polariton hypothesis, such as employing samples of different thicknesses, varying the incidence angle of the excitation field or attempting coupling with cavity polaritons.

CHAPTER 6 RESONANT EXCITATION OF AN EXCITONIC QUBIT IN ZnSe

A significant step in the characterization of an optically addressable qubit (OAQ), as mentioned earlier, is the demonstration of optical coherent control of its quantum state. Here, we performed resonant excitation on ZnSe:Te₂ Samples B and C (Fig. 3.1) with the hopes of observing a signature of coherent interaction between an excitonic qubit and the light field in the form of Rabi oscillations (Sect. 2.4.1), which rotate the state of the former about a single axis on the Bloch sphere. This was done, as detailed in Sect. 3.3.4, by resonantly exciting one of the two detectable transitions of a Te₂-bound exciton (X or Y) with a laser pulse and detecting its orthogonally-polarized LO-phonon replica (respectively $Y-LO$ and $X-LO$). By varying the pulse area (in this case with the excitation power (P_{ex})), different rotation angles could be achieved, and a Rabi curve was constructed.

Rabi oscillations found in textbooks [12,169] and recent publications [25,33,36,38,42,44,45,47] present a well-defined sinusoidal pattern from which the dipole moment and an evidence of excitation-induced dephasing (EID, i.e. a diminution in fringes visibility due to a coherence time reduction as a function of P_{ex}) can be extracted, two properties we sought to characterize in our study. We also aimed at identifying the optimum conditions for the observation of Rabi oscillations in our system. The obtained behavior was not as straightforward to analyze and understand as in the literature, as coherence could be observed for some of the single emitters and was strongly limited by extrinsic factors. In total, three distinct behaviors were observed, which were attributed to the influence of the environment on the quantum properties of the studied emitters.

The results also gave insight on the excitation mechanisms at play during resonant excitation in the pulse regime and on the impact of the environmental charge fluctuations on the coherent behavior. In particular, we uncovered the effect of a Rabi frequency (Ω) fluctuation on the resonant-emission signature of a coherent emitter. Two methods were attempted to stabilize the environment and mitigate its influence: a weak, non resonant (NR) laser on Sample B and an electric field on Sample C.

The chapter is organized as follows: after briefly reviewing the NR emission characteristics of emitters in Sample B, a comprehensive model of resonant emission for the bound exciton is

elaborated, including both coherent and incoherent population contributions to the emission signal. Then, the different observed emission behaviors are presented, with a discussion on how the model can reproduce them. Finally, the performance of the environment-stabilization measures is evaluated.

6.1 Statistical distribution of the emission properties of excitons measured in Sample B

19 distinct emitters were thoroughly studied under resonant excitation in Sample B. The X exciton-emission energy (E_X) in non resonant (NR) excitation conditions, its full width at half maximum (FWHM) and the fine-structure splitting (FSS or ΔE_{XY}) between X and Y varied considerably from one emitter to the other. The E_X distribution indeed spanned over an interquartile range $Q_3 - Q_1$ of 4.813 meV (Q_1 and Q_3 are respectively the first and third quartiles) and was centered at a mean of 2.775 724 eV (Fig. 6.1 (a)). The FSS had a mean value of 431 μ eV (panel (b)), with half of the population situated within a Q_1 of 177 μ eV and a Q_3 of 555 μ eV. The FWHM was for its part limited by the resolution of the CCD camera to about 120 μ eV, with an average value of 165 μ eV (panel(c)). Most of the distribution was concentrated between 120 and 170 μ eV, but a few rare excitons had widths as high as 329 μ eV.

6.2 Modelling of the resonant PL data

Resonant PL signal from single Te_2 molecules in ZnSe could be categorized in three distinct behaviors, as illustrated in upcoming Sect. 6.3. Fig. 6.2 presents an example of the most striking of them, a single Rabi oscillation cycle of the emission intensity (I_{em}) superimposed to a monotonous increase that rises above the oscillation maximum. This data was obtained with a stabilizing NR laser power (P_{NR}) of 1 μ W, the effect of which is detailed later.

I_{em} , the area of the first LO phonon replica, is plotted as a function of $P_{\text{ex}}^{1/2}$, which is proportional to the rotation angle performed by the laser pulse upon coherent interaction (Eq. 2.28). P_{ex} is the excitation power and refers to the portion of the excitation beam transmitted by the non-polarizing beam-splitter cube on the setup (see Fig. 3.3), as its monitoring was most convenient experimentally. The range available was 0–1600 μ W. To convert the displayed values to the power at the position of the sample, one must apply a factor of 0.1276, correcting for the optics transmission in the beam path. Also, since the linewidth of the emit-

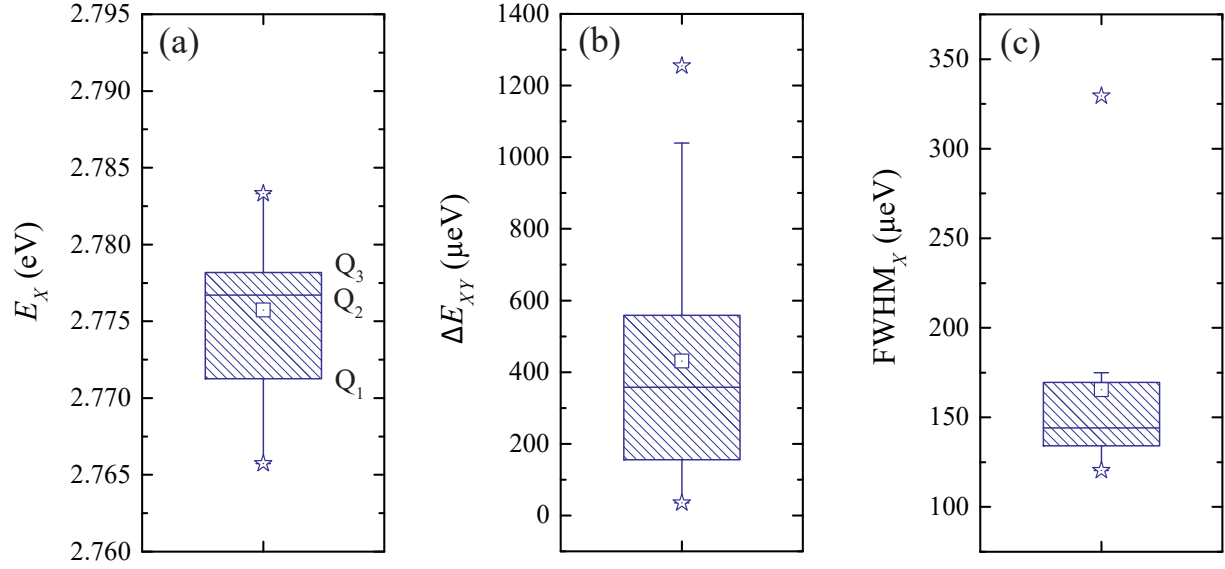


Figure 6.1 NR emission statistics for Sample-B excitons investigated in the resonant PL experiment, (a) exciton emission energy (E_X), (b) fine-structure splitting (ΔE_{XY}) and (c) full width at half maximum of the X transition (FWHM_X). The vertical limits of the hatched boxes are the quartiles (Q_1 and Q_3) and the middle line, the median (Q_2). Their bracket extensions mark the position of the farthest data point in 1.5 times the interquartile range ($Q_3 - Q_1$) below Q_1 or above Q_3 . The square marker indicates the mean and the stars, the minimum and maximum values of the data set.

ter ($\sim 16.5 \mu\text{eV}$) is negligible compared to that of the pulsed resonant laser (4.7–13.3 meV), the effective P_{ex} is reduced by an additional factor of ~ 0.0014 on average, calculated from area ratio of between the pulse and the Lorentzian absorption cross-section.

The behavior displayed in Fig. 6.2 is more complex than a typical Rabi oscillation signature and is composed of a strong coherent part at low $P_{\text{ex}}^{1/2}$ that becomes rapidly damped and exceeded by an incoherent contribution as $P_{\text{ex}}^{1/2}$ increases. Hence, I first wish to present the tools with which I analyze the obtained results in Sect. 6.3. In addition to the coherent contribution described by the optical Bloch equations, I also include an incoherent population mechanism due to the tunneling of excitons from nearby higher-energy Te_2 molecules, which are also resonantly excited by the wide laser pulse. I review both in the next sections, as the knowledge of these models and the impact of their different parameters subsequently facilitate the explanation of the experimental results, where several effects might occur conjointly and vary between repetitions of the experiment (i.e. from pulses to pulses) and with P_{ex} or non-resonant power (P_{NR}).

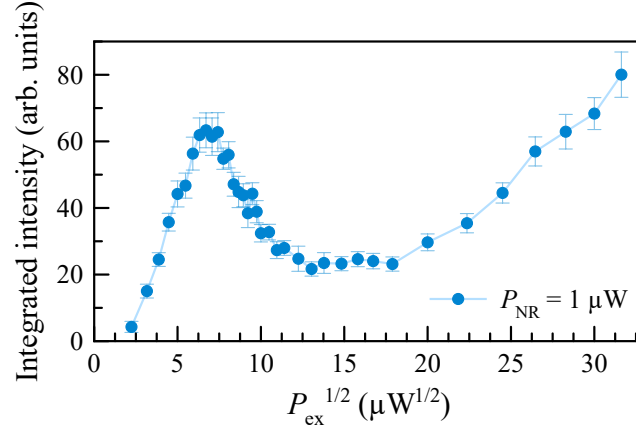


Figure 6.2 Resonant PL data of a single Te_2 -bound exciton, displayed as the intensity of the first LO replica of its orthogonal transition as a function of the square root of the excitation power P_{ex} . This curve presents one of the three behaviors observed, a single oscillation cycle superimposed on a monotonous rise.

6.2.1 Coherent contribution: optical Bloch equations

In Sect. 2.4.2, I have reviewed the optical Bloch equations describing the evolution of the populations and coherences of a two-level system (TLS) as it interacts with an optical electric field. This formalism is now used to simulate the emission behavior of our emitters under pulsed resonant excitation. More precisely, I wish to illustrate the effect of the relaxation time (T_1), coherence time (T_2), dipole moment (d) and detuning (Δ) on the shape of the resonant PL curve. The objectives are to identify the relevant parameters to the modelling of the experimental data and to clarify the mechanisms limiting the coherence of the emitters.

The default values for the parameters are listed in Table 6.1 and are based upon typical values measured in ZnSe:Te_2 or, if unavailable, other similar IC systems such as GaAs:N_2 . If not stated otherwise, these are the values used to produce the graphs presented in the next sections. The value for T_2 measured in Ref. [25] is in fact T_2^* , but I used it directly as a starting point. T_1 was measured for a trion in Ref. [28]. I also assume all parameters related to the gaussian excitation-laser pulse (temporal FWHM (τ_p), repetition rate ($1/\tau_R$) and area (S)) except its root-mean-square power (P_{RMS}) to be constant throughout the experiment.

To fully grasp the effect of all emitter-related parameters in the pulsed-excitation picture,

where the duration of the interaction is fixed by τ_p , Bloch equations were repeatedly solved for a single varying parameter, keeping all others to their default value. Simulation results are then displayed, in most cases, as the excited state population ρ_{XX} as a function of the rotation angle Θ defined by Eq. 2.28. As the population relaxation during the interaction with the pulse is negligible, I_{em} , expressed in number of photons, is indeed proportional to ρ_{XX} at the end of the pulse.

Table 6.1 Default parameters used in the resolution of the optical Bloch equations. Left: emitter, right: excitation laser.

Te ₂ -bound exciton			Laser	
Parameter	Value	Reference	Parameter	Value
d	30 D	[25]	τ_p	1 ps
Δ	0 μeV	–	$1/\tau_R$	80 MHz
T_1	80 ps	[28]	S	0.45 μm^2
T_2	115 ps	[25]		

I discuss next the influence of all four emitter parameters on the resulting ρ_{XX} .

Effect of the relaxation time

The relaxation time (T_1) describes the time scale on which the excited-state population relaxes towards the ground state. Its greatest contribution comes from the radiative lifetime of the $|X\rangle \rightarrow |0\rangle$ transition. Its value is linked to that of T_2 by the inequality $T_2 \leq 2T_1$, and therefore in the case of this simulation must physically be larger than 57.5 ps for $T_2 = 115$ ps.

One can see on Fig. 6.3 that, in the limit of the ultrashort pulses used in this experiment, T_1 has very little impact on the visibility of the oscillations and on the maximum population achieved as it is varied from 57.5 to 1000 ps. In other words, the population does not have time to decay within the pulse duration. The choice of T_1 value is therefore not so critical and, once picked, can be kept constant in the rest of the simulation. Muller *et al.* presented a higher bound for $T_1 = 1/\Gamma_{\text{rad}}$ of 500 ps for a Te₂-bound exciton [94]. Yet, since this value is limited by the resolution of their system, I chose instead $T_1 = 80$ ps, extracted for the trion in Ref. [28] (also limited by their system resolution).

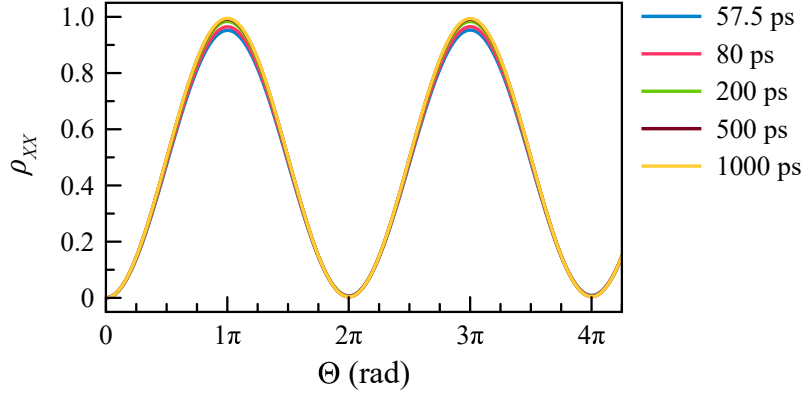


Figure 6.3 Effect of T_1 on the shape of the Rabi curves, with constant parameters $d = 30$ D, $\Delta = 0$ μ eV, $T_2 = 115$ ps and $\tau_p = 1$ ps. Since τ_p is very short, ρ_{XX} does not have time to decay during the interaction. T_1 does not have a significant impact on the final population reached.

Effect of the dipole moment

Since the Rabi frequency (Ω) is proportional to the dipole moment (d), a change in d results in a change in Ω and also in Θ for a particular value of E_0 . This is illustrated in Fig. 6.4, in which d is varied from 5 to 60 D. The excited state population ρ_{XX} undergoes an oscillation of increasing frequency with no change in maximal population or visibility. This emphasizes the increase in interaction strength between the TLS and the field, as a higher d logically requires a weaker field to achieve the same rotation angle.

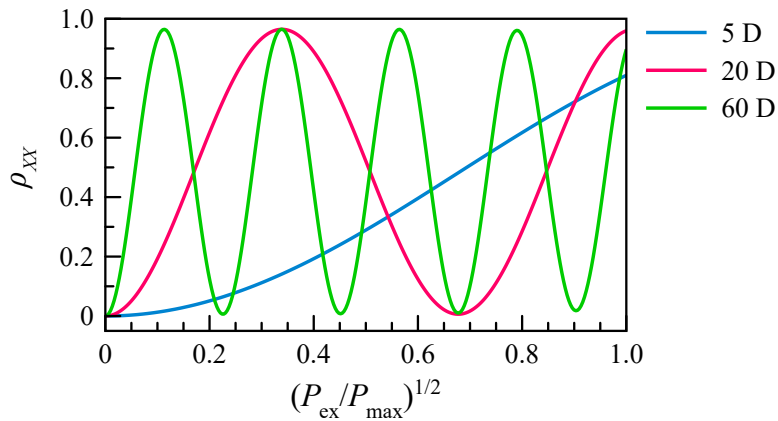


Figure 6.4 Effect of d on the shape of the Rabi curves, with constant parameters $\Delta = 0$ μ eV, $T_1 = 80$ ps, $T_2 = 115$ ps and $\tau_p = 1$ ps. The data is plotted as a function of the square root of P_{ex} (normalized to its maximum value P_{max}) in order to illustrate the dependence of Ω on d .

The observation and fitting of several oscillation cycles in resonant PL data allows to extract an experimental value for d .

Impact of the detuning

Spectral diffusion, i.e. the phenomenon by which the emission energy (E_{em}) of a single emitter drifts due to environmental perturbations, could in principle impact the resonant excitation experiment by randomly varying the detuning (Δ) between the TLS and the driving field. In the case of randomly charging and discharging defects, the fluctuations indeed occur over a time scale of the order of the ps [175], quite comparable to the pulse width $\tau_p = 1$ ps.

The simulation of Fig. 6.5 indicates that an increase in Δ from 0 to 1 meV leads to a reduction of the maximum attainable ρ_{XX} , especially in the first Rabi cycle where Ω is small, and to a slight increase in the generalized Rabi frequency $\tilde{\Omega}$. Below 500 μeV , the pulse is so short with a peak amplitude so great that Δ has a marginal effect on the rotations. The threshold value of 500 μeV is already larger than the most dramatic drifts (300–400 μeV) observed during the PLE experiment (see Sect. 4.5). Therefore, in the ultrashort-pulse regime, even in the presence of an important spectral diffusion, these results suggest that the excitation can be considered resonant with the transition.

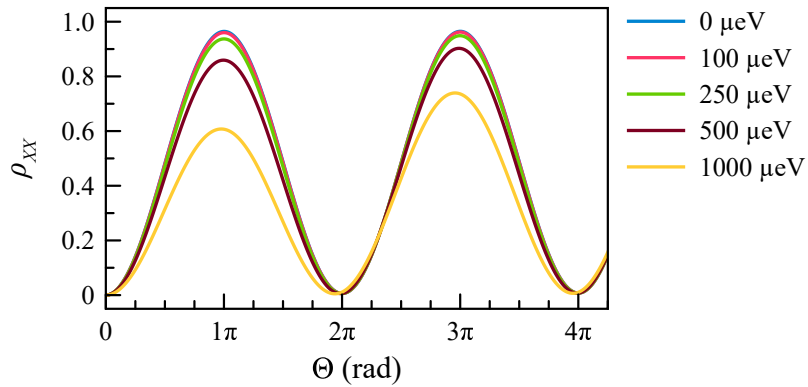


Figure 6.5 Effect of Δ on the shape of the Rabi curves, with constant parameters $d = 30$ D, $T_1 = 80$ ps, $T_2 = 115$ ps and $\tau_p = 1$ ps. Due to the very short and intense excitation pulse, Δ must be very large to have an impact on the oscillations.

Effect of the coherence time

The coherence time (T_2) can significantly affect the visibility of the oscillation, as illustrated by the simulation of Fig. 6.6. Here, T_1 is fixed at 80 ps, hence the upper bound for T_2 is 160 ps. The impact of the latter becomes clearly visible as it approaches the same order of magnitude as the excitation-pulse length, ~ 1 ps. A further decrease to 0.1 ps, an order of magnitude shorter than τ_p , leads to a complete damping of the curve and a saturation of the population (here at $\rho_{XX} \sim 0.4858$).

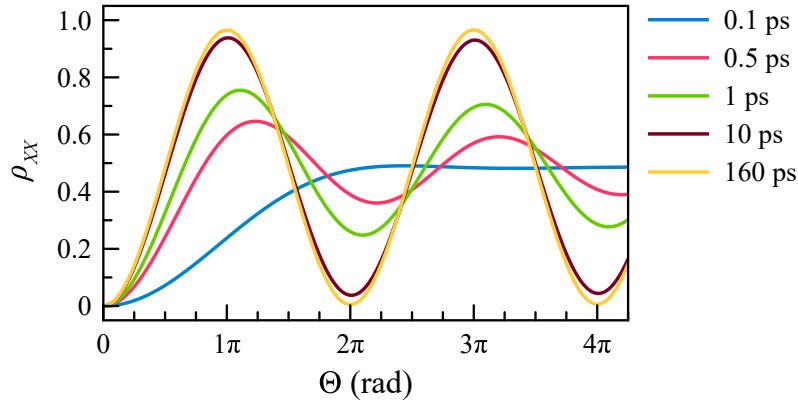


Figure 6.6 Effect of T_2 on the shape of the Rabi curves, with constant parameters $d = 30$ D, $\Delta = 0$ μ eV, $T_1 = 80$ ps and $\tau_p = 1$ ps. When very short, the contrast of the oscillation is lost and ρ_{XX} saturates.

Such very short T_2 values are unexpected in our system, as values for similar systems range in the hundred of ps (e.g. 115 ps for GaAs:N₂ [25]). ZnSe:Te₂ seems to present more defects and charge effects than GaAs:N₂, but it also has less nuclear spins, an important decoherence mechanism in III-V semiconductors. We thus expect a T_2 of the same order of magnitude, or a little shorter, approximately between 10 and 150 ps, but not much less.

6.2.2 Incoherent contribution: tunneling from adjacent Te₂ molecules

The monotonic I_{em} rise superimposed to the single oscillation cycle in Fig. 6.2 cannot be accounted for by the coherent interaction formalism presented above. One must therefore add another contribution to the population in the form of an incoherent mechanism.

As it is fairly common to see more than one Te₂-bound exciton in the same detection volume,

there is a non-negligible probability that our emitter of interest be populated by the tunneling of an exciton from a nearby, higher-energy Te_2 molecule. Phonon-assisted tunneling between adjacent isoelectronic centers has been thoroughly studied in GaP:N_2 [214–217]. As can be seen on the PLE spectra of Fig. 6.7, I_{em} from an ensemble of first-neighbor N_2 molecules (NN_1 , at $\sim 2.816 \text{ eV}$) is enhanced as the excitation laser comes in resonance with further-neighbor molecules ($\text{NN}_3\text{--NN}_7$) and with unpaired N atoms (NN_∞ or A line) [214]. The process has been found to occur on distances up to 5–15 nm, given the large extent of excitonic wavefunctions, at a rate γ_T depending on the distance R between tunneling sites [214, 215, 217]:

$$\gamma_T = \gamma_{T,0} e^{-2R/a_{ij}}, \quad (6.1)$$

with $\gamma_{T,0}$ in the $10^{12}\text{--}10^{13}$ Hz range and a_{ij} an effective exciton radius taking into account the initial and final states (2.2–4.0 nm). The exponential dependence on R comes from an approximation of the shape of the excitonic wavefunction far from its binding site [215]. The farthest tunneling distance of 15 nm gives rise to a higher-bound value of $0.84 \mu\text{s}$ for the tunneling time $1/\gamma_T$, comparable to the 0.1–1- μs exciton radiative lifetime [214, 215, 217]. The process is therefore likely to occur prior to radiative recombination.

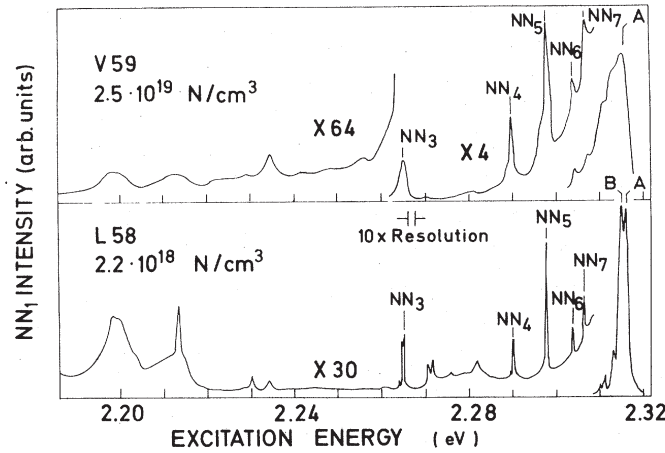


Figure 6.7 PLE spectra of the NN_1 molecule in GaP . I_{em} is increased significantly as the excitation energy comes into resonance with other N_2 molecules (NN_i , $i = \{3, 4, \dots, 7\}$) and with isolated N atoms (A, B), illustrating the efficient tunneling mechanism from higher-energy molecules towards lower-energy ones. Two samples with different N concentration are shown. Reprinted with permission from Ref. [214]. Copyright (1975) by the American Physical Society.

In ZnSe:Te_2 , this process has been observed [175] even if the radiative lifetime is much shorter (80 ps [28]). One therefore expects $\gamma_{T,0}$ to be several orders of magnitude larger than in

GaP:N₂. Also, the Te₂-molecule concentration in our samples is estimated at 4 μm⁻¹ [84,175], leading to an average inter-molecule distance of 500 nm, much larger than the cases studied in GaP:N₂. This points out that the molecules might be unevenly distributed, in greater concentration than expected or that higher-order molecules (second, third-neighbor) play a role, although they have never been reported.

In addition to higher-energy Te₂ molecules, the crystal hosts several other defects states such as dislocations from which the exciton can also tunnel. However, since little is known about the peculiarities of these transfers, the following discussion focuses on the tunneling mechanism involving two Te₂ molecules (Te₂ → Te₂).

Balance of populations describing tunneling in ZnSe:Te₂

Fig. 6.8 presents the energy levels involved in the description of a simple tunneling mechanism leading to the incoherent population of our emitter of interest. A population of excitons n_{Te_2} is created by a laser pulse on n Te₂ molecules in the vicinity of the emitter, at a rate $\Gamma_{\text{ex}} = G_{\text{ex}} P_{\text{ex}}$ (G_{ex} is the pumping rate per unit power and P_{ex} is the excitation power). It can afterward either transfer one exciton to the emitter bright state X at a rate $\gamma_{\text{Te}_2 \rightarrow X}$ or decay towards the ground state population n_0 at a rate Γ_D , which is characterized by the lifetime of the longer-lived dark state of a Te₂-bound exciton. The bright state population n_X can recombine radiatively at a rate $\Gamma_{\text{rad}} = 1/T_1$ or transfer to its associated lower-energy dark state D by an acoustic phonon-assisted spin-flip mechanism at a rate [94, 123, 218]:

$$\gamma_{\text{sf}} = \gamma_0 \left(1 + \frac{1}{e^{\Delta E/(k_B T)} - 1} \right) = \gamma_0 + \gamma'_{\text{sf}}, \quad (6.2)$$

where ΔE is the energy separation between X and D , k_B is Boltzmann's constant, T is the temperature and γ_0 is the $T = 0$ K spin-flip rate. The reverse process from n_X to n_{Te_2} is not considered here, as it involves phonon-assisted tunneling to a single Te atom before transferring to another Te₂ molecule. This two-step mechanism has indeed been evaluated to be at least 10³ times less probable than a transfer from a higher to a lower energy IC in GaP:N₂ [217].

The dark state population n_D for its part can transfer back to n_X by a similar spin-flip process involving the absorption of a phonon at a rate γ'_{sf} , or decay to n_0 at Γ_d . The total population on the emitter of interest $n_{\text{tot}} = n_X + n_D$ is limited to 1, as the defect cannot

host more than one exciton, while the maximum value of n_{Te_2} is n .

These mechanisms are translated in equations by a balance of populations:

$$\begin{aligned}
 \frac{dn_X}{dt} &= (1 - n_{\text{tot}})\gamma_{\text{Te}_2 \rightarrow X} n'_{\text{Te}_2} - (\Gamma_{\text{rad}} + \gamma_{\text{sf}}) n_X + \gamma'_{\text{sf}} n_D \\
 \frac{dn_D}{dt} &= \gamma_{\text{sf}} n_X - (\gamma'_{\text{sf}} + \Gamma_D) n_D \\
 \frac{dn_{\text{Te}_2}}{dt} &= \Gamma_{\text{ex}} n_0 - \Gamma_D n_{\text{Te}_2} - (1 - n_{\text{tot}})\gamma_{\text{Te}_2 \rightarrow X} n'_{\text{Te}_2} \\
 \frac{dn_0}{dt} &= \Gamma_{\text{rad}} n_X + \Gamma_D (n_D + n_{\text{Te}_2}) - \Gamma_{\text{ex}} n_0,
 \end{aligned} \tag{6.3}$$

with n'_{Te_2} a quantity describing the transfer of a single exciton from an adjacent Te_2 molecule to X . It has a value of 1 if $n_{\text{Te}_2} \geq 1$ and the same value as n_{Te_2} otherwise. The exciton transfer efficiency is also modulated by the unoccupancy probability of the emitter, $1 - n_{\text{tot}}$. I_{em} for this contribution, expressed in number of photons, is given by:

$$I_{\text{em}} = \Gamma_{\text{rad}} \int_0^{\tau_R} n_X(t) dt, \tag{6.4}$$

where τ_R is the time separation between two consecutive laser pulses and equals 12.5 ns, a time scale longer than all excitonic processes.

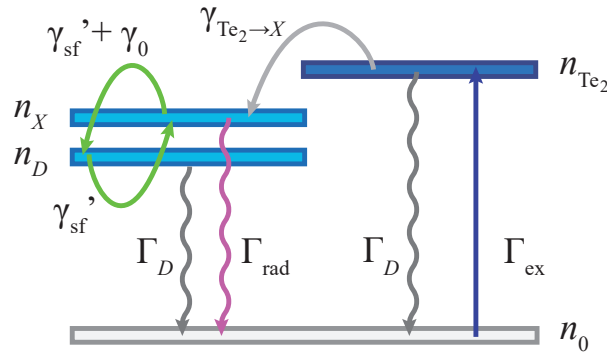


Figure 6.8 Four-level system involved in the balance of the populations model of incoherent excitation of a Te_2 -bound exciton by the means of an adjacent Te_2 molecule. A population n_{Te_2} is created on n defects by the laser pulse (Γ_{ex}), which can transfer one exciton to the Te_2 molecule of interest (n_X) at rate $\gamma_{\text{Te}_2 \rightarrow X}$ or decay at rate Γ_D towards the ground state (n_0). n_X then decays radiatively to n_0 (Γ_{rad}), giving rise an incoherent PL signal, or transfers to its associated dark state (n_D) by a phonon-assisted spin-flip ($\gamma_{\text{sf}} = \gamma'_{\text{sf}} + \gamma_0$). n_D for its part can transfer back to n_X (γ'_{sf}) or decay towards n_0 (Γ_D).

Impact of the transfer rates on the incoherent PL signal

I_{em} obviously depends on the transfer rates, it is therefore crucial to look into their order of magnitude and how they influence the emission response. Figs. 6.9–6.14 present examples of I_{em} -vs- $P_{\text{ex}}^{1/2}$ curves for values of P_{ex} concurring with those of the experiment (0–1600 μW , see beginning of Sect. 6.2 for details), on which each of the involved rates are individually varied. The effects of these variations are discussed below. Table 6.2 summarizes the default values used for the computation. The default temperature is taken as that of the sample holder in the cryostat, 7 K, and the number of neighboring Te_2 molecules (n) is chosen as 2, which defines the maximum number of photons that can be collected per pulse. The pulse parameters are the same as in Table 6.1.

Table 6.2 Default transfer rates used in the resolution of the balance of populations equations describing incoherent PL.

Rate	Value	Reference	Rate	Value
Γ_{rad}	$1/80 \text{ ps}^{-1}$	[28]	G_{ex}	$1/50 \text{ fs}^{-1} \text{ W}^{-1}$
Γ_D	$1/3 \text{ ns}^{-1}$	[94]	$\gamma_{\text{Te}_2 \rightarrow X}$	$1/5 \text{ ps}^{-1}$
γ_0	$1/0.1 \text{ ns}^{-1}$	[123]		

First, $1/\Gamma_D$ is evaluated at 2–4 ns for ZnSe:Te_2 in Ref. [94], so I chose the mean value of 3 ns as a starting point. In Fig. 6.9, one can see that a decrease in Γ_D leads to an increase in the collected PL, as D has more time to transfer back to X before decaying.

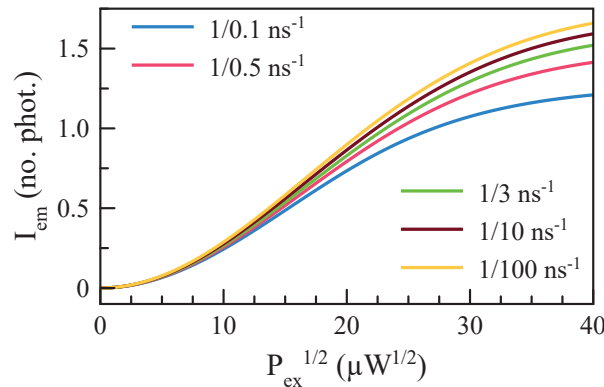


Figure 6.9 Effect of the dark exciton decay rate Γ_D on the incoherent PL intensity I_{em} . A lower Γ_D gives more time to the bound exciton to transfer towards X and consequently increases I_{em} .

Second, I used the same default value of $T_1 = 1/\Gamma_{\text{rad}}$ as in Sect. 6.2.1, 80 ps [28]. As Γ_{rad} diminishes, the number of photons collected within the 12.5-ns window defined by the laser repetition rate unsurprisingly decreases, as shown on Fig. 6.10. It takes indeed more time to the system to emit the same number of photons.

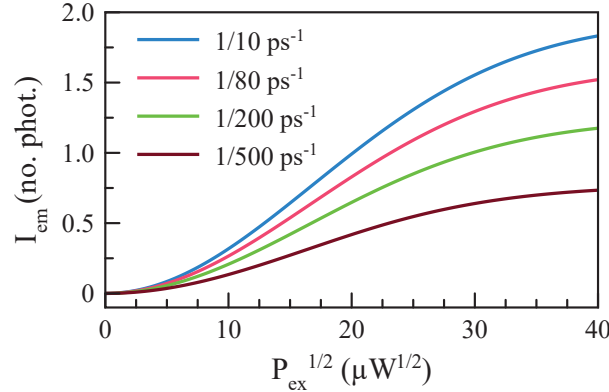


Figure 6.10 Effect of the bright exciton radiative recombination rate Γ_{rad} on the incoherent PL intensity I_{em} . A smaller Γ_{rad} reduces the number of emitted photons during the time interval between two laser pulses.

Third, the $T = 0$ K spin-flip rate γ_0 is assumed in Ref. [94] to be larger than Γ_{rad} , although no value is reported. However, since they probably underestimated Γ_{rad} due to their resolution limit, I used as a starting point the value found for the first-neighbor N_2 molecule in GaP, $1/0.1 \text{ ns}^{-1}$ [123], very similar to that reported for CdSe/ZnS QDs [218]. In Fig. 6.11, increasing γ_0 favors the $X \rightarrow D$ transfer over the reverse process, as the probability of emitting a phonon is substantially greater than that of absorbing one at low temperature. I_{em} is consequently lower for large γ_0 .

Fourth, the sample temperature T at the excitation focal point could be higher than that of the rest of the lattice. However, since I had no experimental means of evaluating the laser-induced heating of the sample, I used the equilibrium temperature of 7 K in the data analysis of Sect. 6.3. The greatest impact of an increase in T is to open more important non-radiative recombination channels that lower I_{em} , which I do not consider in the model. T also change the relative contributions of γ_{sf} and γ'_{sf} , making the phonon absorption process efficiency more or less comparable to that of emission. The increased $D \rightarrow X$ transfer therefore leads to a greater I_{em} (Fig. 6.12), although the effect is not very important compared to other parameters.

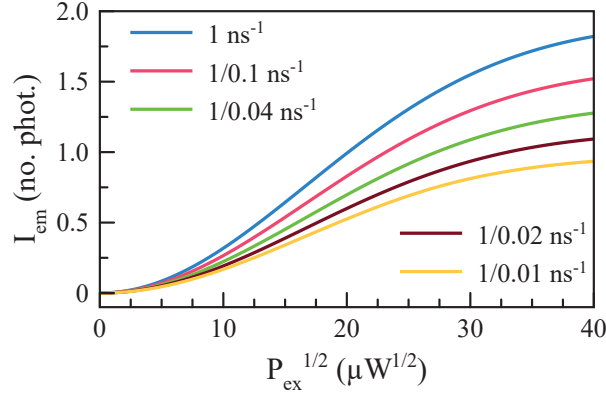


Figure 6.11 Effect of the $T = 0$ K spin-flip rate γ_0 on the incoherent PL intensity I_{em} . At low temperature, the emission of a phonon is more probable than absorption. As γ_0 increases, I_{em} decreases, since the $X \rightarrow D$ transfer process is favored.

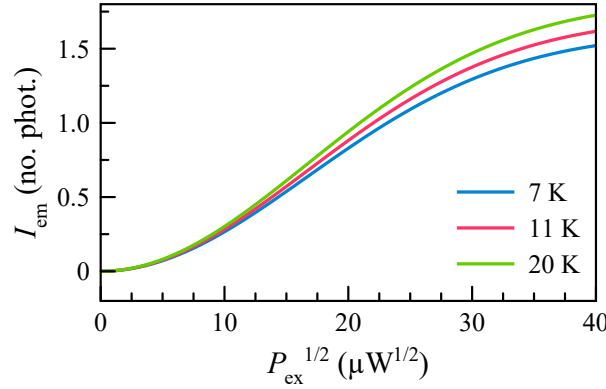


Figure 6.12 Effect of the temperature, which determines the balance between the spin-flip rates γ_{sf} and γ'_{sf} , on the incoherent PL intensity I_{em} . A higher T increases the probability of the $D \rightarrow X$ transfer with respect to that of $X \rightarrow D$, therefore increasing I_{em} .

Fifth, G_{ex} influences the slope of the initial rising portion of the PL curve: a larger G_{ex} implies that I_{em} reaches its maximum value at lower P_{ex} (Fig. 6.13). This rate is determined by the capture of an exciton by a Te_2 molecule. In GaAs:N_2 , such a process has been evaluated to occur at a rate $1/2.5 \text{ ns}^{-1}$ through non-resonant time-resolved PL measurements [83]. Similar measurements on the trion in ZnSe:Te_2 has given a value of $1/110 \text{ ps}^{-1}$, with an excitation at the FX energy [28]. One can however expect the resonant process to be faster, as the exciton is directly created on the molecule and does not have to go through tunneling or energy relaxation mechanisms. Also, as it is illustrated below by the experimental data,

the contribution of the incoherent emission mechanism must compare with that of coherent interaction, which emits up to one photon per pulse. Therefore, a pumping rate such as that reported in [83] would be too small, as I_{em} at the largest P_{ex} would be a negligible $\sim 9 \times 10^{-5}$ photon. These two arguments have led me to choose the default value of $1/50 \text{ fs}^{-1} \text{ W}^{-1}$.

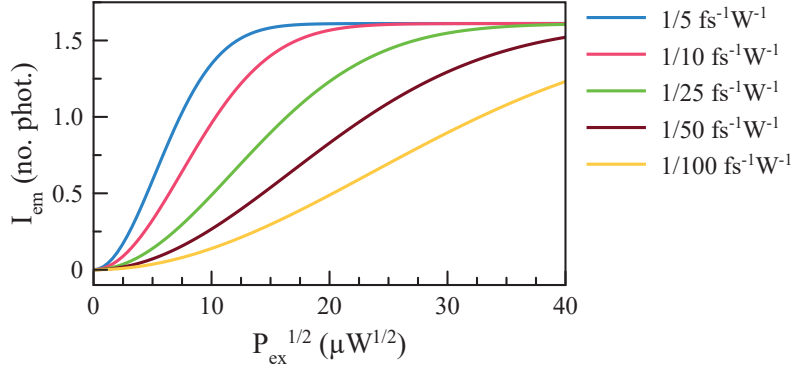


Figure 6.13 Effect of the pumping rate per unit power G_{ex} on the incoherent PL intensity I_{em} . A faster creation of an exciton on a neighboring Te_2 molecule allows reaching the maximum I_{em} at lower P_{ex} . The curves clearly show the saturation behavior of the incoherent PL.

Finally, $\gamma_{\text{Te}_2 \rightarrow X}$ must be greater than Γ_{rad} in order for the incoherent population mechanism to be efficient. I consequently used $1/5 \text{ ps}^{-1}$ as a starting point. However, as can be seen on Fig. 6.14, its impact is not significant, as the maximum I_{em} reached only diminishes slightly if $\gamma_{\text{Te}_2 \rightarrow X} = \Gamma_{\text{rad}}$. To significantly affect the shape of the curve, it would indeed need to be much slower than Γ_{rad} , which is not in agreement with experimental observations of the tunneling efficiency from one Te_2 molecule to another [175].

Due to the very similar effects of most of the rates, I kept the values found in the literature for Γ_D , Γ_{rad} and γ_0 in the analysis of Sect. 6.3, as there is no reason that they would change as a function of P_{ex} or P_{NR} . I also fixed T at 7 K as I do not include other thermally-assisted recombination paths in the model. The tunneling rate $\gamma_{\text{Te}_2 \rightarrow X}$ for its part could be P_{ex} -dependent, and the pumping rate per unit power G_{ex} could vary considerably from emitter to emitter.

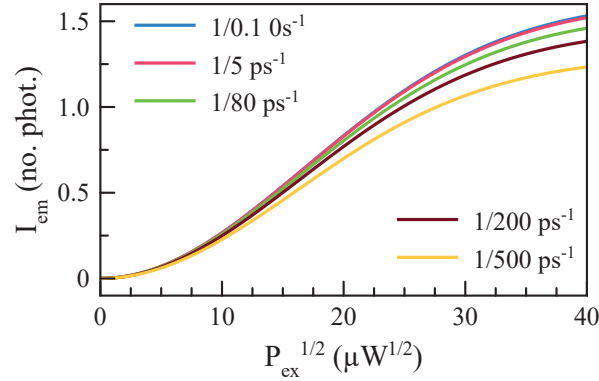


Figure 6.14 Effect of the tunneling rate between two Te_2 molecules $\gamma_{\text{Te}_2 \rightarrow X}$ on the incoherent PL intensity I_{em} . A faster transfer gives rise to a greater n_X population and increases I_{em} .

Impact of the number of neighboring Te_2 molecules participating in the mechanism

According to our model, the number of neighboring Te_2 molecules n establishes a higher-bound value for the exciton reservoir population n_{Te_2} available for tunnelling onto the emitter of interest within the time interval between two laser pulses. It therefore increases the number of photons that can be collected from the radiative recombination of the emitter, as the reservoir feeds the molecule with a new exciton each time the previous one recombines. The maximum possible I_{em} is therefore n photons.

Fig. 6.15 shows the simulation curves as n is varied from 1 to 10. One can see that as n increases, more photons are indeed collected, but that they do not reach their maximum value for large n due to the interplay of the other transfer and decay rates, especially Γ_D which governs the longest Te_2 -molecule lifetime.

The value used for n in Sect. 6.3 depends on the shape of the resonant PL curves and is discussed throughout the text below. A general consideration can nevertheless be made, since the Te_2 molecules in the reservoir are coherently driven by the very broad laser pulse (4.7–13.3 meV). To obtain a truly incoherent population mechanism, n cannot be 1, as the emitter of interest would in this case act as a witness state for the Rabi oscillations undergone by the reservoir, a signal that would be incoherently added to its own Rabi oscillations. It is therefore required to have at least two reservoir molecules with distinct Rabi frequencies that average to an incoherent mechanism over the large number of repetitions within the

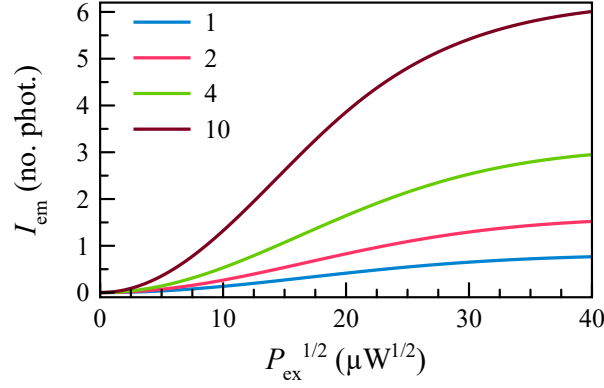


Figure 6.15 Effect of the number of neighboring Te_2 molecules n on the incoherent PL intensity I_{em} . As n increases, the reservoir population n_{Te_2} created by the laser pulse is larger, meaning that more excitons are available to populate the emitter after its radiative recombination. This leads to a greater I_{em} .

acquisition time.

6.3 Resonant excitation behaviors of $\text{ZnSe}:\text{Te}_2$

I now discuss the three different types of behavior experimentally observed in the resonant excitation of a series of Te_2 -bound excitons: a monotonic increase as a function of $P_{\text{ex}}^{1/2}$ without saturation, saturation and a single Rabi oscillation cycle on top of a monotonic increase. The latter consists in a clear evidence of coherent interaction with the light field for some of the emitters. I use the model developed above to reproduce the shape of the I_{em} -vs- $P_{\text{ex}}^{1/2}$ curves and evaluate which parameters are influenced by the environment-stabilizing NR laser. All emission curves presented below were measured with a P_{NR} that did not lead to detectable PL, so that they come exclusively from resonant signal.

6.3.1 Monotonic increase of the resonant PL intensity without saturation

An important fraction of emitters ($\sim 50\%$) presented an increasing I_{em} without saturation within the probed resonant P_{ex} range. The coherent or incoherent nature of the response is at first glance unclear and a comparison with the models must be made.

Some of the emitters, as in Fig. 6.16, underwent a mostly linear rise of their I_{em} as a function

of $P_{\text{ex}}^{1/2}$. Such a response can be best modelled by considering a purely incoherent population mechanism with a large reservoir and a rather small nearby-defect pumping rate (Fig. 6.17). A small difference in the initial curvature at low $P_{\text{ex}}^{1/2}$ still remains. A saturation plateau would most likely be reached at $P_{\text{ex}}^{1/2}$ greater than the highest experimentally-accessible value, respectively 400 and 1000 μW for panels (a) and (b).

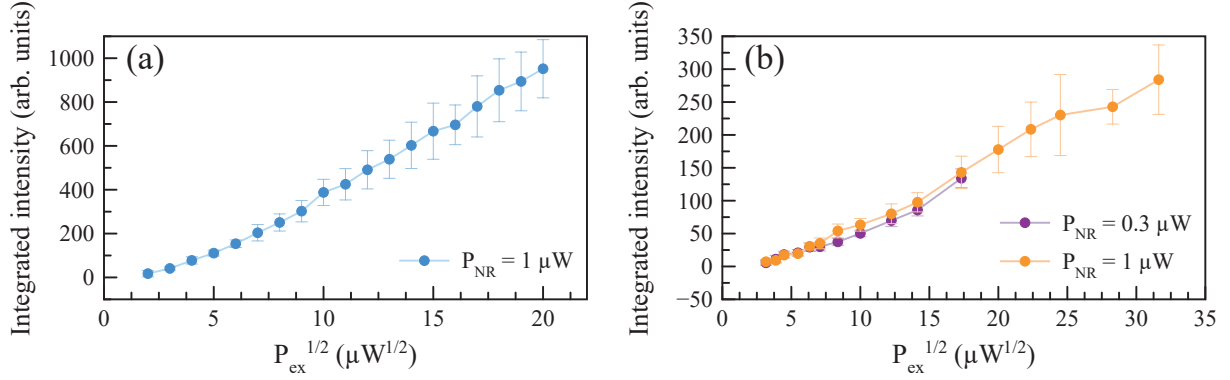


Figure 6.16 Excitons presenting a linear increase of their I_{em} as a function of $P_{\text{ex}}^{1/2}$. A maximum or plateau would probably be reached at higher P_{ex} , if it were experimentally available. In (b), the NR laser does not seem to influence the shape of the curve.

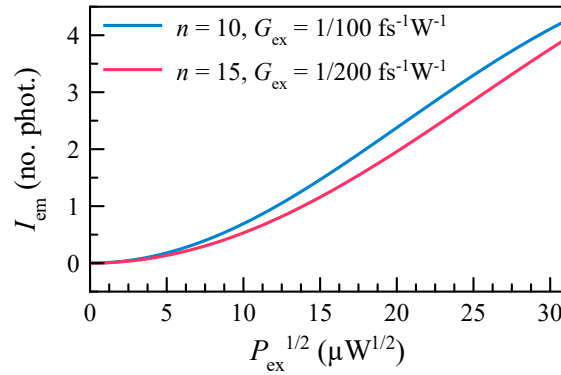


Figure 6.17 Modelization of the linear response with the incoherent mechanism. A similar shape to the experimental data is obtained using a large reservoir size n and a relatively slow pumping rate G_{ex} , except for the initial curvature.

In panel (b), the exciton does not seem to be impacted by the presence of the NR laser. It was indeed observed that, in the pulse regime, environmental stabilization seems to be less effective for certain emitters, most probably due to great number of charges created by the large peak power of the resonant laser pulses. However, the data of Exciton B does not allow

for a deep analysis of the effect of P_{NR} .

Other excitons, as in Fig. 6.18, were segmented in two different linear regimes, a small initial slope that increased at larger $P_{\text{ex}}^{1/2}$. This resonant excitation signature fits both a coherent interaction mechanism with a small d , (resembling the 5-D curve (blue) of Fig. 6.4), or an incoherent population mechanism with a low G_{ex} (such as in Fig. 6.17 or the $1/100\text{-fs}^{-1}\text{W}^{-1}$ (yellow) curve of Fig. 6.13), or a combined result of the two. Both theoretical curves indeed present a change of slope similar to the experimental data. However, due to the similarities with 6.16, I tend to lean toward the incoherent model as the main explanation for the behavior of the excitons in Fig. 6.18. Additionally, the impact of the NR laser in panel (b) remains in this case also unclear.

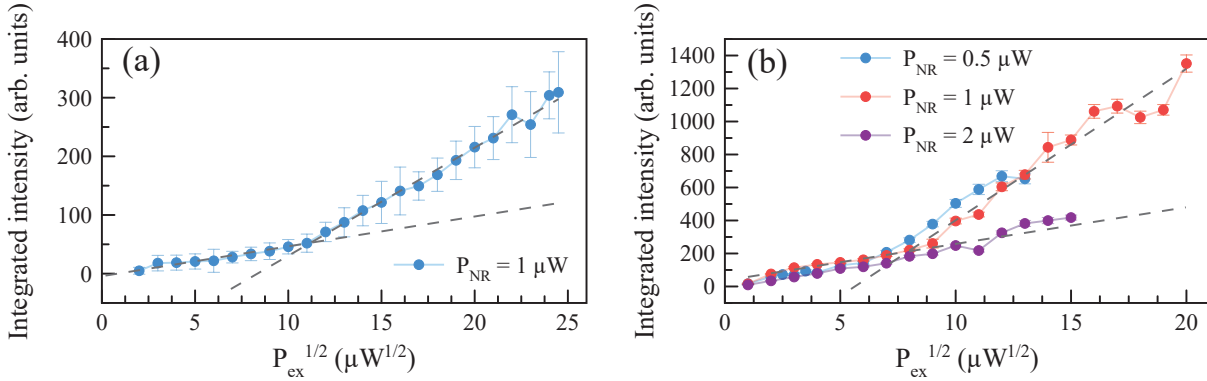


Figure 6.18 Changes of regime in the resonant PL response of two excitons, where curves are formed of two segments of increasing slope. Dashed lines are guides to the eye. It is unclear why the $P_{\text{NR}} = 2\text{ }\mu\text{W}$ curve in (b) has lower I_{em} in the second regime, it could be attributed to an alignment drift.

In summary, both Figs. 6.16 and 6.18 are most likely signatures of a rather inefficient incoherent interaction with the laser field. The presence of the NR laser does not appear in this case to impact greatly the emission signature of the emitters.

6.3.2 Saturation of the resonant PL intensity

About 40 % of the measured emitters presented a saturation of their I_{em} , two examples of which are shown in Fig. 6.19. Similar to the results of the previous section, the contributions of the coherent and incoherent mechanisms to the saturation behavior are not obvious. Both

models are therefore explored in the discussion below, after the presentation of the experimental data.

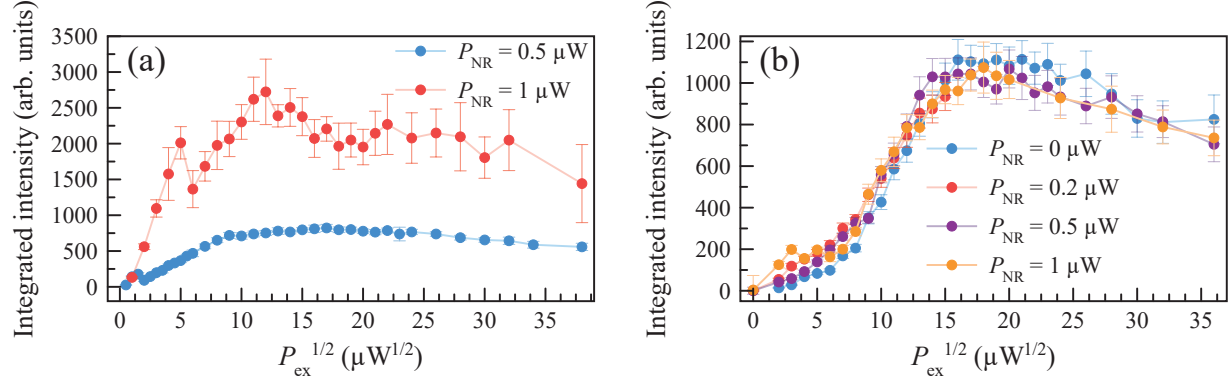


Figure 6.19 Resonant PL I_{em} as a function of resonant $P_{\text{ex}}^{1/2}$ for different P_{NR} , showing a saturation of I_{em} . (a) Emitter for which P_{NR} dramatically influenced I_{em} . (b) Emitter for which P_{NR} did not impact the emission curve.

The two most striking features common to both Fig. 6.19 panels are the reaching of a plateau at a certain $P_{\text{ex}}^{1/2}$ value (i.e. the saturation behavior) and the slight, gradual decrease afterwards. The saturation shape can be obtained both with a coherent and an incoherent model. The first case requires a short T_2 compared to the pulse duration τ_p , namely lower than 1 ps, in order to get an I_{em} rise with completely damped oscillations (as in the 0.1-ps curve (blue) of Fig. 6.6). The second case always produces such a shape, the parameters only changing the initial slope and maximum value, as demonstrated by Figs. 6.9–6.15.

The subsequent I_{em} decrease is modelled in the coherent interaction picture by a d value that allows for only a single complete oscillation cycle in the investigated $P_{\text{ex}}^{1/2}$ range and a T_2 that does not completely damp the oscillations. One obtains for example the curve of Fig. 6.20 with $d = 20$ D and $T_2 = 0.2$ ps, which differs slightly from the experiment as its initial increase is slower and as it starts to increase again at high $P_{\text{ex}}^{1/2}$. This suggests that constant parameters as a function of $P_{\text{ex}}^{1/2}$ do not suffice to reproduce the results or that the incoherent contribution plays a simultaneous role. Our incoherent population model for its part would need to be modified to include a P_{ex} -dependent, non-radiative escaping channel for the Te_2 -bound exciton in order to account for the decrease. This could be for example an efficient tunneling mechanism to lower-energy Te_2 molecules or defects.

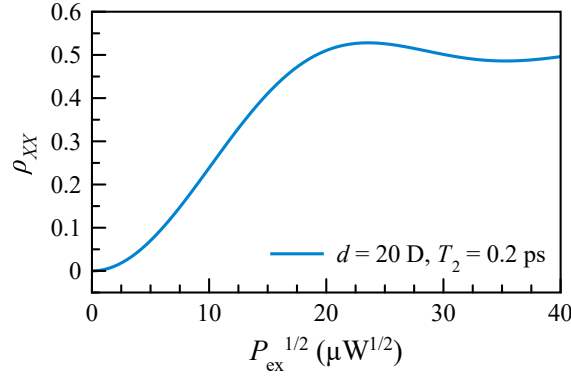


Figure 6.20 Modelization of the I_{em} saturation response with the coherent mechanism. The decrease at higher $P_{\text{ex}}^{1/2}$ is accounted for by using a d value that generates a single oscillation cycle in the $P_{\text{ex}}^{1/2}$ range investigated and a T_2 value that does not completely damp the oscillation.

Another interesting feature in Fig. 6.19 (a) is the strong dependence of I_{em} on the NR field. This suggests a dominant incoherent contribution with at least one P_{NR} -dependent transfer rate, as the coherent model cannot reproduce such behavior. The analysis of Sect. 6.2.2 shows that the maximum I_{em} attained is influenced by a variation of Γ_D , Γ_{rad} , $\gamma_{\text{Te}_2 \rightarrow X}$ and γ_0 , but these rates are not expected to depend on P_{NR} . T could rise due to laser-induced heating of the lattice, leading to an increase in γ_{sf} and γ'_{sf} . However, the T variation would need to be very large to have an important impact, inconsistent with the low P_{NR} used, and would probably activate, as mentioned before, other escape mechanisms for the exciton that are not considered here.

The most plausible explanation for the P_{NR} dependence is that it influences the population of reservoir excitons n_{Te_2} available for tunneling onto the emitter of interest, limited by the number of unoccupied neighboring Te_2 molecules n available to the creation of an exciton by the resonant laser. We have seen in Sect. 2.5.1 that the NR laser discharges the environment by generating free carriers. In order for P_{NR} to increase tunneling from nearby Te_2 molecules, these photo-created charges must remove residing holes that prevent the occupation of long-lived exciton states susceptible to tunnel. As P_{NR} increases, the discharging process becomes more efficient and n_{Te_2} , and consequently I_{em} , increase.

In panel (b), curves for four different P_{NR} , including $P_{\text{NR}} = 0 \mu\text{W}$, follow the exact same behavior and imply the NR laser did not in this case impact the bound-exciton emission. This might be due to a greater coherent contribution that had no P_{NR} -dependent parameters,

or an incoherent population with a tunneling channel from the reservoir already fully open at low P_{NR} . This could indeed be the case if there were a very small number of molecules in the vicinity of the emitter.

To summarize, the saturation behavior most likely involves an incoherent contribution to the bound-exciton population, evidenced by the P_{NR} dependence of the maximum I_{em} in some emitters. However, the decrease in I_{em} after saturation could be the signature of a coherent component with short T_2 , or of an additional escaping mechanism for the bound exciton not taken into account in the incoherent model. We observed a significant variability in the response of distinct emitters, which indicates that the mechanisms at play or their relative importance might differ.

6.3.3 Single Rabi oscillation cycle: evidence of coherent behavior

Only two out of the 19 measured excitons presented a signature that could out of hand be associated with a significant coherent behavior. Fig. 6.21 (a) and (b) show the I_{em} -vs- $P_{\text{ex}}^{1/2}$ curves respectively for Excitons A and B, for different P_{NR} values. Exciton A presents the clearest demonstration of coherent behavior with a high visibility oscillation cycle, which matches well the shape of curves obtained through the resolution of the optical Bloch equations in Sect. 6.2.1 (to be discussed below). It is followed by a slow monotonic rise, which is attributed to incoherent population. Exciton B for its part bares plateau-like features than can be understood as small-amplitude oscillation maxima combined with a similar monotonic increase.

In both cases P_{NR} causes I_{em} to increase significantly within the single oscillation cycle, combined with a displacement of the local maximum $P_{\text{max}}^{1/2}$ towards higher $P_{\text{ex}}^{1/2}$, emphasized in Fig. 6.22. The width of the cycle also increases with P_{NR} . These effects must be the result of the modification, in the presence of the NR field, of the properties responsible for the coherent interaction of the emitter with the resonant excitation field. They cannot be attributed to an emission caused by the NR laser, which was confirmed to be undetectable even at high P_{NR} . The only exception to the I_{em} increasing trend is the 2- μW curve of Exciton A. Its lower signal could be due to a relaxation of the alignment despite our best efforts to maintain its optimization, as these time-consuming measurements were taken over the period of several days.

Excitons A and B did not at first hand show particularly peculiar NR emission characteristics

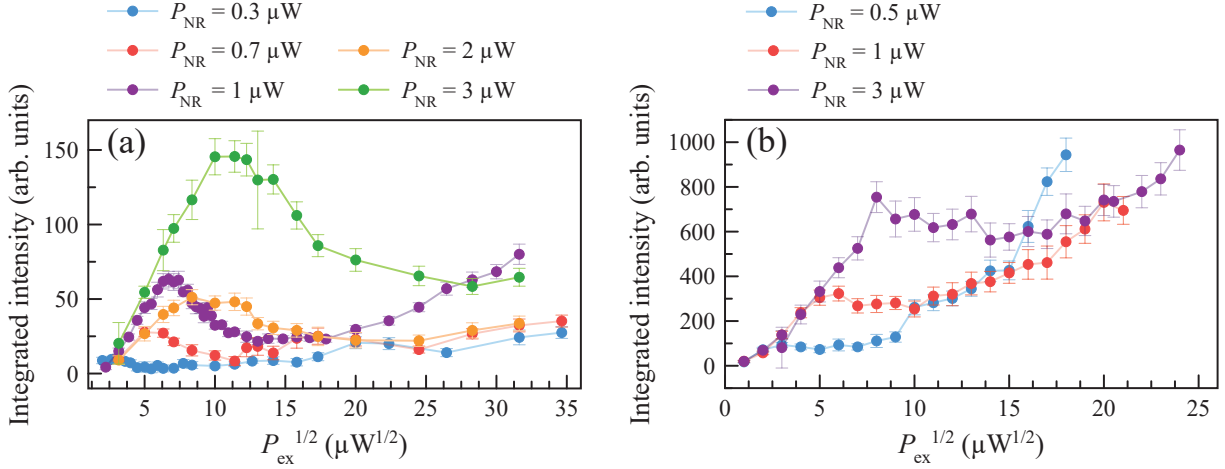


Figure 6.21 Coherent behavior of the resonant PL as a function of resonant $P_{\text{ex}}^{1/2}$ for different P_{NR} values. (a) Exciton A presents a clear single oscillation cycle, with an increasing I_{em} component attributed to incoherent population. (b) Exciton B shows an oscillation taking the form of a plateau.

that could have anticipated a greater coherence. Exciton A had a E_{em} at the bottom of the distribution (2.765 727 eV, see Fig. 6.1), but Exciton B was close to the mean (2.776 694 eV). Exciton A was in the third FSS quartile (545 μeV), while Exciton B was in the first (156 μeV). Both had similar FWHM (134 and 166 μeV), rather typical values. No pattern could be identified.

In light of what was discussed above, the most striking characteristics of the resonant PL data of Excitons A and B are summarized by these four items:

1. Only a single oscillation cycle is observed, any coherent behavior is rapidly damped after.
2. There is a monotonically increasing contribution to I_{em} that makes the latter exceed the oscillation maximum at higher $P_{\text{ex}}^{1/2}$ for half of the curves.
3. The position and width of the oscillation cycle increase with P_{NR} .
4. The amplitude of the single-oscillation maximum increases with P_{NR} .

Using the model developed in Sect. 6.2, I now try to reproduce the important features of the resonant PL signal from Excitons A and B with the objective of identifying the mechanisms at play in their behavior. I investigate how each of the items listed above can be simulated

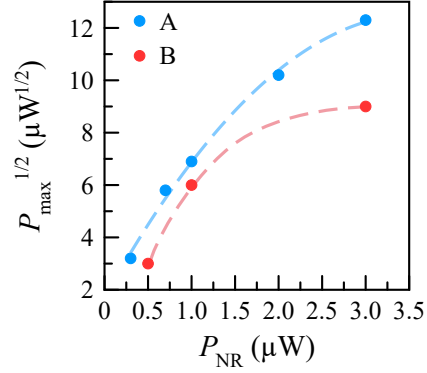


Figure 6.22 $P_{ex}^{1/2}$ at which the local maximum of the oscillation cycle ($P_{max}^{1/2}$) is observed. The value increases with P_{NR} , indicating that d is altered. Dashed lines are guides to the eye.

with the available parameters.

Modelization of a single Rabi oscillation cycle

Item 1 The rapid damping of the oscillation after the first maximum points towards progressive decoherence mechanisms having a dependence on P_{ex} . The first attempt at implementing this in the simulation was to consider excitation-induced dephasing (EID), where T_2 decreases linearly as a function of $P_{ex}^{1/2}$ [25,155]. Fig. 6.23 shows the impact of EID on the Rabi curve, here presented as a number of emitted photons similar to Figs. 6.9–6.15. The gradual decrease in T_2 indeed allows to keep the first cycle rather intact while damping the next ones. One however sees that T_2 must still be shorter than τ_p , the excitation pulse duration, to have an impact, just like in Fig. 6.6. Even then, the damping is not strong enough to reproduce the experimental results, as subsequent oscillation cycles remain clearly defined. EID alone therefore does not appear sufficient to reproduce the results.

In order to retain reasonable T_2 values while approaching the amount of damping sought, another mechanism was introduced: an Ω fluctuation, which could be the result of a reorientation of d with respect to the driving field or a change in its norm. A fluctuation of the dipole orientation is indeed common in high-symmetry systems such as organic molecules [219,220] or colloidal QDs coupled to organic ligands [221], where a small structural, charge distribution or environmental perturbation breaks the rotational symmetry and randomly orients d . To my knowledge, no such fluctuation was ever reported in lower-symmetry systems such as

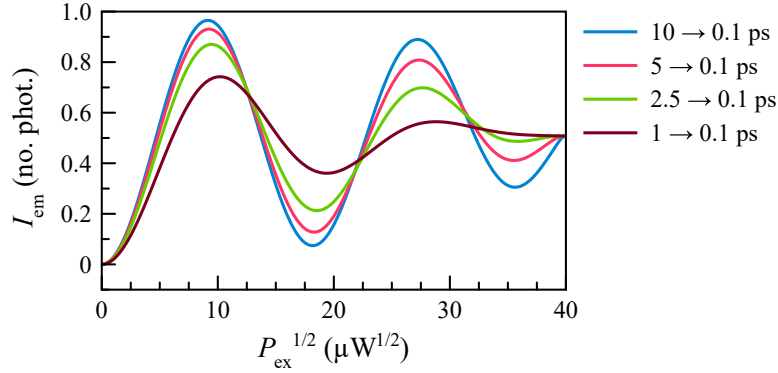


Figure 6.23 Excitation-induced dephasing (EID) on a Rabi curve, providing gradual damping of the oscillations. The curves were obtained for $\tau_p = 1$ ps, $d = 30$ D, $T_1 = 80$ ps and $\Delta = 0$ μ eV. T_2 decreases linearly between the values indicated in the legend for $P_{\text{ex}}^{1/2}$ varying from 0 to $40 \mu\text{W}^{1/2}$.

our C_{2v} bound exciton, where all directions are non equivalent. For example, InGaAs QDs saw their d orientation unchanged upon the application of an in-plane electric field [181]. The inspection of the C_{2v} perturbation Hamiltonian for an electric field (see Appendix B) however informs that a d reorientation or a change in its norm could nonetheless result from HH-LH mixing.

More precisely, as was discussed in Sect. 2.5, the resonant laser creates charges in the environment of the emitter, the presence of which randomly fluctuate in time and space. They generate a dynamical electric field that modulates the mixing of $|X_{hh}\rangle$ and $|Y_{hh}\rangle$ with LH states, leading in turn to a fluctuation of the orientation and magnitude of d (in the latter case, especially if the mixing involves $|D_{lh}\rangle$). This in turn impacts Ω , which depends on the angle formed by d with the field (Eq. 2.18). As the experiment is repeated $\sim 10^{10}$ times within the integration time, during which charge fluctuations invariably occur and perturb d , the acquired signal is formed of a superposition of Rabi curves with different instantaneous Ω . At lower P_{ex} , these curves are mostly in phase, leading to a relatively good visibility of the first maximum, but rapidly dephase and damp the subsequent cycles, resulting in a loss of visibility. Additionally, as P_{ex} increases, the excitation generates even more charges, increasing their fluctuations and consequently that of d and Ω .

Fig. 6.24 was obtained by adding the effect of an Ω fluctuation to EID. As can be seen, this fluctuation leads to the efficient damping of subsequent oscillation cycles, in good agreement with experimental observations. I modelled this by allowing Ω to take random values from a

uniform distribution $[\Omega_{\min}, \Omega_0]$, with the lower bound Ω_{\min} decreasing with $P_{\text{ex}}^{1/2}$ to account for greater fluctuations. Ω_0 referred to the maximum Rabi frequency, when d is minimally mixed and consequently aligned with the field, and was kept constant. The best simulation of a curve having a well-defined first oscillation cycle and strong damping afterwards was achieved for a variation of Ω_{\min} that rapidly increased at low $P_{\text{ex}}^{1/2}$ and then slowed down or saturated. I used for that purpose a simple function that presented these characteristics:

$$\Omega_{\min} = \Omega_0 (1 - \sin \theta), \quad (6.5)$$

where θ increased from 0 to $\pi/2$ with $P_{\text{ex}}^{1/2}$.

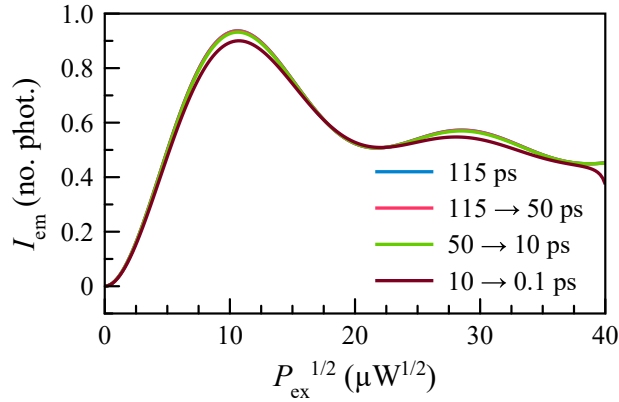


Figure 6.24 Impact of a Ω fluctuation on the Rabi curve, for different T_2 behaviors (constant and with EID). Ω is allowed to take values uniformly distributed between $\Omega_0 (1 - \sin \theta)$ and Ω_0 , with Ω_0 the maximum Rabi frequency. θ increases linearly with $P_{\text{ex}}^{1/2}$ and takes values between 0 and $\pi/2$. The effect of EID becomes negligible and a larger value of T_2 can be used while maintaining the right amount of damping. The curves were obtained for $\tau_p = 1$ ps, $d = 30$ D, $T_1 = 80$ ps and $\Delta = 0$ μ eV.

Fig. 6.24 also highlights that efficient damping was obtained without the need of a short T_2 or even EID, as all curves are very similar regardless of the value and variation of T_2 . EID was consequently discarded in further simulations for the sake of simplicity. T_2 was thus kept at its default value of 115 ps.

To summarize, a fluctuation of Ω in response to the fluctuating charges created by the excitation field appropriately models the single-oscillation behavior. It allows to do so while using a constant and more reasonable value for T_2 and hence is selected as the main damping mechanism for further simulations. Experimentally, this effect could be confirmed by the ob-

servation of polarization changes in the monitored transition due to the environment-induced excitonic-wavefunction mixing and the consequent d reorientation.

Item 2 The monotonic I_{em} increase is most likely due to the incoherent tunneling mechanism of Sect. 6.2.2, which competes with coherent interaction. Every excitation pulse, there is indeed a probability that the emitter receives an exciton from a neighboring Te_2 molecule instead of creating one itself through resonant absorption. The total signal is therefore a mix of coherent and incoherent mechanisms. This was treated in the simulation as a weighted sum of both contributions. Fig. 6.25 presents their combined effect for a reservoir of $n = 2$ neighboring Te_2 molecules and a respective weight of $c_{\text{co}} = 0.6$ and $c_{\text{inc}} = 0.4$, for different values of G_{ex} , which control the initial slope of the incoherent population (as in Fig. 6.13). A higher G_{ex} value attenuates the oscillation, but allows the signal to increase beyond the maximum of the first oscillation cycle.

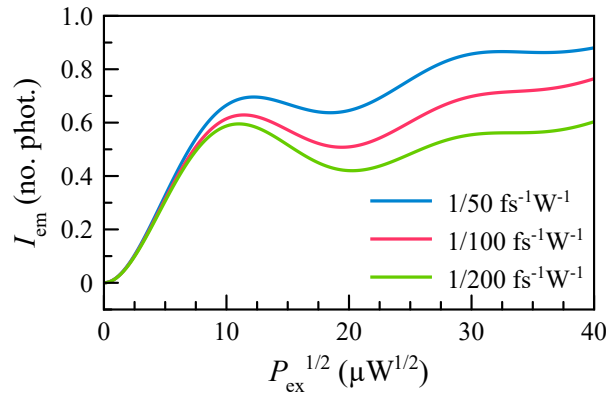


Figure 6.25 Combination of coherent and incoherent population mechanisms during resonant excitation, calculated for $n = 2$ neighboring Te_2 molecules, respective weight of $c_{\text{co}} = 0.6$ and $c_{\text{inc}} = 0.4$ and different G_{ex} . One obtains a clear oscillation maximum followed by a rise. A larger G_{ex} attenuates the oscillation, but allows for the signal to increase above the local maximum. Incoherent components used $\Gamma_{\text{rad}} = 1/80 \text{ ps}^{-1}$, $\gamma_{\text{Te}_2 \rightarrow X} = 1/5 \text{ ps}^{-1}$, $\Gamma_D = 1/3 \text{ ns}^{-1}$, $\gamma_0 = 1/0.1 \text{ ns}^{-1}$ and $T = 7 \text{ K}$. The coherent part is the same as the $T_2 = 115 \text{ ps}$ curve in Fig. 6.24.

Effect of P_{NR}

I now turn to the effect of P_{NR} on the Rabi oscillations, which were summarized by Items 3 and 4 in Sect. 6.3.3. As it was said several times above, the goal of the NR laser was to

stabilize the environment in order to restore the optimum quantum properties of an emitter. In this experiment, the laser had an impact on the shape of the Rabi curve by increasing the position, width and amplitude of the local maximum P_{\max} , but its effect was not strong enough for more than one oscillation cycle to be visible.

Item 3 The displacement of the position of $P_{\max}^{1/2}$ towards higher $P_{\text{ex}}^{1/2}$ and the increase of the oscillation width with P_{NR} suggest a reduction of the magnitude of d , as in Fig. 6.4. A similar effect was reported in Ref. [177] for Rabi oscillations performed on InAs/GaAs QDs in the presence of a NR laser and was tentatively attributed to charges in the vicinity of the dot building up an electric field that modifies the overlap between the electron and hole wavefunctions, decreasing the norm of d . In our system, we instead attribute this d reduction to an effect of motional narrowing, detailed below.

We have argued above that the presence of an environmental electric field caused mixing of HH states with LH states (as predicted by the Hamiltonian in Appendix B), which was responsible for reorienting d and diminishing its norm. At low P_{NR} , our results suggest that d is large since $P_{\max}^{1/2}$ is low ($\sim 3.2 \mu\text{W}^{1/2}$ at $P_{\text{NR}} = 0.1 \mu\text{W}$, see Fig. 6.22). In this situation, important charge fluctuations cause large pulse-to-pulse Ω variations, even at low $P_{\text{ex}}^{1/2}$, and Rabi oscillations are rapidly damped. At higher P_{NR} , $P_{\max}^{1/2}$ increases ($\sim 12.3 \mu\text{W}^{1/2}$ at $P_{\text{NR}} = 3 \mu\text{W}$), suggesting that d diminishes. This could result from the larger P_{NR} reducing the charge fluctuations by increasing the discharging rate, leading to a stabilization of the system in a configuration that, due to HH-LH mixing, has a lower d magnitude.

Item 4 The increasing oscillation amplitude with P_{NR} was addressed in the simulation by considering a decreasing Δ , which could be another direct consequence of motional narrowing. Indeed, the environmental discharging favored by the increase in P_{NR} with respect to P_{ex} could lead to a blueshift of the emission line towards its intrinsic emission energy (E_{em}) [175]. Δ would consequently be larger for lower P_{NR} since the resonant laser was adjusted to the position of the unperturbed E_{em} (determined by the NR emission spectrum, when the environment is fully discharged). As Ω is small at low $P_{\text{ex}}^{1/2}$, a large fluctuation-induced Δ could therefore seriously damp the first oscillation cycle (see Fig. 6.5).

Reproducing the behavior of Excitons A and B

By combining the effects described in Items 1–4, the behavior of Exciton A could be modelled using the parameters in Table 6.3. I used a slower incoherent pumping rate ($G_{\text{ex}} = 1/100 \text{ fs}^{-1}$), a larger reservoir ($n = 5$) and a smaller incoherent population probability ($c_{\text{inc}} = 0.1$) than previously. The two latter choices of parameters led to the same result as using a smaller n and larger c_{inc} . One can see on Fig. 6.26 the resulting simulation side by side with the experimental data. The former grasps satisfactorily the P_{NR} -related features of the latter, namely the displaced oscillation maximum towards higher $P_{\text{ex}}^{1/2}$ with a decrease in d magnitude and the increased I_{em} amplitude as Δ gets smaller. The monotonous I_{em} rise due to incoherent population is also well captured. However, several discrepancies remain:

1. A secondary oscillation maximum is still visible in the simulation and could most likely be removed by refining the dependence of the coherent-behavior damping on $P_{\text{ex}}^{1/2}$.
2. The I_{em} local minimum after the oscillation cycle is not as pronounced in the simulation as in the data, especially for the 1- μW curve. This suggests that c_{co} and c_{inc} could be P_{ex} -dependent.
3. I could not reproduce the large I_{em} increase after the maximum in the 1- μW curve without losing too much contrast on the coherent behavior. A P_{ex} -dependant c_{co} would probably also solve this issue.

Table 6.3 Parameters used in the simulation of the resonant emission from Exciton A. Left: coherent mechanism, center: incoherent mechanism, right: excitation laser. Variable parameters as a function of P_{NR} are marked as “var.,” while “fluct.” means that the corresponding parameter fluctuates at each repetition of the experiment (from pulse to pulse).

Coherent mechanism		Incoherent mechanism		Laser	
Parameter	Value	Parameter	Value	Parameter	Value
d	var. [D]	Γ_{rad}	$1/80 \text{ ps}^{-1}$	τ_{p}	1 ps
Δ	var. [meV]	Γ_D	$1/3 \text{ ns}^{-1}$	$1/\tau_R$	80 MHz
T_1	80 ps	γ_0	$1/0.1 \text{ ns}^{-1}$	S	$0.45 \mu\text{m}^2$
T_2	115 ps	G_{ex}	$1/100 \text{ fs}^{-1} \text{ W}^{-1}$		
c_{co}	0.9	$\gamma_{\text{Te}_2 \rightarrow X}$	$1/5 \text{ ps}^{-1}$		
Ω	fluct. [rad s^{-1}]	n	5		
		T	7 K		
		c_{inc}	0.1		

Other puzzling aspects of the simulation are the necessity of using large Δ values (0–2.5 meV, while values were considered reasonable up to 400 μeV) and an important variation in the

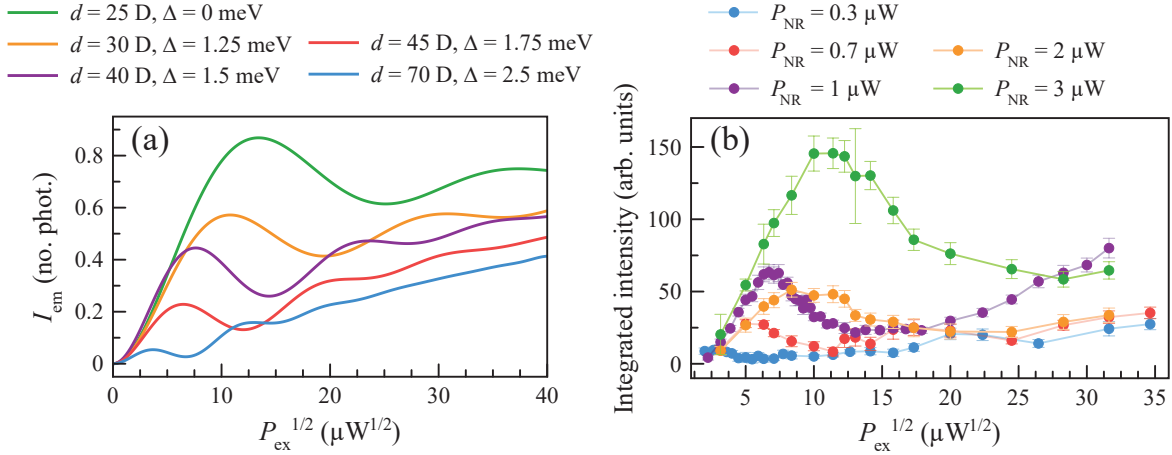


Figure 6.26 Comparison between simulation (a) and experimental data (b) for Exciton A, combining coherent and incoherent contributions. The model reproduces well the general behavior of increasing oscillation period and amplitude by varying the magnitude of d and Δ . The rest of the parameters used to compute the curves in (a) are given in Table 6.3. Ω undergoes pulse-to-pulse fluctuations as described in Item 1.

magnitude of d (45 D) to account for our observations, which were not expected in our system. Nevertheless, the model gives good insight on the physics at play during resonant excitation of a Te_2 -bound exciton.

Exciton B can also be satisfactorily simulated if one considers a larger contribution of the incoherent mechanism. I used $c_{\text{co}} = 0.6$ and $c_{\text{inc}} = 0.4$ to obtain the results of Fig. 6.27 (a), with relevant values of d and Δ (listed on the figure), which compare well with the data in panel (b). The rest of the parameters are the same as those listed in Table 6.3. One can see that the greater incoherent contribution diminishes the visibility of the oscillations and makes the first cycle look more plateau-like. The differences between the simulations and the experimental data mainly reside in the sharpness and length of the plateau, but here again, the model is in fine agreement of the behavior of the emitter of interest.

6.3.4 Conclusion on the resonant excitation model of a Te_2 -bound exciton

In conclusion, the resonant emission behavior of a Te_2 -bound exciton in the pulsed regime can be adequately described by a competition between its coherent interaction with the field, modelled by the optical Bloch equations, and an incoherent population mechanism involving nearby resonantly-populated Te_2 defects, represented by a balance of populations. The model

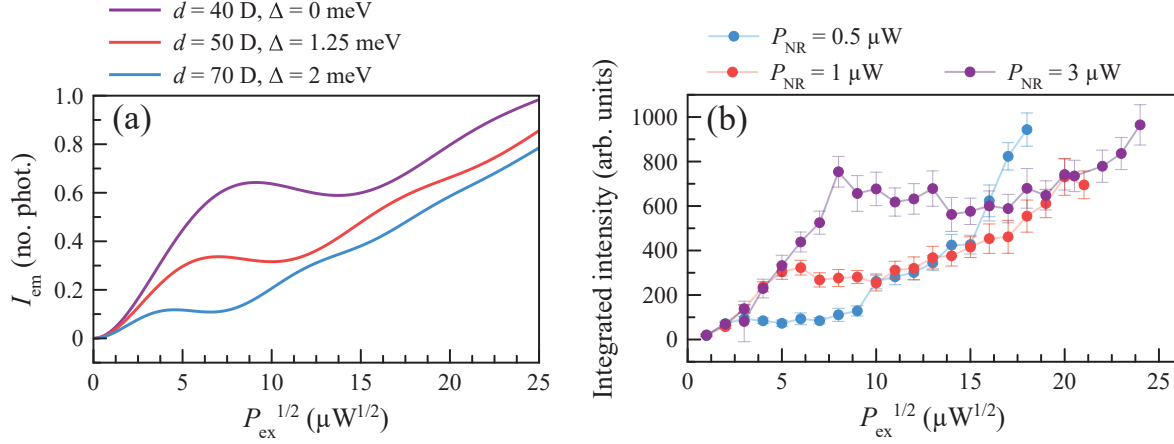


Figure 6.27 Comparison between simulation (a) and experimental data (b) for Exciton B. The parameters used to compute the curves in (a) are mostly the same as for Exciton A, except for $c_{\text{co}} = 0.6$ and $c_{\text{inc}} = 0.4$, d and Δ . Once again, the agreement with the model is quite satisfactory.

accounts for the three different behaviors observed experimentally, namely an I_{em} monotonic increase, a saturation, and the presence of a single Rabi oscillation cycle superimposed to a monotonic increase.

First, the observation of a single Rabi oscillation cycle superimposed to a monotonic I_{em} increase for a small fraction of emitters consists in a demonstration of coherence and illustrates well the interplay between the two population mechanisms. A strong damping of the oscillation amplitude after the first local maximum could be obtained by considering a fluctuating Ω of P_{ex} -dependent magnitude in the optical Bloch equations. The increasing I_{em} oscillation period and amplitude with the application of a weak NR laser could be reproduced by admitting a decrease in the magnitude of d and Δ . The visibility of the coherent oscillation was adjusted by the application of a weighting factor between the coherent and incoherent contributions.

Second, the I_{em} monotonic increase, especially the linear behavior, was for its part associated with a purely incoherent mechanism and could be simulated with the balance of populations equations with a small G_{ex} and a large n . The curves presenting a change of slope could also be modelled with the optical Bloch equations using a small d , but similarities with the linear case made us favor the incoherent explanation.

Third, the I_{em} saturation at high $P_{\text{ex}}^{1/2}$ could be described both with the coherent and incoherent mechanisms. The former needed a very short T_2 to strongly damp the oscillations. The I_{em} decrease at higher $P_{\text{ex}}^{1/2}$ could be reproduced with a judicious choice in T_2 and d . The incoherent description generated well the saturation behavior, but failed to describe the high- $P_{\text{ex}}^{1/2}$ decrease. Additional P_{ex} -dependent, non-radiative escape mechanisms for the exciton should presumably be included to account for this effect. Also, the P_{NR} dependence of the response of some of the emitters suggested that their behavior was mostly incoherent.

Although discrepancies remained between the model and especially the single oscillation cycle, the former allowed to grasp major features of the resonant PL response of a Te_2 -bound exciton. However, the present results suggest that the efficiency of the NR laser at stabilizing the environment of the emitter varies greatly in the pulsed regime and is clearly not sufficient for implementing a satisfactory and reliable control of qubit quantum states. The next section investigates this point further with the application of an electric field.

6.4 Attempts at stabilizing the environment of an emitter

It has been already reviewed in Sect. 2.5 and extensively discussed throughout the text how a fluctuating environment can have deleterious effects on the quantum properties of an emitter. The difficulties encountered while attempting the observation of Rabi oscillations in ZnSe:Te_2 have motivated the trial of stabilization methods in the pulsed regime. Two avenues were explored: a NR, above-gap laser (3.061 eV), which was already thoroughly analyzed above, and an electric field.

6.4.1 Pulsed resonant excitation in the presence of a NR CW laser field

The impact of a neutralizing NR laser for a pulsed resonant excitation is not as dramatic as what was reported for the CW case [175] (detailed in Sect. 2.5.1), and strongly dependent on the emitter. Indeed, some resonant PL curves in our work showed important differences as P_{NR} was varied (as in Fig. 6.19 (a) and 6.21), while others were identical regardless of P_{NR} (Fig. 6.19 (b) and 6.16 (b)). This variability on the impacts of the NR optical pump has also been observed in QDs, where the laser could sometimes quench the emission rather than enhance it [177]. The effect seems to greatly depend on the structure and charge configuration within a sample on a μm scale.

The difference between the pulsed and CW regimes most likely reside in the energy bandwidth and excitation power at play. In Ref. [175], the CW resonant laser had an extremely narrow spectrum (5 MHz) and was applied to the sample at powers of the order of a few hundreds of nW. It probably excited just a few selected surrounding defects, thereby limiting the intensity of the incoherent signal in the single emitter response and the size of the fluctuating charge reservoir. In our experiment, the pulsed laser had conversely a very large spectrum, with peak powers of the order of 0.02–25 W. This most likely led to the excitation of a much larger distribution of defects and made the removal of environmental charges much more challenging.

6.4.2 Impacts of a DC electric field on the emission signature of an emitter

As the effect of the NR laser proved to be inconsistent, we investigated the application of a DC electric field as another mean of removing the charges generated by the optical excitation in the environment of our emitter. This avenue has proven to be a reliable way of stabilizing the environment and charge state of QDs [78, 173, 177]. We performed this experiment on Sample C, which is formed of an 80-nm thick ZnSe layer on GaAs with a patterned Al layer on top (see Sect. 3.1). We used the latter as the front electrode, the back electrode being the copper sample holder in the cryostat. Delamination spots in the Al layer allowed for observation of single Te_2 -bound excitons.

As a first step, we measured the NR PL from a single ZnSe: Te_2 emitter and monitored its emission energy (E_{em}) shift, which indicates the impact of the field on the electrical environment in the vicinity of the trapping molecule. The most common behavior was that the emission line would noticeably shift in the first few applied voltage points, and then would stay relatively constant for the rest of the experiment, regardless of the sign of the electric field (Fig. 6.28). The change seemed somewhat irreversible, as E_{em} did not come back to its original value as the field was removed. The total variation was (690 ± 3) μeV in panel (a), as well as (832 ± 5) μeV for X and (396 ± 6) μeV for Y in panel (b). These values are well above the the resolution limit of the detector (90 μeV).

Such abrupt steps point toward single discharging events occurring at specific voltages, such as, for example, the removal by field-assisted tunneling of a single charge at a distance of about 100 nm from the emitter (calculated from the DC Stark shift Eq. 5.21). The hysteresis

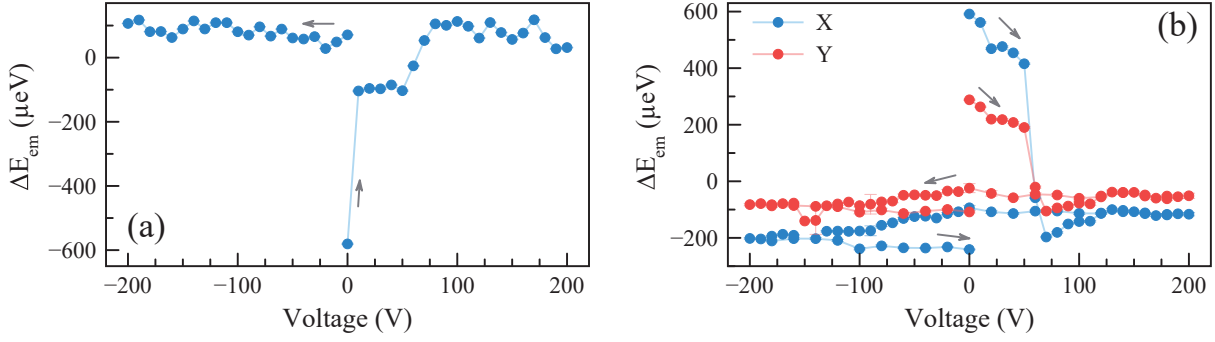


Figure 6.28 Variation of NR E_{em} as a function of voltage, where excitons present an initial abrupt step and then stay constant at any voltage value, regardless of its sign, and even as the field is removed. In (a), the shift is positive, while in (b), it is negative.

in the E_{em} value suggests that the charge (or charges) involved was in a state inaccessible to the laser (i.e. due to a momentum mismatch) and was probably thermally generated before cooldown.

A few emitters presented another type of response formed of plateaus of different signs for positive and negative voltages (Fig. 6.29). The curves nevertheless show a hysteresis, as they present a higher E_{em} value at 0 V after the application of a positive voltage than its original value. The total variation is however smaller ($\sim 170 \mu\text{eV}$ for both transitions) than those of Fig. 6.28, but almost twice the resolution limit. The two plateaus could be the result of distinct neutralization events, a simple example being the removal of two charges of opposite sign by the same field-assisted tunneling mechanism.

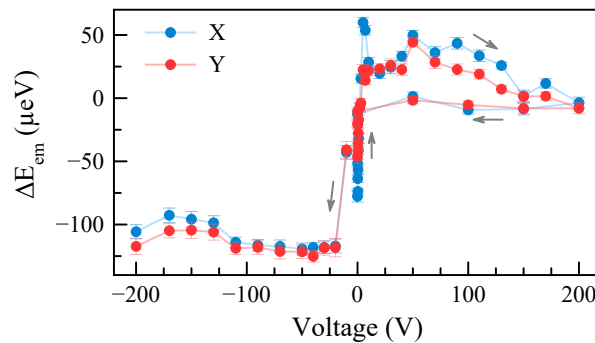


Figure 6.29 Second, less common behavior of an exciton of NR E_{em} as a function of voltage, showing a hysteresis.

Despite the important effect of the field on the NR E_{em} , we did not see any notable modification of the shape of the resonant-excitation behavior upon its application. Fig. 6.30 displays an example of curves taken at 0 and -200 V and a P_{NR} of $0.3 \mu\text{W}$. Both are very similar and most likely the signature of an incoherent population mechanism, similar to the results of Sect. 6.3.1. The presence of the field did not favor a clear coherent interaction, as no Rabi oscillations were observed. However, this experiment was attempted on only a few emitters, and the variability of the observed behaviors in the presence of solely the NR laser (Sect. 6.3) suggests that an effect could be expected for a small portion of emitters.

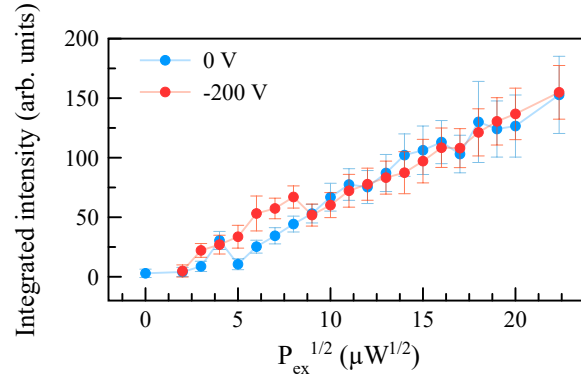


Figure 6.30 Resonant PL measured with $P_{\text{NR}} = 0.3 \mu\text{W}$ for two different applied voltages, 0 and -200 V. The field does not have any noticeable effect on the behavior of the emitter.

In short, although the electric field impacted the NR E_{em} , it did not achieve a sufficient environmental stabilization to lead to a coherent emission behavior. I nevertheless think this avenue is interesting to pursue, as it should allow for more control of the qubit and its environment. One should consider purposely designed samples with proper Schottky diode geometry, grid and contacts (with transparent electrodes, for example) in further experiments to ensure more deterministic field geometries and amplitudes at the position of the emitter.

6.5 Conclusion on the resonant excitation of a Te_2 -bound exciton in the pulsed regime

In this chapter, the resonant excitation of single Te_2 -bound excitons was explored in the pulsed excitation regime. Three different behaviors were experimentally observed. Their main features could be satisfactorily reproduced with a population mechanism involving a coherent contribution, described by the optical Bloch equations, and an incoherent contribu-

tion, involving the tunneling of an exciton from a neighboring higher-energy molecule.

About 50 % of the emitters showed a monotonic increase of their I_{em} with excitation power (represented as $P_{\text{ex}}^{1/2}$), a behavior that most likely resulted from a purely incoherent population with low pumping rate per unit power, G_{ex} , and large reservoir n . The second most common PL response (~ 40 %) corresponded to an I_{em} saturation, which was mainly attributed to the incoherent mechanism due to the occasional dependence of its shape on non-resonant power (P_{NR}). The decrease at higher $P_{\text{ex}}^{1/2}$ could nevertheless result from a coherent component with a short coherence time (T_2) and an adequate dipole moment (d) to present a single oscillation in the studied $P_{\text{ex}}^{1/2}$ range, or an additional escape mechanism for the bound exciton in the incoherent description.

Only 10.5 % of the measured emitters presented a clear coherent behavior in the form of a single Rabi oscillation cycle. This could be simulated by considering a fluctuating Rabi frequency (Ω) from pulses to pulses, taking origin in the mixing of excitonic states by laser-induced random charge fluctuations in the vicinity of the emitter. The amplitude of this fluctuation increased with $P_{\text{ex}}^{1/2}$. The incoherent mechanism also participated in the PL signal and was responsible for a monotonous increase superimposed to the oscillation. No d value could be reliably extracted from the data due to its unusual shape.

The resonant PL signature of an emitter was clearly influenced by its environment, leading to the three observed behavior categories. The impact of a stabilizing agent had variable effects on the signal, from none to major. Indeed, coherent behavior, when present, was systematically influenced by the application of a NR laser, showing a modification of its d magnitude and detuning (Δ) with P_{NR} . Purely incoherent behavior, on the other hand, only showed occasional changes with P_{NR} . The application of an electric field lead to a brusque shift of the NR emission line, but did not result in any change in the emission response of the studied emitters.

Obviously, more work is required to identify the conditions for the systematic observation of coherent interaction, in particular those regarding an efficient environmental stabilization in the pulsed regime, the lack of which proved deleterious to the quantum properties of the emitters in this experiment. In this regard, more elaborate samples structures with, for example, patterned gates would be beneficial. Additionally, the quality of the host material should be reviewed, as it does not appear sufficient for developing ZnSe:Te₂-based qubits. In particular,

the concentration of defects and impurities acting as charge reservoirs and contributing to the incoherent population mechanism should be minimized. A few first steps in doing so could be to reduce the Te concentration to ensure that only a single emitter sits in a single detection volume, which is not exactly the case in our samples, or to increase the size of the buffer layer between the Te δ -doped monolayer and the GaAs substrate, attenuating the perturbation felt by bound excitons caused by charges accumulating at the ZnSe-GaAs interface.

CHAPTER 7 CONCLUSION

The development of a reliable interface converting a material quantum degree of freedom to a photonic one and vice-versa, namely an optically addressable qubit (OAQ), is a crucial step in creating a quantum telecommunication network. As mentioned in Chap. 1, such a system would ideally present optical transitions with a large dipole moment (d) and well-defined selection rules, be scalable and easy to integrate to current electronic technologies, and possess fully-controllable quantum states with long coherence times (T_2). Although tremendous advancements have been made in some well-studied systems, it is still very challenging to meet all of the requirements, therefore leaving room for the investigation of new alternatives.

This thesis focused on examining the exciton bound to a Te_2 molecule in ZnSe ($\text{ZnSe}:\text{Te}_2$) as a potentially advantageous OAQ, especially since it is an atomic defect of well-defined symmetry, it binds a hole as a primary charge, defining a hole spin qubit for which hyperfine interaction is minimized, and it is embedded in a relatively spin-free host compared to other semiconductors such as GaAs. This system also seems to offer new avenues for control, such as a non resonant (NR) ultrafast initialization protocol for a hole spin in the absence of a magnetic field [28]. However, it is not well-understood in the context of quantum applications. The main objective of this thesis was consequently to shed light on some of its emission properties relevant for quantum control.

7.1 Summary of works

Two experiments were conducted on single Te_2 -bound excitons in order to better assess their potential. The first one, photoluminescence-excitation (PLE), probed their emission intensity (I_{em}) for an excitation in energy ranges encompassing the free (FX) and donor-bound (D_0X) excitons in ZnSe, as well as energies where bound-exciton excited states were expected. The idea was to better understand the nature and properties of these excitonic excited states, study the relaxation mechanisms preceding light emission and identify states that could participate in new control protocols. The second experiment, resonant excitation, was performed with the objective of achieving coherent control and extracting performance parameters for the OAQs, such as d , T_2 and their relaxation time (T_1).

The PLE experiment showed that Te_2 -bound excitons are efficiently populated by the capture of FX, and that the shape of their absorption spectrum is strongly influenced by their environment. It also revealed that some emitters were subject to important spectral diffusion, another consequence of their fluctuating electrical environment.

The most spectacular result from this experiment was the modulation of the bound-exciton emission energy (E_{em}) with a monotonic scan of the excitation energy (E_{ex}), which equally impacted all emitters in a given detection volume and was independent of the excitation polarization. The average oscillation period (T_{ex}) and amplitude (A_{em}) were respectively 1.103 meV and 44 μeV . This effect was best modelled by the interaction of the bound exciton with free exciton-polaritons in the ZnSe layer, through a DC Stark effect or exciton-exciton interactions. Other explanations were explored, such as magnetic field-induced effects, a phonon-assisted coupling of the bound-exciton states with free exciton-polaritons and the possibility of each bound-exciton transitions to be formed of a nearly-degenerate doublet, but all were judged unlikely.

Resonant excitation lead to the observation of coherence in the response of only a few single emitters in the form of a unique Rabi oscillation cycle, which was modelled by considering a fluctuating Rabi frequency (Ω) in the optical Bloch equations and was most likely a consequence of environment-induced hole mixing in excitonic states. At higher excitation power (P_{ex}), the signal was dominated by an incoherent population mechanism involving tunneling from an exciton reservoir created on nearby higher-energy Te_2 molecules. The application of a weak, non resonant (NR) laser displaced the oscillation maximum towards higher $P_{\text{ex}}^{1/2}$ and increased the overall I_{em} , suggesting its environment-discharging effect had an impact on the norm of d and on the detuning (Δ) between the transition and the driving field.

Most emitters presented little to no coherence, underlining the deleterious effect environmental charge fluctuations have on their quantum properties. Stabilization of the environment was attempted with the use of the aforementioned NR laser and the application of an electric field. Although both of these methods had an impact on the collected photoluminescence (PL) signal, none offered a sufficient stabilization to observe several Rabi cycles.

7.1.1 Fulfilment of the research objectives

In light of the results obtained throughout this work, the research objectives presented in Sect. 1.3 were for the most part met. Although no evidence of bound-exciton excited states was found, the identification of higher-energy states of interest for control protocols (Objective 1) was fulfilled with the observation of the efficient transfer from the FX towards bound-exciton states, which led to the E_{em} modulation of the latter. Population mechanisms for both resonant and NR excitation were also successfully described (Objective 2).

Objective 3 could only be in part addressed, since coherent behavior proved quite challenging to observe. No performance parameters (T_1 , T_2 , d) could be reliably extracted from the resulting Rabi oscillations due to the presence of a single cycle. Evidence of coherence was nevertheless demonstrated, and means to facilitate its further observation were identified.

The effect of the environment on the PL response of an emitter (Objective 4) was thoroughly documented for both resonant and NR excitation. It was found that it led to spectral diffusion, a fluctuation of the instantaneous Ω , a magnitude reduction of d and a Δ increase. However, our efforts to mitigate its deleterious effects in the resonant pulsed regime were not sufficient to recover perfect coherence.

Finally, numerous mechanisms were explored in order to explain the E_{em} oscillation as a function of E_{ex} during PLE (Objective 5). None of them reproduced all the features of the experimental data, though the polariton model performed quite well in giving rise to a suitable T_{ex} and in reproducing the general shape of the oscillation curve. Its major shortcoming resided in its failure to generate the oscillation within the whole E_{ex} range of interest.

7.1.2 Originality

The originality of the work mainly resides in the new information it provided on a very little-studied OAQ candidate. It unveiled the population mechanisms of a Te_2 -bound exciton under resonant and below-gap, NR excitation conditions. Furthermore, a remote E_{em} modulation of a bound exciton and the potential interaction of the latter with free exciton-polaritons have to my knowledge never been reported for this or any other system and could have great implications for control protocols, allowing for example the fine-tuning of the emitter to a cavity or to another qubit.

This work also led to the first clear observation of a coherent behavior through Rabi oscillations in ZnSe:Te₂, emphasizing a competition between coherent and incoherent population mechanisms with its very unusual shape. Also, the fluctuating instantaneous Ω necessary to the modelling of the drastic Rabi-oscillation damping present in the data has never been reported for a semiconductor system. Finally, the stabilizing effect of a NR laser in the pulsed regime was for the first time clarified for a Te₂-bound exciton.

7.2 Limitations

The study was conducted only on a few samples due to the limited availability of those presenting suitable emission characteristics (i.e. resolvable single emitters in energy ranges accessible to our lasers, absence of other broad emission structures preventing their observation). Since our group does not have the expertise to grow and fabricate specific heterostructures, only few iterations on the sample structure could be made through collaborations. The systematic effect of this parameter on the observed phenomena could therefore not be investigated. It nevertheless appeared clearly from our results that sample quality is nowhere near the level achieved for III-V semiconductors and that substantial development would be required to improve the performance of the emitters as OAQs.

The small PL signal from the emitters and the limited stability of the setup restricted the extent of the measurements performed on a particular exciton. This was especially the case during the PLE experiment, where we could not keep an emitter for more than a day. Therefore, it was most of the time not possible to study the influence of stochastic events on the properties of an emitter of interest or to vary several parameters to get a systematic portrait of it. Signal strength and stability were improved in between PLE and resonant excitation measurement campaigns through the use of a more sensitive CCD camera and more stable and efficient optical and opto-mechanical parts, leading to a more complete data collection in the latter experiment.

7.3 Future research

The intriguing results obtained in this work justify further studies to characterize the performances of the ZnSe:Te₂ system as an OAQ platform. In the near future, several modifications

to the sample structure could be made to improve its homogeneity and emission properties, or to test its impact on the polaritonic field distribution, the electrical stability of the environment and the coherence of a single emitter. Also, several experiments could be easily attempted and, if successful, deepen our understanding of the population and interaction mechanisms identified in this work, or demonstrate crucial coherent control steps. All this progress would most likely establish even more strongly the interest of ZnSe:Te₂-based OAQs.

7.3.1 Sample structure

Our ZnSe samples showed very variable emission properties from areas to areas. Their quality and structure should be improved in the future in order to get better emitter coherence. The reduction of impurity and defect concentrations, as well as the embedment of the emitters in a gated device such as a specifically designed Schottky diode would help mitigate spectral diffusion by limiting the fluctuating charge reservoir and offering a robust mean of stabilizing the charge environment.

Second, the use of cavities and solid-immersion lenses would improve the emission signal-to-noise ratio (SNR) and strengthen the interaction with the driving field. This would simultaneously lead to a reduction of the acquisition and measurement times and consequently allow for more complete experiments to be performed on the same emitter.

7.3.2 E_{em} oscillation and the polariton model

More simulations should be done within the polariton framework to try and generate an E_{em} oscillation below the resonance. Guided polaritons among other things could be explored for that purpose.

On a different note, the observation of an E_{em} oscillation in samples of different thicknesses, or equivalently while varying the incidence angle of the exciting field on a single sample, would add experimental weight to the polariton explanation. Indeed, the polaritonic field distribution in the layer should be modified and the consequent change in T_{ex} would support their involvement in the E_{em} oscillation. Dependence of A_{em} on P_{ex} could also be investigated. In the same vein, coupling to cavity polaritons could be attempted with hopes of improving the efficiency and strength of the interaction.

Finally, the spatial displacement of the excitation with respect to the emitter as was done in Ref. [197], where a bound-exciton emission-line blueshift was observed for coincident excitation with respect to off-center excitation, and time-resolved absorption measurements as in Refs. [193,194], where a blueshift of the FX line was observed for pump-probe delays ranging from tens to a hundred ps, might allow to confirm or refute exciton-exciton interactions as the mechanism behind the E_{em} shift.

7.3.3 Coherent control

The study of the impact of P_{ex} and of the non-resonant power (P_{NR}) on the coherent behavior of a Te_2 -bound exciton would benefit from being pursued. In particular, the Ω fluctuations proposed in Chap. 6, resulting from a mixing of the excitonic states according to the surrounding electric field, which in turn leads to a modification of the dipole orientation and magnitude, could be monitored through polarization changes in the resonant emission. For that purpose, efficient laser rejection strategies that do not rely on polarization would have to be implemented on the setup, such as the use of a Fabry-Perot etalon.

More work must also be done to properly understand the conditions in which the application of a DC electric field sufficiently stabilizes the environment of an emitter to observe coherence. Once the environment is stabilized, lifetime measurements on Te_2 -bound excitons, the demonstration of undamped Rabi oscillations and other coherent control steps such as Ramsey interferometry would lead to the evaluation of the sought-after T_1 , T_2 and d for that type of qubit.

Finally, the application of an electric field would allow controlling the charge state of the defect, facilitating the observation of trions. These excitonic complexes are essential to the control of single hole spins, a more interesting qubit type than the exciton as its T_1 is not limited by a radiative lifetime. Single spin control and readout are still to be demonstrated in $\text{ZnSe}:\text{Te}_2$, or in any isoelectronic center (IC) system for that matter. They are in my opinion the main avenue to pursue once proofs of concept with excitons are achieved, and could have great technological impacts if their properties prove to be as interesting as expected.

REFERENCES

- [1] F. Arute *et al.*, “Quantum supremacy using a programmable superconducting processor,” *Nature*, vol. 574, no. 7779, pp. 505–510, oct 2019. [Online]. Available: <http://dx.doi.org/10.1038/s41586-019-1666-5>
- [2] F. Arute *et al.*, “Hartree-Fock on a superconducting qubit quantum computer,” *Science*, vol. 369, no. 6507, pp. 1084–1089, aug 2020. [Online]. Available: <https://www.science.org/doi/10.1126/science.abb9811>
- [3] P. Frey and S. Rachel, “Realization of a discrete time crystal on 57 qubits of a quantum computer,” *Science Advances*, vol. 8, no. 9, pp. 1–7, mar 2022. [Online]. Available: <https://www.science.org/doi/10.1126/sciadv.abm7652>
- [4] A. Sopena *et al.*, “Simulating quench dynamics on a digital quantum computer with data-driven error mitigation,” *Quantum Science and Technology*, vol. 6, no. 4, p. 045003, oct 2021. [Online]. Available: <https://iopscience.iop.org/article/10.1088/2058-9565/ac0e7a>
- [5] M. Urbanek *et al.*, “Mitigating Depolarizing Noise on Quantum Computers with Noise-Estimation Circuits,” *Physical Review Letters*, vol. 127, no. 27, p. 270502, dec 2021. [Online]. Available: <https://link.aps.org/doi/10.1103/PhysRevLett.127.270502>
- [6] M. P. Harrigan *et al.*, “Quantum approximate optimization of non-planar graph problems on a planar superconducting processor,” *Nature Physics*, vol. 17, no. 3, pp. 332–336, mar 2021. [Online]. Available: <http://www.nature.com/articles/s41567-020-01105-y>
- [7] S. Muel *et al.*, “Hybrid quantum investment optimization with minimal holding period,” *Scientific Reports*, vol. 11, no. 1, p. 19587, dec 2021. [Online]. Available: <https://www.nature.com/articles/s41598-021-98297-x>
- [8] M. Klar *et al.*, “Quantum Annealing based factory layout planning,” *Manufacturing Letters*, vol. 32, pp. 59–62, apr 2022. [Online]. Available: <https://doi.org/10.1016/j.mfglet.2022.03.003>
- [9] M. Fox, “La sphère de Bloch,” in *Optique quantique*. Brussels, Belgium: De Boeck, 2011, ch. 9.6, pp. 209–213.

- [10] T. D. Ladd *et al.*, “Quantum computers,” *Nature*, vol. 464, no. 7285, pp. 45–53, mar 2010. [Online]. Available: <http://dx.doi.org/10.1038/nature08812>
- [11] M. Fox, “Décohérence et correction d’erreur,” in *Optique quantique*. Brussels, Belgium: De Boeck, 2011, ch. 13.4, pp. 307–309.
- [12] M. Fox, “Limite des champs forts : les oscillations de Rabi,” in *Optique quantique*. Brussels, Belgium: De Boeck, 2011, ch. 9.5, pp. 198–208.
- [13] Y. Yamamoto *et al.*, “Optically controlled semiconductor spin qubits for quantum information processing,” *Physica Scripta*, vol. T137, p. 014010, dec 2009. [Online]. Available: <https://iopscience.iop.org/article/10.1088/0031-8949/2009/T137/014010>
- [14] Y. Kodriano *et al.*, “Optical control of single excitons in semiconductor quantum dots,” *Semiconductor Science and Technology*, vol. 29, no. 5, p. 053001, may 2014. [Online]. Available: <https://iopscience.iop.org/article/10.1088/0268-1242/29/5/053001>
- [15] P. Treutlein *et al.*, “Coherence in Microchip Traps,” *Physical Review Letters*, vol. 92, no. 20, p. 203005, may 2004. [Online]. Available: <https://link.aps.org/doi/10.1103/PhysRevLett.92.203005>
- [16] C. Langer *et al.*, “Long-Lived Qubit Memory Using Atomic Ions,” *Physical Review Letters*, vol. 95, no. 6, p. 060502, aug 2005. [Online]. Available: <https://link.aps.org/doi/10.1103/PhysRevLett.95.060502>
- [17] M. Anderlini *et al.*, “Controlled exchange interaction between pairs of neutral atoms in an optical lattice,” *Nature*, vol. 448, no. 7152, pp. 452–456, jul 2007. [Online]. Available: <http://www.nature.com/articles/nature06011>
- [18] J. Benhelm *et al.*, “Towards fault-tolerant quantum computing with trapped ions,” *Nature Physics*, vol. 4, no. 6, pp. 463–466, jun 2008. [Online]. Available: <http://www.nature.com/articles/nphys961>
- [19] W. F. Koehl *et al.*, “Room temperature coherent control of defect spin qubits in silicon carbide,” *Nature*, vol. 479, no. 7371, pp. 84–87, nov 2011. [Online]. Available: <http://dx.doi.org/10.1038/nature10562>
- [20] D. J. Christle *et al.*, “Isolated electron spins in silicon carbide with millisecond coherence times,” *Nature Materials*, vol. 14, no. 2, pp. 160–163, feb 2015. [Online]. Available: <http://www.nature.com/articles/nmat4144>

- [21] M. Widmann *et al.*, “Coherent control of single spins in silicon carbide at room temperature,” *Nature Materials*, vol. 14, no. 2, pp. 164–168, feb 2015. [Online]. Available: <http://www.nature.com/articles/nmat4145>
- [22] H. Seo *et al.*, “Quantum decoherence dynamics of divacancy spins in silicon carbide,” *Nature Communications*, vol. 7, no. May, p. 12935, sep 2016. [Online]. Available: <http://www.nature.com/doifinder/10.1038/ncomms12935>
- [23] K. De Greve *et al.*, “Photon antibunching and magnetospectroscopy of a single fluorine donor in ZnSe,” *Applied Physics Letters*, vol. 97, no. 24, p. 241913, dec 2010. [Online]. Available: <http://aip.scitation.org/doi/10.1063/1.3525579>
- [24] A. Greulich *et al.*, “Spin dephasing of fluorine-bound electrons in ZnSe,” *Physical Review B*, vol. 85, no. 12, p. 121303, mar 2012. [Online]. Available: <https://link.aps.org/doi/10.1103/PhysRevB.85.121303>
- [25] G. Éthier-Majcher *et al.*, “Complete quantum control of exciton qubits bound to isoelectronic centres,” *Nature Communications*, vol. 5, no. May, p. 3980, jan 2014. [Online]. Available: <http://www.nature.com/articles/ncomms4980>
- [26] E. A. Zhukov *et al.*, “All-optical NMR in semiconductors provided by resonant cooling of nuclear spins interacting with electrons in the resonant spin amplification regime,” *Physical Review B*, vol. 90, no. 8, p. 085311, aug 2014. [Online]. Available: <https://link.aps.org/doi/10.1103/PhysRevB.90.085311>
- [27] G. Éthier-Majcher, P. St-Jean, and S. Francoeur, “Light- and heavy-hole trions bound to isoelectronic centers,” *Physical Review B*, vol. 92, no. 15, p. 155436, oct 2015. [Online]. Available: <https://link.aps.org/doi/10.1103/PhysRevB.92.155436>
- [28] P. St-Jean *et al.*, “High-Fidelity and Ultrafast Initialization of a Hole Spin Bound to a Te Isoelectronic Center in ZnSe,” *Physical Review Letters*, vol. 117, no. 16, p. 167401, oct 2016. [Online]. Available: <https://link.aps.org/doi/10.1103/PhysRevLett.117.167401>
- [29] E. A. Zhukov *et al.*, “Discretization of the total magnetic field by the nuclear spin bath in fluorine-doped ZnSe,” *Nature Communications*, vol. 9, no. 1, p. 1941, dec 2018. [Online]. Available: <http://www.nature.com/articles/s41467-018-04359-6>
- [30] N. H. Bonadeo *et al.*, “Coherent Optical Control of the Quantum State of a Single Quantum Dot,” *Science*, vol. 282, no. 5393, pp. 1473–1476, nov 1998. [Online]. Available: <https://www.science.org/doi/10.1126/science.282.5393.1473>

- [31] H. Kamada *et al.*, “Exciton Rabi Oscillation in a Single Quantum Dot,” *Physical Review Letters*, vol. 87, no. 24, p. 246401, nov 2001. [Online]. Available: <https://link.aps.org/doi/10.1103/PhysRevLett.87.246401>
- [32] T. H. Stievater *et al.*, “Rabi Oscillations of Excitons in Single Quantum Dots,” *Physical Review Letters*, vol. 87, no. 13, p. 133603, sep 2001. [Online]. Available: <https://link.aps.org/doi/10.1103/PhysRevLett.87.133603>
- [33] H. Htoon *et al.*, “Interplay of Rabi Oscillations and Quantum Interference in Semiconductor Quantum Dots,” *Physical Review Letters*, vol. 88, no. 8, p. 087401, feb 2002. [Online]. Available: <https://link.aps.org/doi/10.1103/PhysRevLett.88.087401>
- [34] L. Besombes, J. J. Baumberg, and J. Motohisa, “Coherent Spectroscopy of Optically Gated Charged Single InGaAs Quantum Dots,” *Physical Review Letters*, vol. 90, no. 25, p. 257402, jun 2003. [Online]. Available: <https://link.aps.org/doi/10.1103/PhysRevLett.90.257402>
- [35] A. Muller *et al.*, “Determination of anisotropic dipole moments in self-assembled quantum dots using Rabi oscillations,” *Applied Physics Letters*, vol. 84, no. 6, pp. 981–983, feb 2004. [Online]. Available: <http://aip.scitation.org/doi/10.1063/1.1646462>
- [36] A. Greilich *et al.*, “Optical Control of Spin Coherence in Singly Charged (In,Ga)As/GaAs Quantum Dots,” *Physical Review Letters*, vol. 96, no. 22, p. 227401, jun 2006. [Online]. Available: <https://link.aps.org/doi/10.1103/PhysRevLett.96.227401>
- [37] A. Greilich *et al.*, “Mode Locking of Electron Spin Coherences in Singly Charged Quantum Dots,” *Science*, vol. 313, no. 5785, pp. 341–345, jul 2006. [Online]. Available: <https://www.science.org/doi/10.1126/science.1128215>
- [38] K. Goshima *et al.*, “Pulse Area Control of Exciton Rabi Oscillation in InAs/GaAs Single Quantum Dot,” *Japanese Journal of Applied Physics*, vol. 45, no. 4B, pp. 3625–3628, apr 2006. [Online]. Available: <https://iopscience.iop.org/article/10.1143/JJAP.45.3625>
- [39] A. Muller *et al.*, “Resonance Fluorescence from a Coherently Driven Semiconductor Quantum Dot in a Cavity,” *Physical Review Letters*, vol. 99, no. 18, p. 187402, nov 2007. [Online]. Available: <https://link.aps.org/doi/10.1103/PhysRevLett.99.187402>
- [40] J. Berezovsky *et al.*, “Picosecond Coherent Optical Manipulation of a Single Electron Spin in a Quantum Dot,” *Science*, vol. 320, no. 5874, pp. 349–352, apr 2008. [Online]. Available: <http://www.sciencemag.org/cgi/doi/10.1126/science.1154798>

- [41] R. Melet *et al.*, “Resonant excitonic emission of a single quantum dot in the Rabi regime,” *Physical Review B*, vol. 78, no. 7, p. 073301, aug 2008. [Online]. Available: <https://link.aps.org/doi/10.1103/PhysRevB.78.073301>
- [42] D. Press *et al.*, “Complete quantum control of a single quantum dot spin using ultrafast optical pulses,” *Nature*, vol. 456, no. 7219, pp. 218–21, nov 2008. [Online]. Available: <http://www.nature.com/articles/nature07530>
- [43] A. Greilich *et al.*, “Ultrafast optical rotations of electron spins in quantum dots,” *Nature Physics*, vol. 5, no. 4, pp. 262–266, apr 2009. [Online]. Available: <http://dx.doi.org/10.1038/nphys1226>
- [44] D. Press *et al.*, “Ultrafast optical spin echo in a single quantum dot,” *Nature Photonics*, vol. 4, no. 6, pp. 367–370, jun 2010. [Online]. Available: <http://www.nature.com/articles/nphoton.2010.83>
- [45] K. De Greve *et al.*, “Ultrafast coherent control and suppressed nuclear feedback of a single quantum dot hole qubit,” *Nature Physics*, vol. 7, no. 11, pp. 872–878, nov 2011. [Online]. Available: <http://dx.doi.org/10.1038/nphys2078>
- [46] T. M. Godden *et al.*, “Coherent Optical Control of the Spin of a Single Hole in an InAs/GaAs Quantum Dot,” *Physical Review Letters*, vol. 108, no. 1, p. 017402, jan 2012. [Online]. Available: <https://link.aps.org/doi/10.1103/PhysRevLett.108.017402>
- [47] J. R. Schaibley *et al.*, “Direct detection of time-resolved Rabi oscillations in a single quantum dot via resonance fluorescence,” *Physical Review B*, vol. 87, no. 11, p. 115311, mar 2013. [Online]. Available: <https://link.aps.org/doi/10.1103/PhysRevB.87.115311>
- [48] R. J. Warburton, “Single spins in self-assembled quantum dots,” *Nature Materials*, vol. 12, no. 6, pp. 483–493, 2013. [Online]. Available: <https://www.nature.com/articles/nmat3585>
- [49] T. Gaebel *et al.*, “Room-temperature coherent coupling of single spins in diamond,” *Nature Physics*, vol. 2, no. 6, pp. 408–413, jun 2006. [Online]. Available: <http://www.nature.com/articles/nphys318>
- [50] J. Harrison, M. Sellars, and N. Manson, “Measurement of the optically induced spin polarisation of N-V centres in diamond,” *Diamond and Related Materials*, vol. 15, no. 4-8, pp. 586–588, apr 2006. [Online]. Available: <https://linkinghub.elsevier.com/retrieve/pii/S0925963505006266>

- [51] F. Jelezko and J. Wrachtrup, “Single defect centres in diamond: A review,” *physica status solidi (a)*, vol. 203, no. 13, pp. 3207–3225, oct 2006. [Online]. Available: <https://onlinelibrary.wiley.com/doi/10.1002/pssa.200671403>
- [52] A. Batalov *et al.*, “Temporal Coherence of Photons Emitted by Single Nitrogen-Vacancy Defect Centers in Diamond Using Optical Rabi-Oscillations,” *Physical Review Letters*, vol. 100, no. 7, p. 077401, feb 2008. [Online]. Available: <https://link.aps.org/doi/10.1103/PhysRevLett.100.077401>
- [53] G. Balasubramanian *et al.*, “Ultralong spin coherence time in isotopically engineered diamond,” *Nature Materials*, vol. 8, no. 5, pp. 383–387, may 2009. [Online]. Available: <http://www.nature.com/articles/nmat2420>
- [54] L. Robledo *et al.*, “High-fidelity projective read-out of a solid-state spin quantum register,” *Nature*, vol. 477, no. 7366, pp. 574–578, 2011. [Online]. Available: <http://www.nature.com/articles/nature10401>
- [55] L. Robledo *et al.*, “Spin dynamics in the optical cycle of single nitrogen-vacancy centres in diamond,” *New Journal of Physics*, vol. 13, no. 2, p. 025013, feb 2011. [Online]. Available: <https://iopscience.iop.org/article/10.1088/1367-2630/13/2/025013>
- [56] A. Jarmola *et al.*, “Temperature- and Magnetic-Field-Dependent Longitudinal Spin Relaxation in Nitrogen-Vacancy Ensembles in Diamond,” *Physical Review Letters*, vol. 108, no. 19, p. 197601, may 2012. [Online]. Available: <https://link.aps.org/doi/10.1103/PhysRevLett.108.197601>
- [57] C. G. Yale *et al.*, “All-optical control of a solid-state spin using coherent dark states,” *Proceedings of the National Academy of Sciences*, vol. 110, no. 19, pp. 7595–7600, 2013. [Online]. Available: <http://www.pnas.org/cgi/doi/10.1073/pnas.1305920110>
- [58] L. C. Bassett *et al.*, “Ultrafast optical control of orbital and spin dynamics in a solid-state defect,” *Science*, vol. 345, no. 6202, pp. 1333–1337, sep 2014. [Online]. Available: <https://www.science.org/doi/10.1126/science.1255541>
- [59] L. Li *et al.*, “Coherent spin control of a nanocavity-enhanced qubit in diamond,” *Nature Communications*, vol. 6, no. 1, p. 6173, may 2015. [Online]. Available: <http://www.nature.com/articles/ncomms7173>
- [60] T. Chakraborty, J. Zhang, and D. Suter, “Polarizing the electronic and nuclear spin of the NV-center in diamond in arbitrary magnetic fields: analysis of the optical

- pumping process,” *New Journal of Physics*, vol. 19, no. 7, p. 073030, jul 2017. [Online]. Available: <https://iopscience.iop.org/article/10.1088/1367-2630/aa7727>
- [61] E. Neu *et al.*, “Low-temperature investigations of single silicon vacancy colour centres in diamond,” *New Journal of Physics*, vol. 15, no. 4, p. 043005, apr 2013. [Online]. Available: <https://iopscience.iop.org/article/10.1088/1367-2630/15/4/043005>
- [62] L. Rogers *et al.*, “Multiple intrinsically identical single-photon emitters in the solid state,” *Nature Communications*, vol. 5, no. 1, p. 4739, dec 2014. [Online]. Available: <http://www.nature.com/articles/ncomms5739>
- [63] L. J. Rogers *et al.*, “All-Optical Initialization, Readout, and Coherent Preparation of Single Silicon-Vacancy Spins in Diamond,” *Physical Review Letters*, vol. 113, no. 26, p. 263602, dec 2014. [Online]. Available: <https://link.aps.org/doi/10.1103/PhysRevLett.113.263602>
- [64] J. N. Becker *et al.*, “Ultrafast all-optical coherent control of single silicon vacancy colour centres in diamond,” *Nature Communications*, vol. 7, no. 1, p. 13512, dec 2016. [Online]. Available: <http://www.nature.com/articles/ncomms13512>
- [65] A. Sipahigil *et al.*, “An integrated diamond nanophotonics platform for quantum-optical networks,” *Science*, vol. 354, no. 6314, pp. 847–850, nov 2016. [Online]. Available: <https://www.science.org/doi/10.1126/science.aah6875>
- [66] J. N. Becker and C. Becher, “Coherence Properties and Quantum Control of Silicon Vacancy Color Centers in Diamond,” *physica status solidi (a)*, vol. 214, no. 11, p. 1700586, nov 2017. [Online]. Available: <https://onlinelibrary.wiley.com/doi/10.1002/pssa.201700586>
- [67] D. D. Sukachev *et al.*, “Silicon-Vacancy Spin Qubit in Diamond: A Quantum Memory Exceeding 10 ms with Single-Shot State Readout,” *Physical Review Letters*, vol. 119, no. 22, p. 223602, nov 2017. [Online]. Available: <https://link.aps.org/doi/10.1103/PhysRevLett.119.223602>
- [68] Y. Zhou *et al.*, “Coherent control of a strongly driven silicon vacancy optical transition in diamond,” *Nature Communications*, vol. 8, no. 1, p. 14451, apr 2017. [Online]. Available: <http://www.nature.com/articles/ncomms14451>
- [69] J. N. Becker *et al.*, “All-Optical Control of the Silicon-Vacancy Spin in Diamond at Millikelvin Temperatures,” *Physical Review Letters*, vol. 120, no. 5, p. 053603, jan 2018. [Online]. Available: <https://link.aps.org/doi/10.1103/PhysRevLett.120.053603>

- [70] D. A. Steck. (2001) Rubidium 87 D Line Data. [Online]. Available: <https://steck.us/alkalidata/rubidium87numbers.1.6.pdf>
- [71] M. Chwalla, “Precision Spectroscopy With $^{40}\text{Ca}^+$ ions In A Paul Trap,” Ph. D. dissertation, Fakultät für Mathematik, Informatik und Physik, Leopold-Franzens-Universität Innsbruck, Innsbruck, Austria, 2009. [Online]. Available: https://www.quantumoptics.at/images/publications/dissertation/chwalla_diss.pdf
- [72] H.-Y. Lo, “Creation of Squeezed Schrödinger’s Cat States in a Mixed-Species Ion Trap,” Ph. D. dissertation, Department of Physics, ETH Zürich, Zürich, Switzerland, 2015. [Online]. Available: <https://www.research-collection.ethz.ch/handle/20.500.11850/111011>
- [73] E. C. Cook, A. D. Vira, and W. D. Williams, “Resonant two-photon spectroscopy of the $2s3d\ ^1D_2$ level of neutral ^9Be ,” *Physical Review A*, vol. 101, no. 4, p. 042503, apr 2020. [Online]. Available: <https://link.aps.org/doi/10.1103/PhysRevA.101.042503>
- [74] J. Jin and D. A. Church, “Precision lifetimes for the $\text{Ca}^+ 4p\ 2^P$ levels: Experiment challenges theory at the 1% level,” *Physical Review Letters*, vol. 70, no. 21, pp. 3213–3216, may 1993. [Online]. Available: <https://link.aps.org/doi/10.1103/PhysRevLett.70.3213>
- [75] B. K. Sahoo *et al.*, “Lifetimes of the metastable $^2D_{3/2,5/2}$ states in Ca^+ , Sr^+ , and Ba^+ ,” *Physical Review A*, vol. 74, no. 6, p. 062504, dec 2006. [Online]. Available: <https://link.aps.org/doi/10.1103/PhysRevA.74.062504>
- [76] M. Hettrich *et al.*, “Measurement of Dipole Matrix Elements with a Single Trapped Ion,” *Physical Review Letters*, vol. 115, no. 14, p. 143003, oct 2015. [Online]. Available: <https://link.aps.org/doi/10.1103/PhysRevLett.115.143003>
- [77] D. Chen *et al.*, “Characterization of the local charge environment of a single quantum dot via resonance fluorescence,” *Physical Review B*, vol. 93, no. 11, p. 115307, mar 2016. [Online]. Available: <https://link.aps.org/doi/10.1103/PhysRevB.93.115307>
- [78] A. Reigue *et al.*, “Resonance fluorescence revival in a voltage-controlled semiconductor quantum dot,” *Applied Physics Letters*, vol. 112, no. 7, p. 073103, feb 2018. [Online]. Available: <http://aip.scitation.org/doi/10.1063/1.5010757>
- [79] L. Robledo *et al.*, “Control and Coherence of the Optical Transition of Single Nitrogen Vacancy Centers in Diamond,” *Physical Review Letters*, vol. 105, no. 17, p. 177403, oct 2010. [Online]. Available: <https://link.aps.org/doi/10.1103/PhysRevLett.105.177403>

- [80] Y. Chu and M. D. Lukin, “Quantum optics with nitrogen-vacancy centers in diamond,” p. 39, apr 2015. [Online]. Available: <http://arxiv.org/abs/1504.05990>
- [81] J. Davidsson, “Theoretical polarization of zero phonon lines in point defects,” *Journal of Physics: Condensed Matter*, vol. 32, no. 38, p. 385502, sep 2020. [Online]. Available: <https://iopscience.iop.org/article/10.1088/1361-648X/ab94f4>
- [82] R. Schwabe *et al.*, “Photoluminescence of nitrogen-doped VPE GaAs,” *Solid State Communications*, vol. 55, no. 2, pp. 167–173, jul 1985. [Online]. Available: <https://linkinghub.elsevier.com/retrieve/pii/0038109885902728>
- [83] P. St-Jean, G. Éthier-Majcher, and S. Francoeur, “Dynamics of excitons bound to nitrogen isoelectronic centers in GaAs,” *Physical Review B*, vol. 91, no. 11, p. 115201, mar 2015. [Online]. Available: <https://link.aps.org/doi/10.1103/PhysRevB.91.115201>
- [84] S. Marcet, R. André, and S. Francoeur, “Excitons bound to Te isoelectronic dyads in ZnSe,” *Physical Review B*, vol. 82, no. 23, p. 235309, dec 2010. [Online]. Available: <http://link.aps.org/doi/10.1103/PhysRevB.82.235309>
- [85] J. Prieto and I. Markov, “Stranski–Krastanov mechanism of growth and the effect of misfit sign on quantum dots nucleation,” *Surface Science*, vol. 664, no. May, pp. 172–184, oct 2017. [Online]. Available: <https://linkinghub.elsevier.com/retrieve/pii/S0039602817301528>
- [86] F. K. Malinowski *et al.*, “Notch filtering the nuclear environment of a spin qubit,” *Nature Nanotechnology*, vol. 12, no. 1, pp. 16–20, jan 2017. [Online]. Available: <http://www.nature.com/articles/nnano.2016.170>
- [87] M. Veldhorst *et al.*, “An addressable quantum dot qubit with fault-tolerant control-fidelity,” *Nature Nanotechnology*, vol. 9, no. 12, pp. 981–985, dec 2014. [Online]. Available: <http://www.nature.com/articles/nnano.2014.216>
- [88] K. Eng *et al.*, “Isotopically enhanced triple-quantum-dot qubit,” *Science Advances*, vol. 1, no. 4, pp. 1–8, may 2015. [Online]. Available: <https://www.science.org/doi/10.1126/sciadv.1500214>
- [89] J. T. Muhonen *et al.*, “Storing quantum information for 30 seconds in a nanoelectronic device,” *Nature Nanotechnology*, vol. 9, no. 12, pp. 986–991, dec 2014. [Online]. Available: <http://www.nature.com/articles/nnano.2014.211>

- [90] J. J. Hopfield, D. G. Thomas, and R. T. Lynch, “Isoelectronic Donors and Acceptors,” *Physical Review Letters*, vol. 17, no. 6, pp. 312–315, aug 1966. [Online]. Available: <https://link.aps.org/doi/10.1103/PhysRevLett.17.312>
- [91] D. G. Thomas and J. J. Hopfield, “Isoelectronic Traps Due to Nitrogen in Gallium Phosphide,” *Physical Review*, vol. 150, no. 2, pp. 680–689, oct 1966. [Online]. Available: <https://link.aps.org/doi/10.1103/PhysRev.150.680>
- [92] B. Gil *et al.*, “Local symmetry of nitrogen pairs in GaP,” *Physical Review B*, vol. 33, no. 4, pp. 2690–2700, feb 1986. [Online]. Available: <https://link.aps.org/doi/10.1103/PhysRevB.33.2690>
- [93] S. Francoeur, J. F. Klem, and A. Mascarenhas, “Optical Spectroscopy of Single Impurity Centers in Semiconductors,” *Physical Review Letters*, vol. 93, no. 6, p. 067403, aug 2004. [Online]. Available: <https://link.aps.org/doi/10.1103/PhysRevLett.93.067403>
- [94] A. Muller *et al.*, “Time-resolved photoluminescence spectroscopy of individual Te impurity centers in ZnSe,” *Physical Review B*, vol. 73, no. 8, p. 081306, feb 2006. [Online]. Available: <https://link.aps.org/doi/10.1103/PhysRevB.73.081306>
- [95] S. Marcet *et al.*, “Charged excitons and biexcitons bound to isoelectronic centers,” *Physical Review B*, vol. 82, no. 23, p. 235311, dec 2010. [Online]. Available: <https://link.aps.org/doi/10.1103/PhysRevB.82.235311>
- [96] I. L. Kuskovsky *et al.*, “Optical properties of δ -doped ZnSe:Te grown by molecular beam epitaxy: The role of tellurium,” *Physical Review B*, vol. 63, no. 15, p. 155205, mar 2001. [Online]. Available: <http://link.aps.org/doi/10.1103/PhysRevB.63.155205>
- [97] J. S. Coursey *et al.* (2015) Atomic Weights and Isotopic Compositions with Relative Atomic Masses. [Online]. Available: <https://www.nist.gov/pml/atomic-weights-and-isotopic-compositions-relative-atomic-masses>
- [98] T. B. Coplen *et al.*, “Isotope-abundance variations of selected elements (IUPAC Technical Report),” *Pure and Applied Chemistry*, vol. 74, no. 10, pp. 1987–2017, jan 2002. [Online]. Available: <http://www.degruyter.com/view/j/pac.2002.74.issue-10/pac200274101987/pac200274101987.xml>
- [99] S. Adachi, “Zinc Selenide (ZnSe),” in *Optical Constants of Crystalline and Amorphous Semiconductors*. Boston, MA: Springer US, 1999, ch. 8, pp. 161–210. [Online]. Available: http://link.springer.com/10.1007/978-1-4615-5247-5_35

- [100] S. Fujita, H. Mimoto, and T. Noguchi, “Photoluminescence in ZnSe grown by liquid-phase epitaxy from Zn-Ga solution,” *Journal of Applied Physics*, vol. 50, no. 2, pp. 1079–1087, feb 1979. [Online]. Available: <http://aip.scitation.org/doi/10.1063/1.326084>
- [101] P. J. Dean *et al.*, “Donor bound-exciton excited states in zinc selenide,” *Physical Review B*, vol. 23, no. 10, pp. 4888–4901, may 1981. [Online]. Available: <https://link.aps.org/doi/10.1103/PhysRevB.23.4888>
- [102] Y. Shirakawa and H. Kukimoto, “Near-band-edge photoluminescence in ZnSe grown from indium solution,” *Journal of Applied Physics*, vol. 51, no. 4, p. 2014, 1980. [Online]. Available: <http://scitation.aip.org/content/aip/journal/jap/51/4/10.1063/1.327919>
- [103] J. A. Tuchman *et al.*, “Exciton photoluminescence in strained and unstrained ZnSe under hydrostatic pressure,” *Physical Review B*, vol. 46, no. 20, pp. 13 371–13 378, nov 1992. [Online]. Available: <https://link.aps.org/doi/10.1103/PhysRevB.46.13371>
- [104] G. E. Hite *et al.*, “Excitons and the Absorption Edge in ZnSe,” *Physical Review*, vol. 156, no. 3, pp. 850–859, apr 1967. [Online]. Available: <https://link.aps.org/doi/10.1103/PhysRev.156.850>
- [105] J. L. Merz *et al.*, “Optical Properties of Substitutional Donors in ZnSe,” *Physical Review B*, vol. 6, no. 2, pp. 545–556, jul 1972. [Online]. Available: <https://link.aps.org/doi/10.1103/PhysRevB.6.545>
- [106] M. Itoh *et al.*, “Luminescence of highly excited ZnSe,” *Journal of Luminescence*, vol. 18-19, pp. 568–572, jan 1979. [Online]. Available: <http://linkinghub.elsevier.com/retrieve/pii/0022231379901959>
- [107] V. P. Gribkovskii *et al.*, “Optical Absorption near Excitonic Resonance of MOCVD-Grown ZnSe Single Crystals,” *physica status solidi (b)*, vol. 158, no. 1, pp. 359–366, mar 1990. [Online]. Available: <http://doi.wiley.com/10.1002/pssb.2221580136>
- [108] J. Zheng and J. W. Allen, “The origin of the blue luminescence in ZnSe at room temperature,” *Journal of Applied Physics*, vol. 67, no. 4, pp. 2060–2065, feb 1990. [Online]. Available: <http://aip.scitation.org/doi/10.1063/1.345591>
- [109] A. L. Gurskii *et al.*, “Free-exciton spectra in heteroepitaxial ZnSe/GaAs layers,” *Physical Review B*, vol. 61, no. 15, pp. 10 314–10 321, apr 2000. [Online]. Available: <https://link.aps.org/doi/10.1103/PhysRevB.61.10314>

- [110] G. Kudlek *et al.*, “Exciton complexes in ZnSe layers: a tool for probing the strain distribution,” *Journal of Crystal Growth*, vol. 117, no. 1-4, pp. 309–315, feb 1992. [Online]. Available: <https://linkinghub.elsevier.com/retrieve/pii/002202489290765B>
- [111] G. Brownlie *et al.*, “Photoluminescence excitation spectroscopic studies of nitrogen doped ZnSe,” *Journal of Crystal Growth*, vol. 159, no. 1-4, pp. 321–324, feb 1996. [Online]. Available: <https://linkinghub.elsevier.com/retrieve/pii/0022024895007687>
- [112] X. Wang *et al.*, “Thickness dependence of exciton and polariton spectra from ZnSe films grown on GaAs substrates,” *Journal of Applied Physics*, vol. 90, no. 12, pp. 6114–6119, dec 2001. [Online]. Available: <http://aip.scitation.org/doi/10.1063/1.1415061>
- [113] M. E. Levinshtein and S. L. Rumyantsev, “Gallium arsenide (GaAs),” in *Handbook Series on Semiconductor Parameters, Vol. 1*, M. E. Levinshtein, S. L. Rumyantsev, and M. Shur, Eds. Singapore: World Scientific Publishing, nov 1996, vol. 17, no. 5, ch. 4, pp. 77–103. [Online]. Available: https://www.worldscientific.com/doi/abs/10.1142/9789812832078_0004
- [114] S. Satoh and K. Igaki, “Effect of Native Defect Concentration on Free-Exciton Luminescence in Zinc Selenide,” *Japanese Journal of Applied Physics*, vol. 19, no. 10, pp. 1953–1958, oct 1980. [Online]. Available: <http://stacks.iop.org/1347-4065/19/1953>
- [115] S. Feierabend and H. Weber, “Magnetoreflexion of s-excitons in cubic ZnSe,” *Solid State Communications*, vol. 26, no. 3, pp. 191–193, apr 1978. [Online]. Available: <https://linkinghub.elsevier.com/retrieve/pii/0038109878910682>
- [116] B. Gil and H. Mariette, “NN2 trap in GaP: A reexamination,” *Physical Review B*, vol. 35, no. 15, pp. 7999–8004, may 1987. [Online]. Available: <https://link.aps.org/doi/10.1103/PhysRevB.35.7999>
- [117] Y. Zhang *et al.*, “Optical transitions in the isoelectronically doped semiconductor GaP:N: An evolution from isolated centers, pairs, and clusters to an impurity band,” *Physical Review B*, vol. 62, no. 7, pp. 4493–4500, aug 2000. [Online]. Available: <https://link.aps.org/doi/10.1103/PhysRevB.62.4493>
- [118] M. Ikezawa *et al.*, “Single NN pair luminescence and single photon generation in nitrogen δ -doped GaP,” *physica status solidi c*, vol. 6, no. 1, pp. 362–365, jan 2009. [Online]. Available: <https://onlinelibrary.wiley.com/doi/10.1002/pssc.200879830>

- [119] B. Gil *et al.*, “J-J coupling and local-field effects on N-N pair spectra in GaP,” *Physical Review B*, vol. 25, no. 6, pp. 3987–4001, mar 1982. [Online]. Available: <https://link.aps.org/doi/10.1103/PhysRevB.25.3987>
- [120] E. Cohen *et al.*, “Acceptorlike Excited S States of Excitons Bound to Nitrogen Pairs in GaP,” *Physical Review Letters*, vol. 35, no. 23, pp. 1591–1594, dec 1975. [Online]. Available: <https://link.aps.org/doi/10.1103/PhysRevLett.35.1591>
- [121] E. Cohen and M. D. Sturge, “Excited states of excitons bound to nitrogen pairs in GaP,” *Physical Review B*, vol. 15, no. 2, pp. 1039–1051, jan 1977. [Online]. Available: <https://link.aps.org/doi/10.1103/PhysRevB.15.1039>
- [122] G. Éthier-Majcher *et al.*, “Photoluminescence from single nitrogen isoelectronic centers in gallium phosphide produced by ion implantation,” *Journal of Applied Physics*, vol. 114, no. 3, p. 034307, jul 2013. [Online]. Available: <http://aip.scitation.org/doi/10.1063/1.4815883>
- [123] P. St-Jean *et al.*, “Recombination dynamics of excitons bound to nitrogen isoelectronic centers in δ -doped GaP,” *Physical Review B*, vol. 89, no. 7, p. 075308, feb 2014. [Online]. Available: <http://link.aps.org/doi/10.1103/PhysRevB.89.075308>
- [124] P. J. Dean, “Absorption and Luminescence of Excitons at Neutral Donors in Gallium Phosphide,” *Physical Review*, vol. 157, no. 3, pp. 655–667, may 1967. [Online]. Available: <https://link.aps.org/doi/10.1103/PhysRev.157.655>
- [125] P. J. Dean, “Energy-Dependent Capture Cross Sections and the Photoluminescence Excitation Spectra of Gallium Phosphide above the Threshold for Intrinsic Interband Absorption,” *Physical Review*, vol. 168, no. 3, pp. 889–901, apr 1968. [Online]. Available: <https://link.aps.org/doi/10.1103/PhysRev.168.889>
- [126] T. Makimoto and N. Kobayashi, “Sharp photoluminescence lines from nitrogen atomic-layer-doped GaAs,” *Applied Physics Letters*, vol. 67, no. 5, pp. 688–690, jul 1995. [Online]. Available: <http://aip.scitation.org/doi/10.1063/1.115204>
- [127] T. Makimoto, H. Saito, and N. Kobayashi, “Origin of Nitrogen-Pair Luminescence in GaAs Studied by Nitrogen Atomic-Layer-Doping in MOVPE,” *Japanese Journal of Applied Physics*, vol. 36, no. Part 1, No. 3B, pp. 1694–1697, mar 1997. [Online]. Available: <https://iopscience.iop.org/article/10.1143/JJAP.36.1694>
- [128] H. Saito, T. Makimoto, and N. Kobayashi, “Photoluminescence characteristics of nitrogen atomic-layer-doped GaAs grown by MOVPE,” *Journal of Crystal Growth*,

- vol. 170, pp. 372–376, jan 1997. [Online]. Available: <https://linkinghub.elsevier.com/retrieve/pii/S0022024896005234>
- [129] D. Karaiskaj *et al.*, “Excitons bound to nitrogen pairs in GaAs as seen by photoluminescence of high spectral and spatial resolution,” *Physical Review B*, vol. 76, no. 12, p. 125209, sep 2007. [Online]. Available: <https://link.aps.org/doi/10.1103/PhysRevB.76.125209>
 - [130] D. J. Welford *et al.*, “The Nitrogen Isoelectronic Trap in GaAs,” in *Proceedings of the 17th International Conference on the Physics of Semiconductors*. New York, NY: Springer New York, 1985, pp. 627–630. [Online]. Available: http://link.springer.com/10.1007/978-1-4615-7682-2_138
 - [131] X. Liu *et al.*, “Nitrogen pair luminescence in GaAs,” *Applied Physics Letters*, vol. 56, no. 15, pp. 1451–1453, apr 1990. [Online]. Available: <http://aip.scitation.org/doi/10.1063/1.102495>
 - [132] X. Liu, M.-E. Pistol, and L. Samuelson, “Excitons bound to nitrogen pairs in GaAs,” *Physical Review B*, vol. 42, no. 12, pp. 7504–7512, oct 1990. [Online]. Available: <https://link.aps.org/doi/10.1103/PhysRevB.42.7504>
 - [133] D. Karaiskaj *et al.*, “Ultrannarrow photoluminescence transitions of nitrogen cluster bound excitons in dilute GaAsN,” *Physical Review B*, vol. 74, no. 3, p. 035208, jul 2006. [Online]. Available: <https://link.aps.org/doi/10.1103/PhysRevB.74.035208>
 - [134] S. Marcet *et al.*, “Single nitrogen dyad magnetoluminescence in GaAs,” *Physical Review B*, vol. 80, no. 24, p. 245404, dec 2009. [Online]. Available: <https://link.aps.org/doi/10.1103/PhysRevB.80.245404>
 - [135] S. Francoeur *et al.*, “Excitons bound to nitrogen clusters in GaAsN,” *Applied Physics Letters*, vol. 75, no. 11, pp. 1538–1540, sep 1999. [Online]. Available: <http://aip.scitation.org/doi/10.1063/1.124748>
 - [136] T. Kita and O. Wada, “Bound exciton states of isoelectronic centers in GaAs:N grown by an atomically controlled doping technique,” *Physical Review B*, vol. 74, no. 3, p. 035213, jul 2006. [Online]. Available: <https://link.aps.org/doi/10.1103/PhysRevB.74.035213>
 - [137] T. Kita, Y. Harada, and O. Wada, “Fine structure splitting of isoelectronic bound excitons in nitrogen-doped GaAs,” *Physical Review B*, vol. 77, no. 19, p. 193102, may 2008. [Online]. Available: <https://link.aps.org/doi/10.1103/PhysRevB.77.193102>

- [138] Y. Harada *et al.*, “Extremely uniform bound exciton states in nitrogen δ -doped GaAs studied by photoluminescence spectroscopy in external magnetic fields,” *Journal of Applied Physics*, vol. 110, no. 8, p. 083522, oct 2011. [Online]. Available: <http://aip.scitation.org/doi/10.1063/1.3654015>
- [139] Y. Harada *et al.*, “Epitaxial two-dimensional nitrogen atomic sheet in GaAs,” *Applied Physics Letters*, vol. 104, no. 4, p. 041907, jan 2014. [Online]. Available: <http://aip.scitation.org/doi/10.1063/1.4863442>
- [140] M. Jo *et al.*, “Exciton-phonon interactions observed in blue emission band in Te-delta-doped ZnSe,” *Journal of Applied Physics*, vol. 104, no. 3, p. 033531, aug 2008. [Online]. Available: <http://aip.scitation.org/doi/10.1063/1.2966697>
- [141] G. Iseler and A. Strauss, “Photoluminescence due to isoelectronic oxygen and tellurium traps in II–VI alloys,” *Journal of Luminescence*, vol. 3, no. 1, pp. 1–17, apr 1970. [Online]. Available: <https://linkinghub.elsevier.com/retrieve/pii/0022231370900025>
- [142] A. Reznitsky *et al.*, “Localization of excitons and Anderson transition in $\text{ZnSe}_{1-x}\text{Te}_x$ solid solutions,” *Solid State Communications*, vol. 52, no. 1, pp. 13–16, oct 1984. [Online]. Available: <https://linkinghub.elsevier.com/retrieve/pii/0038109884907087>
- [143] D. Lee *et al.*, “Exciton self-trapping in ZnSe-ZnTe alloys,” *Physical Review Letters*, vol. 58, no. 14, pp. 1475–1478, apr 1987. [Online]. Available: <https://link.aps.org/doi/10.1103/PhysRevLett.58.1475>
- [144] H. Stolz *et al.*, “Selective excitation of localised excitons in $\text{ZnSe}_{1-x}\text{Te}_x$ solid solutions,” *Journal of Physics C: Solid State Physics*, vol. 21, no. 29, pp. 5139–5147, oct 1988. [Online]. Available: <https://iopscience.iop.org/article/10.1088/0022-3719/21/29/011>
- [145] T. Yao *et al.*, “Photoluminescence of excitons bound at Te isoelectronic traps in ZnSe,” *Journal of Crystal Growth*, vol. 86, no. 1-4, pp. 552–557, jan 1988. [Online]. Available: <https://linkinghub.elsevier.com/retrieve/pii/002202489090774F>
- [146] Q. Fu *et al.*, “Isoelectronic δ doping in a ZnSe superlattice: Tellurium as an efficient hole trap,” *Physical Review B*, vol. 39, no. 5, pp. 3173–3177, feb 1989. [Online]. Available: <https://link.aps.org/doi/10.1103/PhysRevB.39.3173>
- [147] H. Araki *et al.*, “Photoluminescence in ZnSe:Te Prepared by Solution Growth,” *Japanese Journal of Applied Physics*, vol. 30, no. Part 1, No. 9A, pp. 1919–1923, sep 1991. [Online]. Available: <https://iopscience.iop.org/article/10.1143/JJAP.30.1919>

- [148] C. Lee *et al.*, “Luminescence from free and self-trapped excitons in $\text{ZnSe}_{1-x}\text{Te}_x$,” *Journal of Luminescence*, vol. 48-49, no. PART 1, pp. 116–120, jan 1991. [Online]. Available: <https://linkinghub.elsevier.com/retrieve/pii/002223139190087C>
- [149] C. D. Lee *et al.*, “Free-exciton luminescence from $\text{ZnSe}_{1-x}\text{Te}_x$,” *Physical Review B*, vol. 45, no. 8, pp. 4491–4493, 1992. [Online]. Available: <https://link.aps.org/doi/10.1103/PhysRevB.45.4491>
- [150] C. S. Yang *et al.*, “Optical properties of the $\text{ZnSe}_{1-x}\text{Te}_x$ epilayers grown by molecular beam epitaxy,” *Journal of Applied Physics*, vol. 83, no. 5, pp. 2555–2559, mar 1998. [Online]. Available: <http://aip.scitation.org/doi/10.1063/1.367015>
- [151] A. P. Jacob *et al.*, “Room temperature luminescence from $\text{ZnSe}_{1-x}\text{Te}_x$ ($x < 1\%$) epilayers grown on (001) GaAs,” *Journal of Applied Physics*, vol. 94, no. 4, pp. 2337–2340, aug 2003. [Online]. Available: <http://aip.scitation.org/doi/10.1063/1.1593800>
- [152] Y. Gu *et al.*, “Zn-Se-Te multilayers with submonolayer quantities of Te: Type-II quantum structures and isoelectronic centers,” *Physical Review B*, vol. 71, no. 4, p. 045340, jan 2005. [Online]. Available: <https://link.aps.org/doi/10.1103/PhysRevB.71.045340>
- [153] M. Jo *et al.*, “Luminescence study on evolution from Te isoelectronic centers to type-II ZnTe quantum dots grown by metalorganic molecular-beam epitaxy,” *Journal of Crystal Growth*, vol. 301-302, no. SPEC. ISS., pp. 277–280, apr 2007. [Online]. Available: <http://linkinghub.elsevier.com/retrieve/pii/S0022024806014588>
- [154] S. Francoeur and S. Marcet, “Effects of symmetry-breaking perturbations on excitonic states bound to systems of reduced symmetry,” *Journal of Applied Physics*, vol. 108, no. 4, p. 043710, aug 2010. [Online]. Available: <http://aip.scitation.org/doi/10.1063/1.3457851>
- [155] G. Éthier-Majcher, “Contrôle optique de qubits liés à des centres isoélectroniques d’azote dans le GaAs,” Ph. D. dissertation, Département de génie physique, Polytechnique Montréal, Montréal, Québec, 2016. [Online]. Available: <https://publications.polymtl.ca/2191/>
- [156] P. St-Jean, “Dynamics of excitonic complexes bound to isoelectronic centers: toward the realization of optically addressable qubits,” Ph. D. dissertation, Département de génie physique, Polytechnique Montréal, Montréal, Québec, 2016. [Online]. Available: <https://publications.polymtl.ca/2329/>

- [157] C. F. Klingshirn, “The Concept of Polaritons,” in *Semiconductor Optics*, 4th ed., ser. Graduate Texts in Physics, W. T. Rhodes, H. E. Stanley, and R. Needs, Eds. Berlin, Heidelberg, Germany: Springer Berlin Heidelberg, 2012, ch. 5, pp. 97–128. [Online]. Available: <http://link.springer.com/10.1007/978-3-642-28362-8>
- [158] C. F. Klingshirn, “Ensemble of Uncoupled Oscillators,” in *Semiconductor Optics*, 4th ed., ser. Graduate Texts in Physics, W. T. Rhodes, H. E. Stanley, and R. Needs, Eds. Berlin, Heidelberg, Germany: Springer Berlin Heidelberg, 2012, ch. 4, pp. 77–95. [Online]. Available: <http://link.springer.com/10.1007/978-3-642-28362-8>
- [159] M. Fox, “Phonons,” in *Optical Properties of Solids*, 1st ed. Brussels, Belgium: Oxford University Press, 2001, ch. 10, pp. 204–226.
- [160] C. F. Klingshirn, “Excitons, Biexcitons and Trions,” in *Semiconductor Optics*, 4th ed., ser. Graduate Texts in Physics, W. T. Rhodes, H. E. Stanley, and R. Needs, Eds. Berlin, Heidelberg, Germany: Springer Berlin Heidelberg, 2012, ch. 9, pp. 249–271. [Online]. Available: <http://link.springer.com/10.1007/978-3-642-28362-8>
- [161] P. Y. Yu and M. Cardona, “Excitons,” in *Fundamentals of Semiconductors*, 4th ed., H. E. Stanley and W. T. Rhodes, Eds. Berlin, Heidelberg, Germany: Springer Berlin Heidelberg, 2010, ch. 6.3, pp. 276–292.
- [162] C. Boemare *et al.*, “Observation of Fabry-Pérot modes in the upper branch of the polariton in ZnSe-GaAs epilayers,” *Physical Review B*, vol. 51, no. 12, pp. 7954–7957, mar 1995. [Online]. Available: <https://link.aps.org/doi/10.1103/PhysRevB.51.7954>
- [163] J. Kasprzak *et al.*, “Bose-Einstein condensation of exciton polaritons,” *Nature*, vol. 443, no. 7110, pp. 409–414, sep 2006. [Online]. Available: <http://www.nature.com/articles/nature05131>
- [164] H. Venghaus and R. Lambrich, “Magnetorefectance of the $\Gamma_6 - \Gamma_8$ exciton ground state in cubic ZnSe,” *Solid State Communications*, vol. 25, no. 2, pp. 109–112, jan 1978. [Online]. Available: <https://linkinghub.elsevier.com/retrieve/pii/003810987890368X>
- [165] B. Sermage and G. Fishman, “Resonant Brillouin Scattering of Polaritons in ZnSe: Heavy and Light Excitons,” *Physical Review Letters*, vol. 43, no. 14, pp. 1043–1046, oct 1979. [Online]. Available: <https://link.aps.org/doi/10.1103/PhysRevLett.43.1043>
- [166] B. Sermage and G. Fishman, “Excitons and polaritons in ZnSe,” *Physical Review B*, vol. 23, no. 10, pp. 5107–5118, may 1981. [Online]. Available: <https://link.aps.org/doi/10.1103/PhysRevB.23.5107>

- [167] Y. Chen *et al.*, “Interference of the Exciton-Polariton Waves in GaAs Thin Layers,” *Europhysics Letters*, vol. 14, no. 5, pp. 483–488, mar 1991. [Online]. Available: <https://iopscience.iop.org/article/10.1209/0295-5075/14/5/016>
- [168] D. A. Steck, “Atom-Field Interaction,” in *Quantum and Atom Optics*. Eugene, USA: University of Oregon, 2007, ch. 5.1, pp. 149–155. [Online]. Available: <https://atomoptics.uoregon.edu/~dsteck/teaching/>
- [169] D. A. Steck, “Rabi Flopping,” in *Quantum and Atom Optics*. Eugene, USA: University of Oregon, 2007, ch. 5.2, pp. 155–159. [Online]. Available: <https://atomoptics.uoregon.edu/~dsteck/teaching/>
- [170] D. A. Steck, “Optical Bloch Equations,” in *Quantum and Atom Optics*. Eugene, USA: University of Oregon, 2007, ch. 5.5, pp. 175–184. [Online]. Available: <https://atomoptics.uoregon.edu/~dsteck/teaching/>
- [171] D. A. Steck, “Dressed States,” in *Quantum and Atom Optics*. Eugene, USA: University of Oregon, 2007, ch. 5.3, pp. 159–164. [Online]. Available: <https://atomoptics.uoregon.edu/~dsteck/teaching/>
- [172] A. Berthelot *et al.*, “Unconventional motional narrowing in the optical spectrum of a semiconductor quantum dot,” *Nature Physics*, vol. 2, no. 11, pp. 759–764, nov 2006. [Online]. Available: <http://www.nature.com/articles/nphys433>
- [173] A. Berthelot *et al.*, “Voltage-controlled motional narrowing in a semiconductor quantum dot,” *New Journal of Physics*, vol. 11, no. 9, p. 093032, sep 2009. [Online]. Available: <https://iopscience.iop.org/article/10.1088/1367-2630/11/9/093032>
- [174] J. Houel *et al.*, “Probing Single-Charge Fluctuations at a GaA/AlAs Interface Using Laser Spectroscopy on a Nearby InGaAs Quantum Dot,” *Physical Review Letters*, vol. 108, no. 10, p. 107401, mar 2012. [Online]. Available: <https://link.aps.org/doi/10.1103/PhysRevLett.108.107401>
- [175] M. Pont *et al.*, “Restoring the Coherence of Quantum Emitters through Optically Driven Motional Narrowing Forces,” *Nano Letters*, vol. 21, no. 24, pp. 10 193–10 198, dec 2021. [Online]. Available: <https://pubs.acs.org/doi/10.1021/acs.nanolett.1c02898>
- [176] H. S. Nguyen *et al.*, “Optically Gated Resonant Emission of Single Quantum Dots,” *Physical Review Letters*, vol. 108, no. 5, p. 057401, jan 2012. [Online]. Available: <https://link.aps.org/doi/10.1103/PhysRevLett.108.057401>

- [177] A. Reigue, R. Hostein, and V. Voliotis, “Resonance fluorescence of a single semiconductor quantum dot: the impact of a fluctuating electrostatic environment,” *Semiconductor Science and Technology*, vol. 34, no. 11, p. 113001, nov 2019. [Online]. Available: <https://iopscience.iop.org/article/10.1088/1361-6641/ab4362>
- [178] P. Yu and M. Cardona, “Luminescence Excitation Spectroscopy,” in *Fundamentals of Semiconductors*, 4th ed., H. E. Stanley and W. T. Rhodes, Eds. Berlin, Heidelberg, Germany: Springer Berlin Heidelberg, 2010, ch. 7.1.5, pp. 369–375.
- [179] “Zinc selenide (ZnSe) phonon energies,” in *II-VI and I-VII Compounds; Semimagnetic Compounds*, O. Madelung, U. Rössler, and M. Schulz, Eds. Berlin, Heidelberg, Germany: Springer-Verlag, 1999, pp. 1–8. [Online]. Available: http://materials.springer.com/lb/docs/sm_lbs_978-3-540-31359-5_459
- [180] S. Permogorov, “Hot excitons in semiconductors,” *physica status solidi (b)*, vol. 68, no. 1, pp. 9–42, mar 1975. [Online]. Available: <http://doi.wiley.com/10.1002/pssb.2220680102>
- [181] B. D. Gerardot *et al.*, “Manipulating exciton fine structure in quantum dots with a lateral electric field,” *Applied Physics Letters*, vol. 90, no. 4, p. 041101, jan 2007. [Online]. Available: <http://aip.scitation.org/doi/10.1063/1.2431758>
- [182] Y. Tokura *et al.*, “Surface Exciton Polariton in ZnSe,” *Journal of the Physical Society of Japan*, vol. 50, no. 1, pp. 145–153, jan 1981. [Online]. Available: <https://journals.jps.jp/doi/10.1143/JPSJ.50.145>
- [183] V. Türeci *et al.*, “Effect of random field fluctuations on excitonic transitions of individual CdSe quantum dots,” *Physical Review B*, vol. 61, no. 15, pp. 9944–9947, apr 2000. [Online]. Available: <https://link.aps.org/doi/10.1103/PhysRevB.61.9944>
- [184] E. Hecht, “The Fresnel Equations,” in *Optics*, 4th ed. San Francisco, USA: Addison Wesley, 2002, ch. 4.6.2, pp. 113–115.
- [185] T. Amotchkina *et al.*, “Characterization of e-beam evaporated Ge, YbF₃, ZnS, and LaF₃ thin films for laser-oriented coatings,” *Applied Optics*, vol. 59, no. 5, p. A40, feb 2020. [Online]. Available: <https://www.osapublishing.org/abstract.cfm?URI=ao-59-5-A40>
- [186] K. Papatryfonos *et al.*, “Refractive indices of MBE-grown Al_xGa_{1-x}As ternary alloys in the transparent wavelength region,” *AIP Advances*, vol. 11, no. 2, p. 025327, feb 2021. [Online]. Available: <https://aip.scitation.org/doi/10.1063/5.0039631>

- [187] E. Hecht, “Multiple Beam Interference,” in *Optics*, 4th ed. San Francisco, USA: Addison Wesley, 2002, ch. 9.6, pp. 416–425.
- [188] E. Hecht, “Optical Properties of Metals,” in *Optics*, 4th ed. San Francisco, USA: Addison Wesley, 2002, ch. 4.8, pp. 127–131.
- [189] Y. Chen, A. Tredicucci, and F. Bassani, “Bulk exciton polaritons in GaAs microcavities,” *Physical Review B*, vol. 52, no. 3, pp. 1800–1805, jul 1995. [Online]. Available: <https://link.aps.org/doi/10.1103/PhysRevB.52.1800>
- [190] M. Grundmann, “General information,” in *The Physics of Semiconductors*, 2nd ed., W. T. Rhodes, H. E. Stanley, and R. Needs, Eds. Berlin, Heidelberg, Germany: Springer Berlin Heidelberg, 2010, ch. 1.3, pp. 11–16.
- [191] F. Hargart *et al.*, “Probing different regimes of strong field light–matter interaction with semiconductor quantum dots and few cavity photons,” *New Journal of Physics*, vol. 18, no. 12, p. 123031, dec 2016. [Online]. Available: <https://iopscience.iop.org/article/10.1088/1367-2630/aa5198>
- [192] R. Shankar, “Time-Independent Perturbation Theory,” in *Principles of Quantum Mechanics*, 2nd ed. New York, USA: Springer Science+Business Media, 1994, ch. 17, pp. 346–360.
- [193] D. Hulin *et al.*, “Well-size dependence of exciton blue shift in GaAs multiple-quantum-well structures,” *Physical Review B*, vol. 33, no. 6, pp. 4389–4391, mar 1986. [Online]. Available: <https://link.aps.org/doi/10.1103/PhysRevB.33.4389>
- [194] N. Peyghambarian *et al.*, “Blue Shift of the Exciton Resonance due to Exciton-Exciton Interactions in a Multiple-Quantum-Well Structure,” *Physical Review Letters*, vol. 53, no. 25, pp. 2433–2436, dec 1984. [Online]. Available: <https://link.aps.org/doi/10.1103/PhysRevLett.53.2433>
- [195] S. Schmitt-Rink, D. S. Chemla, and D. A. B. Miller, “Theory of transient excitonic optical nonlinearities in semiconductor quantum-well structures,” *Physical Review B*, vol. 32, no. 10, pp. 6601–6609, nov 1985. [Online]. Available: <https://link.aps.org/doi/10.1103/PhysRevB.32.6601>
- [196] S. Rodt *et al.*, “Repulsive exciton-exciton interaction in quantum dots,” *Physical Review B*, vol. 68, no. 3, p. 035331, jul 2003. [Online]. Available: <https://link.aps.org/doi/10.1103/PhysRevB.68.035331>

- [197] S. Francoeur, “The influence of many-body interactions on the luminescence of a single impurity,” 2004.
- [198] J. Conradi and R. R. Haering, “Oscillatory Exciton Emission in CdS,” *Physical Review Letters*, vol. 20, no. 24, pp. 1344–1346, jun 1968. [Online]. Available: <https://link.aps.org/doi/10.1103/PhysRevLett.20.1344>
- [199] C. M. Chow *et al.*, “Phonon-assisted oscillatory exciton dynamics in monolayer MoSe₂,” *npj 2D Materials and Applications*, vol. 1, no. 1, p. 33, dec 2017. [Online]. Available: <http://dx.doi.org/10.1038/s41699-017-0035-1>
- [200] P. Y. Yu and M. Cardona, “Electron-Phonon Interactions,” in *Fundamentals of Semiconductors*, 4th ed., H. E. Stanley and W. T. Rhodes, Eds. Berlin, Heidelberg, Germany: Springer Berlin Heidelberg, 2010, ch. 3.3, pp. 121–136.
- [201] R. K. Kremer *et al.*, “Vibrational and thermal properties of ZnX ($X = \text{Se}, \text{Te}$): Density functional theory (LDA and GGA) versus experiment,” *Physical Review B*, vol. 85, no. 3, p. 035208, jan 2012. [Online]. Available: <https://link.aps.org/doi/10.1103/PhysRevB.85.035208>
- [202] S. Ferahtia, S. Saib, and N. Bouarissa, “Computational studies of mono-chalcogenides ZnS and ZnSe at high- pressures,” *Results in Physics*, vol. 15, p. 102626, 2019. [Online]. Available: <https://doi.org/10.1016/j.rinp.2019.102626>
- [203] P. Y. Yu and M. Cardona, “Phonons in Superlattices,” in *Fundamentals of Semiconductors*, 4th ed., H. E. Stanley and W. T. Rhodes, Eds. Berlin, Heidelberg, Germany: Springer Berlin Heidelberg, 2010, ch. 9.3, pp. 494–511.
- [204] L. Donetti *et al.*, “Acoustic phonon confinement in silicon nanolayers: Effect on electron mobility,” *Journal of Applied Physics*, vol. 100, no. 1, p. 013701, jul 2006. [Online]. Available: <http://aip.scitation.org/doi/10.1063/1.2208849>
- [205] B. Hillebrands *et al.*, “Evidence for the existence of guided longitudinal acoustic phonons in ZnSe films on GaAs,” *Physical Review Letters*, vol. 60, no. 9, pp. 832–835, feb 1988. [Online]. Available: <https://link.aps.org/doi/10.1103/PhysRevLett.60.832>
- [206] G. Lucovsky, M. H. Brodsky, and E. Burstein, “Extension of a Linear Diatomic-Chain Model for the Calculation of Local-Mode Frequencies in Real Crystals,” *Physical Review B*, vol. 2, no. 8, pp. 3295–3302, oct 1970. [Online]. Available: <https://link.aps.org/doi/10.1103/PhysRevB.2.3295>

- [207] D. N. Talwar and B. K. Agrawal, “Local-mode frequencies due to isoelectronic impurities in zinc-blende-type crystals,” *Physical Review B*, vol. 9, no. 6, pp. 2539–2543, mar 1974. [Online]. Available: <https://link.aps.org/doi/10.1103/PhysRevB.9.2539>
- [208] V. K. Kalevich, K. V. Kavokin, and I. A. Merkulov, “Dynamic Nuclear Polarization and Nuclear Fields,” in *Spin Physics in Semiconductors*, ser. Springer Series in Solid-State Sciences, M. I. Dyakonov, Ed. Berlin, Heidelberg, Germany: Springer Berlin Heidelberg, 2008, ch. 11, pp. 306–346.
- [209] K. J. Morse *et al.*, “A photonic platform for donor spin qubits in silicon,” *Science Advances*, vol. 3, no. 7, pp. 1–11, jul 2017. [Online]. Available: <https://www.science.org/doi/10.1126/sciadv.1700930>
- [210] B. Urbaszek *et al.*, “Nuclear spin physics in quantum dots: An optical investigation,” *Reviews of Modern Physics*, vol. 85, no. 1, pp. 79–133, jan 2013. [Online]. Available: <http://link.aps.org/doi/10.1103/RevModPhys.85.79>
- [211] D. Gammon *et al.*, “Electron and Nuclear Spin Interactions in the Optical Spectra of Single GaAs Quantum Dots,” *Physical Review Letters*, vol. 86, no. 22, pp. 5176–5179, may 2001. [Online]. Available: <http://link.aps.org/doi/10.1103/PhysRevLett.86.5176>
- [212] G. Sallen *et al.*, “Nuclear magnetization in gallium arsenide quantum dots at zero magnetic field,” *Nature Communications*, vol. 5, no. 1, p. 3268, dec 2014. [Online]. Available: <http://www.nature.com/articles/ncomms4268>
- [213] F. Heisterkamp *et al.*, “Inhomogeneous nuclear spin polarization induced by helicity-modulated optical excitation of fluorine-bound electron spins in ZnSe,” *Physical Review B*, vol. 92, no. 24, p. 245441, dec 2015. [Online]. Available: <https://link.aps.org/doi/10.1103/PhysRevB.92.245441>
- [214] P. J. Wiesner, R. A. Street, and H. D. Wolf, “Exciton Energy Transfer in GaP:N,” *Physical Review Letters*, vol. 35, no. 20, pp. 1366–1369, nov 1975. [Online]. Available: <https://link.aps.org/doi/10.1103/PhysRevLett.35.1366>
- [215] J. A. Kash, “Exciton tunneling inhibited by disorder in GaAs_{1-x}Px:N,” *Physical Review B*, vol. 29, no. 12, pp. 7069–7072, jun 1984. [Online]. Available: <https://link.aps.org/doi/10.1103/PhysRevB.29.7069>
- [216] P. Leroux-Hugon and H. Mariette, “Stochastic transfer of excitations and enhancement of the NN_α-pair luminescence in GaP:N,” *Physical Review B*, vol. 30, no. 3, pp.

- 1622–1625, aug 1984. [Online]. Available: <https://link.aps.org/doi/10.1103/PhysRevB.30.1622>
- [217] Q. Hong, K. Dou, and X. Zhang, “Radiative and nonradiative recombination of bound excitons in GaP:N. III. Reverse tunneling of bound excitons,” *Physical Review B*, vol. 41, no. 3, pp. 1386–1389, jan 1990. [Online]. Available: <https://link.aps.org/doi/10.1103/PhysRevB.41.1386>
- [218] O. Labeau, P. Tamarat, and B. Lounis, “Temperature Dependence of the Luminescence Lifetime of Single CdSe/ZnS Quantum Dots,” *Physical Review Letters*, vol. 90, no. 25, p. 257404, jun 2003. [Online]. Available: <https://link.aps.org/doi/10.1103/PhysRevLett.90.257404>
- [219] A. V. Aggarwal *et al.*, “Fluctuating exciton localization in giant π -conjugated spoked-wheel macrocycles,” *Nature Chemistry*, vol. 5, no. 11, pp. 964–970, nov 2013. [Online]. Available: <http://www.nature.com/articles/nchem.1758>
- [220] F. Steiner *et al.*, “Spontaneous Fluctuations of Transition Dipole Moment Orientation in OLED Triplet Emitters,” *The Journal of Physical Chemistry Letters*, vol. 6, no. 6, pp. 999–1004, mar 2015. [Online]. Available: <https://pubs.acs.org/doi/10.1021/acs.jpclett.5b00180>
- [221] K. T. Early *et al.*, “Linear Dipole Behavior in Single CdSe-Oligo(phenylene vinylene) Nanostructures,” *ACS Nano*, vol. 3, no. 2, pp. 453–461, feb 2009. [Online]. Available: <https://pubs.acs.org/doi/10.1021/nn800785s>

**APPENDIX A PLE MAPS OF ALL TE₂-BOUND EXCITONS
PRESENTING AN OSCILLATION OF THEIR EMISSION ENERGY AS A
FUNCTION OF THE EXCITATION ENERGY**

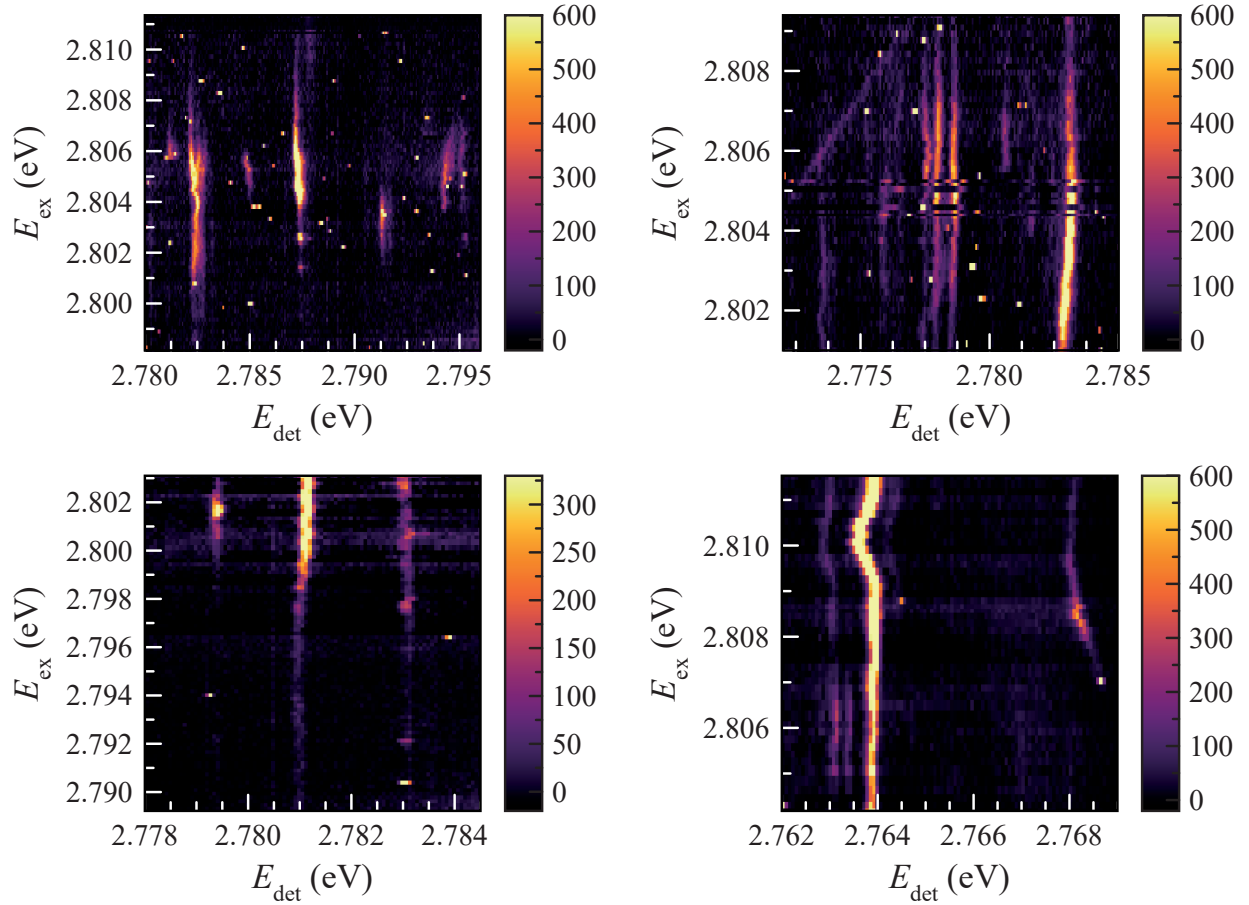


Figure A.1 PLE maps of all excitons presenting an E_{em} oscillation as a function of E_{ex} (1 of 3).

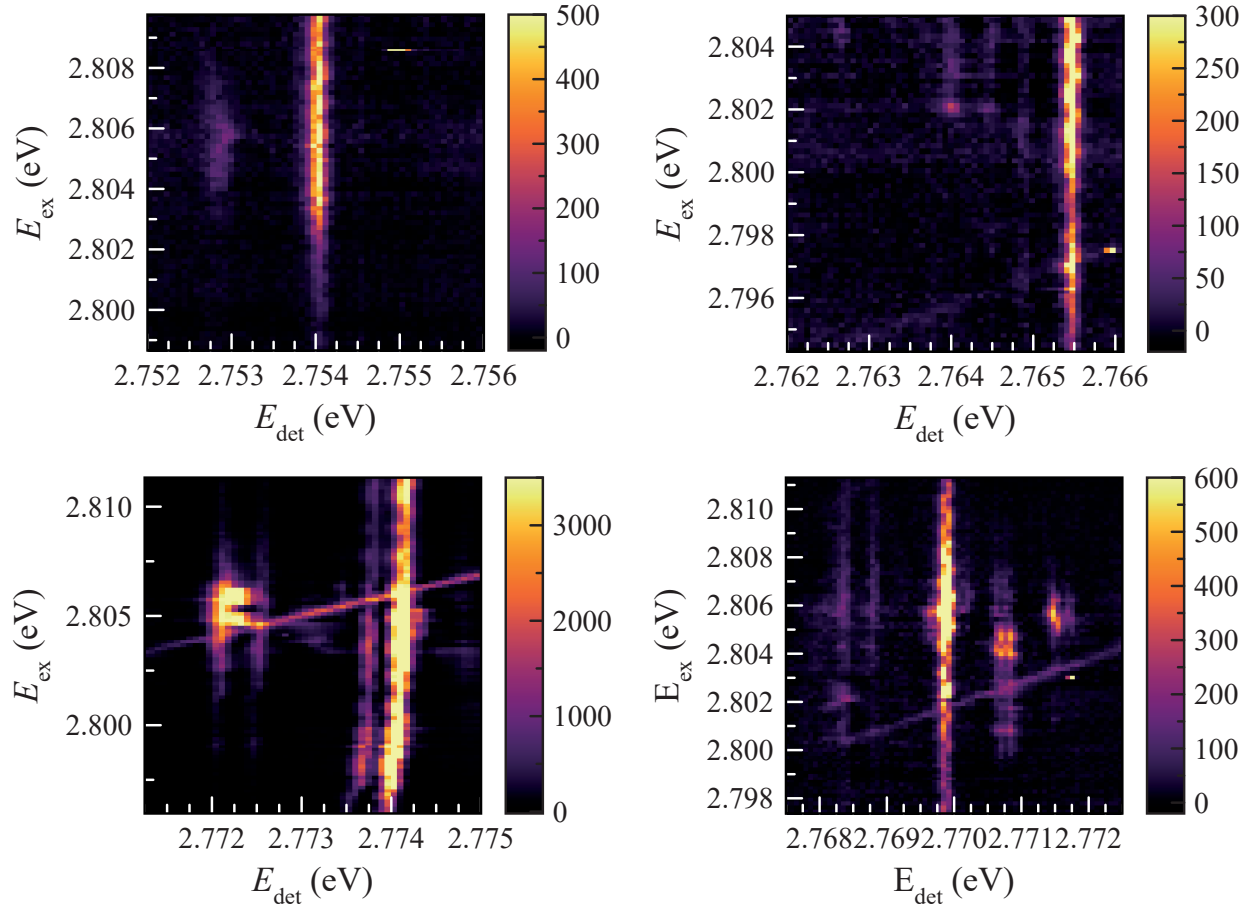


Figure A.2 PLE maps of all excitons presenting an E_{em} oscillation as a function of E_{ex} (2 of 3).

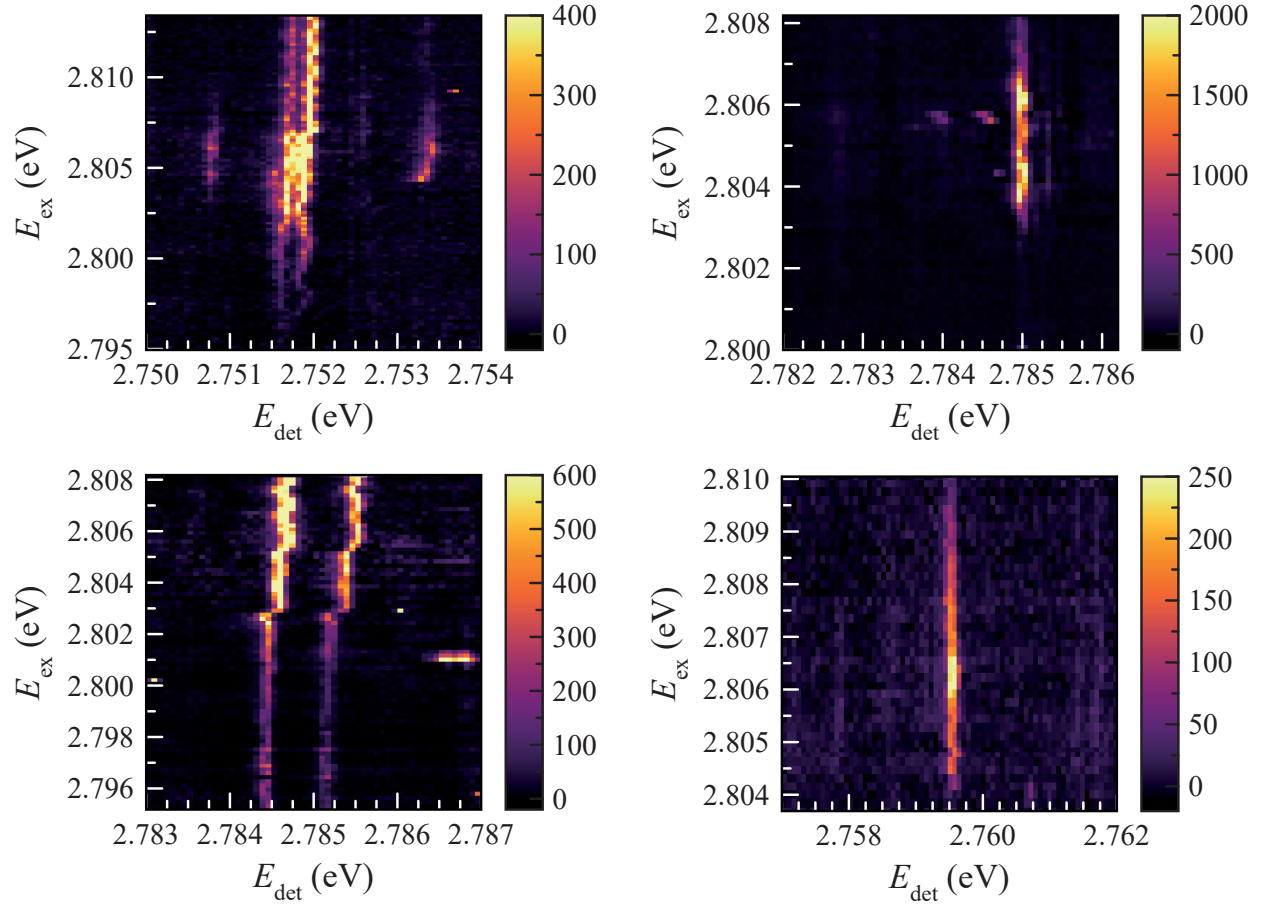


Figure A.3 PLE maps of all excitons presenting an E_{em} oscillation as a function of E_{ex} (3 of 3).

APPENDIX B PERTURBATION HAMILTONIAN IN MATRIX FORM FOR AN EXCITON BOUND TO A C_{2v} -SYMMETRY DEFECT

We have already seen in Sect. 2.2.3 that the total excitonic Hamiltonian in a C_{2v} system can be expressed as a sum of Hamiltonians acting on the electron and the hole alone (H_e and H_h), plus an exchange term involving both (H_{ex}). The unperturbed electron and hole energies are not presented here, as we take interest only in the perturbations in our discussion, more precisely in the effect of an electric field or a magnetic field on the excitonic energy levels. The following treatment is taken from Ref. [154] and concerns only the spin and angular parts of the excitonic wavefunction.

The general form of the perturbation Hamiltonian for the electron in its spin basis and for any kind of perturbation is:

$$H_e = c_1 Z_+ + 2c_2 \sigma_x Y_- + 2c_3 \sigma_y X_- + 2c_4 \sigma_z R_-, \quad (\text{B.1})$$

where the c_i ($i = \{1, 2, 3, 4\}$) are parameters depending on the perturbation, the $+$ ($-$) subscript refers to time-reversal (anti-) symmetry and the σ_i ($i = \{x, y, z\}$) are Pauli matrices. X , Y , Z and R refer respectively to perturbations of Γ_2 , Γ_4 , Γ_1 and Γ_3 irreps. In matrix form, with the C_{2v} exciton wavefunction basis presented in Sect. 2.2.3 (Eq. 2.4) ordered as $\{|Z_{hh}\rangle, |X_{hh}\rangle, |D_{hh}\rangle, |Y_{hh}\rangle, |Z_{lh}\rangle, |X_{lh}\rangle, |D_{lh}\rangle, |Y_{lh}\rangle\}$, this leads to:

$$H_e = \begin{bmatrix} c_1 Z_+ & -ic_3 X_- & -ic_4 R_- & -ic_2 Y_- \\ ic_3 X_- & c_1 Z_+ & -ic_2 Y_- & ic_4 R_- \\ ic_4 R_- & ic_2 Y_- & c_1 Z_+ & -ic_3 X_- \\ ic_2 Y_- & -ic_4 R_- & ic_3 X_- & c_1 Z_+ \end{bmatrix} \quad (\text{B.2})$$

which must be extended to a 8×8 basis by a Kronecker product with a 2×2 identity matrix, $H_e^{(8 \times 8)} = \mathbb{1}^{(2 \times 2)} \otimes H_e$.

The hole perturbation Hamiltonian is expressed as follows in its total angular-momentum

basis, which only considers $J = 3/2$ holes:

$$\begin{aligned}
H_h = & 4 \left(v_1 J_z^2 + v_2 J_x^2 + v_3 J_y^2 \right) Z_+ + \frac{2}{\sqrt{3}} v_4 \{J_y, J_z\} Y_+ \\
& + \frac{2}{\sqrt{3}} v_5 \{J_z, J_x\} X_+ + \frac{2}{\sqrt{3}} v_6 \{J_x, J_y\} R_+ \\
& + \frac{4}{\sqrt{3}} v_7 \{J_x, \{J_y, J_z\}\} Z_- + \left(2v_8 J_x + 8v_9 J_x^3 + 4v_{10} \{J_x, J_y^2 - J_z^2\} \right) Y_- \\
& + \left(2v_{11} J_y + 8v_{12} J_y^3 + 4v_{13} \{J_y, J_z^2 - J_x^2\} \right) X_- \\
& + \left(2v_{14} J_z + 8v_{15} J_z^3 + \frac{2}{\sqrt{3}} v_{16} \{J_z, J_x^2 - J_y^2\} \right) R_-
\end{aligned} \tag{B.3}$$

with v_i ($i = \{1, 2, \dots, 16\}$) constant parameters and J_i ($i = \{x, y, z\}$) the 4×4 total angular-momentum matrices. The same Hamiltonian in matrix form in the C_{2v} exciton basis is:

$$H_h = \begin{bmatrix} z_1 Z_+ & 0 & 0 & 0 & -z_3 Z_+ & v_5 X_+ & -v_6 R_+ & v_4 Y_+ \\ -ix_3 X_- & z_1 Z_+ & 0 & 0 & -v_5 X_+ & -z_3 Z_+ & -v_4 Y_+ & -v_6 R_+ \\ ir_2 R_- & -iy_3 Y_- & z_1 Z_+ & 0 & v_6 R_+ & v_4 Y_+ & -z_3 Z_+ & -v_5 X_+ \\ iy_3 Y_- & ir_2 R_- & ix_3 X_- & z_1 Z_+ & -v_4 Y_+ & v_6 R_+ & v_5 X_+ & -z_3 Z_+ \\ iv_7 Z_- & -ix_1 X_- & -iv_{16} R_- & -iy_1 Y_- & z_2 Z_+ & 0 & 0 & 0 \\ ix_1 X_- & iv_7 Z_- & iy_1 Y_- & -iv_{16} R_- & -ix_2 X_- & z_2 Z_+ & 0 & 0 \\ iv_{16} R_- & -iy_1 Y_- & iv_7 Z_- & ix_1 X_- & -ir_1 R_- & iy_2 Y_- & z_2 Z_+ & 0 \\ iy_1 Y_- & iv_{16} R_- & -ix_1 X_- & iv_7 Z_- & -iy_2 Y_- & -ir_1 R_- & ix_2 X_- & z_2 Z_+ \end{bmatrix} \tag{B.4}$$

where all non-diagonal elements must be summed with their conjugate transpose in order for the Hamiltonian to be hermitian. x_i , y_i , z_i and r_j ($i = \{1, 2, 3\}$, $j = \{1, 2\}$) are new parameters function of the v_i :

$$\begin{aligned}
x_1 &= \sqrt{3} (v_{11} + 7v_{12} + v_{13}) & y_1 &= \sqrt{3} (-7v_9 - v_8 + v_{10}) \\
x_2 &= 2v_{11} + 20v_{12} - 3v_{13} & y_2 &= 2v_8 + 20v_9 - 3v_{10} \\
x_3 &= 6v_{12} + 3v_{13} & y_3 &= -6v_9 + 3v_{10} \\
z_1 &= 9v_1 + 3v_2 + 3v_3 & r_1 &= \sqrt{3} (v_{11} + 7v_{12} + v_{13}) \\
z_2 &= v_1 + 7v_2 + 7v_3 & r_2 &= 2v_{11} + 7v_{12} - 3v_{13} \\
z_3 &= 2\sqrt{3} (-v_2 + v_3)
\end{aligned} \tag{B.5}$$

The explicit dependence on external perturbations of the exchange-interaction Hamiltonian, as presented in Sect. 2.2.3 of the main text, has been left out for the sake of simplicity.

B.1 Effect of an electric field

Electric fields along x , y and z , which are even under time-reversal symmetry, are represented by X_+ , Y_+ and Z_+ (neglecting quadratic terms). Thus, from Eq. B.2, only E_z affects an electron by equally shifting all of its energy levels by the same amount, leading to no change in their energy separation.

However, electric fields cause mixing between LH and HH states leading to different energy shifts depending on the states involved, as it can be seen in the upper anti-diagonal block of the B.4 matrix. Thus, the hole Hamiltonian contributes to an energy separation change between excitonic levels when an electric field is applied.

The presence of an electric field also modifies the exchange interaction by changing the spatial overlap of the electron and hole wavefunctions, as mentioned in Sect. 4.5.

B.2 Effect of a magnetic field

Perturbations linear in magnetic field are represented by X_- (B_y), Y_- (B_x) and R_- (B_z), while those quadratic (B_x^2, B_y^2, B_z^2) transform as Z_+ . Electron wavefunctions expressed in the C_{2v} -symmetry basis are, similarly to the electric field case, equally affected by Z_+ perturbations, but this time mixed by X_- , Y_- and R_- terms. Hole wavefunctions, for their part, are again mixed by all four perturbation types. A magnetic field of any orientation therefore gives rise to a shift and lift of degeneracy of all excitonic energy levels.

APPENDIX C SECOND-ORDER ENERGY SHIFT OF AN HYDROGEN-LIKE EXCITON INDUCED BY THE DC STARK EFFECT

One is looking to evaluate the second-order correction to the energy of an hydrogen-like exciton under an electric field \mathcal{E} , i.e. the following sum:

$$E_{100}^{(2)} = e^2 \mathcal{E}^2 \sum_{nlm \neq 100} \frac{\langle 100 | z | nlm \rangle \langle nlm | z | 100 \rangle}{E_{100}^{(0)} - E_{nlm}^{(0)}}. \quad (\text{C.1})$$

In Eq. C.1, $E_{nlm}^{(0)}$ stands for the eigenvalue of the hydrogen Hamiltonian $H_0 = [-\hbar^2/(2m_X)]\nabla^2 - e^2/(4\pi\epsilon r^2)$ associated with the $|nlm\rangle$ eigenstate, with e the elementary charge, m_X the exciton reduced mass and ϵ is the permittivity of ZnSe.

One would therefore like to exploit the completeness relation $\sum_{nlm} |nlm\rangle \langle nlm| = 1$ to remove the sum. First, one must get rid of the denominator by defining an operator Ω that commutes with H_0 to give the Stark effect Hamiltonian $H_{\text{SE}} = e\mathcal{E}z$ for an electric field \mathcal{E} along z [192]:

$$H_{\text{SE}} |100\rangle = [\Omega, H_0] |100\rangle = (\Omega H_0 - H_0 \Omega) |100\rangle. \quad (\text{C.2})$$

With $z = r \cos \theta$ in spherical coordinates and $|100\rangle = 1/(\sqrt{\pi}a_0^{3/2})e^{-r/a_0}$, where a_0 is the exciton Bohr radius, it can be verified that Ω is:

$$\Omega = -\frac{m_X a_0 e \mathcal{E}}{\hbar^2} \cos \theta \left(\frac{r^2}{2} + a_0 r \right). \quad (\text{C.3})$$

Using this result in Eq. C.1 leads to:

$$\begin{aligned} E_{100}^{(2)} &= \sum_{nlm \neq 100} \frac{\langle 100 | H_{\text{SE}} | nlm \rangle \langle nlm | \Omega H_0 - H_0 \Omega | 100 \rangle}{E_{100}^{(0)} - E_{nlm}^{(0)}} \\ &= \sum_{nlm \neq 100} \frac{\langle 100 | H_{\text{SE}} | nlm \rangle (E_{100}^{(0)} - E_{nlm}^{(0)}) \langle nlm | \Omega | 100 \rangle}{E_{100}^{(0)} - E_{nlm}^{(0)}} \\ &= \sum_{nlm} \langle 100 | H_{\text{SE}} | nlm \rangle \langle nlm | \Omega | 100 \rangle - \langle 100 | H_{\text{SE}} | 100 \rangle \langle 100 | \Omega | 100 \rangle \\ &= \langle 100 | H_{\text{SE}} \Omega | 100 \rangle, \end{aligned} \quad (\text{C.4})$$

where the completeness relation has been used and $\langle 100 | H_{\text{SE}} | 100 \rangle = 0$.

With the expressions for Ω (Eq. C.3) and $|100\rangle$, one can calculate the final matrix element in Eq. C.4 and get the energy correction:

$$E_{100}^{(2)} = -\frac{9}{4} \left(4\pi\epsilon a_0^3 \mathcal{E}^2 \right). \quad (\text{C.5})$$

APPENDIX D HYPERFINE HAMILTONIAN IN THE COUPLED HH EXCITON-NUCLEAR SPIN BASIS

The basis for the development of the hyperfine Hamiltonian H_{hf} is the tensor product between the HH C_{2v} exciton wavefunctions of Eq. 2.4 and the two z projections of a nuclear spin, $|\uparrow_n\rangle$ ($I_z = 1/2$) and $|\downarrow_n\rangle$ ($I_z = -1/2$): $|X, \uparrow_n\rangle$, $|X, \downarrow_n\rangle$, $|Y, \uparrow_n\rangle$, $|Y, \downarrow_n\rangle$, $|Z, \uparrow_n\rangle$, $|Z, \downarrow_n\rangle$, $|D, \uparrow_n\rangle$ and $|D, \downarrow_n\rangle$. Without hyperfine interaction, basis elements with the same excitonic part are degenerate.

One is looking now to express H_{hf} :

$$H_{\text{hf}} = A' \left[S_z I_z + \frac{1}{2} (S_+ I_- + S_- I_+) \right] \quad (\text{D.1})$$

in matrix form. Here, as mentioned in Sect. 5.2.4, $A' = AV_0|\psi(\mathbf{r}_n)|^2$ describes the strength of the interaction (with A the hyperfine constant, V_0 the unit cell volume and $\psi(\mathbf{r}_n)$ the electron envelope wavefunction at the position of the nucleus), S_z and I_z are the z -projection spin operators for the electron and the nucleus and S_{\pm} and I_{\pm} are the corresponding ladder operators.

Even though H_{hf} does not act on the hole, the spin of the latter is still considered in the calculation of the matrix elements. For example, $H_{\text{hf},11}$ gives:

$$\begin{aligned} H_{\text{hf},11} &= \langle X, \uparrow_n | H_{\text{hf}} | X, \uparrow_n \rangle = \frac{1}{\sqrt{2}} (\langle \downarrow \uparrow | + \langle \uparrow \downarrow |) \langle \uparrow_n | H_{\text{hf}} \frac{1}{\sqrt{2}} (|\downarrow \uparrow\rangle + |\uparrow \downarrow\rangle) |\uparrow_n\rangle \\ &= \frac{1}{2} (\langle \uparrow \uparrow | \uparrow \rangle \langle \downarrow \uparrow_n | H_{\text{hf}} |\downarrow \uparrow_n\rangle + \langle \uparrow \uparrow | \downarrow \rangle \langle \downarrow \uparrow_n | H_{\text{hf}} |\uparrow \uparrow_n\rangle + \langle \downarrow \uparrow | \uparrow \rangle \langle \uparrow \uparrow_n | H_{\text{hf}} |\downarrow \uparrow_n\rangle \\ &\quad + \langle \downarrow \uparrow | \downarrow \rangle \langle \uparrow \uparrow_n | H_{\text{hf}} |\uparrow \uparrow_n\rangle) \\ &= \frac{A'}{2} \left(\langle \downarrow \uparrow_n | S_z I_z + \frac{1}{2} (S_+ I_- + S_- I_+) |\downarrow \uparrow_n\rangle + \langle \uparrow \uparrow_n | S_z I_z + \frac{1}{2} (S_+ I_- + S_- I_+) |\uparrow \uparrow_n\rangle \right) \\ &= \frac{A'}{2} (\langle \downarrow \uparrow_n | S_z I_z |\downarrow \uparrow_n\rangle + \langle \uparrow \uparrow_n | S_z I_z |\uparrow \uparrow_n\rangle) = \frac{A' \hbar^2}{8} (-1 + 1) = 0 \end{aligned} \quad (\text{D.2})$$

Indeed, the eigenvalues of the S_z and I_z operators are $\pm \hbar/2$, while $S_{\pm} |s_z\rangle = \hbar \sqrt{s(s+1) - s_z(s_z \pm 1)} |s_z \pm 1\rangle$ and $I_{\pm} |i_z\rangle = \hbar \sqrt{i(i+1) - i_z(i_z \pm 1)} |i_z \pm 1\rangle$. Here, s and i stand for the norm of electron and nuclear spins, and s_z and i_z are their z projections.

The final Hamiltonian is:

$$H_h = \frac{A'\hbar^2}{4} \begin{bmatrix} 0 & 0 & i & 0 & 0 & 1 & 0 & -i \\ 0 & 0 & 0 & -i & -1 & 0 & -i & 0 \\ -i & 0 & 0 & 0 & 0 & i & 0 & 1 \\ 0 & i & 0 & 0 & i & 0 & -1 & 0 \\ 0 & -1 & 0 & -i & 0 & 0 & -i & 0 \\ 1 & 0 & -i & 0 & 0 & 0 & 0 & i \\ 0 & i & 0 & -1 & i & 0 & 0 & 0 \\ i & 0 & 1 & 0 & 0 & -i & 0 & 0 \end{bmatrix} \quad (\text{D.3})$$

Its diagonalization leads to two states of energy $-3A'\hbar^2/4$ and six states of energy $A'\hbar^2/4$, which are unsurprisingly the same eigenvalues as the simpler case of a single electron spin and a nuclear spin.